DISSERTATION

USING ANTIMONY AS A MODEL ANODE TO STUDY THE CHEMICAL AND MECHANICAL STABILITY OF ELECTRODES IN LI-ION AND NEXT GENERATION BATTERIES

Submitted by

Maxwell Connor Schulze

Department of Chemistry

In partial fulfillment of the requirements

For the Degree of Doctor of Philosophy

Colorado State University

Fort Collins, Colorado

Fall 2019

Doctoral Committee:

Advisor: Amy Prieto

Matthew Shores
James Neilson
Chris Weinberger

ABSTRACT

USING ANTIMONY AS A MODEL ANODE TO STUDY THE CHEMCIAL AND MECHANICAL STABILITY OF ELECTRODES IN LI-ION AND NEXT GENERATION BATTERIES

As humanity grapples with the ever-increasing global demand for electrical energy, we are concurrently trying to curb global greenhouse gas emissions on massive scales to avoid potentially catastrophic changes in the global climate. Strategies to address these problems include transitioning away from a fossil fuel powered society where electrical grid energy is instead generated from renewable sources and internal combustion engine vehicles are replaced with electrified ones. Both of these transitions require energy storage technologies that can deliver high efficiencies, large energy densities, large power outputs, long lifetimes, and good safety factors all while remaining affordable and sustainable to produce. Li-ion batteries have already proven their merit as an effective energy storage technology with high enough energy densities, low enough costs, and long enough lifetimes to be ubiquitous in powering portable electronic devices. While the performance metrics of Li-ion batteries have also started to allow all-electric vehicles and grid-level energy storage to become commercially feasible, limitations in their cycle lifetimes and safety concerns arising from their flammable nature still limit their widespread implementation for these application. Ultimately, the interactions between constituent materials of a battery and the modes of their degradation limit a battery's performance. As such, research to understand and mitigate the degradation of battery materials,

including those that move beyond Li-ion battery chemistry, is necessary to promote the widespread, tunable, and diverse use of batteries in overcoming the challenges discussed.

Herein, I present a study that uses antimony as a model anode material to develop an understanding of the critical limiting factors of next-generation battery materials. Antimony-based anodes exhibit degradation and concomitant short cycle-lifetimes that are typical of many promising next-generation battery materials, including those that move beyond Li-ion chemistries. Thus, antimony-based model anodes can be used to study such degradation, which is primarily due to chemical and mechanical instability of the electrode and its interfaces with other battery cell components. In the following chapters, strategies to improve the chemical or mechanical stability of the antimony-anode and its interfaces are developed and can be more generally applied to other promising next-generation electrode materials.

The following is a journal format dissertation, with each chapter being a document that is published, submitted, or in preparation to a peer-reviewed journal. The first chapter reviews the basic operating principles of rechargeable batteries as well as critically discusses the electrochemical experiments that are common in battery materials research. In particular, the first chapter emphasizes the limits of testing half-cell configurations in representing the cycle lifetimes of full-cell batteries, the key metric needed for long cycle lifetimes in full-cells being extremely high coulombic efficiencies. Chapter two explores and develops mitigation strategies for detrimental mechano-chemical interactions at the interface between the active Cu-Sb anode and the current collector that arise from the existence of a ternary Li-Cu-Sb phase with structural similarity to both Cu_2Sb and Li_3Sb. While the existence of the ternary phase results in good reversibility of Cu-Sb electrodes when cycled in Li-ion batteries, it also results in the formation of voids at Cu-Sb interfaces that exacerbates delamination during cycling to result in short cycle lifetimes.

Chapter three develops a procedure for the electrodeposition of antimony carbon nanotube composites as a strategy to address the bulk mechanical instability of the anode during cycling in Li- and Na-ion batteries. Results of chapter three reveal significant chemical instability at the anode-electrolyte interface and motivate much of the work performed in chapter four, which departs from focusing on antimony as an anode material and instead uses antimony to explore the properties of anode coatings. Chapter four is a systematic study that explores how annealing conditions affect properties of polyacrylonitrile coatings relevant to the chemical stabilization of the electrode-electrolyte interface. This study reveals that ion diffusion in annealed polyacrylonitrile films is correlated to the delocalization of electrons in conjugated domains within the polyacrylonitrile films. Finally, chapter five reviews the materials properties that have made the Li-ion battery so successful, such as the mechanically and chemically stable interfacial layers that form at the electrode-electrolyte interfaces. The chapter additionally highlights some recent progress in the battery materials field and suggests that electrolyte additives, interfacial coatings, and solid-state electrolytes as the most impactful types of materials to continue researching and developing for the future.

ACKNOWLEDGEMENTS

I think it is easy to forget that as individuals we are not isolated entities, but rather beings that are shaped and influenced by those around us. As such, I would like to recognize all those who played a role in my desire and ability to produce this dissertation.

First, I would like to thank the past and present members of the Prieto research group for creating such a good group environment. I'd especially like to thank Dr. Everett Jackson, Dr. Dan Agocs, Dr. Max Braun, Jacob Schneider, Becca Miller, Jeffrey Ma, Chris Rom, and Leslie Kraynak for many of the insightful scientific discussions and feedback that have helped to shape me as a scientist. I cannot imagine a more generous advisor than Dr. Amy Prieto; thank you for mentoring me and giving me the opportunity to become a successful scientist. Your group has been incredibly enjoyable to be a part of.

I would also like to thank the friends I've made in graduate school. Amy, Ethan, Paul, Becca, Andy, Matt, and Tonya, thanks for all the great times hackysacking during recess or ripping around on mountain bikes. The weekend (and weekday) backcountry ski tours we've been on are largely responsible for my enduring enthusiasm and optimism during graduate school.

I am also deeply grateful to my family, who has had the largest influence on my academic career. Peter, Voltron, Stephanie, and Carl, thank you for all you've done to make me who I am today; you've been incredible role models both inside and outside of science.

Finally, to my amazing wife, Amy: Thank you for everything you do for us. My PhD (and most everything else I do) has been made possible with the foundation that you help create. Let's keep striving to be better scientists so we can help make the world a better place!

DEDICATION

To Werner Schulze (Opa)

1929-2019

Alles hat ein Ende, nur die Wurst hat zwei

TABLE OF CONTENTS

CHAPTER 1 – CRITICAL CONSIDERATIONS IN THE DESIGN AND ELECTROCHEMCIAL TESTING OF BATTERY ELECTRODE MATERIALS[1]

Overview

Next generation batteries will use electrode materials that are known to exhibit significant energy storage density improvements over current battery technologies. However, the performance reported for many electrode materials cycled in half-cell configurations can be unrepresentative of their performance in full-cell configurations; this factor results in many electrode materials reported with superior performance never being developed to commercialization. Here, we review critical design factors and electrochemical experiments that are commonly used in the study of new electrode materials. We make recommendations on how to report data from these experiments so that accurate conclusions can be drawn from the results to ensure progress in the development of next generation electrode materials.

Introduction

Rechargeable batteries are already ubiquitous in modern society, being a critical technology that has enabled the widespread use of portable consumer electronics. The lithium-ion battery with intercalation electrodes in particular is the most widespread chemistry used in rechargeable batteries due to its long lifetime, high efficiency, and high energy storage density compared to other rechargeable electrochemical storage technologies. Lithium-ion batteries even see application in all electric vehicles and storage of large-scale energy to help accommodate transient renewable power sources. However, the performance metrics desired for these technologies are starting to exceed what current Li-ion battery materials can provide. It is thus

---

[1] This chapter will be submitted to the American Chemical Society Journal: Chemistry of Materials for review with Maxwell C. Schulze and Amy L. Prieto as authors. The paper written by Maxwell C. Schulze with guidance from Amy L. Prieto.

critical that new energy storage materials be developed that deliver higher energy/power densities while maintaining low cost, environmental sustainability, and adequate safety factors.

There are many known electrode materials including high capacity alloy anodes, alkali metal anodes, high voltage cathodes, and conversion cathodes that can theoretically provide much higher energy storage densities than those used currently in Li-ion battery technology. However, despite nearly 50 years of research of new electrode materials, very few of reported electrodes with superior performance ever get developed to commercial use. This may be in part to prohibitively expensive or non-scalable synthetic procedures, but is also largely attributable to the fact that the vast majority of studies report cycling performance data collected using half-cell configurations, which often are not representative of an electrode's performance in a full-cell battery. Additionally, while a reported electrode may be exhibit superior performance in one performance metric such as deliverable energy density, unless that is balanced with performance metrics like cycle lifetime, the superiority of the electrode material is unusable. Therefore, it is necessary to perform analysis of enough factors to give at least a balanced overview of a battery's most relevant performance metrics: cycle lifetime, energy density, and power density.

Herein, we first review the basics of electrochemical energy storage highlighting in particular the factors that go into the deliverable energy densities for a set of electrode materials. By applying these considerations to a commonly explored class of anode materials, we identify some critical design factors that researchers should consider when studying and reporting on electrode materials in general. While there are other publications that review common methods and protocols used to initially study electrode materials [1], we focus on some pitfalls of these experiments and recommend the most important information to report. In particular, we discuss the limitations of galvanostatic cycling of a half-cell configuration in representing an electrode's performance in a full-cell battery. Finally, we discuss a few other commonly used electrochemical experiments used in the study of electrode material properties such as rate capability experiments, cyclic voltammetry, electrochemical impedance spectroscopy, and intermittent titration techniques. Overall, this document should serve as an introduction and resource to those who are new to the field while still emphasizing some of the most important considerations when performing electrode material research.

Basic Requirements for electrochemical energy storage and practical limits of electrode materials

There are many types of battery cell formats, including small-scale coin/button cells like those typically found in a wristwatch to larger pouch/prismatic cells that are typically found in things like laptop computers and car batteries. Despite their varying external appearances, all cell formats have the same underlying electrode geometry that is shown in Figure 1.1. In such an electrochemical cell, there are two electrodes where redox reactions occur at different potentials, the electrode with the more positive potential being the cathode and the electrode with the more negative potential being the anode. The electrodes are separated by an electrolyte, which selectively conducts charge compensation ions between electrodes, but does not allow electrons through. When a battery delivers its stored energy, the electrons associated with the redox reactions conduct from the anode to the cathode through the current collectors and an external circuit to power the desired device. For the cell to be rechargeable, the redox reactions at each electrode must be reversible with high efficiency. The amount of energy stored by the cell can be estimated using:

$$[\ Energy = V_{average} * Q_{cell}\ ]$$

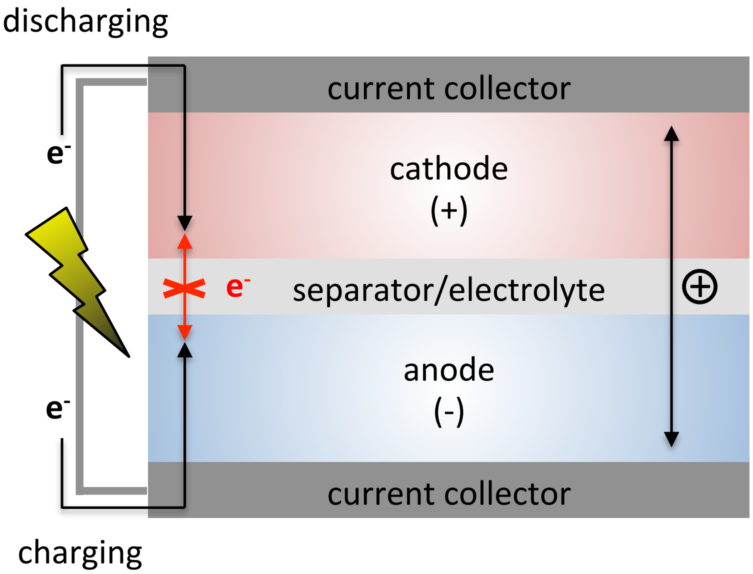

Figure 1.1: A schematic depicting an electrochemical energy storage cell where two electrodes that can conduct both electrons and charge compensating ions are separated by an electrolyte that conducts only the ions. Redox reactions that occur in the electrodes are coupled to electrons that travel through an external circuit to either power a device or recharge the cell.

where the average difference between the redox potentials of each electrode determine the cell potential[2] ($V_{average}$) and the cell capacity (Q_{cell}) is simply a count of how many redox active electrons (and their charge compensating cations) can be stored in the cell. The types, amounts, and configurations of materials used for each electrode determine each of these values.

By knowing an electrode's capacity and redox potential, its theoretical energy storage density when paired with another electrode can be estimated. It is important to note here that the ability to store energy in an electrochemical cell comes from the *pairing* of electrodes at different potentials, and any calculations of the "energy density" of a single electrode material are dubious. As such, it is important to know that the following relationship results in the cell capacity (Q_{cell}) never exceeding the lesser of the electrode capacities (Q_{anode}, $Q_{cathode}$):

$$\frac{1}{Q_{cell}} = \frac{1}{Q_{anode}} + \frac{1}{Q_{cathode}}$$

The capacity of each electrode is typically reported as a gravimetric (mAh/g) or volumetric (mAh/cm^3) value. The gravimetric capacity is determined by the stoichiometry of the ion-storing phases in the electrodes, though it is important not to double count the mass of the stored ions in both electrodes, as the redox-active ions will only be in one electrode or the other.[3] The volumetric capacity is determined using the crystal density of the ion storing phase in the electrodes, and it is important to take into consideration the density of both the parent and host phases to understand the maximum and minimum volumes of each electrode material depending

---

[2] Calculating a cell's energy using $V_{average}$ is still an approximation. To calculate a more accurate energy, especially for electrodes that exhibit multiple redox reaction at different potentials or across a range of potentials, the voltage should be integrated over the entire capacity of the cell:

$$Energy = \int_{0}^{Q_{cell}} V(q)\,dq$$

[3] Li-ions (Li^+) are monovalent so there is one redox-active electron per ion and the electrode capacity is equivalent to the ion stoichiometry. This is in contrast to chemistries using multivalent ions (Mg^{2+}, Al^{3+}) where the electrode capacities are 2 and 3 times the ion stoichiometry, respectively.

on the cell's state of charge. The redox potentials of electrode materials are typically found experimentally, though they can also be predicted using theory [2].

While there are a plethora of known or possible electrode materials to choose to study [3-5], we have chosen to focus on electrode materials for Li-ion batteries, the most heavily commercialized type of rechargeable battery [6], though everything discussed is generally applicable to all electrode materials, including those using commonly considered multivalent ions (Mg^{2+}, Al^{3+}, Ca^{2+}, Zn^{2+}). The prototypical Li-ion battery contains graphite as the anode material and lithium cobalt oxide ($LiCoO_2$) as the cathode material to make a ~3.7 V cell. Table 1.1 shows the redox potentials and capacities for those electrodes along with several other high capacity anode materials that are commonly researched such as Sb, Sn, and Si [3]. Each of these anode materials offers much greater storage capacities than graphite, and their theoretical maximum energy densities when paired with a $LiCoO_2$ cathode can be calculated using the listed values and the equations discussed above. This is also the case if a battery could be designed were the redox reaction at the anode were simply the electrochemical plating and stripping of lithium metal, which would be the anode that could provide that greatest theoretical energy density with any given cathode [6].

In addition to the theoretical maximum energy densities that can be exactly calculated, there are practical considerations that go into the fabrication of an actual battery cell that limit its achievable energy densities. Figure 1.2 (top) depicts a schematic of a full cell stack that can be layered repeatedly (often by rolling/folding) until the desired cell format is achieved. The full-cell stack includes so called "dead" components like the current collects, porous separators, and electrolyte, which are essential to the functioning of the cell but don't contribute any energy storage capacity. The amount of current collector and separator materials are limited only by

Table 1.1: Common Li-ion battery electrode materials and their approximate lithiation potentials and storage capacities. The lithium metal electrode has an "infinite" gravimetric capacity when paired with $LiCoO_2$ due to the mass of the lithium being accounted for in the cathode.

Electrode Material		Lithiated phase	Average Lithiation Potential (V vs. Li/Li^+)	Capacity	
				(mAh/g)	(Ah/L)
Lithium Cobalt Oxide (baseline cathode)		$LiCoO_2$	3.9	150	758
Graphite (baseline anode)		LiC_6	0.125	372	791
High capacity anode materials	Antimony	Li_3Sb	0.948	660	1771
	Tin	$Li_{4.4}Sn$	0.504	993	2111
	Silicon	$Li_{15}Si_4$	0.400	3579	2194
	Lithium (metal)	Li	0	"infinite"	2058

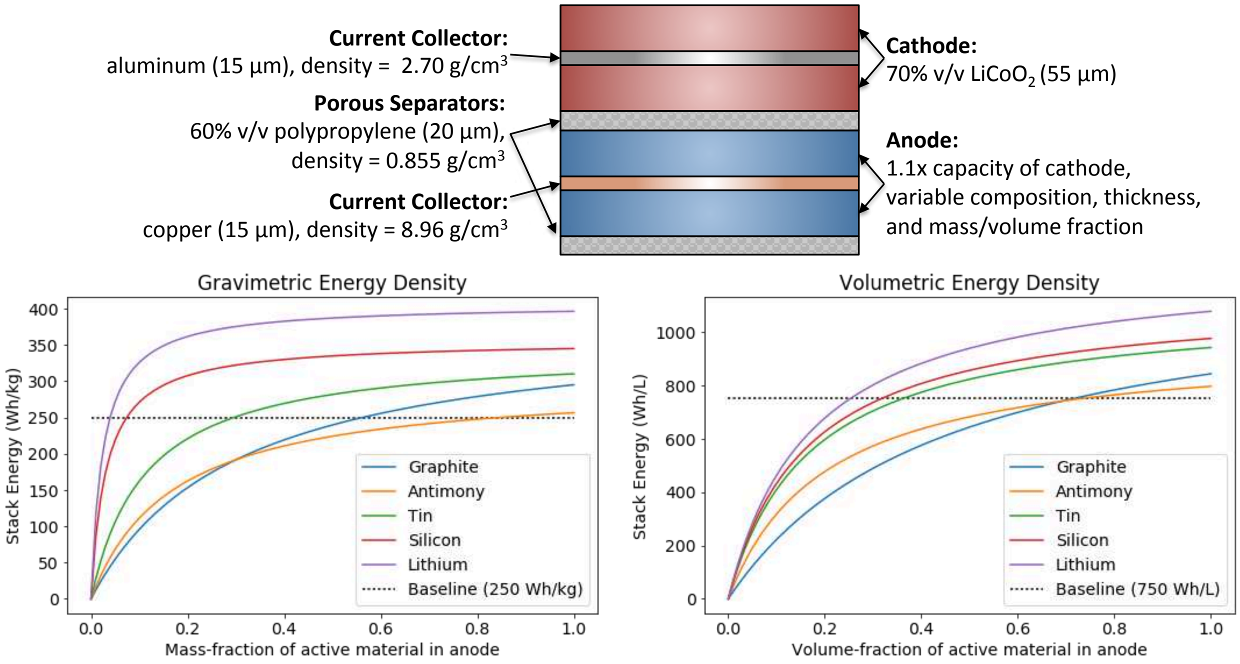

Figure 1.2: (top) The model full-cell stack used to estimate the effect of various anode materials on the full-cell stack energy density. The model was adapted from a review publication by M. N. Obrovac and V. L. Chevrier [3]. The model can be used to estimate energy density values of the full-cell stack using several common anode active materials. The estimated gravimetric/volumetric energy densities as a function of the mass/volume fraction of the active material in the anode are shown on the left and right, respectively. The Python code used to generate these plots can be found in Appendix B.

their processing/manufacturing given that they remain thick enough to provide adequate current flow and prevent internal shorting between electrodes, respectively [7]. The amount of electrolyte is limited to the minimum amount required to maintain optimal ion transfer between electrodes over the lifetime of the cell by efficiently filling all available pore space [8]. The amount of electrolyte needed to achieve this is a complex and non-trivial value to determine. In fact, the decomposition of the electrolyte during charging-discharging cycles can hinder ion transfer and often is the main mechanism that limits a cell's lifetime, as will be discussed later. Most electrolytes are liquid solutions soaked into porous separators but solid electrolytes can double as the separator when used.

Electrodes are typically thought of as the component of the battery containing the active material where the redox reaction occurs. However, they also contain other "dead" components that are often neglected in calculations but are necessary for the electrode to operate with high stability and reversibility. Such dead components include:

1. Binders: keep the active material mechanically consolidated and attached to the current collector.
2. Conductive additives: maintain electron conductivity throughout the entire electrode.
3. Inactive buffer material: stabilize the volume changes of high capacity active materials.
4. Pore space: allows electrolyte to percolate through entire electrode.

Because these "dead" components contribute to the mass and volume of the electrodes, it is important to include the mass and volume fraction of active material in each electrode when calculating their gravimetric or volumetric capacities. These calculations can be taken one step further, accounting for all of the dead components in a full-cell stack to estimate more realistically achievable energy densities from a pair of electrode materials. Figure 1.2 shows the results of such a full-cell stack energy density model that has been modified from a model previously reported by Obrovac and Chevrier [3]. Briefly, the model fixes the porosity and thickness of a $LiCoO_2$ cathode at reasonable values and pairs it with one of the high capacity anode materials listed in Table 1.1. The amount of the anode material is chosen to match 1.1x the absolute capacity provided by the $LiCoO_2$ cathode, and the calculated gravimetric and volumetric energy densities are plotted as a function the mass and volume fraction of the active material in the anode, respectively. The Python code used to perform the calculations and generate the plots can be found in Appendix B.

The horizontal lines in the full-cell stack energy density plots (Figure 1.2, left/right) represent "baseline" energy density values that are typical of actual graphite/$LiCoO_2$ cells with realistic mass/volume fractions less than 1. The other traces show the energy densities achievable when substituting the graphite with one of the high capacity anode materials, with the maximum improvement achievable at a mass/volume fraction equal to 1. In the case of Sb, there is little to no improvement over the baseline energy despite Sb having a larger storage capacity than graphite. This is primarily due to the smaller full-cell voltage of ~2.9 V when Sb is paired with $LiCoO_2$, demonstrating that both the capacity and potential of an electrode need to be taken into consideration. The other high capacity anodes (Sn, Si, and Li) demonstrate ~25-60% maximum achievable improvements (gravimetrically and volumetrically) over the baseline. For the researcher who substitutes a graphite anode with a Si anode (~10 times the gravimetric capacity) and naively expects an order of magnitude improvement in energy density, these results may seem modest and disappointing, but demonstrates the need for such a full-cell analysis to be performed and understood before fantastically-high improvements in energy density are reported.

The full-cell stack energy density model also provides guidance for the practical design of electrodes. By examining the shape of the energy density curves at mass/volume fractions less than 1, the design parameters required to actually provide energy density gains for any give electrode active material can be estimated before any experiments are ever performed. For example, Si and Li both show >30% gravimetric energy density improvements even at low mass fractions (~0.3), though they show no volumetric energy density improvement at low volume fractions (~0.3). These observations already inform a potential design of electrodes using these active materials by demonstrating that while dense "dead" components can be accommodated in the electrode, the active material's volume fraction must remain high to produce significant volumetric energy density gains. Such a design happens to be practically challenging, as high-capacity anode active materials (Sb, Sn, Si) have been shown to require significant compounding with inactive components (carbons, binders, etc.) to achieve practically long lifetimes [3]. The inactive components significantly reduce the volume fraction of active material in the electrode, and could negate any energy density gains intended by using a high capacity anode material. Therefore it is important that new electrodes be reported with measurements/estimates of the overall electrode density (active and inactive components) or active material volume fraction.

The discussed model can be applied to calculate comparative energy densities of any set of electrode materials, including cathode materials. It is worth emphasizing here that one of the most significant limiting factors in improving energy density of a battery by using high capacity anode materials happens to be the comparatively low capacities of most cathodes. Because the cell capacity can never exceed the lesser of the electrode capacities, more significant energy density improvements are only achievable if the capacities of both electrodes in a battery are large. The high capacity of a sulfur cathode is the primary factor that results in the Li-sulfur battery having such a high theoretical energy density despite a comparatively small full-cell voltage of ~2 V [9].

Galvanostatic cycling of half-cells

Not surprisingly, performing electrochemical tests on new electrode materials is the first step in actually measuring how they could perform in a battery cell. Figure 1.3 shows a half-cell configuration, which is an electrochemical cell that is commonly used to initially assess the cycling performance of new electrode materials due to its ease of assembly and testing. In a half-cell, the working electrode is the electrode that one wishes to study, while the counter electrode is always a metal foil of the working ion (Li metal foil for a Li-ion electrode material). The metal foil counter electrode serves not only as an "unlimited" source of ions for the working electrode to react with, but it also acts as an electrochemical reference electrode.[4] The electrodes are separated by an electrolyte soaked into a porous separator, and the amount of electrolyte is typically in great excess. The type of cell depicted in Figure 1.3 is a coin cell, which typically allows for good reproducibility and consistency of electrode spacing and applied pressure. This is in contrast to a Swagelok cell (not shown), which is more suitable for experiments where the cell can be easily disassembled to characterize an electrode after electrochemical experiments.

Typically the first electrochemical experiment to assess an electrode's performance using a half-cell is galvanostatic cycling. If the electrode material is in its oxidized form (with no stored ions), a constant negative current is first applied to reduce and drive ions into the electrode material (referred to as the "discharge") until the cell potential reaches a lower limit at which point the same but positive current is applied to oxidize and drive ions out of the electrode material (referred to as the "charge") until the cell potential reaches an upper limit. The top plot

---

[4] In some cases, a metal foil electrode does not serve as a stable reference electrode, especially for experiments with large current densities (>1 mA/cm^2) that can polarize the electrode potential or produce metal dendrites. For such experiments we recommend that a three-electrode cell be used for accurate measurements of potential [10].

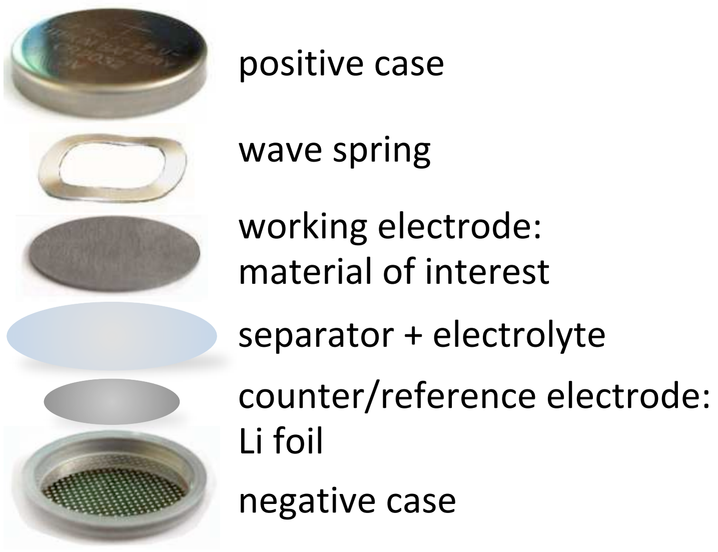

Figure 1.3: Schematic of the Li-ion half-cell configuration that is commonly used to initially assess the cycling performance on new electrode materials. This cell configuration can be used to study electrodes for different working ions by simply substituting the electrolyte composition and the counter/reference electrode for the desired materials (i.e. Na electrolyte and Na-metal, respectively, for a Na-ion battery electrode material.

in Figure 1.4 shows both the applied current (red) and measured potential (blue) of an example half-cell during galvanostatic cycling. The lower and upper potential limits are chosen to bound the potentials at which the electrode material is fully reduced and fully oxidized, though they can be adjusted to target a specific electrochemical reaction if multiple exist. Driving the half-cell potential from the upper limit, to the lower limit, then back to the upper limit constitutes a single "cycle" and simulates what the electrode would experience if it were fully charged then fully discharged in an actual battery. The number of cycles during which the electrode exhibits the desired reversible capacity (typically >80% of the initial reversible capacity) is referred to as the "cycle lifetime" of the electrode.

The potential of the half-cell during the charge or discharge of any given cycle can be plotted versus the capacity of charge passed during that cycling step, as shown by the voltage profiles in the left plot of Figure 1.4. The capacity is simply a count of the amount of charge (current*time = number of electrons or ions) that is passed during the step, and can be normalized to the mass, surface area, or volume of the electrode (in grams, cm^2, or cm^3 respectively). The flat regions of the voltage profiles are the potentials at which the redox reactions are actually occurring and can include multiple reactions occurring at very closely-spaced potentials. The differential of the capacity (dQ/dV) can be plotted versus the voltage of the half-cell to more easily visualize some of the subtle changes in plateau voltage as shown in the right plot of Figure 1.4. In such a differential capacity plot, each peak corresponds to a discrete reaction, with the negative peaks corresponding to the discharge (reduction, electrons/ions into electrode) and the positive peaks corresponding to the charge (oxidation, electrons/ions out of electrode).

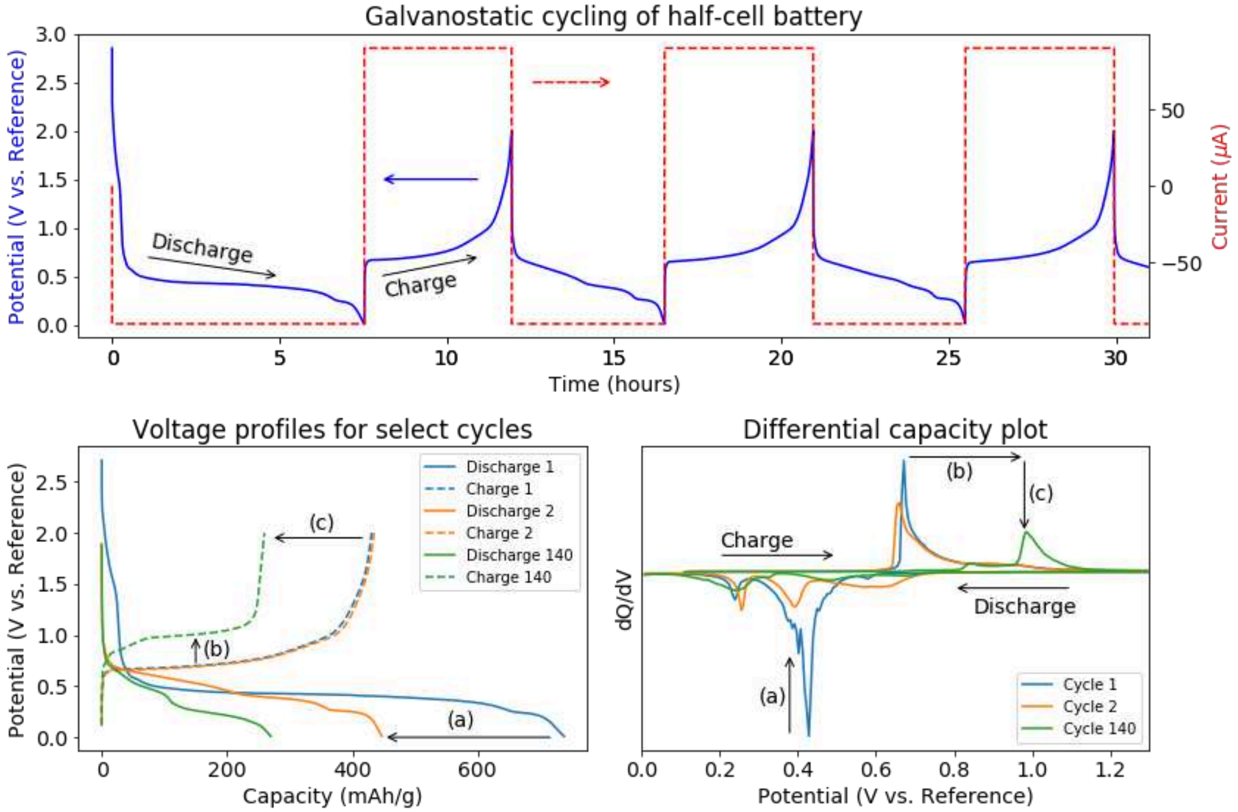

Figure 1.4: **(top)** Typical square-wave current profile (dashed red trace) for galvanostatic cycling of half-cell and the corresponding voltage profile of the cell (solid blue trace) between 0.01-2 V vs. Li. **(left)** The voltage profiles plotted vs. the capacity for select cycles and the corresponding differential capacity traces (dQ/dV) vs. voltage **(right)** for the same cycles. The voltage data displayed in this figure was collected from a Na-ion half-cell with an Sb-based working electrode, though the features discussed are generally applicable to any electrode in a half-cell configuration, including Li-ion or other types of half-cells.

The voltage profiles and the corresponding differential capacity plot can be examined over many cycles to learn how the electrode behavior evolves over the life of the cell. The voltage and differential capacity profiles for cycles 1, 2, and 140 are shown in Figure 1.4 along with several examples how of the electrode behavior changes over many cycles; the examples are marked by (a), (b), and (c). The first example (a) is commonly referred to as the first cycle capacity loss, and is the difference between the discharge capacity and charge capacity for the first cycle. This difference represents the amount of electrons and ions involved in any non-reversible reactions, which is often significantly larger on the first cycle than any of the following due to the decomposition of electrolyte on the electrode surface to form the highly studied solid electrolyte interface (SEI) layer [11]. An electrode's first cycle capacity loss in particular plays a significant role in the reversible capacity of a battery over its cycle lifetime, as will be discussed later. Another example of changing electrode behavior is a shifting potential over many cycles (b). Such a shift in potential is indicative of poor electron or ion transport to the electrode active material, often a result of the buildup of excessive SEI layer in a half-cell. It is important to examine the voltage profiles and differential capacity plots over all cycles to determine if a change in potential is actual due to the shifting of a reaction's redox potential over many cycles, or if it is due to the disappearance of a reaction with the concomitant appearance of a new reaction at a different potential. A third example of electrode behavior change is the loss of reversible capacity over many cycles (c), which is the ultimate determining factor in the cycle lifetime of a cell with that electrode material. In a half-cell the loss of reversible capacity is often due primarily to the degradation of the electrode where active material becomes electrically isolated and therefore redox inactive. However, reversible capacity loss in a half-cell can also be due to the buildup of excessive SEI that impedes electron or ion transport to the active material to such an extent that the redox reactions need to be driven by overpotentials that become outside the potential limits of the cell. This type of capacity loss would be concurrent with the shifting of a reaction's redox potential to and beyond the potential limits set for the galvanostatic cycling experiment. It is important to keep in mind that all the electrode behaviors just discussed are described for a half-cell configuration, where the working-ion inventory and amount of electrolyte can be considered to be unlimited, which would not be the case for an actual battery that is designed to maximize its energy storage density.

Performance of half-cells versus full-cells

An actual battery is referred to as a full-cell configuration, where electrodes would be paired to result in a large cell potential and the amounts of each are in such a proportion that the absolute capacity of each electrode approximately match. To learn about how an electrode would influence the reversible capacity and cycle lifetime of a full-cell, the reversible capacity of a galvanostatically cycled half-cell can be plotted versus the cycle number (cycle lifetime plot), as shown in Figure 1.5A. In such a plot, both the discharge and charge capacities are normalized to the mass or volume of all the components in the electrode (active material, binder, conductive additives, etc.). In Figure 1.5A in particular, the capacities are displayed up to a rapid rollover loss of capacity (the steep decline ~120-150 cycles). While not all electrodes display this type of rapid rollover capacity loss [12], a cycle lifetime plot should be scaled to show if and at how many cycles such an event occurs; otherwise the cycle lifetime plot should be scaled to show how many cycles it takes for the electrode to reach <80% of its initial capacity. Cycle lifetime plots typically also include the coulombic efficiency (CE) for every cycle, and can be calculated using the equation inlayed in Figure 1.5A. The CE of a cycle is simply an accounting of the

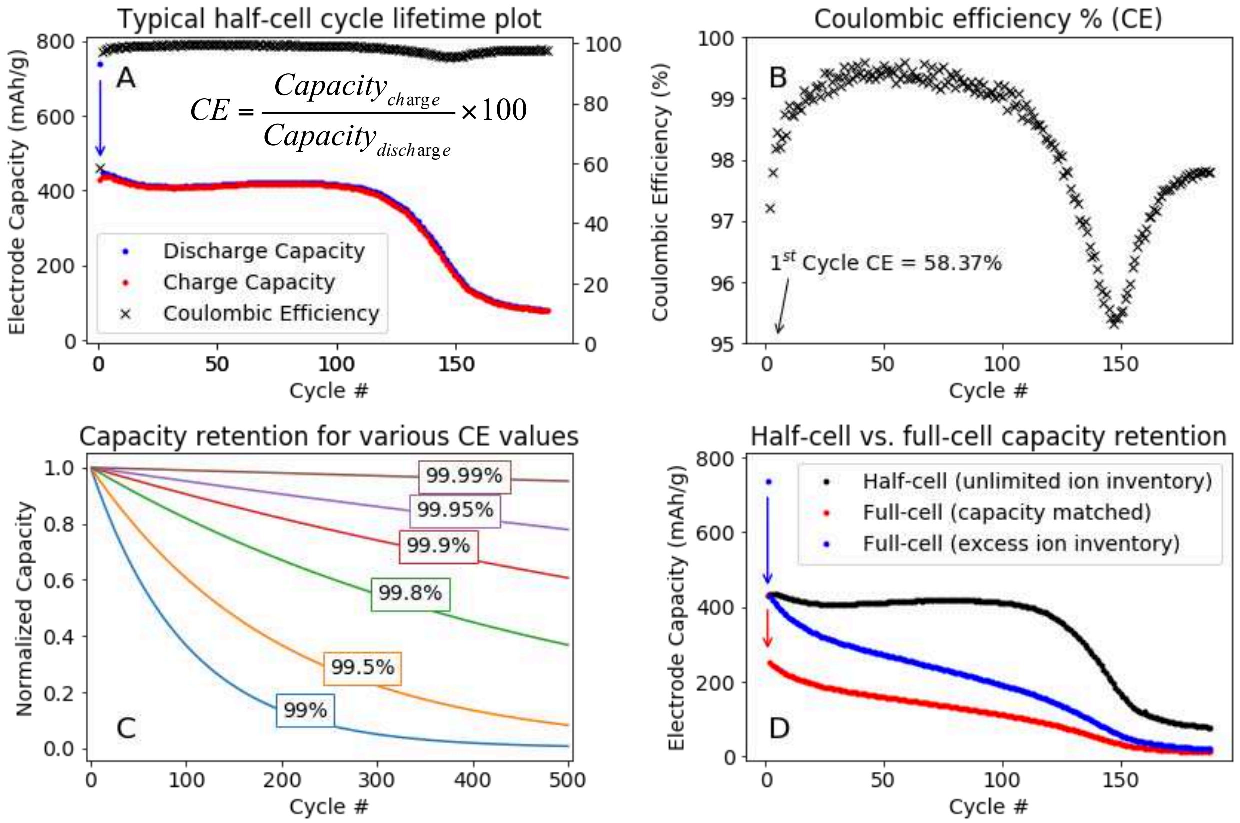

Figure 1.5: **(A)** A cycle lifetime plot (as typically reported in literature) showing specific discharge capacity, charge capacity, and coulombic efficiency as a function of cycle number of a half-cell. The arrow represents the first cycle capacity loss of the half-cell battery. **(B)** The coulombic efficiency of the half-cell, plotted at a more informative scale. **(C)** Simulated capacity retention curves for full-cells with various coulombic efficiency values. **(D)** Simulated cycle lifetime plots if the half-cell electrode in the top plots were to be assembled into a full-cell with limited ion inventory. The arrows represent the first cycle capacity losses for the corresponding simulated full-cells.

amount of redox reaction that is reversible, and any value <100% indicates that electrons are participating in irreversible side reactions, many of which can also deplete active ion inventory.

Figure 1.5A is presented in such a way that the performance looks ok, with a stable reversible capacity for ~100 cycles and a CE near 100% for most of those cycles. However, the figure is unrepresentative of how the electrode would perform in a full-cell. In a full-cell with a limited inventory of working ions, very high CE values are required for long cycle lifetimes, so we recommend plotting the CE to a more informative scale as shown in Figure 1.5B. By doing so we now see that the CE rises to above 99.0% within ~10 cycles, but never exceeds ~99.5% over 100 cycles, before declining to nearly 95% during the rapid rollover loss of capacity. To put these values into perspective, Figure 1.5C shows the simulated cycle lifetimes for a full-cell with various CE values. Here, a couple of assumptions are made that result in the displayed behavior. First, the full-cell has a limited working ion inventory, with just enough working ions to match the reversible capacity of the electrode. Second, we assume that any side reactions occurring when the CE is <100% also irreversibly consume working ions, which is often not the case in real batteries where some of the side reactions can involve the reduction or oxidation of other electrolyte components like the solvent. Given these assumptions, the simulated cycle lifetimes demonstrate that extremely high (>>99.0%) CE values are required for long cycle lifetimes. For example, 99.0% CE is comparatively low, with 1% of ions being consumed every cycle to result in a short cycle lifetime of fewer than 100 cycles of useful capacity. This is in contrast to a CE of >99.95% that results in a cycle lifetime with more than 500 cycles of useful capacity.

Figure 1.5D shows the cycle lifetime plot of an electrode in a half-cell (black) as well as simulated cycle lifetimes if that same electrode were put into full-cell configurations (red and blue). The assumption made in these simulations is that all of the side reactions are reactions that consume working ions. The cycle lifetime shown in black is the same as in Figure 1.5A because of the unlimited working ion inventory in its half-cell configuration. If that electrode were placed in a full-cell configuration with the working ion inventory exactly matching the first cycle's capacity (red), the second cycle would have 58.37% the capacity of the first cycle, because that is the first cycle CE of the electrode at shown in Figure 1.5B. Each consecutive cycle would have only a fraction of the previous cycle's capacity as determined by the electrode's CE for each cycle, and the cycle lifetime plot would exhibit the steady decline of the red trace in Figure 1.5D. The significant loss of capacity between the first and second cycles can be partially addressed by building the full-cell with excess ion inventory to account for the low CE of the first cycle (typically referred to as the first cycle irreversible capacity or first cycle capacity loss). The blue trace in Figure 1.5D show the cycle lifetime of the electrode in a full-cell with a proportional excess inventory of working ion to account for the low CE of just the first cycle. The capacity of the electrode still exhibits immediate and steady decline because the working ion inventory is not unlimited in the full-cell configuration and the electrodes CE values (Figure 1.5B) are comparatively low. The strategy of including excess working ion inventory to address the first cycle irreversible capacity is only somewhat effective, as the excess ions are often added as excess electrode (cathode) material. After the ions are consumed there is a large portion of non-active electrode material remaining that is essentially dead weight to the electrode that lowers the cell's energy density. Thus, it is especially important for the CE of the first cycle to be as high as possible, as it can have a major impact on the energy density achieved by a full-cell.

It is typical for novel electrode materials or designs to be tested in half-cells first, so that electrodes with sufficiently high performance can be selected for testing in full-cells. The assembly and testing of full-cells produces more representative performance data but becomes somewhat more complicated than the testing of half-cells [13]. The absolute capacity of both electrodes in a full-cell must be approximately matched by varying the amount of active material in one or both. Excess anode capacity can help prevent the plating of unwanted metal dendrites, while excess cathode material can account for ion consumption in side reactions[5] as discussed before. The amount of electrolyte in a full cell depends on the format of the cell as well as the type of electrode and electrolyte used, though should be the minimum amount required to optimize the cell's performance [14]. Full-cells can additionally be in any cell format or size (coin, Swagelok, pouch, cylinder), with larger scale cells generally giving more reproducible and reliable results. Galvanostaic cycling of full-cells will elucidate the true working cell voltages for a given set of electrodes and will show the true effect of the electrodes' CE values on the cell's cycle lifetime. Additionally, full-cells can elucidate any detrimental interactions between electrodes, such as the polysulfide shuttle in Li-sulfur batteries [15,16].

Kinetic experiments, advanced electrochemical techniques, and non-electrochemical characterization

While galvanostatic cycling is an effective way to explore the performance of electrode materials, there are many other experiments that are useful for correlating an electrode's material properties to its performance. One such set of electrochemical experiments involves the testing of an electrode's kinetic limitations and power output. The simplest of these is the galvanostatic rate capability experiment where the applied current density during galvanostatic cycling is varied during different cycles, as shown in Figure 1.6A. Typically, the current density is set at a small initial value for the first few cycles, before it is incrementally increased every few cycles to

---

[5] Excess cathode material can only account for ion consumption in side reactions if the cathode contains the full-cell's ion inventory when it is initially assembled. This is typically the case, as many cathodes are ion containing metal oxide materials that can be stably handled in air, like $LiCoO_2$.

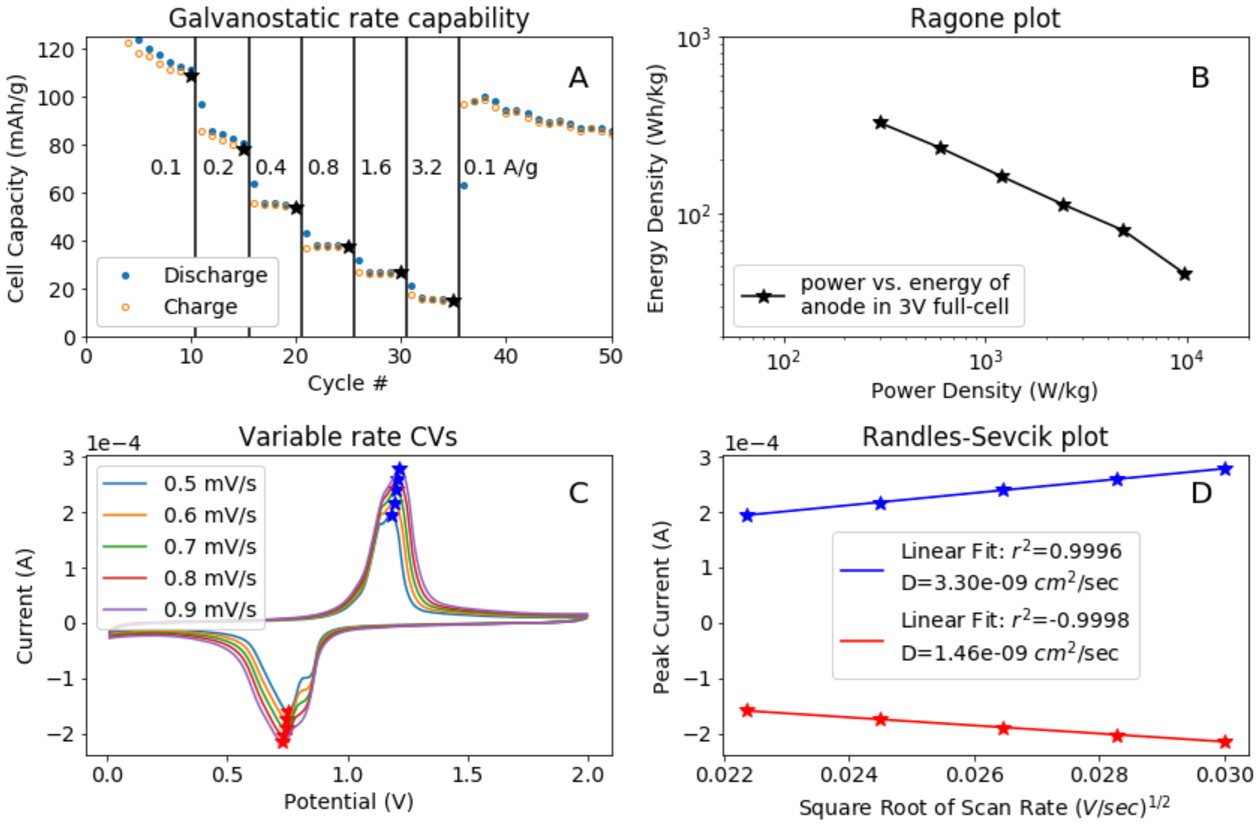

Figure 1.6: **(A)** Capacity vs. cycle number data where the current used to galvanostatically cycle the cell is change at predetermined cycles. **(B)** Ragone plot where the capacity values marked by the stars in panel A are used to calculate energy density vs. power density of a 3V full-cell. **(C)** Variable rate cyclic voltammograms of a half-cell swept between 2-0.01 V vs. Li at the indicated rates. **(D)** Randles-Sevcik plot where the current values marked by the stars in panel C are plotted vs. the square root of the scan rate. The Randles-Sevcik equation relates the slope of the linear fits of these data to a bottleneck ion diffusivity value in the cell.

a maximum value, before returning to the initial value. During the experiment, the measured capacity decreases with increasing current densities due to fewer ions getting to and reacting with the electrode active material before the potential limits of the galvanostatic cycling are reached. The initial current density value should be chosen such that there are few kinetic limitations on the electrode and a capacity near the expected theoretical value is measured. The maximum value should be chosen such that the electrode is severely kinetically limited and the measured capacity is approaching zero. The electrode should be cycled at each current density for enough cycles to verify that the measured capacity is consistent from cycle to cycle. The electrode should also be cycled at the small initial current density at the end of the experiment, where a capacity that returns to its original value would indicate that no irreversible damage occurred to the electrode at high current densities. The capacities measured during a rate capability experiment can be used to calculate and relate the energy density to the power density of a set of electrodes, as shown by the Ragone plot in Figure 1.6B. The power density is the product of the cell's potential and applied current density, while the energy density is the product of the cell's potential and the measured cell capacity (the capacity values used to generate Figure 1.6B are marked by stars in Figure 1.6A). It is important here to recall that an "energy density" calculated from a single electrode's capacity misrepresents the energy it can store when paired with another electrode, and the cell capacity is the value that should be used to calculate energy density in a Ragone plot.

Galvanostatic rate capability experiments are useful for measuring the empirical power output for a set of electrodes, a value that can be influenced not just by the electrodes but also the electrolyte of the cell. Variable rate cyclic voltammetry (CV) is a similar type of experiment that can be useful for learning which components most influence the cell's kinetic limitations [17-

19]. Figure 1.6C shows the variable rate CV data of a half-cell, where the current is varied so that the cell potential sweeps at a constant rate between the potential limits. The potential sweep rates should span a small range and be low enough that peaks in the current response can be resolved before the potential limits are reached, typically less than 1 mV/sec. The current responses reach maxima because the sweeping potential drives the redox reactions to rates that exceed the mass transport of ions (diffusivity) to or from the active material, thus limiting the observed reaction rate (proportional to the measured current). While the ions have to diffuse through media with different transport properties such as the electrolyte, SEI layer, and electrode, the peak current that is measured is limited primarily by the medium with the lowest diffusivity (i.e. the bottleneck). The peak current measured (i_p) varies proportionally to the square root of the applied potential sweep rate ($\nu^{1/2}$) as determined by the Randles-Sevcik equation, which can be expressed as follows:

$$D_{I^+}^{\frac{1}{2}} = \left(\frac{i_p}{\upsilon^{\frac{1}{2}}}\right)\left(\frac{(RT)^{\frac{1}{2}}}{0.4463 * n^{\frac{3}{2}} F^{\frac{3}{2}} AC}\right)$$

The peak current values marked by stars in Figure 1.6C can be plotted versus the square root of the potential scan rate, as shown in Figure 1.6D. The slope of a linear fit to the data ($i_p / \nu^{1/2}$) can then be used to calculate the bottleneck diffusivity (D_{I+}) of the cell using the above relationship, where R is the gas constant (J K^{-1} mol^{-1}), T is the temperature (K), n is the number of electrons in redox process (1 for Li^+ chemistry), F is Faraday's constant (C/mol), A is the area of the electrode (cm^2), and C is the ion concentration (mol/cm^3).

There are a number of electrochemical techniques for studying electrodes that are easily accessible with the right equipment, though their analysis and interpretation are more advanced. For example, galvanostatic intermittent titration technique (GITT) and its potentiostatic variation

(PITT) can be used for measuring an electrode's equilibrium potential and calculating its ion diffusion coefficients at various states of charge [20-22]. Briefly, the technique involves charging and discharging a cell with short constant currents pulses (small potential increments for PITT), followed by periods of open-circuit relaxation back the cell's equilibrium potential. The ion diffusion coefficients can then be calculated by fitting the voltage response (or current response in PITT) during each step of the titration experiment. It is common for diffusivity values determined by multiple methods to be reported together to verify that the values are representative of a real processes [23]. Another technique that can elucidate the mass transport and charge transport limitations in electrodes is electrochemical impedance spectroscopy (EIS) [24-28]. Briefly, EIS involves the application of a sinusoidal current or potential wave to a cell across a range of frequencies while measuring the magnitude and phase shift of the sinusoidal response. This data is commonly reported in Nyquist plots (which have the archetypal semicircular spectral shapes) which can be fit with equivalent circuit models to extract parameters about the cell such as its series resistance, the charge transfer resistance of the redox reactions, and the electrode's ion conductivity. When fitting data collected using EIS, researchers should take care to include in their equivalent circuit model only elements that correspond to real processes/components in the cell to ensure that the extracted parameters are meaningful.

Common materials characterization techniques are also complementary to the electrochemical experiments used to test electrodes and other battery materials. Most of these can easily be performed ex situ, both before and after the material has been cycled or otherwise tested in an electrochemical cell. Common ex situ techniques include X-ray diffraction (XRD) to elucidate crystalline structural features and transformations, while X-ray photoelectron, infrared, and energy dispersive X-ray spectroscopies are surface-sensitive techniques that are useful in the compositional study of electrodes, coatings, or SEI layers [1]. Microscopy techniques such as scanning and transmission electron microscopy (TEM) are also used to characterize how electrode morphology influences or is affected by electrochemical cycling experiments. In situ techniques such as NMR [29], XRD [30] and TEM [31] are able to be performed during electrochemical experiments, though specialized equipment is required to do so.

Conclusions

With the ever-increasing global interest in producing batteries with greater energy densities and longer cycle lifetimes, this paper can be used as an introduction to researchers who are new to the field. By understanding the critical factors that influence achievable energy densities in electrochemical energy storage cells, researchers can target the study of new materials that are more likely to lead to timely advancements in battery electrode technology. Additionally, we review some of the most common electrochemical experiments that are used to characterize new electrode materials. We highlight the limits of testing half-cell configurations in representing the lifetimes of electrodes material in full-cell batteries: particularly, the necessity of extremely high coulombic efficiencies (highly reversible reactions) for achieving long cycle lifetimes. These critical considerations for studying electrode materials can help to not only optimize the performance of existing Li-ion battery materials but also enable the next generation of materials that move beyond Li-ion chemistries.

CHAPTER 1 REFERENCES

[1] E. Talaie, P. Bonnick, X. Sun, Q. Pang, X. Liang, L.F. Nazar, Methods and Protocols for Electrochemical Energy Storage Materials Research, Chem. Mater. (2016) acs.chemmater.6b02726–50. doi:10.1021/acs.chemmater.6b02726.

[2] A. Urban, D.-H. Seo, G. Ceder, Computational understanding of Li-ion batteries, Computational Materials. 2 (2016) 16002. doi:10.1038/npjcompumats.2016.2.

[3] M.N. Obrovac, V.L. Chevrier, Alloy Negative Electrodes for Li-Ion Batteries, Chem. Rev. 114 (2014) 11444–11502. doi:10.1021/cr500207g.

[4] L. Li, Y. Zheng, S. zhang, J. Yang, Z. Shao, Z. Guo, Recent progress on sodium ion batteries: Potential high-performance anodes, Energy Environ. Sci. (2018) 1–28. doi:10.1039/C8EE01023D.

[5] J.W. Choi, D. Aurbach, Promise and reality of post-lithium-ion batteries with high energy densities, Nat. Rev. Mater. 1 (2016) 16013–17. doi:10.1038/natrevmats.2016.13.

[6] M. Winter, B. Barnett, K. Xu, Before Li ion batteries, Journal of Chemical Education. 23 (2018) 11433–11456. doi:10.1021/acs.chemrev.8b00422.

[7] S.S. Zhang, A review on the separators of liquid electrolyte Li-ion batteries, Journal of Power Sources. 164 (2007) 351–364. doi:10.1016/j.jpowsour.2006.10.065.

[8] F.J. Günter, C. Burgstaller, F. Konwitschny, G. Reinhart, Influence of the Electrolyte Quantity on Lithium-Ion Cells, J. Electrochem. Soc. 166 (2019) A1709–A1714. doi:10.1149/2.0121910jes.

[9] Q. Pang, X. Liang, C.Y. Kwok, L.F. Nazar, Review—The Importance of Chemical Interactions between Sulfur Host Materials and Lithium Polysulfides for Advanced Lithium-Sulfur Batteries, J. Electrochem. Soc. 162 (2015) A2567–A2576. doi:10.1149/2.0171514jes.

[10] D.S. Tchitchekova, D. Monti, P. Johansson, F. Bardé, A. Randon-Vitanova, M.R. Palacin, et al., On the Reliability of Half-Cell Tests for Monovalent (Li+, Na+) and Divalent (Mg2+, Ca2+) Cation Based Batteries, J. Electrochem. Soc. 164 (2017) A1384–A1392. doi:10.1149/2.0411707jes.

[11] M. Winter, The Solid Electrolyte Interphase – The Most Important and the Least Understood Solid Electrolyte in Rechargeable Li Batteries, Zeitschrift Für Physikalische Chemie. 223 (2009) 1395–1406. doi:10.1524/zpch.2009.6086.

[12] J.C. Burns, A. Kassam, N.N. Sinha, L.E. Downie, L. Solnickova, B.M. Way, et al., Predicting and Extending the Lifetime of Li-Ion Batteries, J. Electrochem. Soc. 160 (2013) A1451–A1456. doi:10.1149/2.060309jes.

[13] V. Murray, D.S. Hall, J.R. Dahn, A Guide to Full Coin Cell Making for Academic Researchers, J. Electrochem. Soc. 166 (2019) A329–A333. doi:10.1149/2.1171902jes.

[14] S.J. An, J. Li, D. Mohanty, C. Daniel, B.J. Polzin, J.R. Croy, et al., Correlation of Electrolyte Volume and Electrochemical Performance in Lithium-Ion Pouch Cells with Graphite Anodes and NMC532 Cathodes, J. Electrochem. Soc. 164 (2017) A1195–A1202. doi:10.1149/2.1131706jes.

[15] Y.V. Mikhaylik, J.R. Akridge, Polysulfide Shuttle Study in the Li/S Battery System, J. Electrochem. Soc. 151 (2004) A1969–8. doi:10.1149/1.1806394.

[16] A. Rosenman, E. Markevich, G. Salitra, D. Aurbach, A. Garsuch, F.F. Chesneau,

Review on Li-Sulfur Battery Systems: an Integral Perspective, Adv. Energy Mater. 5 (2015) 1500212–21. doi:10.1002/aenm.201500212.

[17] D.Y.W. Yu, C. Fietzek, W. Weydanz, K. Donoue, T. Inoue, H. Kurokawa, et al., Study of LiFePO4 by cyclic voltammetry, J. Electrochem. Soc. 154 (2007) A253–A257. doi:10.1149/1.2434687.

[18] L.R. Faulkner, A.J. Bard, Electrochemical methods: fundamentals and applications, 2nd ed., John Wiley and Sons, Hoboken, NJ, 2002.

[19] P.T. Kissinger, W.H. Heineman, Cyclic voltammetry, Journal of Chemical Education. 60 (1983) 702–706. doi:10.1021/ed060p702.

[20] W. Weppner, R.A. Huggins, Determination of the Kinetic Parameters of Mixed-Conducting Electrodes and Application to the System Li3Sb, J. Electrochem. Soc. 124 (1977) 1569–1578. doi:10.1149/1.2133112.

[21] C.J. Wen, B.A. Boukamp, R.A. Huggins, W. Weppner, Thermodynamic and Mass Transport Properties of " LiAl ," J. Electrochem. Soc. 126 (1979) 2258–2266. doi:10.1149/1.2128939.

[22] Y. Zhu, C. Wang, Galvanostatic Intermittent Titration Technique for Phase-Transformation Electrodes, The Journal of Physical Chemistry C. (2010). doi:10.1021/jp9113333.

[23] N. Ding, J. Xu, Y.X. Yao, G. Wegner, X. Fang, C.H. Chen, et al., Determination of the diffusion coefficient of lithium ions in nano-Si, Solid State Ionics. 180 (2009) 222–225. doi:10.1016/j.ssi.2008.12.015.

[24] J. Jamnik, J. Maier, Treatment of the Impedance of Mixed Conductors Equivalent Circuit Model and Explicit Approximate Solutions, J. Electrochem. Soc. 146 (1999) 4183–4188. doi:10.1149/1.1392611.

[25] T.S. Ong, H. Yang, Symmetrical Cell for Electrochemical AC Impedance Studies of Lithium Intercalation into Graphite, Electrochem. Solid-State Lett. 4 (2001) A89–4. doi:10.1149/1.1373377.

[26] M. Dollé, F. Orsini, A.S. Gozdz, J.-M. Tarascon, Development of Reliable Three-Electrode Impedance Measurements in Plastic Li-Ion Batteries, J. Electrochem. Soc. 148 (2001) A851–7. doi:10.1149/1.1381071.

[27] R.A. Huggins, Simple method to determine electronic and ionic components of the conductivity in mixed conductors a review, Ionics. 8 (2002) 300–313. doi:10.1007/BF02376083.

[28] S. Buteau, D.C. Dahn, J.R. Dahn, Explicit Conversion between Different Equivalent Circuit Models for Electrochemical Impedance Analysis of Lithium-Ion Cells, J. Electrochem. Soc. 165 (2018) A228–A234. doi:10.1149/2.0841802jes.

[29] O. Pecher, J. Carretero-González, K.J. Griffith, C.P. Grey, Materials' Methods: NMR in Battery Research, Chem. Mater. 29 (2016) 213–242. doi:10.1021/acs.chemmater.6b03183.

[30] L. Zhang, X. Guo, J. Huang, Y. Qu, C. Niu, Z. Du, et al., Coin-Cell-Based In Situ Characterization Techniques for Li-Ion Batteries, Front. Energy Res. 6 (2018) 652–8. doi:10.3389/fenrg.2018.00016.

[31] Y. Yuan, K. Amine, J. Lu, R. Shahbazian Yassar, Understanding materials challenges for rechargeable ion batteries with in situ transmission electron microscopy, Nature Communications. 8 (2017) 1–14. doi:10.1038/ncomms15806.

CHAPTER 2 – ELECTRODEPOSITED THIN-FILM CU$_X$SB ANODES FOR LI-ION BATTERIES: ENHANCEMENT OF CYCLE LIFE VIA TUNING OF FILM COMPOSITION AND ENGINEERING OF THE FILM-SUBSTRATE INTERFACE[1]

Overview

Electrodeposited Cu-Sb thin films on Cu and Ni substrates are investigated as alloy anodes for Li-ion batteries to elucidate the effects of both the film composition and substrate interactions on anode cycling stability and lifetime. Thin films of composition Cu_xSb ($0<x<2$) exhibit the longest cycle lifetimes nearest $x=1$. Additionally, the Cu-Sb films exhibit shorter cycle lifetimes when electrodeposited onto Cu substrates when compared to equivalent films on Ni substrates. Ex-situ characterization and differential capacity analysis of the anodes reveal that significant interdiffusion occurs during cycling between pure Sb films and Cu substrates. The great extent of interdiffusion results in mechanical weakening of the film-substrate interface that exacerbates film delamination and decreases cycle lifetimes of Cu-Sb films on Cu substrates regardless of the film's composition. The results presented here demonstrate that the composition of the anode alone is not the most important predictor of long term cycle stability; the composition coupled with the identity of the substrate is key. These interactions are critical to understand in the design of high capacity, large volume change materials fabricated without the need for additional binders.

Introduction

Informing design principles for next generation secondary batteries is a step toward achieving the high energy density and long cycle lifetime requirements of grid-scale energy storage and the electrification of transportation [1,2]. In particular, alloy anodes for Li-ion and

---

[1] This chapter is published (J. Mater. Chem. A, 2018, 6, 12708) with Maxwell C. Schulze, Roland K. Schulze, and Amy L. Prieto as authors. With exception of the XPS analysis performed by Roland K. Schulze, all of the experimental work was performed and the paper written by Maxwell C. Schulze with guidance from Amy L. Prieto.

Na-ion batteries show promise for achieving higher energy densities by storing more working ions ($I^+ = Li^+$, Na^+) per unit volume and mass than traditional intercalation anodes [3]. The specific capacity of an active alloy material (A) is determined by the stoichiometry of the produced phase in the reversible alloy reaction:

$$A + xI^+ + e^- \leftrightarrow I_xA$$

Elements that have shown reasonable functionality as alloy anodes include but are not limited to Si, Sn, Sb, Al, and Mg for Li-ions [3] and Sn, Sb, Ge, and P for Na-ions [1,4]. However, these anodes typically exhibit very large volume changes upon cycling, and hence demonstrate significant capacity fading within a few cycles that limit their lifetimes.

The capacity fade is commonly attributed to two coinciding and interacting failure modes [5]:

a) Uncontrolled formation of the surface-electrolyte-interface (SEI) layer and

b) Mechanical instability of the active material.

The SEI is a heterogeneous layer that forms as electrolyte electrochemically decomposes on the anode surface during device cycling. The SEI layer can cause performance degradation and irreversible capacity loss by slowing, blocking, or consuming the working ions. Alloy anodes also undergo large volume changes during alloying and dealloying that can cause fracturing of the active material. Not only can the fracturing cause irreversible capacity loss as active material loses electrical connectivity with the rest of the electrode, it also degrades the existing SEI and exposes new surfaces of the electrode that result in additional SEI formation [3,6,7].

Strategies that successfully alleviate the mechanical instability of alloy anodes often times exacerbate deleterious effects of SEI formation. Structuring of the anode active material at nanoscale dimensions has proven to be effective at accommodating volume changes to prevent mechanical fracturing during cycling [8]. However, the increased surface area of nanostructures results in greater amounts of SEI formation [9,10]. Another approach is to use conversion type anodes that store working ions the following reaction: $MA + xI^+ + e^- \leftrightarrow I_xA + M$

where an inactive component M is extruded from the structure during alloying [7,11]. While this conversion style chemistry can alleviate mechanical degradation of the active material by lessening the magnitude of volume change, exposing a fresh surface of extruded inactive component every cycle can lead to excessive SEI formation and degradation of battery performance [12]. Design strategies to mitigate the limited cycle lifetimes of alloy anodes must therefore concurrently address both the SEI formation and mechanical instability of anode materials.

The compound Cu_2Sb has been shown to be a promising conversion anode material, where its good cycling performance has been attributed to the reversibility exhibited during lithiation and delithiation. The compound reforms its original structure during alloying/dealloying cycles with lithium, likely due to structural relationships between Cu_2Sb, the fully lithiated Li_3Sb, and intermediate Li-Cu-Sb ternary phases [13-15]. Furthermore, Sb-based anodes have shown promise in Na-ion battery systems [1,16-18], making the Cu-Sb system more widely relevant for next generation secondary batteries.

Building off of the wealth of literature on Cu-Sb anodes [19-22], our group has recently reported on the electrodeposition and cycle performance Cu-Sb anodes in Li-ion batteries in both thin film [12,23] and nanowire array [9] architectures. Producing the anodes by carefully tuned electrodeposition methods offers compositional control, conformal coverage, good mechanical adhesion, and by the nature of the technique, good electrical contact to the current collector, which eliminate the need for carbon additives and binders of traditional slurry anodes [23].

Because the nature of the SEI on alloy/conversion anodes is known to be different than on graphite-based intercalation anodes [5], the absence of the carbon additives and binders allowed us to investigate the performance effects of SEI that are intrinsic to just the active material. By utilizing this strategy in a Cu-Sb nanowire-array anode with minimized mechanical instability but exaggerated SEI effects, we demonstrated that electrolyte additives can improve the stability of the SEI on Cu-Sb anodes [9].

While the interplay of mechanical instability with the SEI at the anode-electrolyte interface is known to affect cycle performance, chemical and mechanical interactions between the active material and the current collector can also have significant effect on cycling stability of the anodes. Previous reports demonstrate that mechanical adhesion and cycle performance of electrodeposited Sn-based Li-ion anode thin-films can be improved by using textured instead of smooth Cu substrates [24,25]. Additionally, annealing of Sn-based thin film anodes causes interdiffusion between the active material and substrate, which can both improve or worsen cycling performance depending on the intermetallic phases formed [24-26]. These types of substrate-interface interactions are especially important in electrodeposited anode materials where there is direct contact between the active material and current collector during electrochemically driven structural changes. Incomplete adhesion and incoherent interface development at a film-substrate interface can result in film delamination, which in a battery anode means electrical isolation from the current collector and an associated irreversible capacity loss.

Herein, we demonstrate enhancement of cycle lifetimes of Cu-Sb thin film anodes by controlling substrate-film interactions. First, using electrodeposited pure Sb films on Cu foil substrates we show that substrate-film interdiffusion forms Kirkendall-like voids that weaken the interface and exacerbate mechanical degradation and film delamination during cycling. Pure Sb films were chosen as a starting point to exaggerate volume expansion issues as well as to exaggerate the concentration gradient at the Sb-Cu interface. We then show that this degradation mode occurs in Cu-Sb films on Cu substrates regardless of their composition and how it can be eliminated to improve anode cycle lifetimes by using Ni foil substrates or Ni-blocking layers, where no substrate-film interdiffusion occurs. Additionally, while Sb metal and Cu_2Sb are commonly reported as Li-ion battery anodes, we show how cycle performance can be further improved using off-stoichiometric Cu_xSb ($0<x<2$) compositions that balance competing failure modes. While these design strategies are explored in our specific system, the principles of balancing failure modes are likely applicable to battery systems where different alloy anode materials and working ions are used.

Results and discussion

Electrodeposited Sb thin films cycle longer on Ni substrates than on Cu

As an initial measure of substrate type effects on the cycling of Sb based anodes, equivalent Sb films were electrodeposited to charge loadings of 702 mC/cm^2 (~440 nm approximate thickness) onto Cu and Ni foil substrates and used as-deposited in Li-ion half cells. Figure 2.1A shows the retained reversible capacity of these anodes as measured by charge capacity relative to the initial capacity. The substantial capacity loss of the Sb film on the Cu foil (Sb@Cu) within 10 cycles indicates unstable cycling behavior and a relatively short cycle lifetime. The Sb film on the Ni foil (Sb@Ni) shows a comparatively lesser capacity decline beginning around 30 cycles, indicating a more stable cycling behavior and a longer cycle lifetime. Pre- and post-cycling ex-situ SEM imaging of the films identifies cracking and film delamination typical of alloy-anodes as the main cause of capacity loss and anode failure.

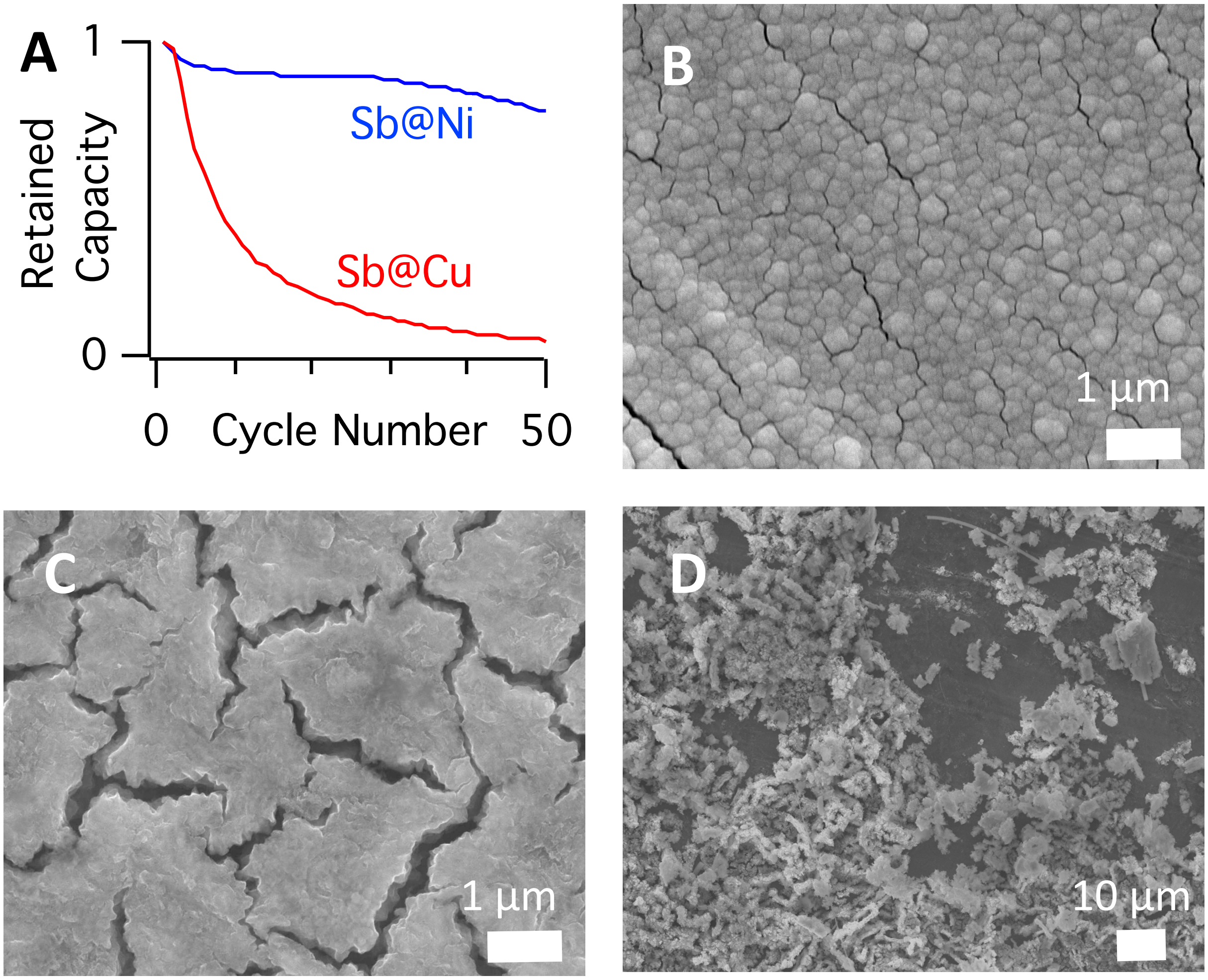

Figure 2.1: (A) Cycle performance of equivalent Sb thin films on Cu and Ni metal substrates. SEM micrographs show Sb film morphology before cycling (B) and after cycling on a Ni substrate (C,D).

The as-deposited films exhibit comparable surface morphologies on both the Cu and Ni foils (Figure 2.1B), exhibiting uniform and conformal coverage while cracks indicate some internal stress of these films. After 50 cycles the Sb@Ni anode shows expanded cracks (Figure 2.1C) and areas of delamination (Figure 2.1D). Imaging of the Sb@Cu anode after 50 cycles was not possible because the film had totally delaminated from the Cu foil as a black powder during battery disassembly. Post-cycling observations of the thin films is consistent with commonly observed mechanical instability failure modes and seems to be exacerbated on the Cu foil substrates. To elucidate the effects of the substrate metal on the cycling stability of the Sb films, additional in-situ and post-cycling characterizations were performed.

Thin film Sb on Cu substrate converts to Cu_2Sb during cycling

To further investigate the cause for the drastic differences in cycle performance on Cu and Ni substrates for Sb films, thin film anodes of Sb@Cu and Sb@Ni with charge loadings of 228 mC/cm^2 (~140 nm approximate thickness) were prepared and characterized using ex-situ XRD before and after cycling. The thinner samples and fewer cycles lead to less severe degradation of the Sb@Cu anode, allowing for post-cycling characterization to be performed. Voltage-capacity traces for charge and discharge of the Sb@Cu anode (Figure 2.2A) show an irreversible capacity loss above 1V on the first discharge, lithiation plateaus between 0.5-1.0V, and delithiation plateaus around 1V, all of which are typical for Sb-based anodes. Differential capacity plots that more clearly display the anode electrochemistry (Figure 2.2B) show evolution of the anode electrochemistry over 6 cycles. The (a) peaks in Figure 2.2B are typical lithiation/delithiation potentials for Sb metal [10] while the (b) peaks are typical of Cu_2Sb lithiation/delithiation potentials [27]. The evolution of peaks from (a) to (b) indicates significant conversion of the Sb film to Cu_2Sb over only 6 cycles.

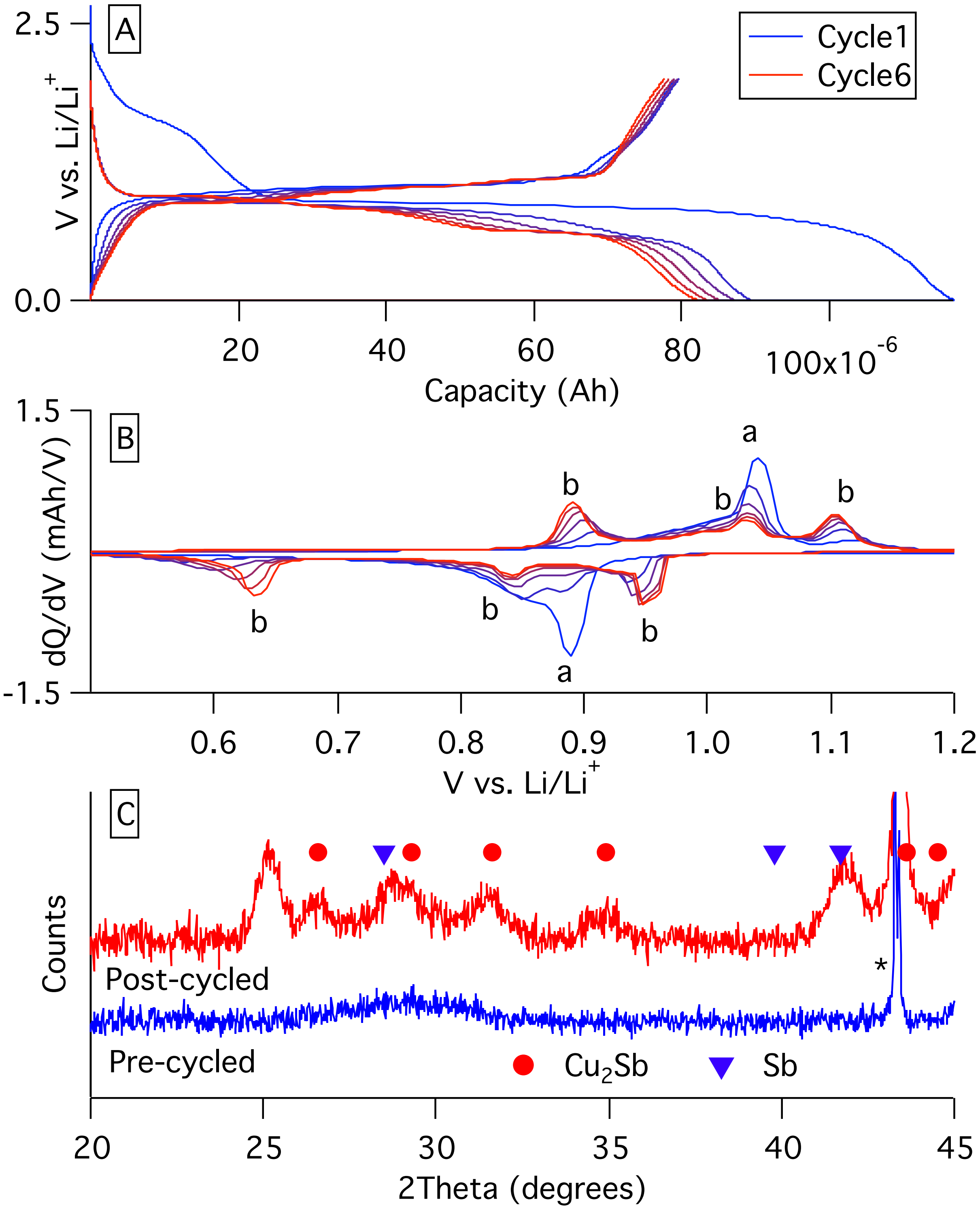

Figure 2.2: Characterization of Sb@Cu anode cycled in a Li-ion battery: (A) charge-discharge curves for 6 cycles between 0.05-2 V vs. Li/Li+, (B) the corresponding differential capacity plots, (C) and ex-situ XRD before and after cycling. The Cu substrate is marked by *.

Such a materials transformation from an amorphous Sb to a crystalline Cu_2Sb film is consistent with the pre- and post-cycling XRD (Figure 2.2C). Ex-situ Auger spectroscopy depth profiles of the pre- and post-cycled anodes confirms the interdiffusion of the Sb film with the Cu substrate (Figure 2.3).

There is no analogous conversion from Sb to a crystalline Ni-Sb intermetallic phase when cycling the Sb@Ni anode, as evidenced by voltage profiles typical of Sb and post-cycling XRD that shows only crystalline Sb reflections (Figure 2.4) during more than 10 cycles. The structural similarities between Li_3Sb, Li-Cu-Sb intermediates, and Cu_2Sb and the fast solid-state diffusion of Cu into Sb [28] is most likely what allows for the material transformation during cycling in the Sb@Cu but not the Sb@Ni anodes. The ex-situ XRD of the Sb films additionally shows the pre-cycled material as a broad amorphous reflection around 29° and the post-cycled material contains evidence of Sb_2O_5 with a Bragg reflection at 25°. The presence of oxygen through the full thickness of the films on both Cu and Ni substrates is confirmed by Auger spectroscopy (Figure 2.3). The presence of oxygen in the film and its amorphous nature may also play a role in the extent of Cu-Sb interdiffusion. Poor cycling stability of the Sb@Cu anode compared to the Sb film of the Sb@Ni anode could arise from the Cu-Sb composition formed from the interdiffusion. Variable composition Cu_xSb ($0<x<2$) films on Ni foils where the Cu:Sb ratio stays constant during cycling can be used to determine the effect of only composition on cycling stability.

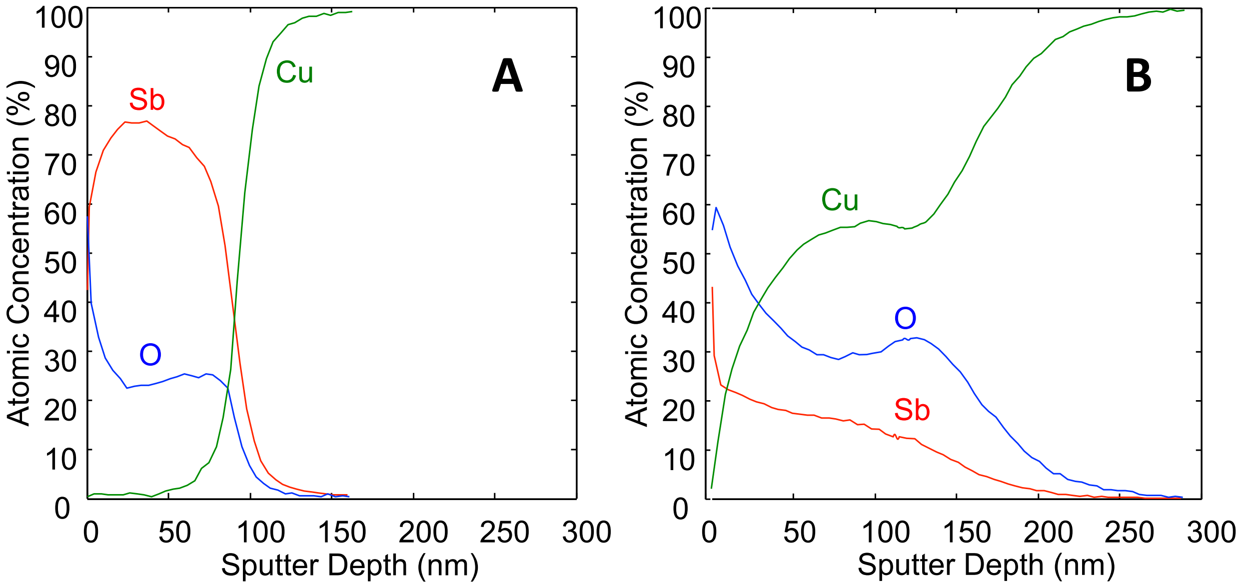

Figure 2.3 Auger depth profiles of amorphous Sb@Cu anodes before (A) and after (B) cycling in a Li-ion half-cell.

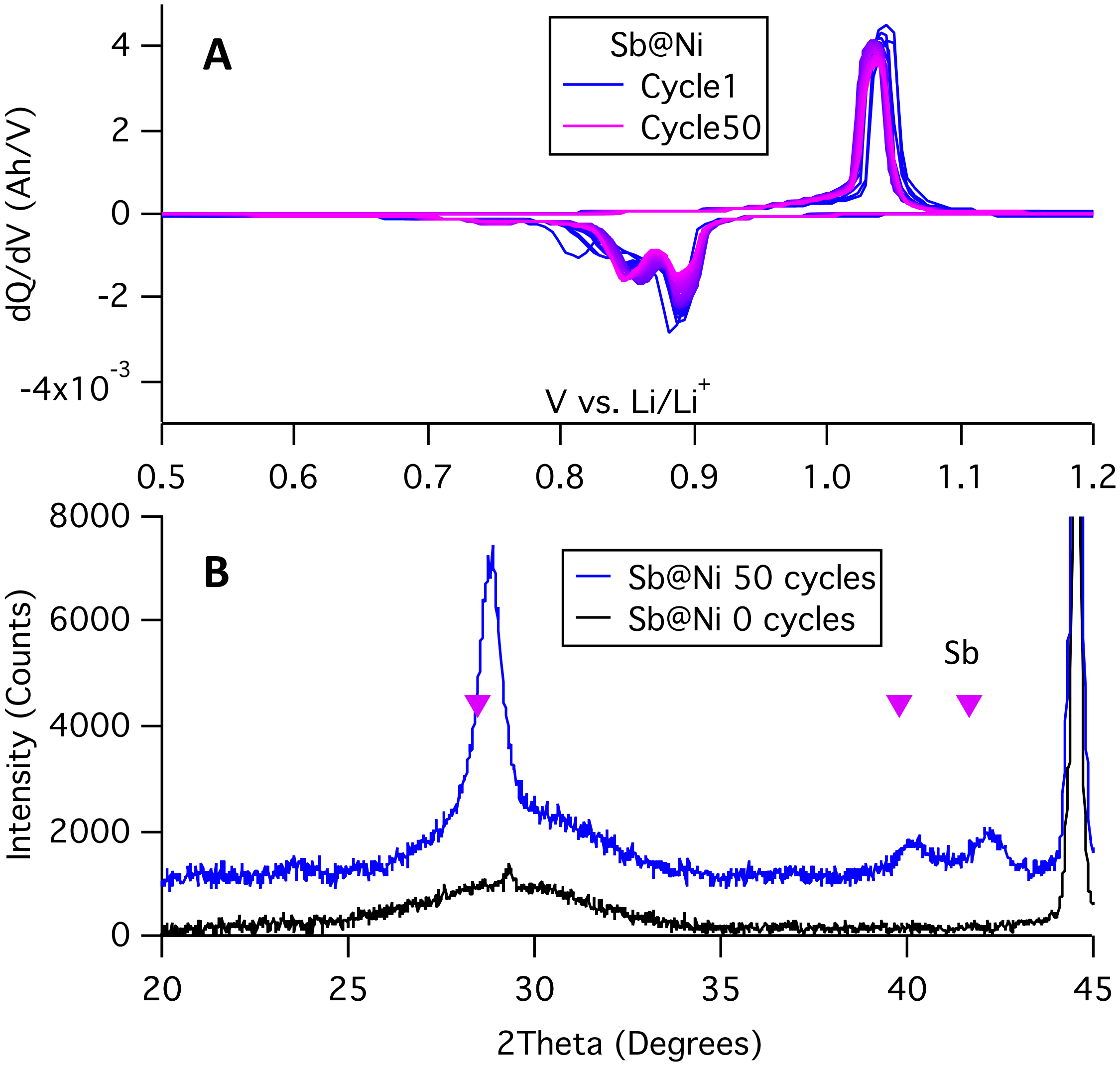

Figure 2.4 (A) Differential capacity plot of an amorphous Sb@Ni anode cycled in a Li-ion half-cell. (B) PXRD of the same Sb@Ni anode both before and after cycling.

Electrodeposited Cu_xSb thin film anodes show composition dependent cycle lifetimes

To investigate the dependency of cycling stability on film composition, thin film Cu_xSb ($0<x<2$) anodes were electrodeposited onto Ni foil substrates to a charge loading of 232 mC/cm^2 (~110-140 nm approximate thickness). The film compositions were controlled by changing the concentration of $CuCl_2$ in the deposition solution and determined using EDS. Imaging using SEM of the as-deposited films shows similar surface morphology between films of different compositions and to the film in Figure 2.1B. Analysis by EDS (Figure 2.5) indicates about 30-50 atom% oxygen in the films (which includes oxygen that is likely present in the SEI layer), and Auger spectroscopy depth profiling shows the oxygen is present through the full thickness of the films. The incorporation of Sb_2O_3 into electrodeposited films of Sb has been previously reported [29], and has been shown to boost the lithium storage capacity and cycle lifetimes of the films through the partially reversible formation of Li_2O. While the oxygen content varies between the electrodeposited films, we believe the Cu:Sb ratio plays a more significant role in the reversible capacity and cycling stability of these films. Deposition of these films onto Ni foil substrates ensures that the Sb:Cu ratio of the films stays constant during cycling, unlike Sb@Cu anodes where Cu from the substrate can diffuse into the film during cycling. Figure 2.6 shows the cycle lifetimes of the Cu_xSb@Ni anodes as measured by the specific delithiation capacity for each cycle.

Generally, the initial specific capacity of the anodes decreases with increasing Cu content, which is consistent with film compositions that have larger inactive component (Cu) to active component (Sb) ratios. There are exceptions to this trend that may arise from loading discrepancies between samples, such as in the case of the Sb-only Sb@Ni anode that falls far short of its theoretical maximum capacity of 660 mAh/g. Coulombic inefficiencies during

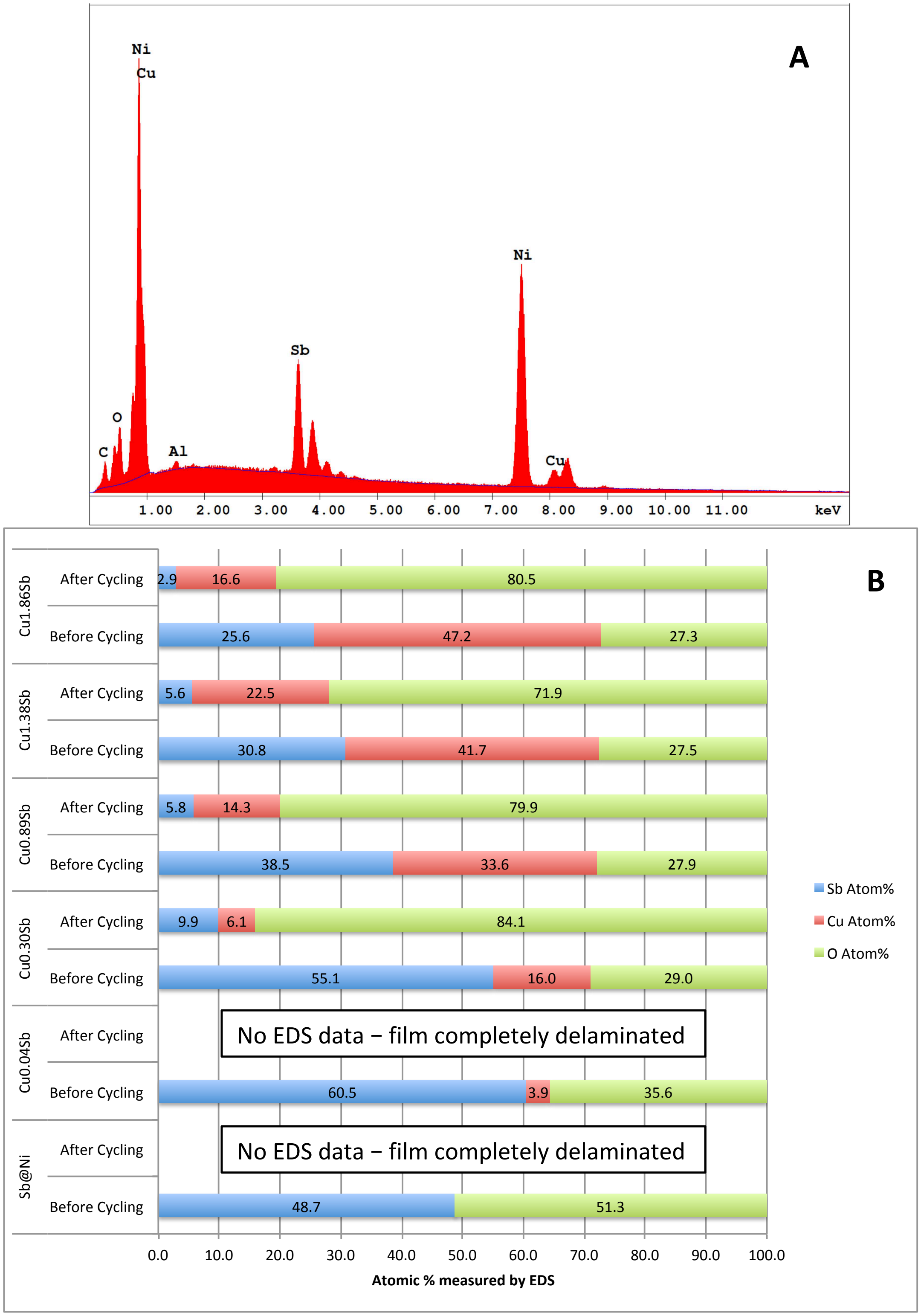

Figure 2.5: (A) Representative EDS spectrum used to quantify the composition of the electrodeposited films, (B) Composition of the amorphous Cu_xSb films as measured by EDS both before and after cycling in Li-ion half-cells.

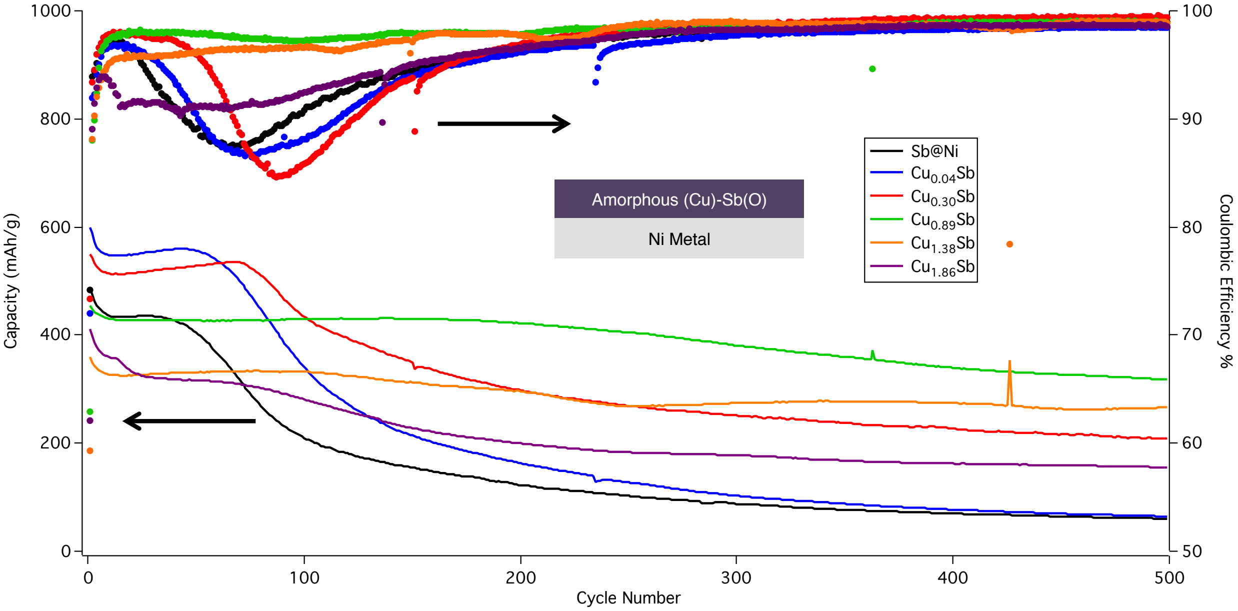

Figure 2.6: Cycle performance of variable composition amorphous Cu-Sb thin films on Ni substrates.

electrodeposition give rise to overestimations of anode loading as determined via counting the charge passed during deposition. The disparity of the Sb@Ni anode capacity is attributed to a lower coulombic efficiency in a deposition solution without Cu^{2+} ions. This observation is consistent with our previous report of induced underpotential deposition of Cu_2Sb from aqueous solution [30].

Regardless of error in the specific capacity magnitude between anodes, examination of the capacities' evolution over many cycles gives insight about how the anode composition affects cycling stability. The anodes with low Cu contents exhibit first cycle coulombic efficiencies around ~70% while those with higher Cu contents have ~60% efficiency, suggesting the higher Cu contents results in more extensive SEI formation on the first lithiation. Note that coulombic efficiency here refers to the ratio of current out/current in, and with these anodes we expect significant surface roughening (hence the observed increase in capacity over many cycles), leading to fresh surface exposed for SEI formation. The rising coulombic efficiencies and steep drops in specific capacities within the first few cycles of all compositions suggest that the SEI continues to form over the first few cycles. Additional steep drops in the specific capacities and dips to around 90% in coulombic efficiency at later cycles mark the regions of "anode failure" characterized by significant and rapid capacity loss as lithiated active material looses contact with the current collector. The number of cycles where such an anode failure region begins serves as a rough quantitative measure of that anode's cycling stability. Anode failure begins around 40 cycles for the Sb-only Sb@Ni anode where the main mechanism of capacity loss seems to be mechanical degradation and film delamination like seen in Figure 2.1D. The beginning of anode failure is extended to around 50 and 70 cycles in the $Cu_{0.04}Sb$@Ni and $Cu_{0.30}Sb$@Ni anodes, respectively, which is expected as the inclusion of more inactive Cu in the film would better buffer volume changes and slow the mechanical degradation and delamination. At higher Cu concentrations, the films' specific capacities start out smaller but diminish to a lesser extent. The $Cu_{0.89}Sb$@Ni anode shows negligible capacity loss for around 150 cycles before slowly and steadily losing capacity. A similar behaviour is seen in the $Cu_{1.38}Sb$@Ni anode, though its capacity diminishes slightly around 100 cycles. The $Cu_{1.86}Sb$@Ni anode shows a capacity drop around cycle 20 before beginning another failure around 70 cycles. Overall, most capacity loss of the anodes is attributed to loss of active material by delamination, while slight increases in capacity may be a result of increased surface area from mechanical roughening that opens new lithiation/delithiation avenues or results in additional SEI layer formation. Post-cycling EDS analysis (Figure 2.5) of the anodes shows significantly increased oxygen contents over the pristine anodes, which is consistent with substantial SEI formation and its oxidation upon exposure and storage in air before analysis.

Generally it seems that the anodes with the best cycling stability have compositions close to Cu_1Sb. This cycling behaviour is consistent with our recent report on Cu_xSb@Cu thin film anodes with compositions of $1<x<3$ where the anode with $x=1$ exhibits the best cycling stability [12]. At anode compositions where $x>1$, the mechanisms that negatively impact cycling stability are two-fold. With increased Cu content, Li can become more easily trapped in the film by Cu-rich phases during delithiation. Additionally, greater amounts of Cu being repeatedly extruded and reincorporated during cycling result in repeated SEI formation on the newly exposed electroactive surfaces. At a composition near $x=1$, we believe the impact of the above mechanisms of capacity loss to be minimized while maintaining enough Cu content for the anode to access Li-Cu-Sb intermediate phases during cycling. Access to these phases significantly alleviates mechanical stresses during cycling by allowing access to multiple lithiation and delithiation events that occur stepwise and at distinct potentials rather than the lithiation and delithiation events consolidated to relatively small voltage regions in Sb metal anodes. Additionally, the fully lithiated cubic Li_3Sb phase (F*m*-3*m)* is more structurally similar to the cubic Li-Cu-Sb intermediate phases (F-43*m*) than the rhombohedral Sb metal phase (R-3*mH*) [13-15]. The structural similarities and stepwise reactions during lithiation and delithiation lessen the impact of the volume changes on the film's mechanical integrity. The access to the intermediate Li-Cu-Sb phases can be seen as the three lithiation and delithiation peaks in the differential capacity plots, like those shown as the (b) peaks in Figure 2.2B. The $Cu_{0.89}Sb$@Ni and higher Cu concentration anodes show these peaks in the differential capacity plots (Figure 2.7), giving rise to generally better cycling stability than the anodes with lower Cu concentrations.

Thin film Cu-Sb anodes show substrate dependent cycle lifetimes

Given that anode compositions with some Cu content display better cycling stability than pure Sb metal on Ni substrates, Sb@Cu anodes may perform worse than the Sb@Ni anodes due to the process of Cu-Sb interdiffusion rather than a composition resulting from said interdiffusion. To test how film-substrate interactions affect cycling stability regardless of film composition in Li-ion half-cells, we electrodeposit and cycle variable composition Cu-Sb thin film anodes on both Cu and Ni substrates. For these particular anodes, we modified a previously reported deposition method to produce films of higher crystallinity and oxygen contents of about 10-30 atom% (see Figures 2.8, 2.9, and 2.10). Changing the concentration of the Cu precursor in the deposition solution was used to vary the Cu:Sb ratio in the film. The anode films were all deposited to charge loadings of 228 mC/cm^2 (~110-140 nm approximate thickness). As such, varying coulombic inefficiencies between depositions contribute error to the specific delithiation

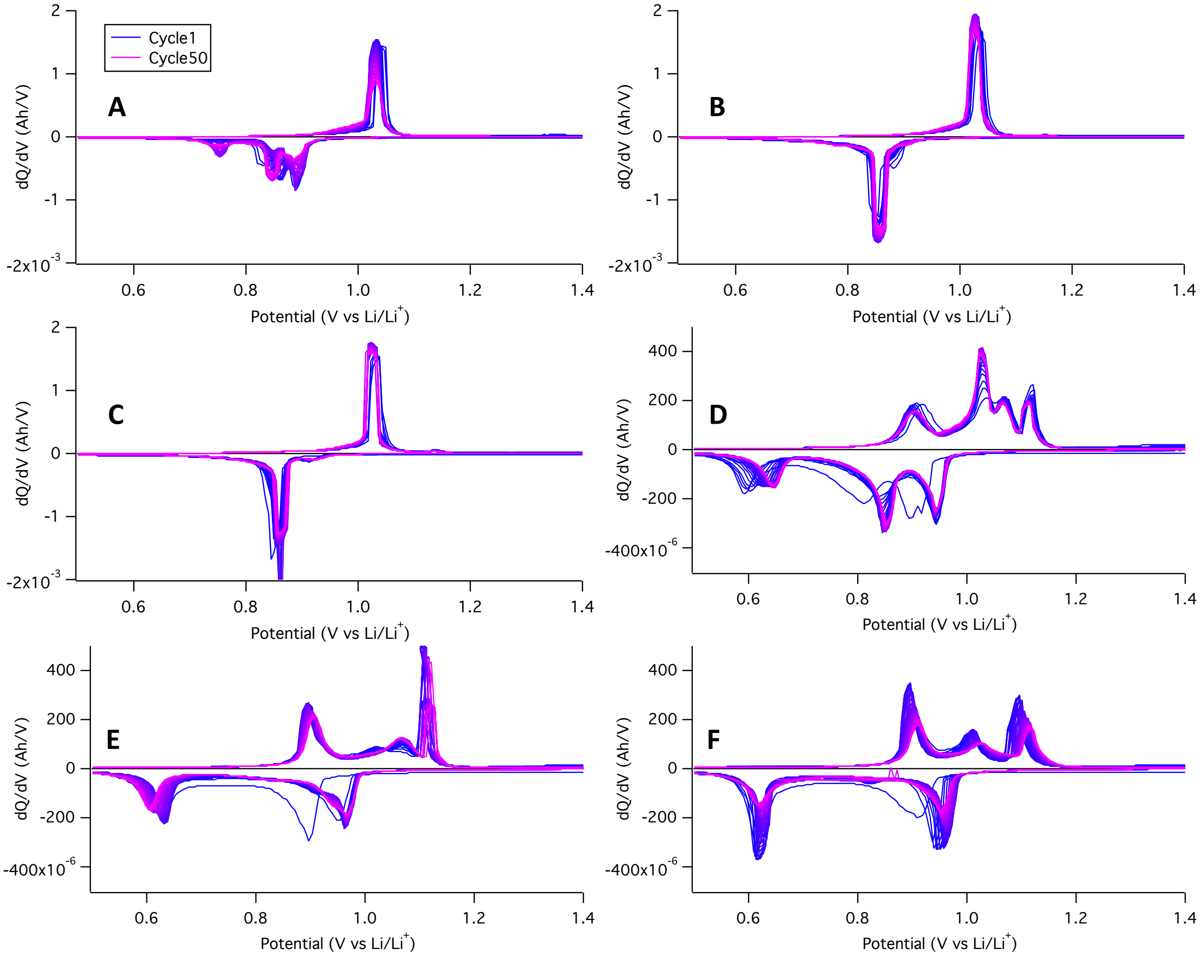

Figure 2.7: Differential capacity plots for the first 50 cycles of the amorphous Cu-Sb@Ni anodes in Li-ion half-cells. The compositions of the anodes are: (A) Sb-only, (B) $Cu_{0.04}Sb$, (C) $Cu_{0.30}Sb$, (D) $Cu_{0.89}Sb$, (E) $Cu_{1.38}Sb$, (F) $Cu_{1.86}Sb$.

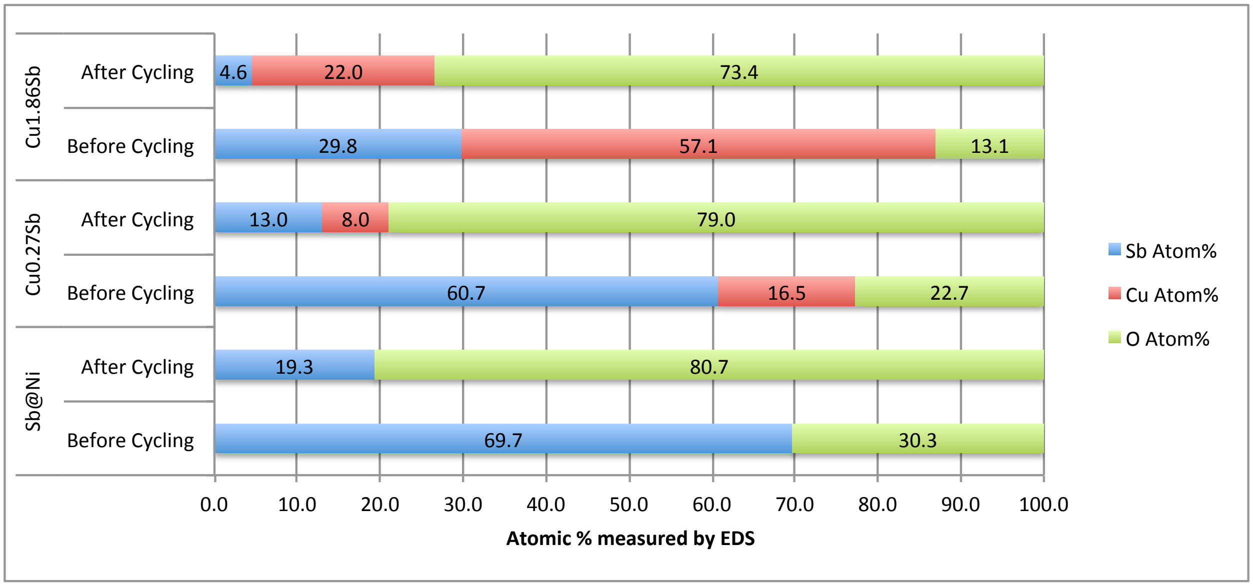

Figure 2.8: Composition of the crystalline $Cu_xSb@Ni$ films as measured by EDS both before and after cycling in Li-ion half-cells.

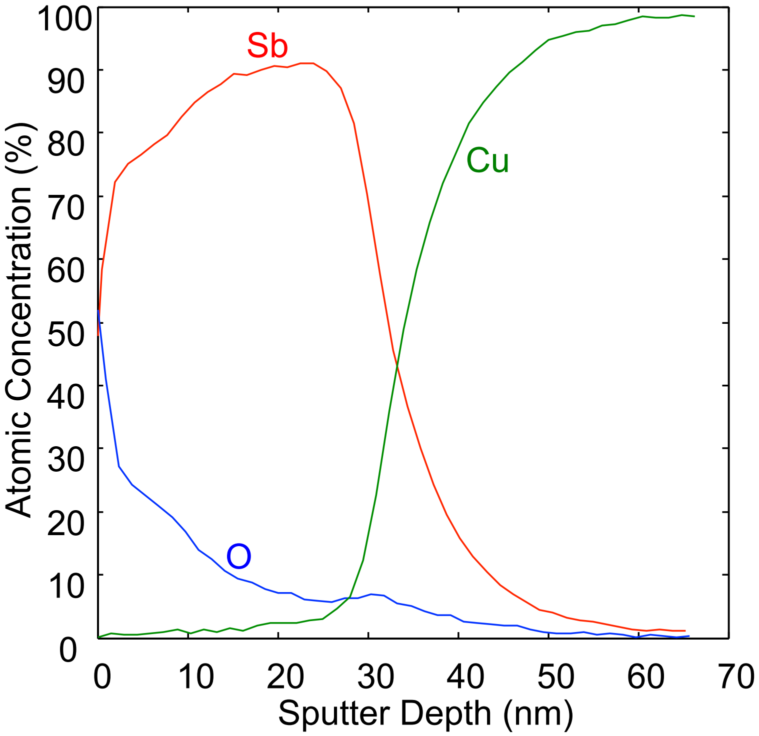

Figure 2.9: Auger depth profile of a crystalline Sb@Cu anode before cycling.

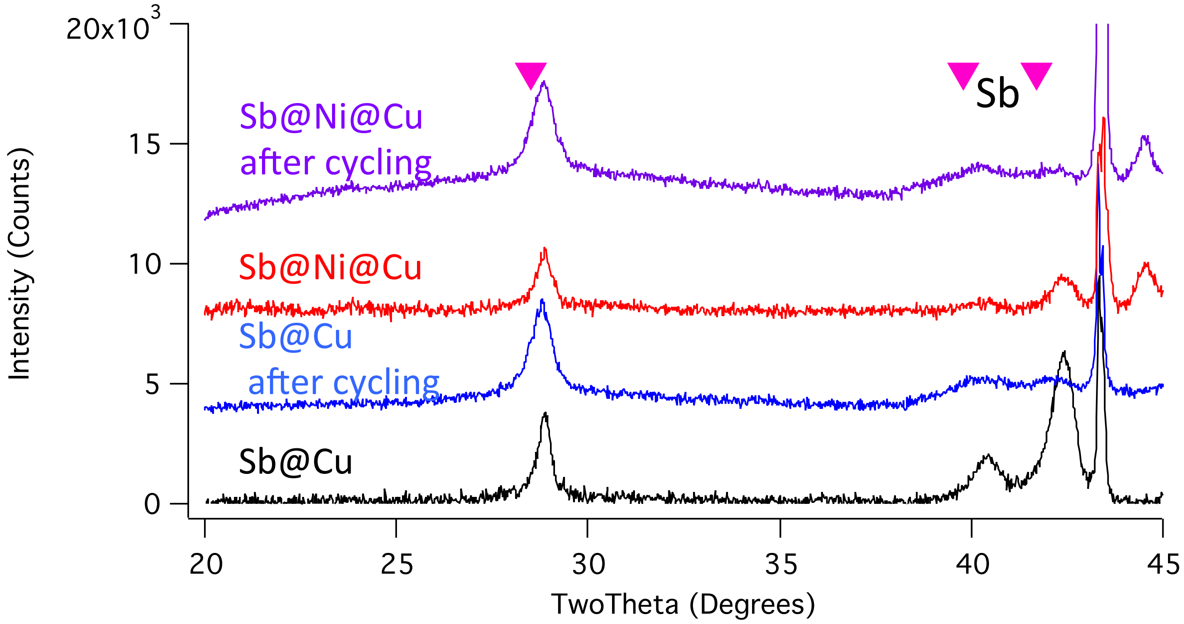

Figure 2.10: PXRD of crystalline anodes before and after cycling in Li-ion half-cells.

capacities shown in Figure 2.11, though examining the capacities over many cycles can be used to assess cycling stability. The first cycle coulombic efficiencies are generally lower in the anodes with higher Cu content, again suggesting more extensive SEI formation on the first lithiation with more Cu content in the anode. The lack of steep drops in capacity in the first few cycles suggests the SEI forms faster on the crystalline films with lower oxygen content. Though compositions continuous across the complete Cu_xSb ($0<x<2$) range were not tested, anodes on the Ni substrates shown in Figure 2.11 (solid traces) show better cycling stability with higher Cu contents, which is consistent with the composition effects on cycling stability discussed previously. The corresponding anodes of identical compositions but on Cu substrates (dashed traces) all exhibit anode failure features where steep drops in capacity and dips to ~90% coulumbic efficiency occur before 30 cycles. These capacity drops on the Cu substrates that are relatively delayed on Ni substrates indicate that film-substrate interactions such as Cu-Sb interdiffusion may negatively impact cycling stability regardless of the film's composition. Post-cycling EDS analysis (Figure 2.8) of the anodes again shows significantly increased oxygen contents attributed to the exposure of formed SEI layers prior to analysis.

To determine if interdiffusion between Cu-Sb is a contributing factor to the poor cycling stability of the crystalline Cu-Sb@Cu anodes when compared to the crystalline Cu-Sb@Ni anodes, ex-situ characterization and close examination of the cycling data was performed. Unlike the amorphous Sb@Cu anode discussed previously, post-cycling XRD of the crystalline Sb@Cu anode after 10 cycles (Figure 2.10) shows no crystalline Cu_2Sb reflections. This disparity suggests that the significant Cu-Sb interdiffusion in the amorphous Sb@Cu anode is driven by the amorphous nature of that film. While XRD does not indicate significant Cu-Sb interdiffusion

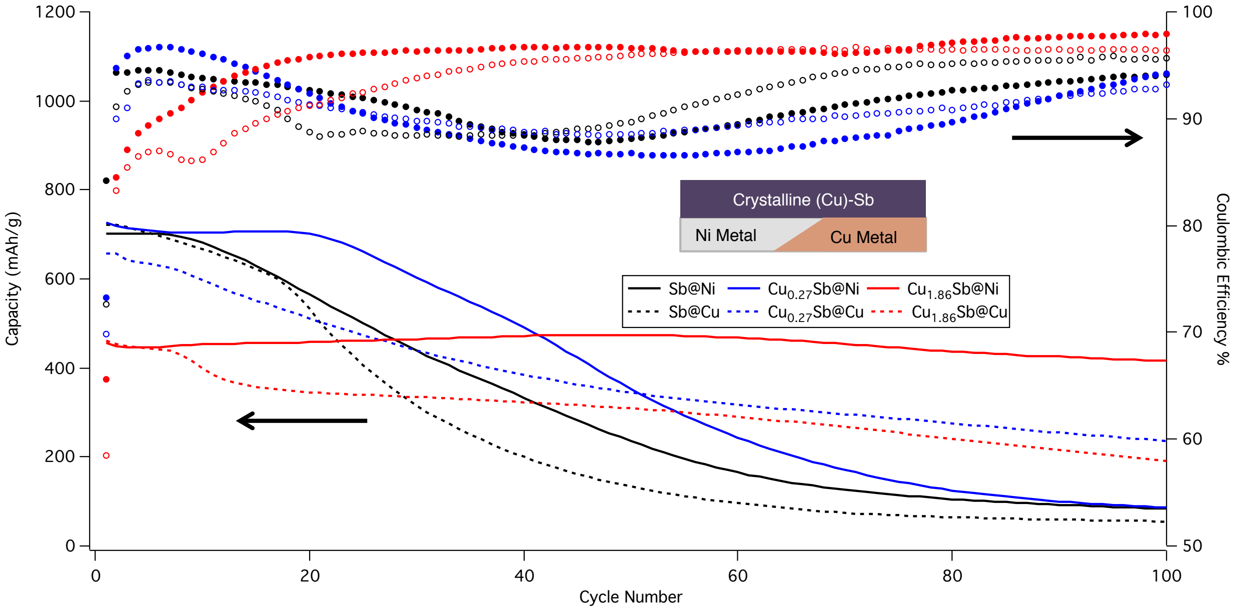

Figure 2.11: Cycle performance of variable composition crystalline Cu-Sb thin films on both Ni (solid traces/filled dots) and Cu (dashed traces/open circles) substrates.

is occurring during cycling of the crystalline Sb@Cu anodes, the differential capacity plot of the crystalline Sb@Cu anode over 10 cycles shows a small amount of lithaition/delithiation chemistry typical of Cu_2Sb as the circled peaks in Figure 2.12A. The peaks indicate Cu-Sb interdiffusion is occurring, but likely localized to the film-substrate interface where both Cu and Sb are present. It is this process of interface localized interdiffusion that may be responsible for the poor cycling stability of the anodes on Cu substrates.

Interdiffusion and void formation at film-substrate interfaces prevented by Ni blocking layers

We have shown that the use of Ni substrates prevents film-substrate interdiffusion and improves the cycling stability of these anodes. However, a Ni layer electrodeposited in between a Cu substrate and an electrodeposited Sb film can also achieve the same effect. Figure 2.12B shows the differential capacity plot of a crystalline Sb@Ni@Cu anode where a Ni blocking layer is electrodeposited between the Sb film and Cu substrate. The plot shows no evidence of Cu_2Sb lithiation/delithaition chemistry indicating the Ni blocking layer effectively prevents even localized Cu-Sb interdiffusion. The cycle lifetime behavior of the Sb@Ni@Cu anode (Figure 2.13) closely matches that of an Sb@Ni anode with better cycling stability than an Sb@Cu anode. Similar Ni blocking layers are commonly used with microelectronic solders to prevent interdiffusion between Au-Cu and Sn-Cu contacts [31]. At such contacts, a phenomenon known as the Kirkendall effect occurs when one metal diffuses into the other at a faster rate. This can cause the collection of structural vacancies into Kirkendall voids [32]. Such voids can mechanically weaken contact interfaces and can result in device failures [33]. Given that the Kirkendall effect has been reported in Cu-Sb systems [34], void formation at the film-substrate interface may be a mechanism for the exacerbated film delamination and poor cycling stability of Sb@Cu and Cu-Sb@Cu anodes.

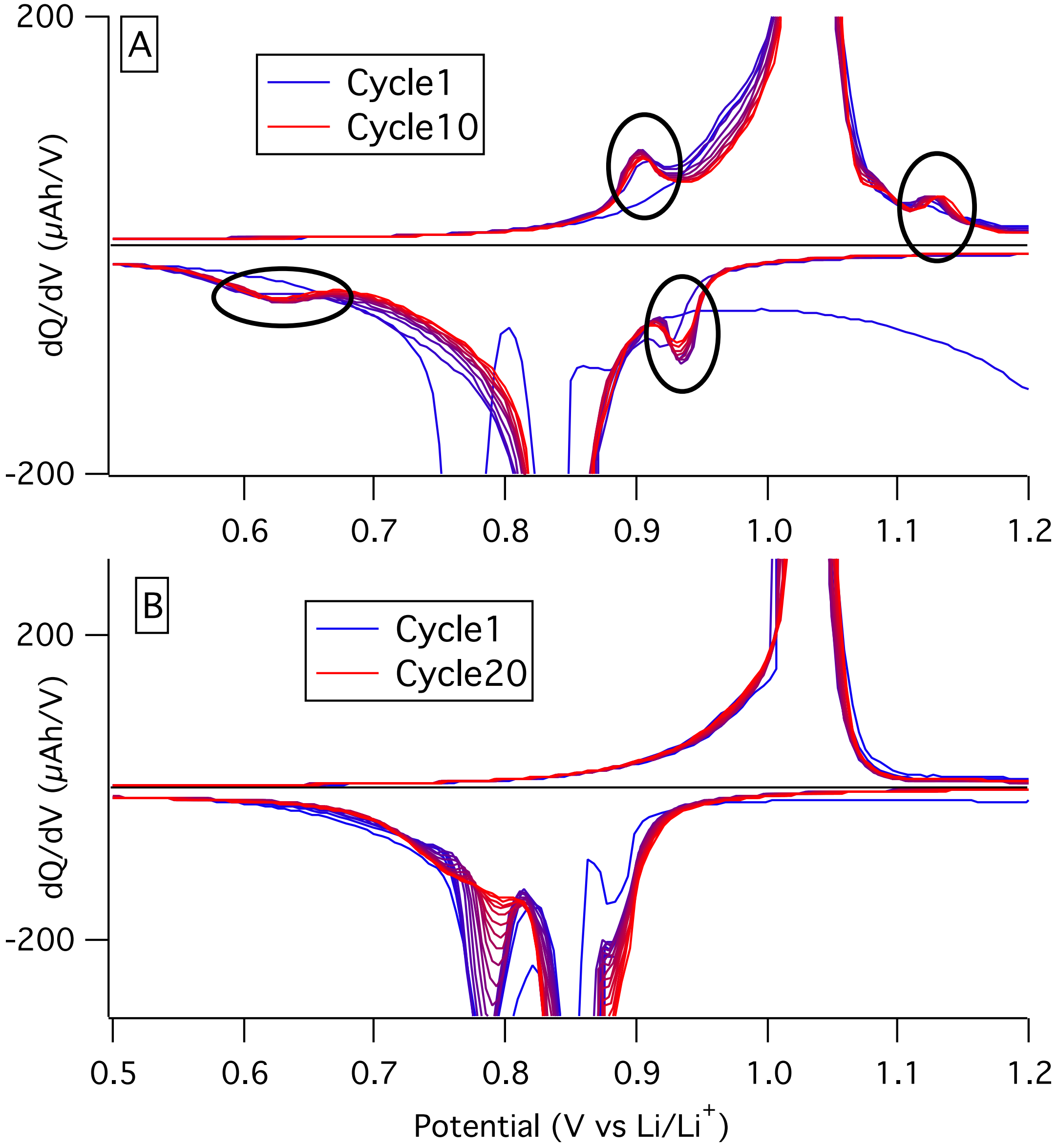

Figure 2.12: Differential capacity plots of: (A) a crystalline-Sb@Cu anode and (B) a crystalline-Sb@Ni@Cu anode.

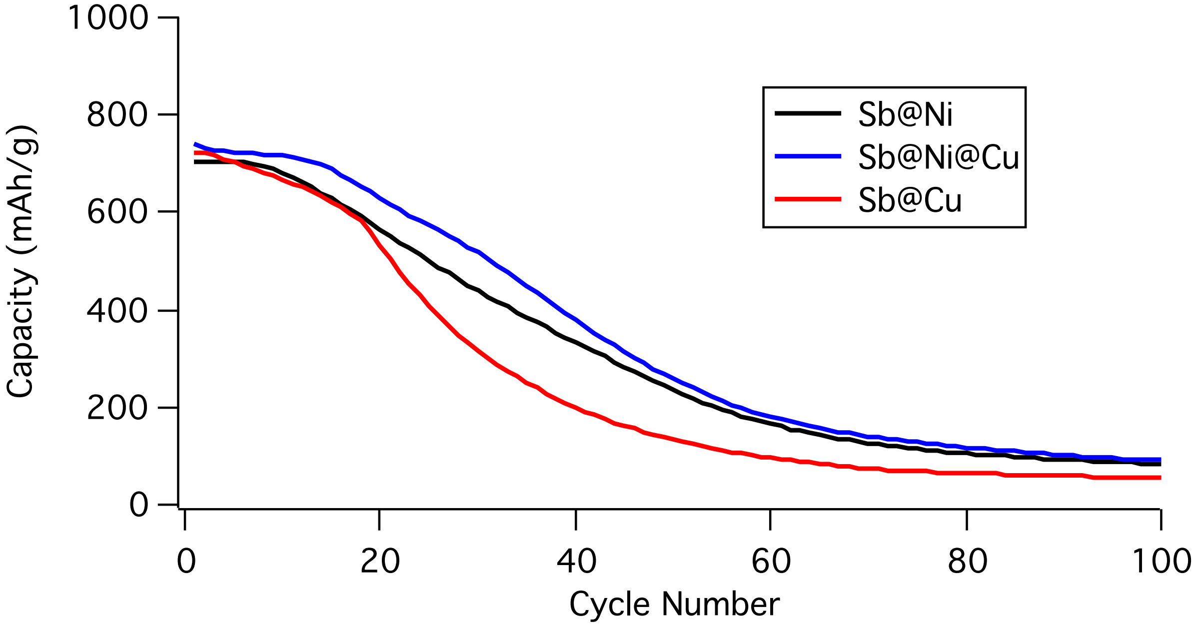

Figure 2.13: Cycle lifetime plot comparing crystalline anodes with the following architectures: Sb@Cu, Sb@Ni, Sb@Ni@Cu.

By examining cross sectional SEM images, we see evidence of Kirkendall-like voids forming as a result of the Cu-Sb interface of Sb@Cu anodes. A ~500 nm layer of Cu evaporated onto a Si wafer with a ~50 nm Cr adhesion layer was used as a substrate so that clean cross-sectional surfaces could be formed by cleaving the wafer. A crystalline Sb film was electrodeposited onto the Cu@Cr@Si as described previously, and the Sb@Cu@Cr@Si anode was cycled a single time in a Li-ion half-cell between 0.5-2.0V to prevent any lithiation of the Si substrate. Figure 2.14A shows the cross-section of the cycled anode where voids have formed at the Cr-Cu interface. The voids can be more clearly visualized when the top Sb@Cu layers are delaminated from the Cr@Si substrate using adhesive tape. The underside of the delaminated Cu layer shown in Figure 2.14B exhibits pitting that is reminiscent of pitting observed in an annealing study of Cu@Sb@Si samples [35].

We believe the formation of these voids to be a result of interdiffusion at the Cu-Sb interface rather than any effect of the Cr@Si substrate. The voids collect at the Cr-Cu interface because it acts as a nucleation zone for vacancy coalescence and void formation in the Sb@Cu@Cr@Si anodes. EDS of the Cu layer underside shows no Cr signal, suggesting Cr-Cu interdiffusion is negligible during cycling and does not play a role in the Kirkendall void formation. To exclude effects of the Cr@Si substrate, an Sb@Cu anode was made and cycled for 100 cycles to totally delaminate the Sb film. The surface of the exposed Cu foil is shown in Figure 2.14C. Its corroded looking morphology suggests the same Kirkendall void formation occurs in the absence of Cr@Si and is a function of interdiffusion at the Cu-Sb interface only.

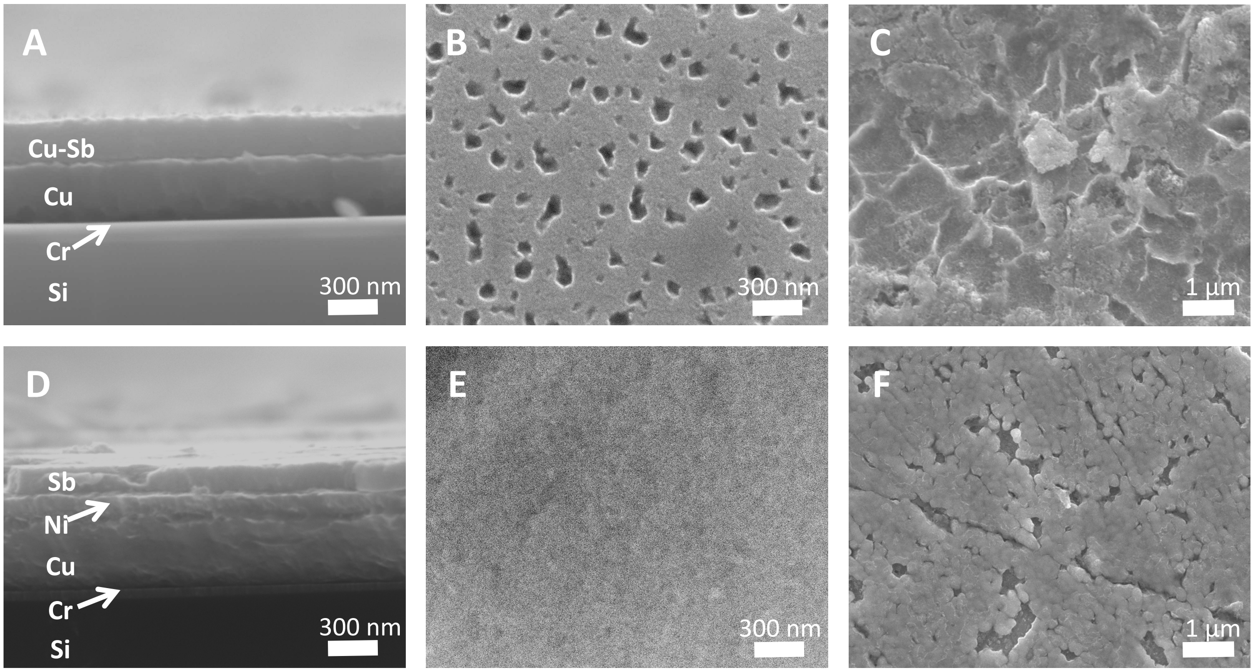

Figure 2.14: SEM micrographs of cycled anode materials: (A) Cross section of Sb@Cu@Cr@Si, (B) Underside of Cu layer mechanically delaminated at the Sb@Cu-Cr interface, (C) Cu foil substrate surface where Sb delaminated during cycling, (D) Cross section of Sb@Ni@Cu@Cr@Si, (E) Underside of Cu layer mechanically delaminated at the Sb@Ni@Cu-Cr interface, (F) Surface of Ni@Cu substrate where Sb delaminated during cycling.

Pitting and corroded Cu surfaces are also observed in cycled Cu_2Sb@Cu@Cr@Si and Cu_2Sb@Cu anodes. This observation indicates that the void formation behaviour also occurs in Cu-containing films on Cu substrates, probably due to the repeated extrusion and reincorporation of Cu during cycling.

To confirm that the voids form as a function of interdiffusion at the Cu-Sb interface, Ni blocking layers were used to prevent void formation in the cross sectional imaged anodes. Figure 2.14D shows the cross section of an Sb@Ni@Cu@Cr@Si anode cycled a single time where a Ni blocking layer separates the Cu and Sb. There is no evidence of voids at the Cr-Cu interface, which is confirmed by the absence of pitting in the underside of the Cu layer (Figure 2.14E) when delaminated by adhesive tape. Figure 2.14F shows the exposed surface of a Ni blocking layer on a Cu foil after 100 cycles caused total film delamination of an Sb@Ni@Cu anode. Aside from small portions of the Ni blocking layer that delaminated with the Sb during cycling, the Ni blocking layer is intact and has its original surface morphology (Figure 2.15). Because the surface is not nearly as corroded at the one shown in Figure 2.14C, the Ni is effectively preventing the Kirkendall void formation that results from Cu-Sb interdiffusion. These observations are consistent with the ability of a Ni substrate or blocking layer to prevent film-substrate interdiffusion, interface weakening, and concomitant decrease of cycling stability that is observed in Sb@Cu anodes.

Relevance of interdiffusion and interface weakening for Sn anodes, Na-ion batteries, and other devices

Figure 2.16A shows a model of an Sb-Cu interface where the direct contact results in excessive interdiffusion, void formation, and interface weakening. While this process may be driven by repeated lithiation and delithiation cycles in a battery, it also occurs during static

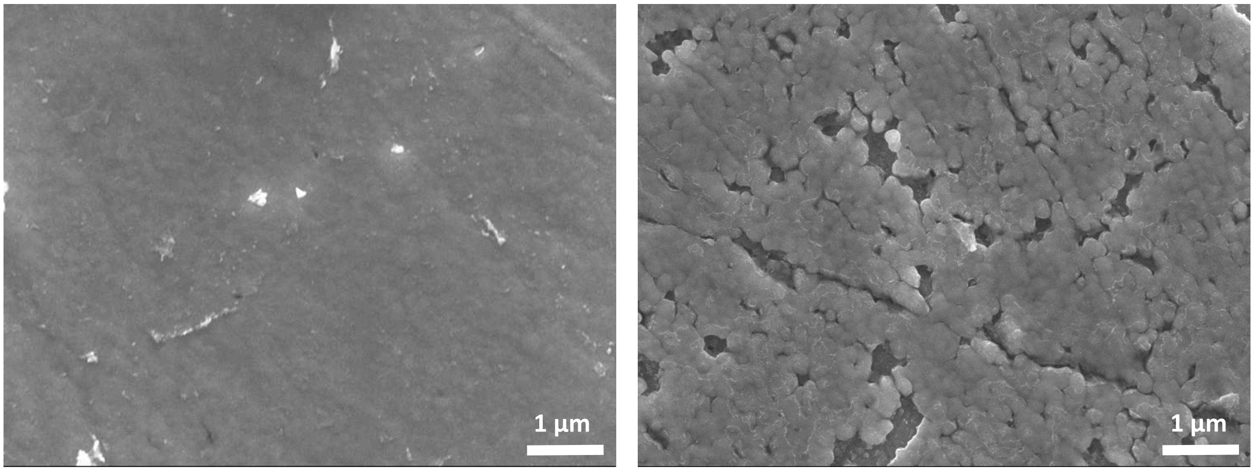

Figure 2.15: SEM images comparing a pre- (left) and post-cycled (right) Ni-blocking layer.

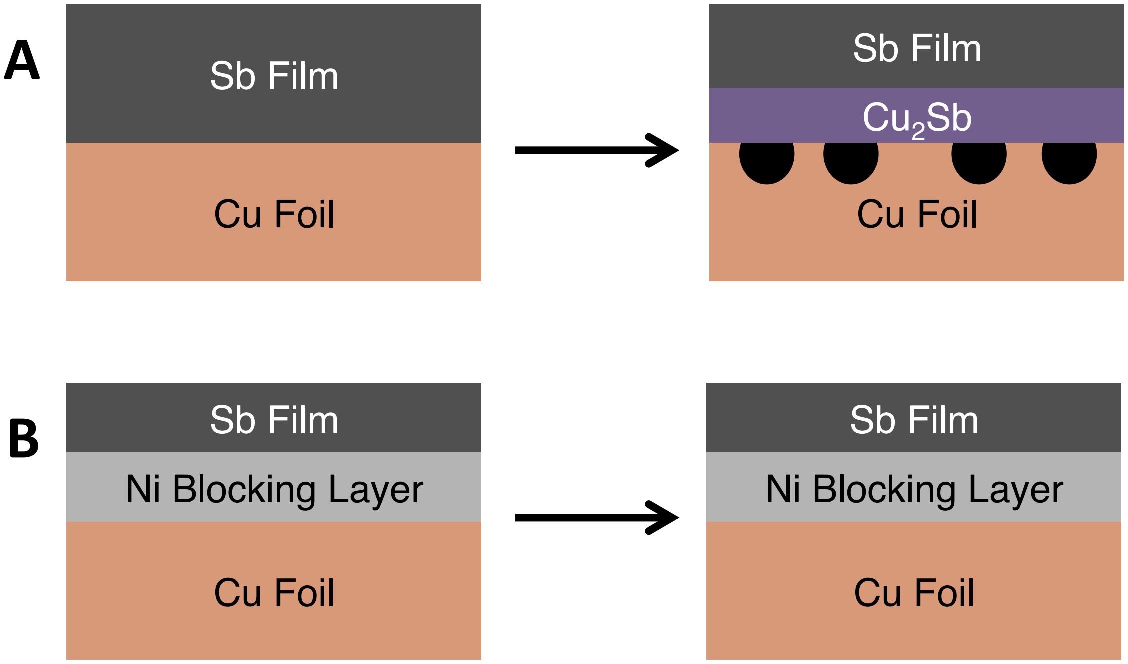

Figure 2.16: Cross sectional models of Sb thin films on Cu substrates: (A) crystalline-Sb@Cu and (B) crystalline-Sb@Ni@Cu.

conditions at ambient temperature and a relevant rate. The delaminated underside of the Cu layer from an Sb@Cu@Cr@Si anode evolves from a pristine non-pitted surface (like Figure 2.14E) immediately after deposition to a pitted surface (like Figure 2.14B) after only a single day of being stored under vacuum. An analogous pitting process is observed at ambient temperature in electrodeposited Sn@Cu@Cr@Si anodes. The pitting from Sn-Cu contact is consistent with previous reports of Kirkendall void formation at those interfaces [36] indicating Sn based anodes could also exhibit substrate dependent cycle lifetimes if interdiffusion between the film and substrate results in Kirkendall voids localized to the interface. Figure 2.16B illustrates how a Ni blocking layer between Cu and Sb prevents interdiffusion and void formation, thus producing better cycling stability. The Ni blocking layer also prevents interdiffusion between Sn and Cu layers at ambient temperature as indicated by the absence of pitting on a delaminated Sn@Cu undersurface. Thus, Ni blocking layers have the potential to prevent Kirkendall void formation in any device where Sb@Cu or Sn@Cu contacts require mechanical stability, such as Na-ion batteries. More generally, interfacial layers that prevent or slow interdiffusion enough to prevent Kirkendall void formation can enhance the mechanical stability of that interface.

Conclusions

To help achieve the longer cycle lifetimes required for realization of high energy density Li-ion batteries, we have presented multiple strategies for improving cycling stability in Cu-Sb based anodes. Electrodeposition of Cu-Sb thin films onto metal foil substrates from aqueous solution is a facile anode production method where composition of the deposited film is easily controlled. We have shown that for thin films of $Cu_{2-x}Sb$ ($0<x<2$), optimal cycling stability is achieved near a composition of $x=1$. This off-stoichiometric composition allows access to the Li-

Cu-Sb ternary phases that improve cycling stability, while minimizing the amount of Cu that may cause excessive SEI growth when repeatedly extruded.

We have also shown how interdiffusion between Cu-Sb thin film anodes and Cu foil substrates during ambient temperature storage or cycling results in the formation of Kirkendall voids at the interface. The presence of the voids weakens the interfaces, exacerbated film delamination, and results in diminished cycling stability of any film composition on a Cu substrate. The lack of any analogous interdiffusion and weakening at Ni interfaces results in improved cycling stability of Cu-Sb films on Ni foil substrates. While interdiffusion can benefit cycling stability by forming intermetallic compositions, we propose the appearance of Kirkendall voids, especially when concentrated at an interface, to be a simple empirical threshold of when interdiffusion occurs to too great of an extent, or too quickly. These strategies for improving cycling stability can be generalized as design considerations for Li-ion and Na-ion batteries:

a) Electrodeposition of anodes allows access to off-stoichiometric compositions that may outperform pure metal or intermetallic phases.

b) Interdiffusion that results in the formation of voids, especially when concentrated at interfaces, results in decreased cycling stability.

c) Blocking layers such as Ni provide a facile solution for preventing undesired interdiffusion that could form voids and weaken interfaces.

Experimental

Anode electrodeposition

The thin film anodes were electrodeposited using a Gamry Reference 3000 potentiostat. Depositions were performed using a Cu foil (McMaster Carr, 99.0% Cu) or Ni foil (Sigma-Aldrich, >99.9% Ni) substrate working electrode, platinum mesh counter electrode (McMaster

Carr, Alloy 316 mesh), and a saturated calomel (SCE) reference electrode. Foil substrates were cleaned in a concentrated HNO_3 solution for 30-60 seconds followed by rinsing in Millipore water and drying. The substrate foils were then masked with Kapton tape or a rubber gasket pressed to the metal surface to define a known area for electrodeposition on one side of the substrate. All electrodepositions were performed at ambient temperature between 21-24 ˚C. To minimize variability in the material loading and thicknesses between anode films to be compared, the amount of electrodeposited material was monitored via coulometry. By doing so the depositions could be normalized to a given amount of charge passed per unit area, what we herein refer to as the "charge loading" and given in units of mC/cm^2.

Anode deposition solutions used in sections 2.1, 2.2, and 2.3 were prepared by first dissolving 1, 5, 14, 20, or 30 mM $CuCl_2 \bullet 2H_2O$ (Sigma-Aldrich, dihydrate, 99+%) in a solution of 200 mM sodium gluconate (Sigma, >99%) in Millipore water (18.2 Mohm). Once completely dissolved, 30 mM $SbCl_3$ (Sigma-Aldrich, anhydrous, >99.0%) was dissolved in the solution and the resulting aqueous solutions were then titrated to a pH of 6.0 using a concentrated NaOH solution. Depositions from this solution were done potentiostatically at -1.60 V vs. SCE.

Anode deposition solutions used in sections 2.4, 2.5, and 2.6 were prepared by first dissolving 25 mM Sb_2O_3 (Sigma-Aldrich, nano-powder, >99.9%) in a solution of 400 mM citric acid (Sigma-Aldrich, >99.5%) in Millipore water (18.2 Mohm) by mixing at 60 ˚C for at least 12 hours. Once the Sb_2O_3 was completely dissolved, 5, 40, or 80 mM $Cu(NO_3)_2 \bullet 2.5H_2O$ (Sigma-Aldrich, >99.99%) was added and the solution was slowly titrated to a pH of 6.0 by addition of a concentrated KOH solution. Depositions from this solution were done potentiostatically at -1.05 V vs. SCE.

The Ni blocking layers used in sections 2.5 were deposited from a previously reported Ni plating bath [37]. Briefly, the bath is an aqueous solution of 280 g/L $NiSO_4 \cdot 6H_2O$, 45 g/L $NiCl_2 \cdot 6H_2O$, 17 g/L citric acid, 2 g/L sodium saccharin, 0.2 g/L 2-butyne-1,4-diol, titrated to a pH of 3.0. The Ni blocking layers were deposited onto the substrates from this solution potentiostatically at -1.0 V vs. SCE for 60 seconds each. The coated substrates were then rinsed with Millipore water before being used as substrates for the Cu-Sb anodes.

Scanning electron microscopy, energy-dispersive X-ray spectroscopy, X-ray diffraction, and Auger depth profiling

Scanning electron microscopy (SEM) analyses were done using the JEOL JSM-6500F microscope. Energy-dispersive x-ray spectroscopy (EDS) was done at 1kx magnification at three different spots to obtain an average film composition. Preparation of cross-sectional samples was done by scoring the back of the Si substrate with a diamond scribe, then cleaving the substrate and deposited film immediately before imaging. Powder X-ray diffraction (PXRD) measurements were done using a Bruker D8 Discover DaVinci powder X-ray diffractometer. Auger spectroscopy and the Auger sputter ion depth profiles were obtained using a Physical Electronics 5600ci multi-technique surface analysis system. Auger spectroscopy and depth profiles were acquired with 5 keV primary electrons in spot analysis mode (<1 um diameter spot size) on a uniform blank location on the plated films. 4 keV Ar ions were used in the sputter profile analysis with sputter rate calibration on SiO_2 at 2.0 nm/minute erosion rate. In order to determine relative atomic concentrations from the Auger data, the following sensitivity factors determined for the system were used: O (0.296), Cu (0.307), Sb (0.704).

Li-ion half-cell cycling

The electrochemical activity of thin film anodes was studied using two electrode Swagelok cells. The anodes did not require any additives or binders, as the active material was directly deposited onto the Cu foil. Circular disks of ½ inch diameter were punched from the deposited thin films and used as working electrodes in Swagelok cells assembled in an Argon atmosphere glove box. Li metal was used as the reference and counter electrode. The electrolyte used was BASF Selectilyte Sample Series A6 (a mixture of diethyl carbonate, dimethyl carbonate, lithium tetrafluoroborate, and other minor additives), which was absorbed into a Whatman glass filter sandwiched between two polymer separators in between the electrodes. The assembled cells were allowed to rest for at least 12 hours before cycling in order to reach a steady state open circuit voltage (OCV). The battery cells were galvanostatically cycled at ambient temperature using an Arbin Instruments battery tester. The cells were all cycled at a rate of C/5 between 0.01 V and 2.0 V vs. Li/Li^+ unless specified otherwise. The current densities for a C/5 rate and the specific anode loadings were calculated using the charge loading measured during electrodepositon and the fraction of active component (Sb) as determined by EDS. Before post-cycling analysis, the cells were held at 2.0 V vs. Li/Li^+ until current became negligible to ensure complete delithiation of the active material. The cells were then disassembled in air and the anode films rinsed with ethanol and dried before ex-situ SEM and PXRD.

CHAPTER 2 REFERENCES

[1] J.-Y. Hwang, S.-T. Myung, Y.-K. Sun, Sodium-ion batteries: present and future, Chem. Soc. Rev. 334 (2017) 928. doi:10.1039/C6CS00776G.

[2] J.B. Goodenough, Energy storage materials_ A perspective, Energy Storage Materials. 1 (2015) 158–161. doi:10.1016/j.ensm.2015.07.001.

[3] M.N. Obrovac, V.L. Chevrier, Alloy Negative Electrodes for Li-Ion Batteries, Chem. Rev. 114 (2014) 11444–11502. doi:10.1021/cr500207g.

[4] D. Kundu, E. Talaie, V. Duffort, L.F. Nazar, The Emerging Chemistry of Sodium Ion Batteries for Electrochemical Energy Storage, Angew. Chem. Int. Ed. 54 (2015) 3431–3448. doi:10.1002/anie.201410376.

[5] M.R. Wagner, P.R. Raimann, A. Trifonova, K.C. Moeller, J.O. Besenhard, M. Winter, Electrolyte Decomposition Reactions on Tin- and Graphite-Based Anodes are Different, Electrochem. Solid-State Lett. 7 (2004) A201–5. doi:10.1149/1.1739312.

[6] M. Ebner, F. Marone, M. Stampanoni, V. Wood, Visualization and Quantification of Electrochemical and Mechanical Degradation in Li Ion Batteries, Science. 342 (2013) 716–720. doi:10.1126/science.1241882.

[7] D. Larcher, S. Beattie, M. Morcrette, K. Edström, J.C. Jumas, J.-M. Tarascon, Recent findings and prospects in the field of pure metals as negative electrodes for Li-ion batteries, J. Mater. Chem. 17 (2007) 3759–3772. doi:10.1039/b705421c.

[8] C.K. Chan, H. Peng, G. Liu, K. McIlwrath, X.F. Zhang, R.A. Huggins, et al., High-performance lithium battery anodes using silicon nanowires, Nature Nanotechnology. 3 (2008) 31–35. doi:10.1038/nnano.2007.411.

[9] E.D. Jackson, A.L. Prieto, Copper antimonide nanowire array lithium ion anodes stabilized by electrolyte additives, ACS Appl. Mater. Interfaces. 8 (2016) 30379–30386. doi:10.1021/acsami.6b08033.

[10] M. He, K. Kravchyk, M. Walter, M.V. Kovalenko, Monodisperse Antimony Nanocrystals for High-Rate Li-ion and Na-ion Battery Anodes: Nano versus Bulk, Nano Lett. 14 (2014) 1255–1262. doi:10.1021/nl404165c.

[11] C.M. Ionica, P.E. Lippens, J.O. Fourcade, J.C. Jumas, Study of Li insertion mechanisms in transition metal antimony compounds as negative electrodes for Li-ion battery, Journal of Power Sources. 146 (2005) 478–481. doi:10.1016/j.jpowsour.2005.03.054.

[12] E.D. Jackson, J.M. Mosby, A.L. Prieto, Evaluation of the Electrochemical Properties of Crystalline Copper Antimonide Thin Film Anodes for Lithium Ion Batteries Produced by Single Step Electrodeposition, Electrochimica Acta. 214 (2016) 253–264. doi:10.1016/j.electacta.2016.07.126.

[13] L. Fransson, J.T. Vaughey, R. Benedek, K. Edström, J.O. Thomas, M.M. Thackeray, Phase transitions in lithiated Cu 2 Sb anodes for lithium batteries: an in situ X-ray diffraction study, Electrochem. Comm. 3 (2001) 317–323. doi:10.1016/S1388-2481(01)00140-0.

[14] S. Matsuno, M. Noji, T. Kashiwagi, M. Nakayama, M. Wakihara, Construction of the Ternary Phase Diagram for the Li-Cu-Sb System as the Anode Material for a Lithium Ion Battery, J. Phys. Chem. C. 111 (2007) 7548–7553. doi:10.1021/jp070397u.

[15] S. Matsuno, M. Noji, M. Nakayama, M. Wakihara, Y. Kobayashi, H. Miyashiro,

Dynamics of Phase Transition in Li–Cu–Sb Anode Material for Rechargeable Lithium Ion Battery, J. Electrochem. Soc. 155 (2008) A151–7. doi:10.1149/1.2815477.

[16] E.D. Jackson, S. Green, A.L. Prieto, Electrochemical Performance of Electrodeposited Zn 4Sb 3Films for Sodium-Ion Secondary Battery Anodes, ACS Appl. Mater. Interfaces. 7 (2015) 7447–7450. doi:10.1021/am507436u.

[17] L. Baggetto, E. Allcorn, A. Manthiram, G.M. Veith, Cu2Sb thin films as anode for Na-ion batteries, Electrochemistry Communications. 27 (2013) 168–171. doi:10.1016/j.elecom.2012.11.030.

[18] A. Darwiche, C. Marino, M.T. Sougrati, B. Fraisse, L. Stievano, L. Monconduit, Better Cycling Performances of Bulk Sb in Na-Ion Batteries Compared to Li-Ion Systems: An Unexpected Electrochemical Mechanism, J. Am. Chem. Soc. 134 (2012) 20805–20811. doi:10.1021/ja310347x.

[19] H. Bryngelsson, J. Eskhult, L. Nyholm, K. Edström, Thin films of Cu2Sb and Cu9Sb2 as anode materials in Li-ion batteries, Electrochimica Acta. 53 (2008) 7226–7234. doi:10.1016/j.electacta.2008.05.005.

[20] D. Applestone, S. Yoon, A. Manthiram, Cu2Sb–Al2O3–C nanocomposite alloy anodes with exceptional cycle life for lithium ion batteries, J. Mater. Chem. 22 (2012) 3242–7. doi:10.1039/c2jm13479a.

[21] T. Yang, H. Wang, J. Xu, L. Wang, W.-C. Song, Y. Mao, et al., Preparation of a Sb/Cu2Sb/C composite as an anode material for lithium-ion batteries, RSC Adv. 6 (2016) 78959–78962. doi:10.1039/C6RA14072F.

[22] E. Allcorn, A. Manthiram, FeSb 2–Al 2O 3–C Nanocomposite Anodes for Lithium-Ion Batteries, ACS Appl. Mater. Interfaces. 6 (2014) 10886–10891. doi:10.1021/am500448f.

[23] J.M. Mosby, A.L. Prieto, Direct Electrodeposition of Cu 2Sb for Lithium-Ion Battery Anodes, J. Am. Chem. Soc. 130 (2008) 10656–10661. doi:10.1021/ja801745n.

[24] J. Park, S. Rajendran, H. Kwon, Effects of substrate morphology and ageing on cycle performance of a Sn-anode fabricated by electroplating, Journal of Power Sources. 159 (2006) 1409–1415. doi:10.1016/j.jpowsour.2005.11.064.

[25] N.-R. Shin, Y.-M. Kang, M.-S. Song, D.-Y. Kim, H.-S. Kwon, Effects of Cu substrate morphology and phase control on electrochemical performance of Sn–Ni alloys for Li-ion battery, Journal of Power Sources. 186 (2009) 201–205. doi:10.1016/j.jpowsour.2008.09.095.

[26] N. Tamura, R. Ohshita, M. Fujimoto, S. Fujitani, M. Kamino, I. Yonezu, Study on the anode behavior of Sn and Sn–Cu alloy thin-film electrodes, Electrochimica Acta. 107 (2002) 48–55. doi:10.1016/S0378-7753(01)00979-X.

[27] M. Morcrette, D. Larcher, J.M. Tarascon, K. Edström, J.T. Vaughey, M.M. Thackeray, Influence of electrode microstructure on the reactivity of Cu2Sb with lithium, Electrochimica Acta. 52 (2007) 5339–5345. doi:10.1016/j.electacta.2007.01.083.

[28] R. Halimi, A. Merabet, Kinetics of compound formation in Cu-Sb thin films, Surface Science. 223 (1989) 599–606. doi:10.1016/0039-6028(89)90684-5.

[29] Hanna Bryngelsson, Jonas Eskhult, Leif Nyholm, Merja Herranen, A. Oscar Alm, K. Edström, Electrodeposited Sb and Sb/Sb2O3 Nanoparticle Coatings as Anode Materials for Li-Ion Batteries, Chem. Mater. 19 (2007) 1170–1180. doi:10.1021/cm0624769.

[30] J.M. Mosby, D.C. Johnson, A.L. Prieto, Evidence of Induced Underpotential Deposition of Crystalline Copper Antimonide via Instantaneous Nucleation, J. Electrochem. Soc. 157 (2010) E99–E105. doi:10.1149/1.3392292.

[31] M. Paunovic, P.J. Bailey, R.G. Schad, D.A. Smith, Electrochemically Deposited Diffusion Barriers, J. Electrochem. Soc. 141 (1994) 1843–1850. doi:10.1149/1.2055015.

[32] D. Kim, J.-H. Chang, J. Park, J.J. Pak, Formation and behavior of Kirkendall voids within intermetallic layers of solder joints, J Mater Sci: Mater Electron. 22 (2011) 703–716. doi:10.1007/s10854-011-0357-2.

[33] T.S. Huang, H.W. Tseng, Y.H. Hsiao, C.H. Cheng, C.T. Lu, C.Y. Liu, Abnormal Cu3Sn Growth and Kirkendall Formation Between Sn and (111) and (220) Preferred-Orientation Cu Substrates, Electrochem. Solid-State Lett. 14 (2011) H393–4. doi:10.1149/1.3608248.

[34] K. Hoshino, Y. Iijima, K. Hirano, Interdiffusion and Kirkendall Effect in Cu–Sb Alloys, Transactions of the Japan Institute of Metals. 22 (1981) 527–534.

[35] M. Nasser, B. Mokhtar, B. Mahfoud, R. Mounir, Z. Fouzia, B. Chaouki, Effect of the antimony thin-fil deposition sequence on copper-silicon interdiffusion, Materials and Technology. 46 (2012) 139–144.

[36] J.M. Park, S.H. Kim, M.H. Jeong, Effect of Cu–Sn intermetallic compound reactions on the Kirkendall void growth characteristics in Cu/Sn/Cu microbumps, Jpn. J. Appl. Phys. 53 (2014) 05HA06. doi:10.1143/JJAP.51.05EE05.

[37] T. Doi, K. Mizumoto, S. Tanaka, T. Yamashita, Bright nickel plating from nickel citrate electroplating baths, Metal Finishing. 102 (2004) 26–35. doi:10.1016/S0026-0576(04)90236-X.

CHAPTER 3 – ELECTRODEPOSITION OF SB/CNT COMPOSITE FILMS AS ANODES FOR LI-ION AND NA-ION BATTERIES[7]

Overview

Antimony is a known high capacity anode material for both Li- and Na-ion batteries that has the potential to improve the energy storage density over commercial graphite anode-based Li-ion batteries. As with other high capacity anode materials (such as silicon), the large storage capacity of antimony results in large volume changes of the anode during discharge/recharge cycles. This results in the formation of significant cracking of the anode, causing active material to lose electrical connection to the current collector, which ultimately causes the cell to fail. To address this type of failure, we incorporate carbon nanotubes into antimony carbon nanotube composite electrodes (Sb/CNT) using a one-step electrodeposition procedure. The advantage of directly depositing functional anodes from solution is that no binders are used and there is no post-processing required. This means that the electrical and mechanical behavior of these materials can be probed directly in functioning battery cells, without the convolution of other materials. The Sb/CNT composite films cycle with higher reversible capacities and for longer than Sb films electrodeposited without CNT's in both the Li-ion and Na-ion cells. Post-cycling characterization of the anodes confirms the ability of the CNT's to keep the anode film more mechanically and electrically connected, despite large volume changes and significant solid-electrolyte-interface layer formation.

---

[7] This chapter is under review for publication in Energy Storage Materials (Elsevier) with Maxwell C. Schulze, Ryan M. Belson, Leslie A. Kraynak, and Amy L. Prieto as authors. Maxwell C. Schulze performed the experiments and wrote this chapter with guidance from Amy L. Prieto. Ryan M. Belson performed experiments for the SbSn/CNT section with guidance from Maxwell C. Schulze, while Leslie A. Kraynak contributed by performing the XPS analysis.

Introduction

The continuing trends of vehicle electrification and powering electricity grids with intermittent renewable energy sources requires continued development of next generation rechargeable battery technologies [1-3]. There are many known strategies for increasing important performance metrics such as energy/power density, cycle lifetimes, affordability, and safety factors of new battery technologies. However, improving one performance metric often comes at the expense of the others [3]. Thus, additional exploration of emerging battery chemistries can help to identify how different strategies interplay with each other to create battery systems with optimized performance for specific applications.

One of the main strategies for improving energy and power density is to substitute the prototypical graphite anode in rechargeable batteries with alloy anodes that can store greater amounts of Li or Na [4]. Commonly employed alloy anode materials include Si, Ge, Sn, and Sb for Li-ions [4] and P, Sn, Sb for Na-ions [5,6]. These materials suffer from volume changes during (de)alloying with Li or Na that are sufficiently large such that they cause mechanical degradation (cracking) that can disrupt electrical connectivity to the electrodes' current collectors, rendering the isolated material electrochemically inactive. To avoid this mode of electrode degradation, the anode materials can be nanostructured, alloyed with inactive components, and/or formulated with polymer binders and conductive additives.

However, each of those strategies decreases gains in energy density as well as exacerbates a different mode of electrode degradation: excessive buildup of the solid-electrolyte-interface (SEI) layer. The SEI layer forms to passivate any electroactive surfaces exposed to the electrolyte, consuming electrolyte components like Li/Na-salts and solvent molecules [7]. Large surface area (nanostructured) electrodes and newly exposed surfaces (from mechanical degradation) can result in excessive amounts of SEI layer that render intolerable amounts of Li or Na unusable to the cell or impede/block ion movement to and from the electrode [8,9].

At 660 mAh/g storage capacity for Li^+ and Na^+, Sb exhibits a modest increase in Li^+ storage capacity over graphite (372 mAh/g for Li^+) as well as the ability to store Na^+. However, the alloying potential of Sb (~0.9 V vs. Li, ~0.6V vs. Na) is greater than that of graphite (~0.1 V vs. Li^+), resulting in lower energy densities in a full-cell battery despite a larger storage capacity. The higher alloying potential does impart an additional safety factor to cells with Sb anodes, as the alloying potentials are sufficiently positive of the Li or Na plating potentials, essentially eliminating the hazard of Li or Na dendrite growth during charging that can be responsible for internal short circuiting and resulting explosions. An additional advantage of Sb anodes is their ability to be easily produced via electrodeposition [10-14].

Producing anode films via electrodeposition ensures good electrical connectivity to metal foil current collectors, and if well controlled, good mechanical adhesion [15]. The technique also allows anodes to be deposited onto non-planar substrates, enabling 3-dimensional battery architectures that are not easily accessible by typical formulation and slurry coating methods of electrode manufacturing [16]. However, many electrode films produced by electrodeposition are susceptible to mechanical degradation because they lack the porosity and mechanical resiliency that give formulated slurry-coated electrodes their good cycling stability. The advantages of electrodeposition can be combined with the mechanical durability of slurry electrodes by developing new electrodeposition procedures that co-deposit the active material with binders or other additives. Carbon nanotubes (CNTs) are a good candidate for co-depositing via electrodeposition [17-20]. Not only could their large aspect ratios provide strong mechanical support to a deposited film over multi-micron length scales, but their electronic conductivity could help keep otherwise mechanically separated portions of active material electrically connected [21]. There are many examples of using CNTs to enhance the performance of battery electrode materials made using electrodeposition [22-24], slurry coating [25], and other methods [24,26-28].

Herein, we report an aqueous electrodeposition procedure that co-deposits CNTs with an Sb-based active material. This is the first report of an Sb/CNT composite formed via electrodeposition that are cycled without the use of any additional conductive additives or binders. Not only do SEM and XPS analysis confirm the presence of numerous CNTs in the composite film, but the presence of the CNTs also alters the morphology of the deposited film to form a “beads-on-a-string” like porous morphology. We compare the cycling performance of the Sb/CNT composite films to electrodeposited Sb films without CNTs in both Li-ion and Na-ion half cell batteries. The inclusion of the CNTs into the electrodeposited films enhances the performance of the electrodes in both the Li-ion and Na-ion cells, which we attribute to the porous morphology and improved mechanical/electrical connectivity of the Sb/CNT composite films. Post-cycling characterization of the electrode films was used to elucidate specific failure modes of these types of electrodes as well as limitations that need to be addressed before they could be used effectively in full cell batteries. Finally, we show the applicability of this electrodeposition towards another Li-ion alloy system, producing SnSb/CNT films and cycling them in Li-ion half cells.

Experimental

Preparation of electrodeposition solutions

Typical electrodeposition solution batches were made using 200 mM sodium gluconate (20 mmol, 4.363 g, Sigma, >99%), 30 mM hexadecyltrimethylammonium bromide (CTAB, 3 mmol, 1.093 g, Sigma, >98%), 30 mM $SbCl_3$ (3 mmol, 0.684 g, Sigma-Aldrich, anhydrous, >99.0%), and amine functionalized carbon nanotubes (ACNT, excess, cheaptubes.com, >99wt%, 13-18 nm OD, 3-30 μm length, 7.0% +/- 1.5% functional content) in Millipore water (100 mL, 18.2 Mohm). Typically, the sodium gluconate and CTAB were dissolved in the water first, to form a slightly cloudy/opalescent solution. The $SbCl_3$ (and/or $SnCl_2$ Sigma-Aldrich, dihydrate, 98%) was then added and sonicated to first form a cloudy white mixture, which quickly turned to a clear colorless solution upon continued sonication. As a final step (excluded for deposition solutions to be used for depositing films without CNTs), ACNTs were added in excess (5 heaping scoopulas for 100 mL batch) and the mixture sonicated in a bath sonicator for 2 hours. The mixture was transferred to centrifuge tubes and centrifuged at 5000 rpm for 5 minutes to precipitate any unsuspended agglomerations of ACNTs. The homogenous suspension of ACNTs was decanted and used for electrodeposition of the Sb/CNT composite films; the suspended ACNTs remain stably suspended for more than several months.

Cyclic voltammetry and electrodeposition

A Gamry Reference 3000 potentiostat was used to perform cyclic voltammetry (CV) and electrodepositions. The CVs of the deposition solutions were obtained at 20 mV/s using a three electrode setup with a saturated calomel reference electrode, Pt mesh counter electrode, and Pt working electrode. The electrodepositions were performed using ½” diameter circular disks of either Ni foil (McMaster Carr, 99.0% Ni, Alloy 200/201, 0.001” thickness) or textured Cu (tCu) foil (Oak-Mitsui, TLB-DS Cu foil) substrate working electrode, stainless steel mesh counter electrode, and a saturated calomel (SCE) reference electrode. Foil substrates were cleaned in a 12 M HCl solution for 15 seconds followed by rinsing in Millipore water and drying. The substrate foils were then fixed horizontally in an electrodeposition cell where a rubber O-ring defines a

0.713 cm^2 deposition area. The cell fixes the counter electrode ~2 cm above the substrate foil with the reference electrode in between. All electrodepositions were performed at ambient temperature between 21-24 ˚C and deposited by holding the potential of the working electrode at -1.05 V vs. SCE until the charge passed equaled 3 C/cm^2 or 10 C/cm^2 for the "high-loading" electrodes. The deposited films were removed from the cell, rinsed with water and then ethanol, then dried in air at ambient temperature.

Scanning electron microscopy, energy-dispersive X-ray spectroscopy, X-ray diffraction, and X-ray Photoelectron Spectroscopy

Scanning electron microscopy (SEM) analyses were done using a JEOL JSM-6500F microscope equipped with an Oxford 80 X-MAX (80mm) SDD energy-dispersive X-ray spectroscopy (EDS) detector. EDS measurements were made at 15 keV and 1kx magnification at three different spots to obtain an average film composition and standard deviation based on the different measurement locations. Quantification of the EDS data was performed using the factory standards included in Oxford AZtec software (3.3 SP1). Samples for cross-sectional imaging were prepared by submerging foil in liquid nitrogen and tearing the foil in half. Powder X-ray diffraction (PXRD) measurements were done using a Bruker D8 Discover DaVinci powder X-ray diffractometer. X-ray photoelectron spectroscopy (XPS) measurements were performed with a Physical Electronics (PHI) 5800 series Multi-Technique ESCA system with a monochromatic Al Kα (hν = 1486.6 eV) X-ray source operating at 350.0 W. High resolution (HRES) spectra for the elements of interest were collected with a pass energy of 23.5 eV in intervals of 0.100 eV/step over a 0.6 x 2.0 mm analysis area. After collecting spectra of the pristine films, the samples were sputtered for 60 s using a 3 x 3 mm 5 keV Ar^+ beam to remove adventitious carbon. The binding energies of the HRES spectra were calibrated by shifting the metallic antimony $3d_{5/2}$ peak to 528.0 eV. Peak fitting and quantification of the XPS HRES spectra was performed using CasaXPS (Version 2.3.16). For peak fitting, a nonlinear Shirley background was used, and a 30% Lorentzian/ 70% Gaussian line shape was used for all peaks except those corresponding to metallic antimony and sp^2 carbon, which were fit with a 30% Lorentzian/ 70% Gaussian lineshape modified with an exponential blend function. Quantification was based on PHI relative sensitivity factors corrected for angular distribution.

Assembly and cycling of half-cell batteries

The ½" diameter electrode foils with the deposited Sb or Sb/CNT composite films were used as working electrodes in two electrode Swagelok cells assembled in an Argon atmosphere glove box. Metallic Li or Na was pressed into the cell with a stainless steel mesh and spring and was used as the reference and counter electrode. The electrolyte used was either 1.0M $LiPF_6$ in ethylene carbonate (EC):diethylcarbonate (3:7 by volume) or 1 M $NaPF_6$ in EC:dimethylcarbonate:fluorethylenecarbonate (425:425:50 by volume) for the Li- and Na-ion half cells, respectively. The electrolyte was absorbed into a Whatman glass filter sandwiched between two polymer separators in between the electrodes. The assembled cells were allowed to rest for at least 12 hours before cycling in order to reach a steady state open circuit voltage (OCV). The battery cells were galvanostatically cycled at ambient temperature using an Arbin Instruments battery tester. The cells were all cycled at a rate of 0.1 mA/mg between 0.01 V and 2.0 V vs. Li/Li^+ or Na/Na^+ unless specified otherwise. The current densities were determined using the gravimetrically measured film loading (~0.9 mg for 3 C/cm^2, ~2.7-3.0 mg for 10 C/cm^2 charge loadings). The cells were disassembled in a delithiated state in air and the anode films rinsed with ethanol and dried before post-cycling SEM imaging.

Results and Discussion

Electrodeposition of Sb and Sb/CNT composite films

To co-electrodeposit Sb with CNTs, we modified an aqueous antimony deposition solution by adding a dispersant and amine functionalized CNTs. To facilitate the migration of the CNTs towards the negatively biased substrate and their subsequent inclusion into the electrodeposited film, we rationally designed the solution to impart the suspended CNTs with a positive zeta potential. Using the cationic surfactant CTAB as the dispersant imparts the suspended CNTs with such a positive zeta potential. Additionally, amine functionalization of the CNTs has been shown to result in a positive zeta potential, especially at an acidic pH [29,30]. The solution composition used for the electrodepositions is shown in Figure 3.1a along with CVs that show similar electrochemical behaviors of the solutions with and without suspended CNTs. Figure 3.1b shows a PXRD pattern that is representative of films electrodeposited potentiostatically at -1.05 V vs. SCE to 3 C/cm^2 from solutions with and without suspended CNTs onto Ni foil substrates; the resulting films will be referred to as Sb/CNT@Ni and Sb@Ni, respectively. The PXRD pattern shows that both the Sb@Ni and Sb/CNT@Ni films exhibit poor crystallinity, which is typical of films deposited from these types of solutions [14].

Imaging the deposits with SEM reveals significant morphological differences between the Sb@Ni and Sb/CNT@Ni films. Figure 3.2a-b shows severe cracking in the Sb@Ni film, indicating significant internal stress, though its surface is smooth and uniform with no dendritic growth. Cross sectional imaging of the Sb@Ni film shown in Figure 3.2c provides a film thickness of ~3.5 μm that is dense and free of porosity, while EDS mapping reveals that oxygen is concentrated at the surface of the film. Figure 3.2d-e show less severe cracking of the Sb/CNT@Ni film and rough and porous morphology, with Sb grains nucleating and growing

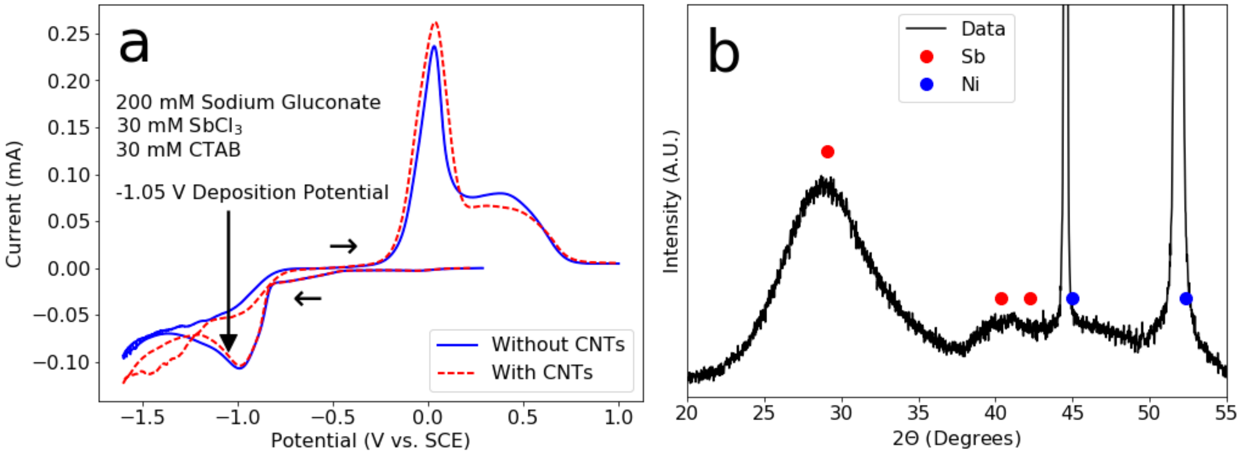

Figure 3.1 (a) Cyclic Voltammograms of the listed electrodeposition solution with and without suspended CNTs. (b) A representative powder X-ray diffraction pattern of either the Sb or Sb/CNT composite films electrodeposited @-1.05 V vs. SCE onto Ni foil substrates.

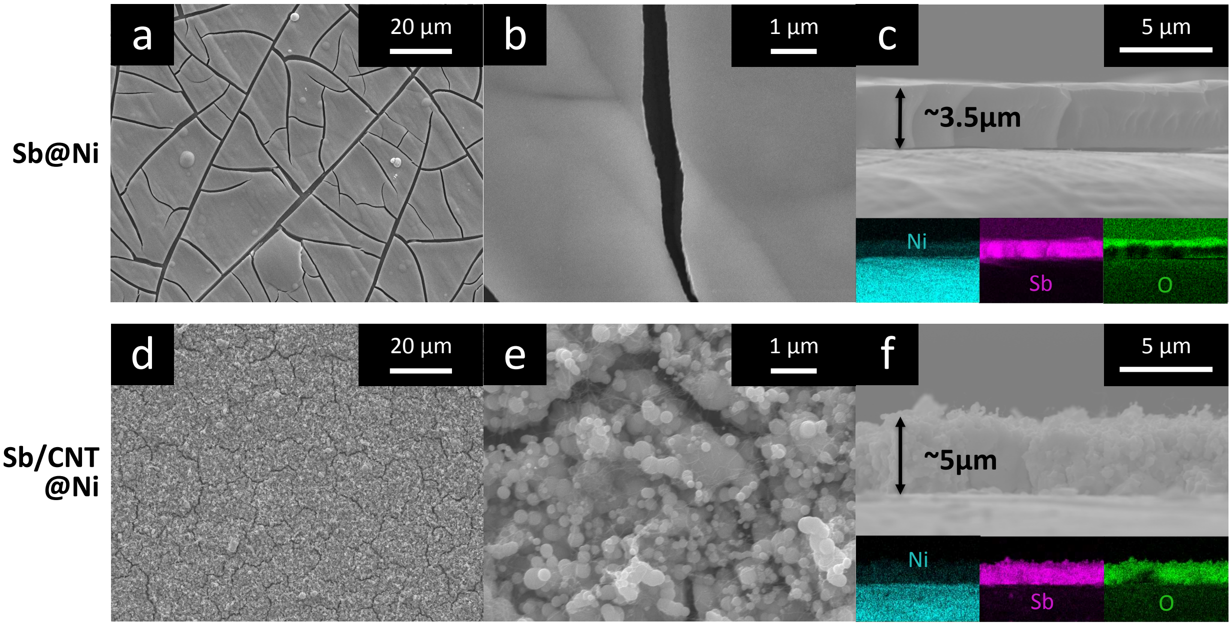

Figure 3.2 SEM images of: (a-b) top surface of an Sb@Ni film, (c) cross-section of Sb@Ni film with an EDS map inlay, (d-e) top surface of an Sb/CNT@Ni composite film, (f) cross-section of an Sb/CNT composite film with EDS map inlay.

along the length of CNTs like beads on a string. Cross sectional imaging of the Sb/CNT@Ni film shown in Figure 3.2f provides a film thickness of ~5 µm, while EDS reveals that oxygen is dispersed homogenously through the full thickness of the film, indicating significant porosity throughout where more surfaces can be exposed to and oxidized by air. The error in elemental quantification by EDS shown in Figure 3.3 makes the films compositionally indistinguishable, likely because the oxygen and carbon signals are dominated by adventitiously adsorbed species. For this reason, other methods such as XPS needed to be used to confirm the presence of CNTs in the Sb/CNT@Ni film.

To confirm that CNTs are included within the bulk of the Sb/CNT@Ni film, and not just adsorbed onto the surface, XPS analysis was performed before and after sputtering for 60 seconds. Figure 3.4a-b shows high-resolution spectra of the Sb 3d, O 1s, and C 1s binding environments before sputtering, where there is a mixture of Sb metal, Sb oxide, sp^2 carbon from the CNTs, and various C and O environments from adventitiously surface adsorbed species. Figure 3.4d-e shows high-resolution spectra of the Sb 3d, O 1s, and C 1s binding environments after 60 seconds of sputtering. The ratio of Sb:Sb(ox) binding environments has increased compared to the presputtered measurement, indicating that some of the oxide is due to surface oxidation but some is also formed in the bulk of the film during electrodeposition. Additionally, the C and O environments due to adventitiously adsorbed species are gone, leaving only the sp^2 C binding environment from embedded CNTs. This is consistent with CNTs being incorporated throughout the film thickness. Figure 3.5 shows the same XPS measurements done on the Sb@Ni film, and the absence of any C binding environment after sputtering confirms that 60 seconds of sputtering is sufficient to remove adventitiously adsorbed species and that the single C environment in Figure 3.4d is due to CNTs embedded within the Sb/CNT@Ni film.

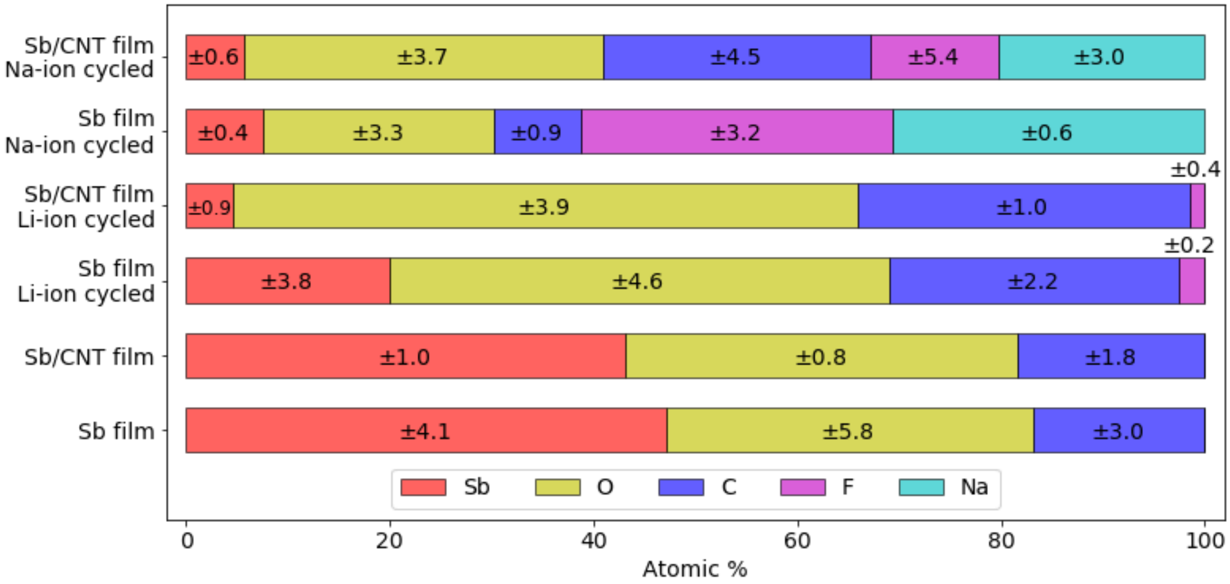

Figure 3.3 Elemental composition obtained from EDS of Sb and Sb/CNT composite films before and after cycling in Li-ion and Na-ion half-cells. Signal from the substrate metals was excluded from the composition quantification for clarity of film composition. The listed numbers are the standard deviations from quantification of three different spots on each sample to give a representation of the entire sample surface.

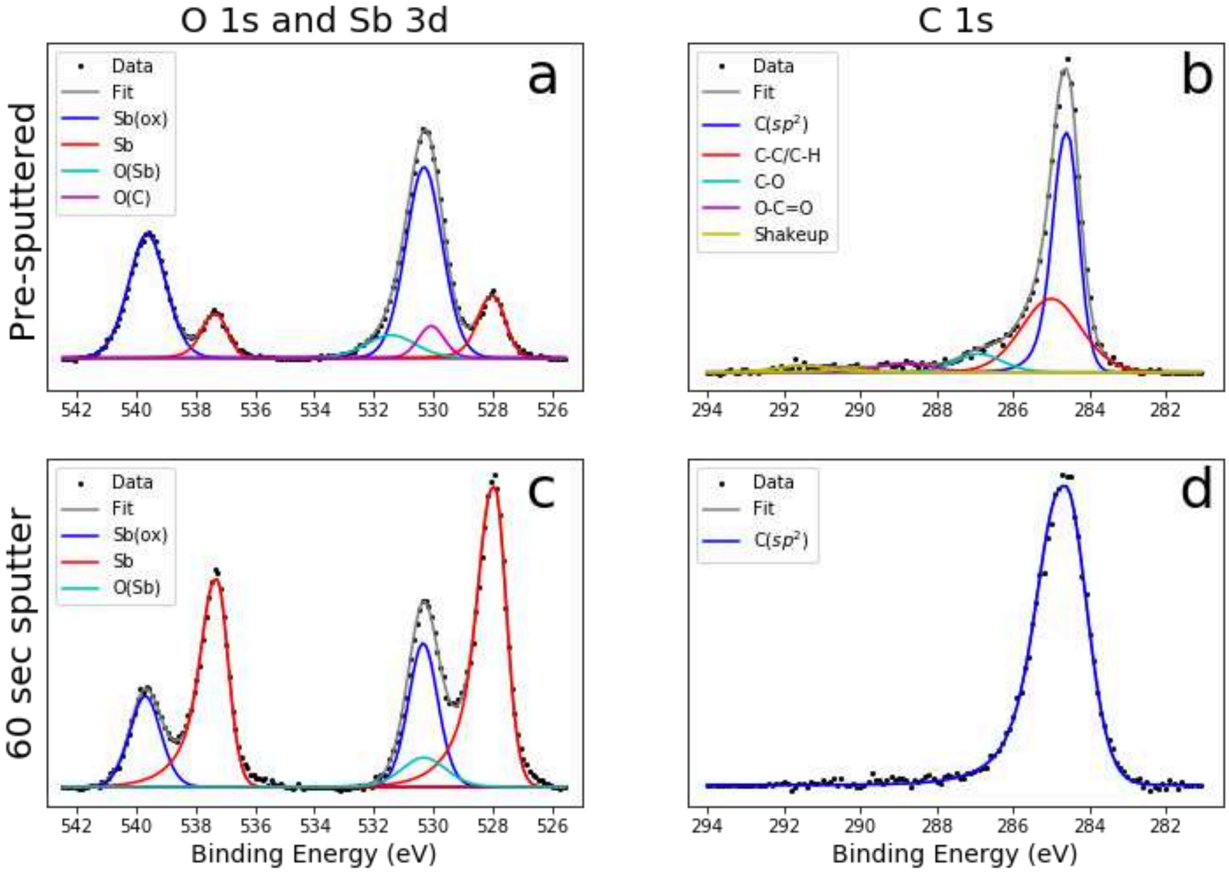

Figure 3.4 XPS spectra of Sb/CNT@Ni composite film (a-b) before sputtering and (c-d) after 60 seconds of sputtering.

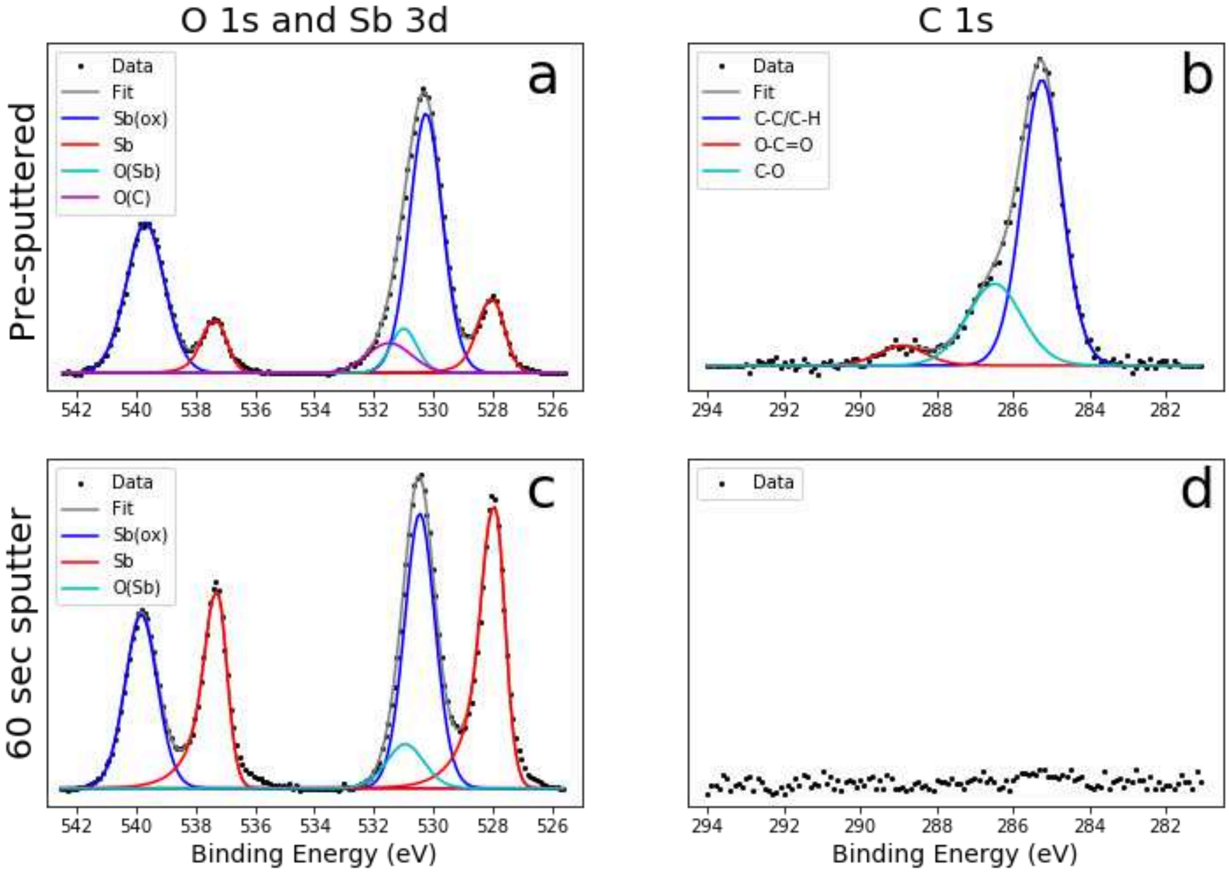

Figure 3.5 XPS spectra of Sb@Ni film (a-b) before sputtering and (c-d) after 60 seconds of sputtering.

Electrochemical performance of Sb and Sb/CNT composite films in Li-ion half cells

The electrochemical performance as Li-ion battery anodes of the Sb@Ni and Sb/CNT@Ni films was assessed by galvanostatically cycling the films in Li-ion half-cells (see Figure 3.6). We chose to electrodeposit and cycle the films on Ni instead of Cu, which is typical of anode materials, due to deleterious effects of Cu-Sb interactions. We previously reported on the phenomenon of interdiffusion at Cu-Sb interfaces during cycling in a Li-ion battery that results in void formation at that interface, and is ultimately responsible for delamination and premature failure of the anode material [14]. This remains the case for Sb/CNT@Cu deposits (see Figure 3.7). Figure 3.6a shows the voltage profiles for (de)lithiation of Sb@Ni and Sb/CNT@Ni, both of which are typical of Sb. The Sb/CNT@Ni film passes more current in the 1.2-2 V vs. Li/Li^+ range than the Sb@Ni film, likely due to the larger surface area of the Sb/CNT@Ni film that results in greater amounts of SEI formation/dissolution. Differential capacity analysis of the potential profiles is shown for the (de)lithiation potential regions in Figure 3.6b-c. The peak potentials for (de)lithiation of both films do not shift significantly over many cycles and capacity loss for both occurs by diminishing peak areas without significant peak shifting. This suggests that the failure mode for both films is dominated by active material loss (delamination), as capacity loss by excessive SEI that impedes ion flow would be characterized by peaks shifting to overpotentials.

Figure 3.6d shows the specific capacity of each film as a function of cycle number, with the approximate areal capacity calculated using a nominal mass loading of ~1.26 mg/cm^2 for both films. For both films, the 1st lithiation capacity is significantly greater than the films' reversible capacities, as significant charge goes towards establishing the SEI on the electrode surface [31,32]. The reversible capacity of Sb@Ni stabilizes well below the theoretical capacity

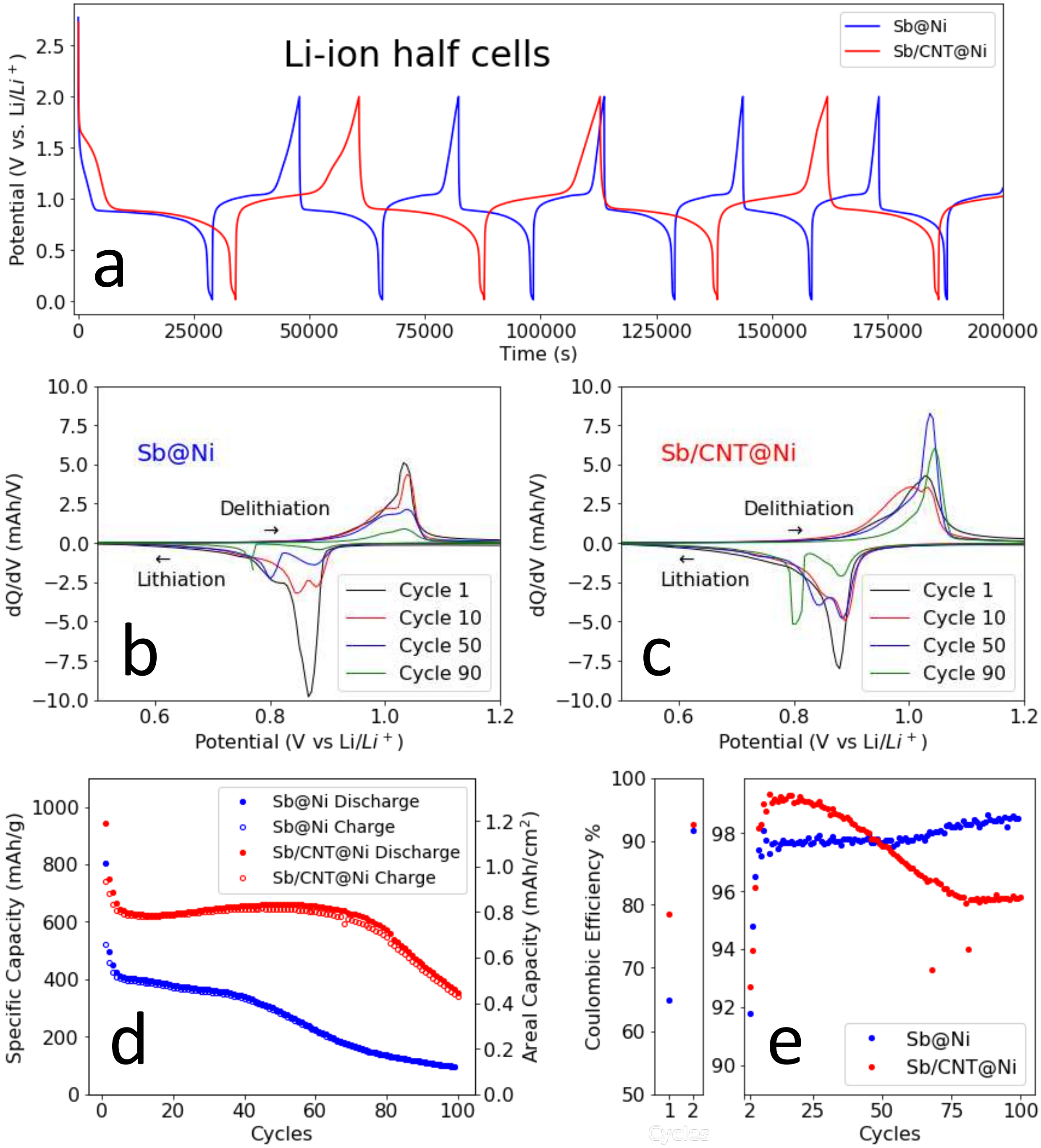

Figure 3.6 Cycling data in Li-ion batteries: (a) Charge-discharge potential profiles and their corresponding differential capacity plots for both (b) Sb@Ni and (c) Sb/CNT@Ni electrodes in Li-ion half cells. (d) Specific capacity of both electrodes vs. cycle number and (e) their corresponding coulombic efficiencies.

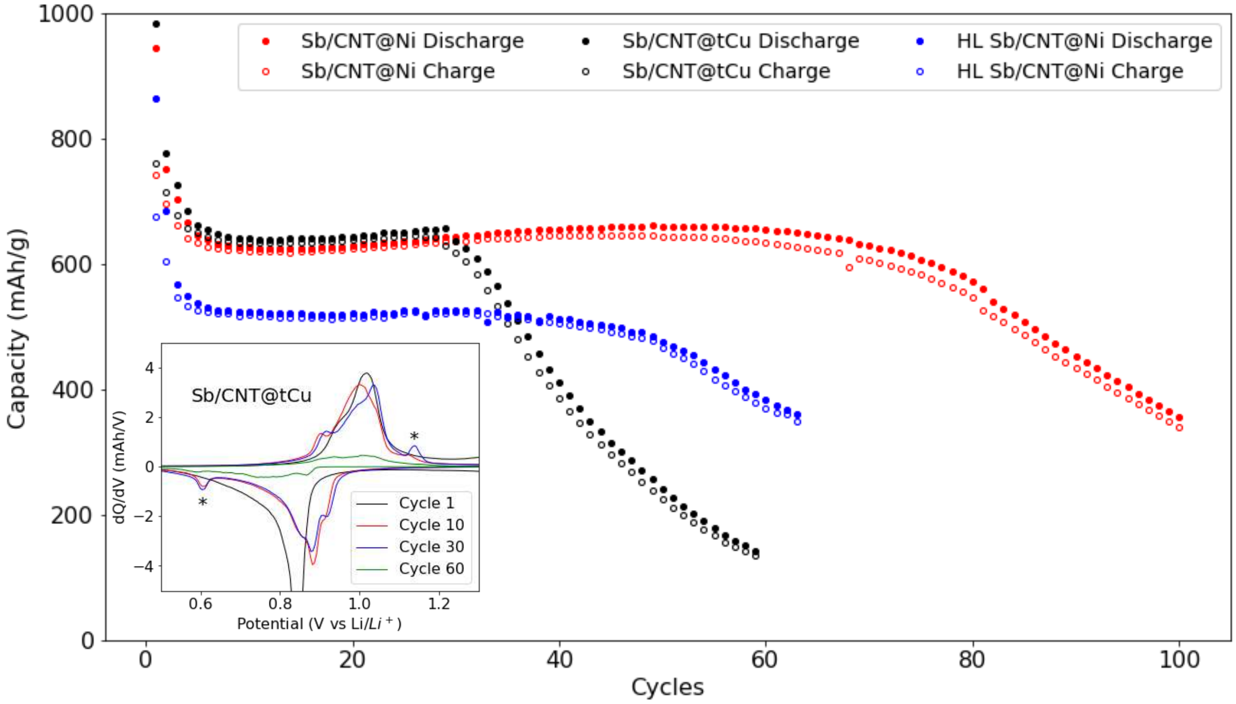

Figure 3.7 Specific capacity vs. cycle number in Li-ion half cells of the following electrodes: (red) Sb/CNT@Ni, (black) Sb/CNT on textured Cu (Sb/CNT@tCu), (blue) and high loading (HL) of 10 C/cm^2 of electrodeposition charge Sb/CNT@Ni. The inlay shows the differential capacity of the Sb/CNT@tCu electrode for select cycles with the asterisks marking chemistry typical of Li-Cu-Sb ternary phase lithiation/delithiation, the formation of which is likely responsible for the sudden onset of capacity loss of the Sb/CNT@tCu electrode around 25 cycles.

for Sb (660 mAh/g), and diminishes continually over 100 cycles, where the cell was stopped for post-cycling analysis. We attribute this poor performance to immediate and severe pulverization of the film, which is expected for a thick and dense film exhibiting internal stress even before cycling. Additionally, because the Sb@Ni film lacks any porosity, the small reversible capacity could be limited by the large solid-state diffusion distances that Li needs to travel to access all the active material. The reversible capacity of the Sb/CNT@Ni film stabilizes above 600 mAh/g for ~60 cycles, before beginning a steady loss of capacity out to 100 cycles where the cell was stopped for post-cycling analysis. We attribute the larger reversible capacity and better stability of the Sb/CNT@Ni film compared to the Sb@Ni film to the presence of the CNTs. The embedded CNTs not only generate the porous pseudo-3D morphology of the Sb/CNT@Ni film that is more resilient to volume changes during (de)lithiation, but they also maintain mechanical and electrical connectivity to the current collector even when active material cracks. Figure 3.7 shows the capacity vs. cycle number of an Sb/CNT@Ni film with higher loading (10 C/cm^2 deposition charge) that was cycled in a Li-ion half cell. The higher loading results in a smaller reversible specific capacity and less stability, showing that the reversible capacity is kinetically limited at these rates and loadings and the larger volume change of a thicker film exacerbates mechanical degradation and hastens the onset of capacity loss. Rate capability experiments of the Sb@Ni and Sb/CNT@Ni films shown in Figure 3.8 also demonstrate how the inclusion of CNTs helps to maintain reversible capacity at higher cycling rates, likely due to the porosity and short solid-state diffusion distances in the Sb/CNT@Ni film.

The coulombic efficiency (CE) of both films shown in Figure 3.6e identifies the low (CE) of both electrodes (≤99%) as a major challenge that still needs to be addressed before these electrodes can be cycled effectively in a full cell battery. The 1st cycle CE of the Sb@Ni film is

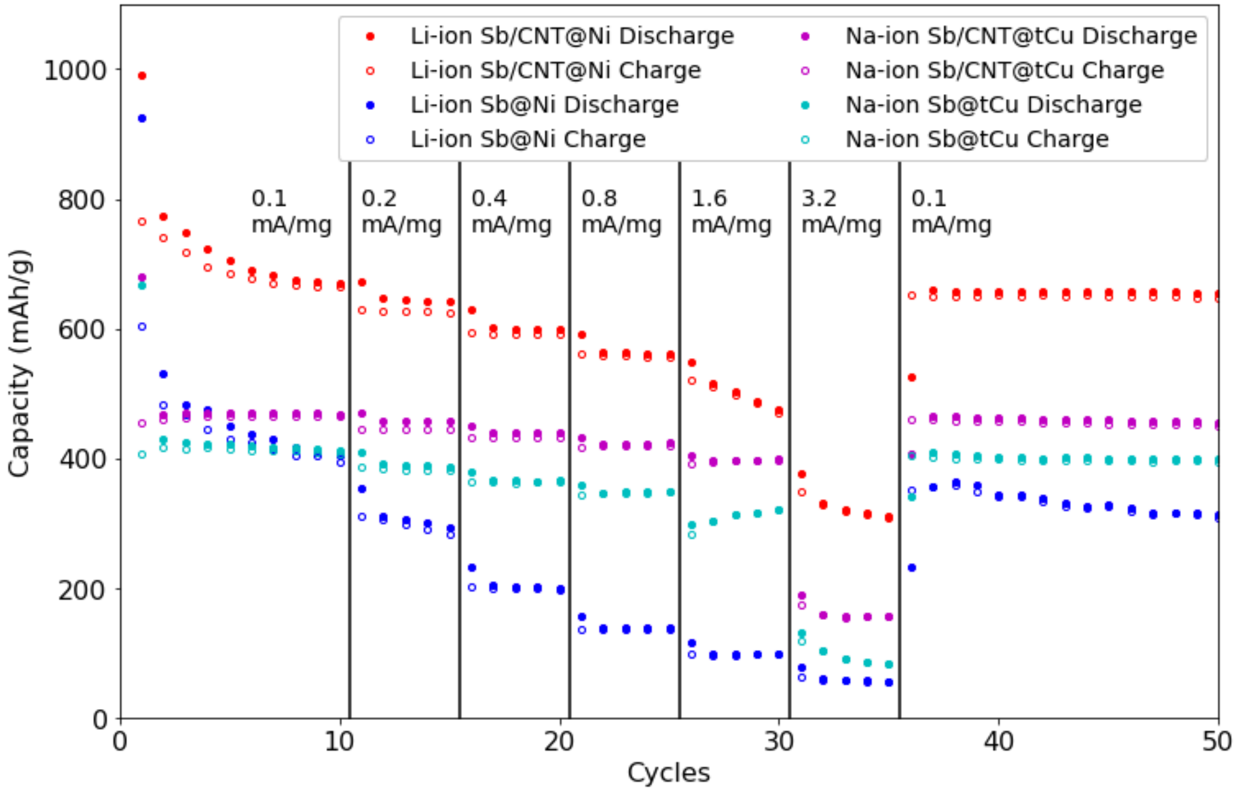

Figure 3.8 Rate capability experiments for the cycling of Sb and Sb/CNT electrodes in Li-ion and Na-ion half cells.

65%, which is likely due to a combination of extensive pulverization, active material loss, and SEI formation. The 1st cycle CE of the Sb/CNT@Ni film is higher, at ~78.5%, despite a larger surface area, suggesting that active material loss is not as prevalent, with SEI formation mostly contributing to the low CE. It takes about 5 cycles for each film to stabilize at higher CE values, though both remain ≤99%, resulting in intolerable levels of Li consumption. We attribute these low CE values to an SEI that cannot accommodate the magnitude of volume expansion of these electrode materials, and thus forms cracks in the film, exposing new surfaces that must be passivated by additional SEI on every cycle. Given that the electrolyte used for cycling these cells comprises components optimized for graphitic electrodes, the excessive SEI problem could likely be partially alleviated by developing new electrolyte additives or coatings. Compositional quantification by EDS of the films after cycling shown in Figure 3.3 reveals the presence of F and significant increase in C and O content compared to the pre-cycled films. This compositional change confirms that significant amounts of SEI are present on the films' surfaces, with the Sb/CNT@Ni film having greater amounts of SEI (larger C:Sb and O:Sb ratios) than the Sb@Ni film. Figure 3.9 shows the cumulative difference between the discharge and charge capacity summed over cycle number, which we refer to as the 'excess capacity'. It is striking that the amount of excess capacity going towards SEI formation on the Sb/CNT@Ni film exceeds the reversible capacity of that film by cycle 50, despite the Sb/CNT@Ni film having the higher CE of the two for the first 50 cycles. Such an enormous amount of capacity going towards Li consuming side reactions like SEI formation would result in full cell batteries requiring significant prelithiation or excessive cathode loadings, low energy densities, and short lifetimes.

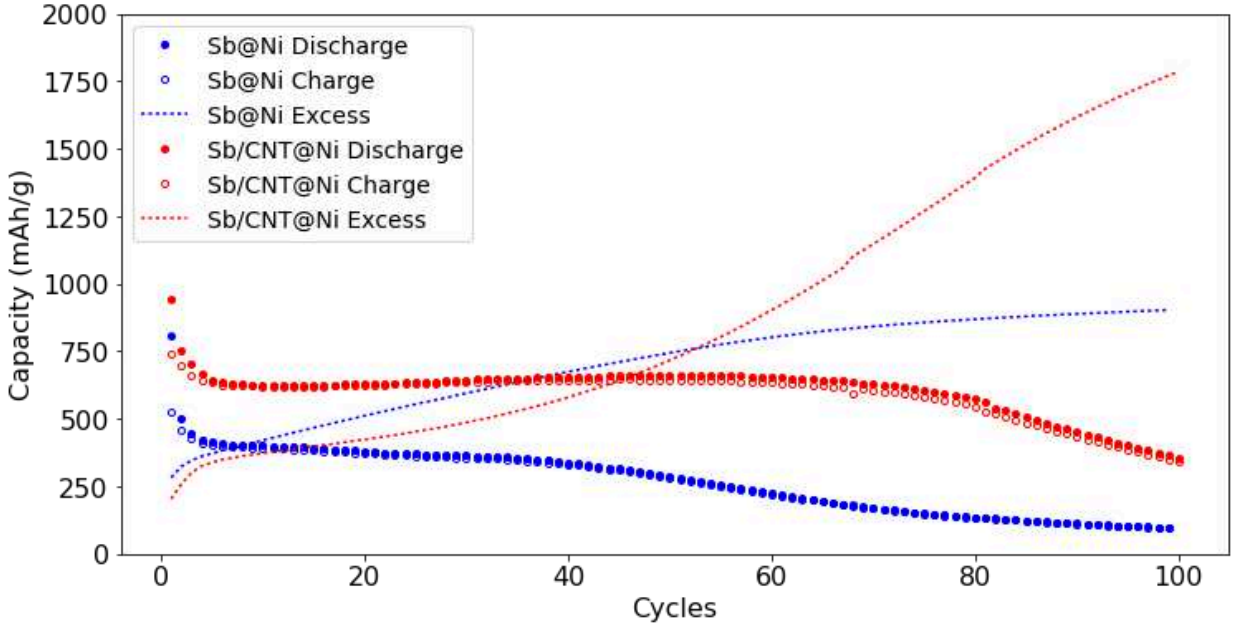

Figure 3.9 Specific capacity vs. cycle number in Li-ion half cells of the following electrodes: (blue) Sb@Ni and (red) Sb/CNT@Ni. The dashed traces show the cumulative difference between the discharge and charge capacities and represent how much excess capacity has gone towards non-reversible electrochemistry such as SEI formation or other side reactions. The approximate trajectory mirroring of the excess capacity traces with the reversible capacity traces suggest the reversible capacity loss is due to active material loss, such as film delamination.

Post-cycling SEM imaging of Sb@Ni and Sb/CNT@Ni Li-ion electrodes confirms active material loss as the main mode of capacity loss for both films. Figure 3.10a-b shows how the Sb@Ni electrode is severely pulverized and delaminated, which is typical of alloy anode materials with no porosity or binders. Figure 3.10c-f shows how the Sb/CNT@Ni electrode is significantly delaminated but still contains large intact pieces of the film. It seems that the CNT inclusion helps to keep the active material mechanically and electrically connected. The dominant mechanism of reversible capacity loss for the Sb/CNT@Ni film seems to be active material loss through film delamination, rather than pulverization, making the substrate-film interface the weak point of the system. Work is in progress investigating strategies to improve film adhesion strength by using textured substrates or substrates with electrochemically embedded CNTs. It is striking to note that there is a significant increase in film thickness during cycling, with the film being ~5 μm before cycling (Figure 3.2f) and ~30 μm after (Figure 3.10f). We rationalize this 500% increase in film thickness as the filling of the film with SEI that is formed to passivate newly exposed surfaces from film cracking that occurs on every cycle. Such a large amount of SEI formation agrees with the substantial O, C, and F contents revealed by EDS in Figure 3.3 and the large excess capacity shown in Figure 3.9. Despite continuous SEI formation, it seems that the CNTs still maintain mechanical and electrical connectivity, allowing the film to cycle as long as it doesn’t delaminate.

Electrochemical performance of Sb and Sb/CNT composite films in Na-ion half cells

To test the electrochemical performance as Na-ion battery anodes, the Sb and Sb/CNT films were electrodeposited and galvanostatically cycled on textured Cu foils as the Sb@tCu and Sb/CNT@tCu electrodes, respectively. We chose to electrodeposit and cycle the films on Cu instead of Ni, as was done with the Li-ion half cells, because of the absence of deleterious Cu-Sb

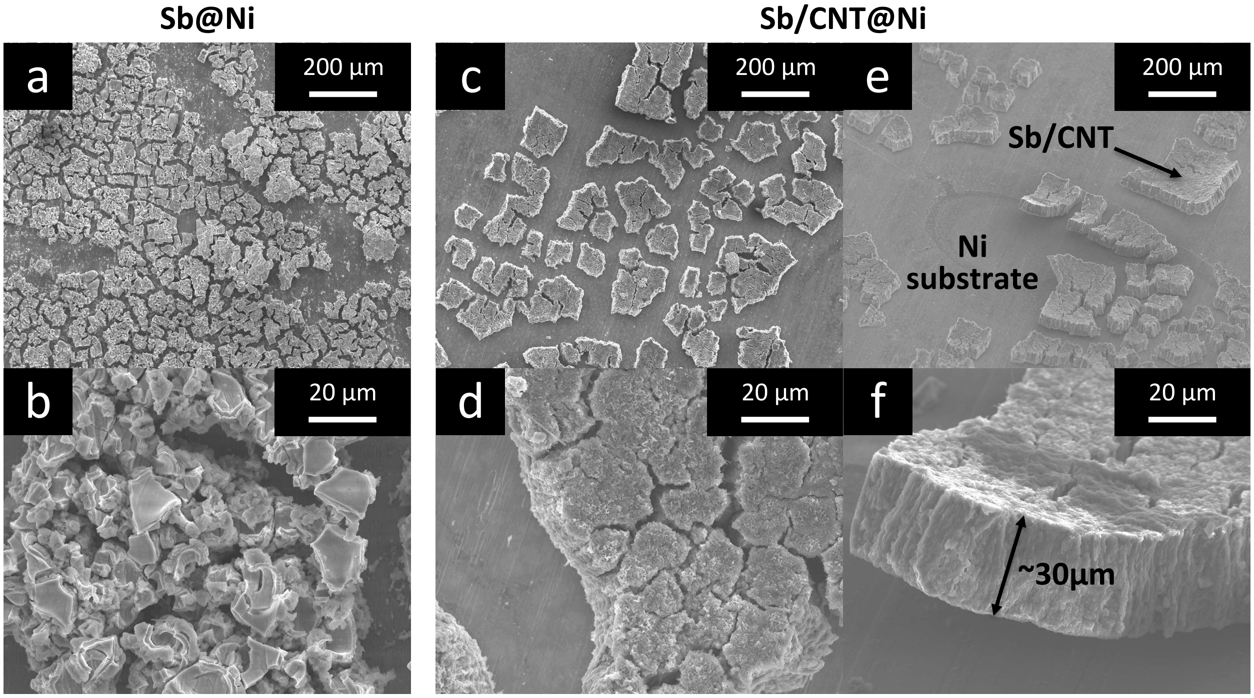

Figure 3.10 SEM images of the following electrodes after being cycled in Li-ion half cells: (a-b) Sb@Ni (c-f) Sb/CNT@Ni.

interactions when cycled in Na-ion half cells. We hypothesize that the absence of Na-Cu-Sb ternary phases makes the interdiffusion of Cu and Sb negligible during cycling in a Na-ion cell, contrary to the significant interdiffusion and void formation at Cu-Sb interfaces when cycled in a Li-ion cell, likely facilitated by the Li-Cu-Sb intermediate phases. Given that textured Cu foils are readily available and known to help adhesion of electrodeposited films [33,34], we chose them as the substrates for the films cycled in the Na-ion cells. Figure 3.12 demonstrates the early and sudden failure of an Sb/CNT@Ni film cycled in a Na-ion cell, which we attribute to film delamination from lack of film-substrate adhesion strength. Figure 3.11a shows the voltage profiles for (de)sodiation of Sb@tCu and Sb/CNT@tCu, both of which are typical of Sb. Note that the Sb/CNT@tCu film exhibits less discrete potential plateaus than the Sb@tCu film, likely due to its porous and high surface area morphology where different parts of the active material are at slightly different potentials to one another during cycling. Differential capacity analysis of the potential profiles is shown for the (de)sodiation potential regions in Figure 3.11b-c. For both films, the diminishing of peak areas over many cycles coincides with a significant shifting of the peaks to overpotentials. This suggests that excessive amounts of SEI form on both films that impedes (de)sodiation and contributes to active material loss as a mechanism of capacity loss.

Figure 3.11d shows the specific capacity of each film as a function of cycle number, with the approximate areal capacity again calculated using a nominal mass loading of ~1.26 mg/cm^2 for both films. For both films, the 1st sodiation capacity is significantly greater than the films' reversible capacities, as significant charge goes towards establishing the SEI on the electrode surface [31,32]. The films stabilize at ~400 mAh/g for the Sb@tCu film and ~500 mAh/g for the Sb/CNT@tCu film upon the 1st desodiation, and both cycle stably at those capacities for >100 cycles. The Sb@tCu film starts to lose capacity rapidly around cycle 120, while the

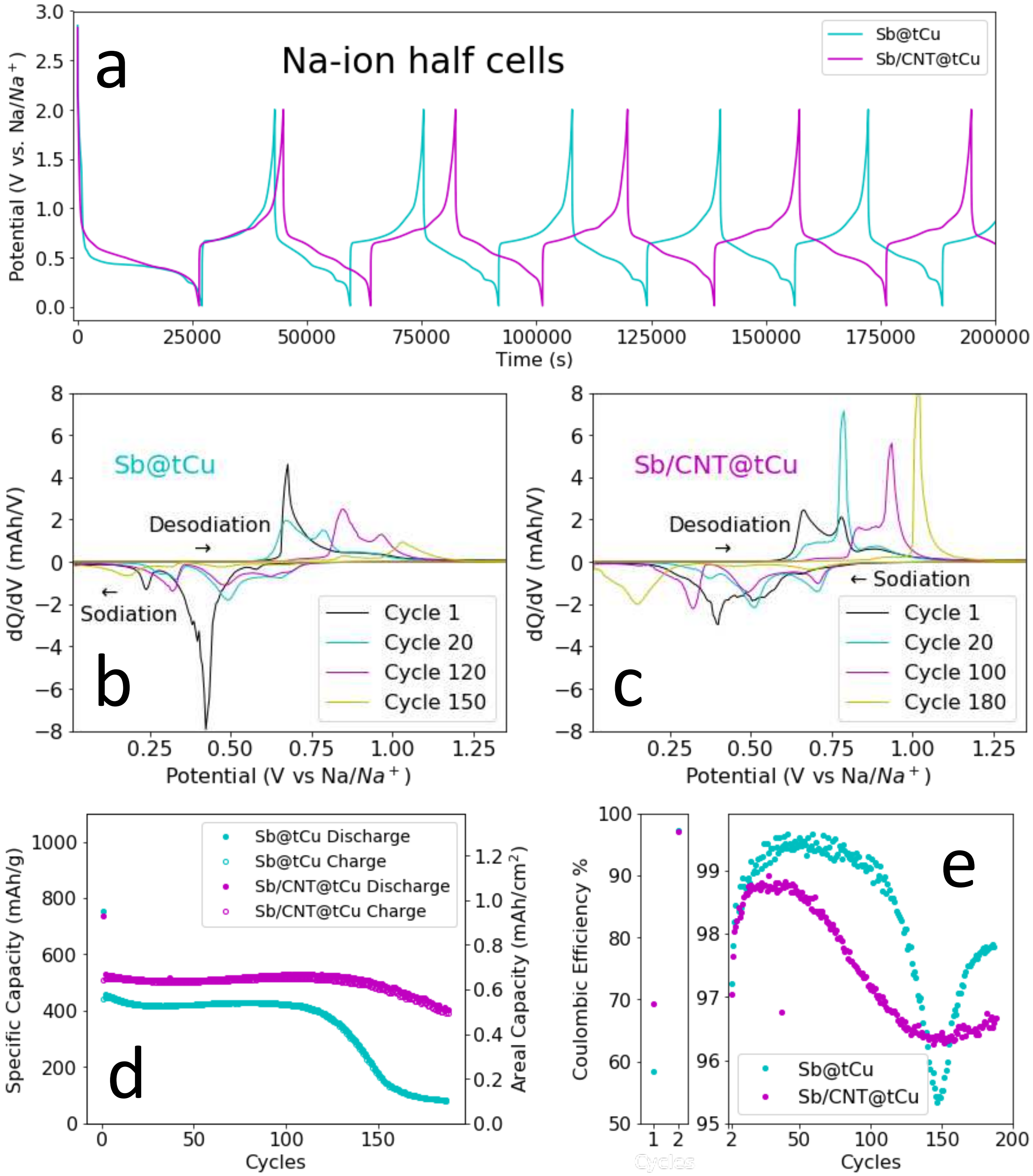

Figure 3.11 Cycling data in Na-ion batteries: (a) Charge-discharge potential profiles and their corresponding differential capacity plots for both (b) Sb@tCu and (c) Sb/CNT@tCu electrodes in Na-ion half cells. (d) Specific capacity of both electrodes vs. cycle number and (e) their corresponding coulombic efficiencies.

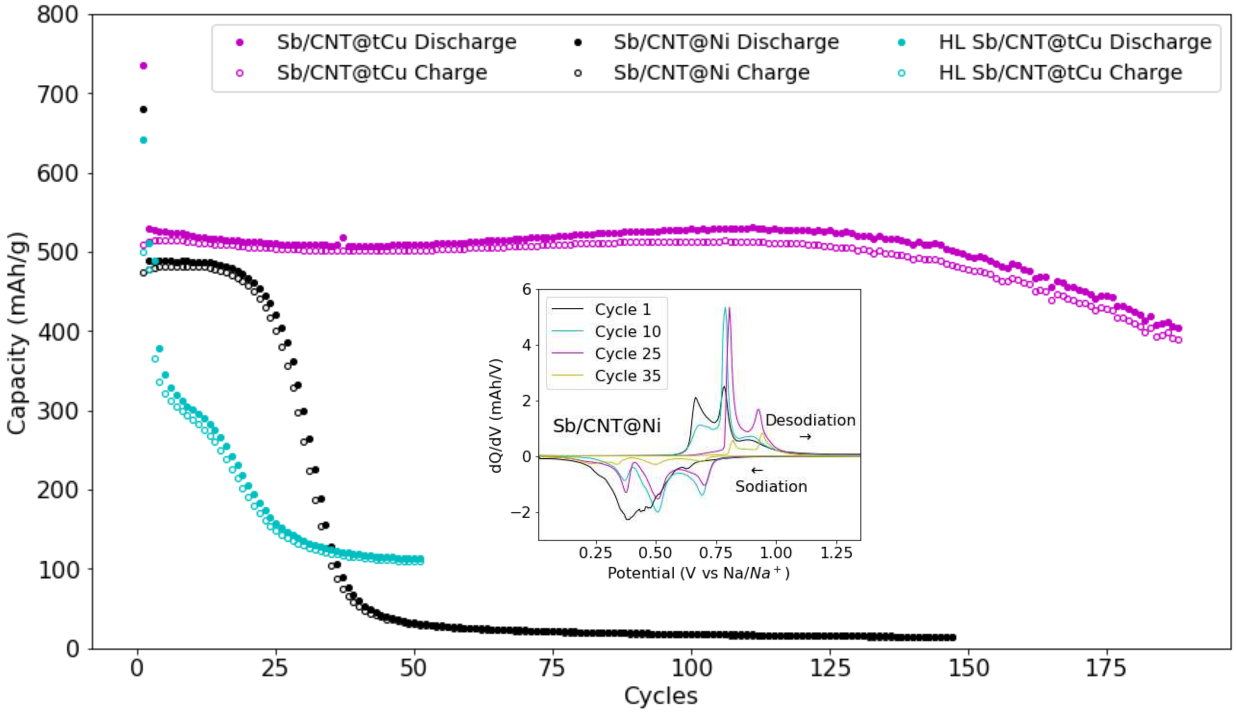

Figure 3.12 Specific capacity vs. cycle number in Na-ion half cells of the following electrodes: (magenta) Sb/CNT@tCu, (black) Sb/CNT@Ni, (cyan) and high loading (HL) of 10 C/cm^2 of electrodeposition charge Sb/CNT@tCu. The inlay shows the differential capacity of the Sb/CNT@Ni electrode for select cycles and shows no significant difference from the differential capacity plot of the Sb/CNT@tCu electrode (Figure 3.11c) other than the capacity loss manifesting as diminishment of peak area rather that peak potential shifting, suggesting capacity loss of the Sb/CNT@Ni electrode is dominated by active material delamination. The considerable capacity loss of the HL Sb/CNT@tCu indicates that the large volume expansion in the Na-ion system exacerbates delamination and capacity loss more when compared to the HL Sb/CNT@Ni electrode cycled in the Li-ion cell (Figure 3.7).

Sb/CNT@tCu begins to lose capacity slowly at around cycle 150. Both films were stopped after 190 cycles for disassembly and post-cycling analysis. The marginally better reversible capacity and stability of the Sb/CNT@tCu film shows that while the inclusion of the CNTs in the film is beneficial to cycling in a Na-ion cell, the benefit is not nearly as significant as in the Li-ion cells. Indeed, the rate capability experiments shown in Figure 3.8 demonstrate comparable losses in reversible capacities at high cycling rates between the Sb@tCu and Sb/CNT@tCu films, showing the CNT inclusion is not beneficial to rate capability in these Na-ion electrodes. Figure 3.12 shows the capacity vs. cycle number of an Sb/CNT@tCu film with higher loading (10 C/cm^2 deposition charge) that was cycled in a Na-ion half cell. The higher loading results in extremely fast capacity loss after only 2 cycles with reversible capacities comparable to the lower loading films. The larger magnitude of volume change going from Sb → Na_3Sb compared to Sb → Li_3Sb could result in exacerbated active material loss by delamination, making a Sb/CNT film more sensitive to loading dependent stability in a Na-ion than a Li-ion cell.

The low CEs of the Na-ion cell electrodes shown in Figure 3.11e are again a major challenge to be overcome. While the 1st cycle CEs for the Sb@tCu and Sb/CNT@tCu are 59% and 69%, respectively, the CE of the Sb/CNT@tCu is generally worse than that of Sb@tCu over many cycles. This might suggest that the Sb@tCu film loses more active material on the 1st cycle than the Sb/CNT@tCu film, resulting in a smaller 1st cycle CE, despite have a smaller surface area. The higher surface area of the Sb/CNT@tCu film may require more SEI formation over subsequent cycles, resulting in its CE always being <99%. Composition quantification of the films after cycling shown in Figure 3.3 reveals significant amounts of SEI on both films, with the increase in C:Sb and O:Sb ratios as well as the presence of significant Na and F. Interestingly, the majority of the Sb/CNT@tCu film's composition after cycling is C and O, while the majority of the Sb@tCu film's composition after cycling is Na and F. The presence of the CNTs in the Sb/CNT@tCu film may promote the formation of an SEI with more organic speciation, compared to the more inorganic-like SEI of the Sb@tCu film after cycling. Regardless, the CE of the Sb/CNT@tCu film is too low considering the excess capacity shown in Figure 3.13 exceeds the reversible capacity by around cycle 40. The intolerable levels of Na consumed in side reactions like SEI formation on every cycle would result in a full cell using this electrode material with excessive cathode loading, low energy density, and a short lifetime. The irreversible Na consumption by Sb@tCu electrode is more manageable, with the CE being ≥99% for ~100 cycles, resulting in the excess capacity shown in Figure 3.13 being comparable to the reversible capacity for ~100 cycles. The dip in CE around cycle 150 coincides with significant capacity loss, likely from rapid active material loss as the excess capacity trace shown in Figure 3.13 mirrors the decrease in reversible capacity of the Sb@tCu film.

Post-cycling SEM imaging of Sb@tCu and Sb/CNT@tCu Na-ion electrodes identifies different mechanisms of reversible capacity loss in these films. Figure 3.14a-b shows some delamination of the Sb@tCu film after cycling. It is interesting to note that despite cycling stably for >100 cycles, the Sb@tCu film increased from 3.5 μm (Figure 3.2c) to only ~10 μm in thickness (Figure 3.14b). This suggests that less SEI forms on the Sb@tCu film than the Sb/CNT@tCu film, which agrees with its comparatively smaller excess capacity shown in Figure 3.13 thus making active material delamination the dominant form of reversible capacity loss in the Sb@tCu film. Additionally, the compositional quantification of the Sb@tCu film shown in Figure 3.3 reveals the SEI is highly inorganic in nature with more Na and F content than C and O after cycling, which may also contribute to the compact nature of the post-cycled Sb@tCu film. Figure 3.14c-f shows the Sb/CNT@tCu electrode after cycling, which exhibits negligible

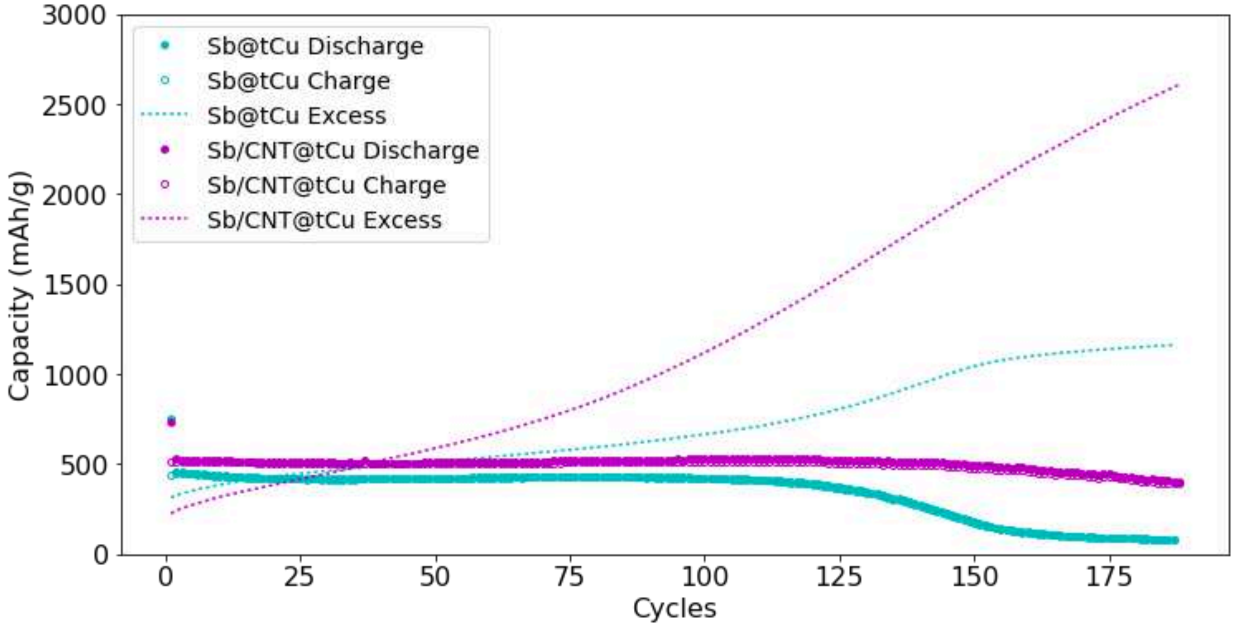

Figure 3.13 Specific capacity vs. cycle number in Na-ion half cells of the following electrodes: (cyan) Sb@tCu and (magenta) Sb/CNT@tCu. The dashed traces show the cumulative difference between the discharge and charge capacities and represent how much excess capacity has gone towards non-reversible electrochemistry such as SEI formation or other side reactions. The close trajectory mirroring of the excess capacity trace with the reversible capacity trace of the Sb@tCu electrode suggests the reversible capacity loss of that electrode is dominated by active material loss, such as film delamination. In contrast, the continual steep increase of the excess capacity of the Sb/CNT@tCu electrode despite only a slight decline in reversible capacity suggests that the film is mechanically stable but is susceptible to excessive amounts of side reactions.

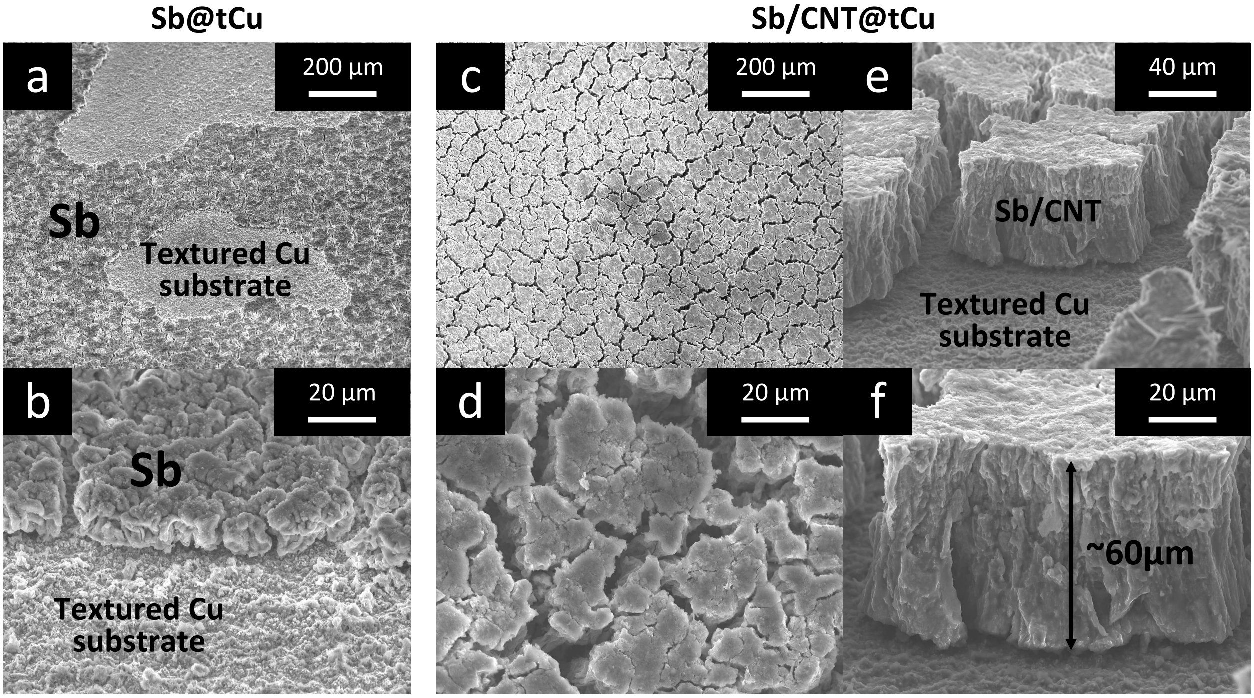

Figure 3.14 SEM images of the following electrodes after being cycled in Na-ion half cells: (a-b) Sb@tCu (c-f) Sb/CNT@tCu.

delamination and completely intact pieces of film present. The Sb/CNT@tCu film increased substantially in thickness, from ~5 μm before cycling (Figure 3.2f) to ~60 μm after (Figure 3.14f), an 1100% increase. The mechanism of this increase in film thickness is analogous to previously described, where cracks in the film fill with SEI on every cycle. The larger magnitude of thickness increase is probably a result of cycling longer and agrees with the excessively large excess capacity shown of the Sb/CNT@tCu film shown in Figure 3.13. It seems the CNT inclusion as well as the textured substrate help keep the active material mechanically and electrically consolidated and well adhered. The loss in reversible capacity of the Sb/CNT@tCu is likely dominated by excessive SEI making the active material more difficult for the Na^+ to access, thus pushing the (de)sodiation events to higher overpotentials as seen in Figure 3.11C.

Electrodeposition and cycling performance of Sn-Sb/CNT composite films

As a test of the applicability of this type of CNT composite electrodeposition procedure to different Li alloy anode materials, we substituted the $SbCl_3$ with $SnCl_2$ in the deposition solution and electrodeposited thin films using an analogous procedure. We chose Sn as a Li alloy material because it can be electrodeposited and exhibits larger theoretical specific capacities and lower average lithiation potentials than Sb, both of which could contribute to a higher energy density than Sb alone. Interestingly, the Sn/CNT@Ni film shown in Figure 3.15a-b shows poor inclusion of CNTs and the absence of "beads on a string" morphology (Figure 3.2e) that is indicative of electrochemical nucleation and growth of the material onto the CNTs. By depositing from solutions with 15mM $SbCl_3$ and 15mM $SnCl_2$, we produced SnSb@Ni and SnSb/CNT@Ni films seen in Figure 3.15c-f. The SnSb@Ni film has a composition of $Sn_{60}Sb_{40}$ as measured by EDS and exhibits cracking similar to that seen in Sb@Ni films (Figure 3.2b). The SnSb/CNT@Ni film has a composition of $Sn_{47}Sb_{53}$ as measured by EDS and exhibits similar

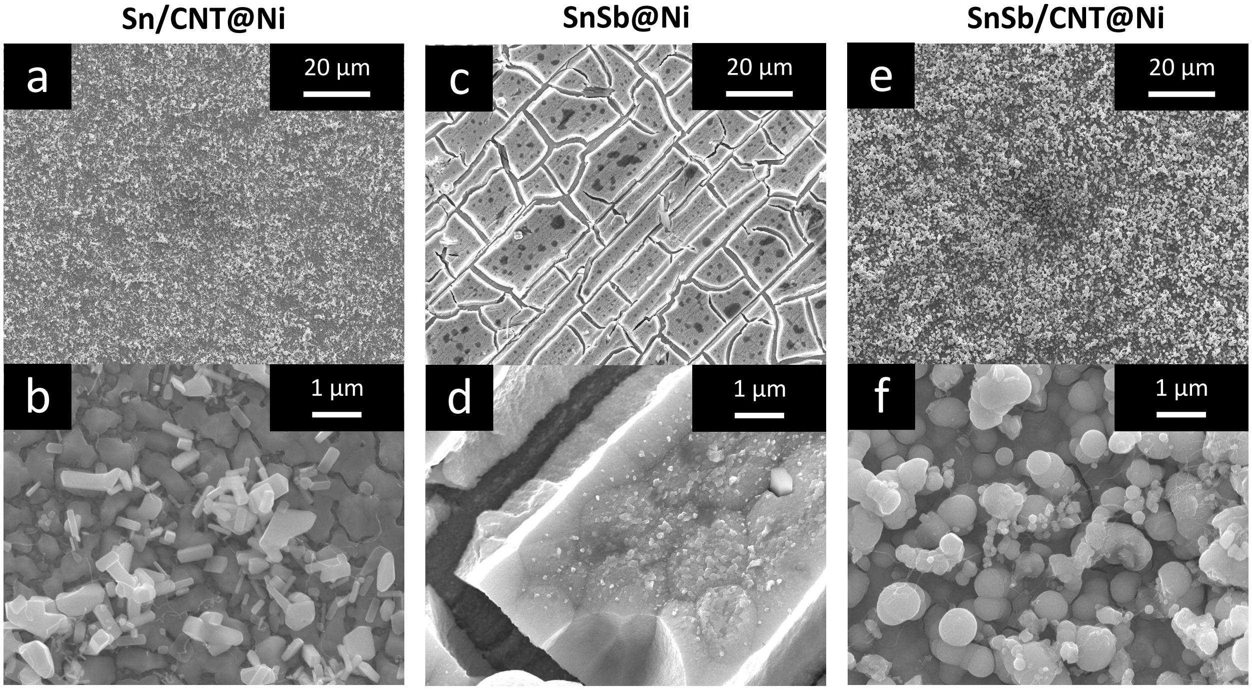

Figure 3.15 SEM images of the following electrodes: (a-b) Sn/CNT@Ni deposited from a solution of 200 mM NaGluconate, 30 mM CTAB, 30 mM SnCl2, ACNTs, -1V vs. SCE, 600 seconds (c-d) SnSb@Ni deposited from a solution of 200 mM NaGluconate, 30 mM CTAB, 15 mM $SbCl_3$, 15 mM $SnCl_2$, -1.05V vs. SCE, 2138 mC, (e-d) SnSb/CNT@Ni deposited from a solution of 200 mM NaGluconate, 30 mM CTAB, 15 mM $SbCl_3$, 15 mM $SnCl_2$, ACNTs, -1.05V vs. SCE, 2138 mC.

porous morphology and increased nucleation along the nanotubes as the Sb/CNT@Ni films (Figure 3.2e). It seems that the presence of Sb is required to achieve good integration of CNTs and promote the deposition along the nanotubes, a phenomenon that may be worth investigating more closely.

The electrochemical performance of SnSb@Ni and SnSb/CNT@Ni films as Li-ion battery anodes was assessed by galvanostatically cycling the films in Li-ion half cells. Figure 3.16a shows the voltage profiles for (de)lithiation of the SnSb@Ni and SnSb/CNT@Ni. For both, the presence of Sn contributes a significant amount of capacity below 0.75 V and 0.9 V vs. Li/Li^+ for the lithiation and delithiation, respectively, when compared to the cycling of the Sb@Ni or Sb/CNT@Ni films in Figure 3.6a. Similarly to the Sb/CNT@Ni film, the SnSb/CNT@Ni film also passes more current above 1.2 V vs. Li/Li^+ than the SnSb@Ni film due to the higher surface area of the CNT composite. The differential capacity plots (Figure 3.16b-c) also differ significantly from the pure Sb films (Figure 3.6b-c), with the SnSb films exhibiting more electrochemical events at lower potentials due to the (de)lithiation of Sn. The specific capacity and coulombic efficiency as a function of cycle number for both the SnSb@Ni and SnSb/CNT@Ni are shown in Figure 3.16d-e. They show an analogous improvement in cycling stability due to the inclusion of the CNTs, with the SnSb/CNT@Ni film cycling around 600 mAh/g for around 75 cycles while the SnSb@Ni film begins losing significant capacity within the first few cycles and exhibits negligible reversible capacity by cycle 50. Post cycling analysis of the films by SEM (not shown) identifies active material loss by delamination as the ultimate failure mode for both films, though it occurs much more rapidly in the SnSb@Ni film. The SnSb/CNT@Ni film also exhibits a near 10-fold increase in film thickness during cycling, indicating the formation of excessive amounts of SEI that agrees with its low coulombic

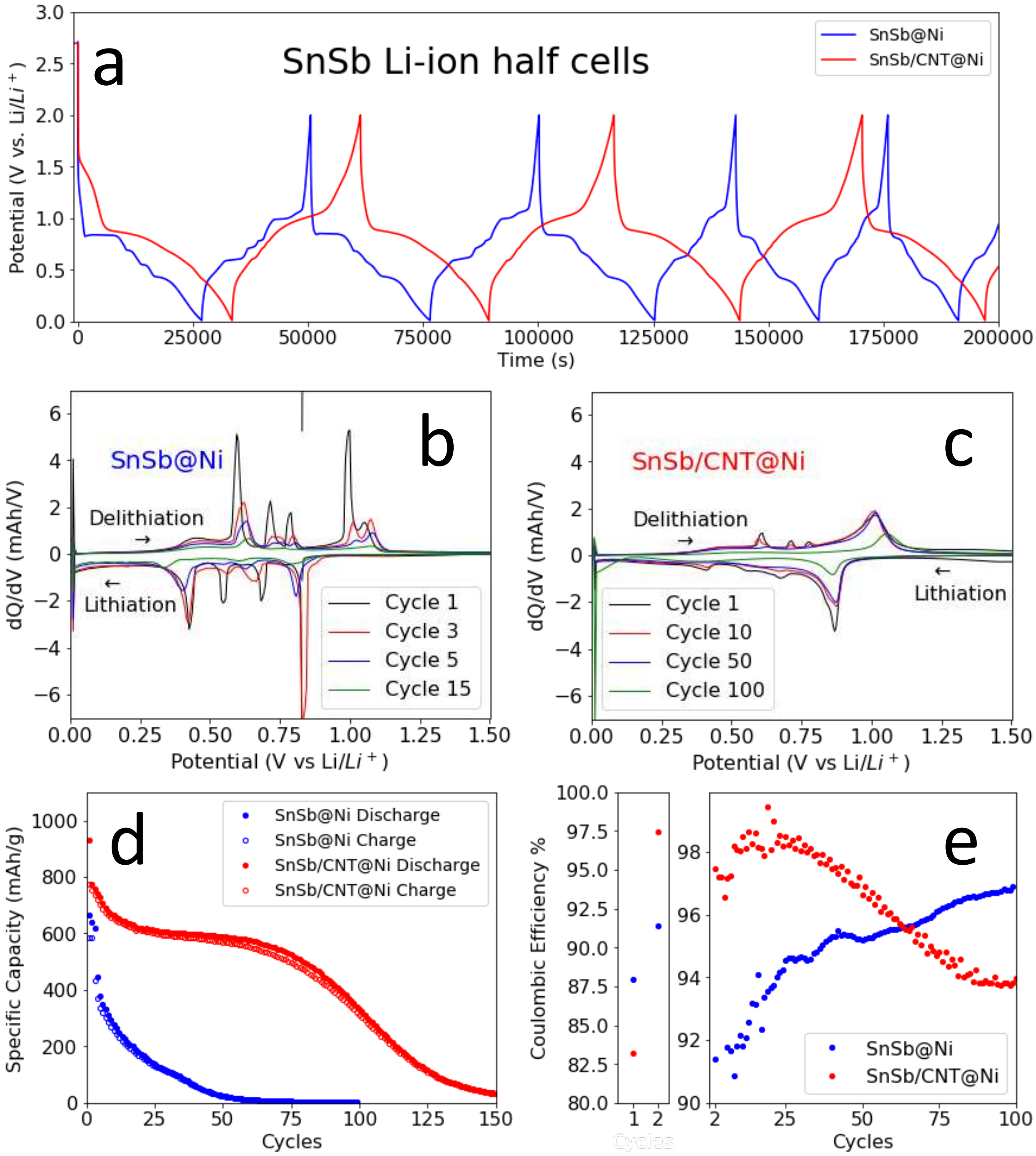

Figure 3.16 Cycling data of SnSb electrodes in Li-ion batteries: (a) Charge-discharge potential profiles and their corresponding differential capacity plots for both (b) SnSb@Ni and (c) SnSb/CNT@Ni electrodes in Li-ion half cells. (d) Specific capacity of both electrodes vs. cycle number and (e) their corresponding coulombic efficiencies.

efficiencies shown in Figure 3.16e. While it is clear that the electrodeposition of CNT composite films of other alloy materials like SnSb is an effective strategy to improve cycling stability in Li-ion batteries, the composite films still suffer from the main failure modes of delamination and, more importantly, unacceptably low coulombic efficiency. These degradation mechanisms could be alleviated through the use of high surface area electrodes (3D architectures) where the active material films could be locally thinner as well as better developed electrolyte additives or flexible coatings respectively.

Conclusion

Towards the goal of creating batteries with higher energy density, better safety, and longer lifetimes, we have demonstrated the application of performance improving strategies to make Sb/CNT composite anodes for Li and Na-ion batteries. The Sb/CNT composite anodes can be electrodeposited from aqueous mixtures, making the synthesis of these types of anodes commercially feasible and applicable to non-planar (3D) electrode architectures. When cycled in Li-ion and Na-ion half-cells, the composite anodes exhibit larger reversible capacities and longer cycle lifetimes than anodes without CNTs, an improvement that is more substantial in the Li-ion cells. We attribute the better performance of the composite anodes to the mechanical and electrical connectivity that the CNTs provide as well as the porous morphology that results from CNT incorporation. Post-cycling characterization of the composite anodes reveals different modes for reversible capacity loss between the Li-ion and Na-ion cells. The Li-ion anodes suffer mainly from active material loss in the form of film delamination from the substrate. The Na-ion anodes exhibit improved film-substrate adhesion, in large part from the textured substrate used, though lose reversible capacity as excessive amounts of SEI build-up around the active material. We additionally demonstrated that the electrodeposition of CNT composite anodes could be extended to other alloy active materials, namely SnSb/CNT composites. This work successfully demonstrates that the incorporation of CNTs improves the mechanical and electrical connectivity of the composite electrodes' active material, resulting in extended cycle lifetimes of those electrodes in both Li-ion and Na-ion half-cells. This is a key work in conjunction with efforts to develop better electrolyte additives, electrode coatings, or solid electrolytes to address the low coulombic efficiencies (<99%) of these types of electrodes so they can be used effectively in full-cell batteries.

CHAPTER 3 REFERENCES

[1] T.M. Gür, Review of electrical energy storage technologies, materials and systems: challenges and prospects for large-scale grid storage, Energy Environ. Sci. 11 (2018) 2696–2767. doi:10.1039/C8EE01419A.

[2] J.B. Goodenough, Energy storage materials_ A perspective, Energy Storage Materials. 1 (2015) 158–161. doi:10.1016/j.ensm.2015.07.001.

[3] J. Meng, H. Guo, C. Niu, Y. Zhao, L. Xu, Q. Li, et al., Advances in Structure and Property Optimizations of Battery Electrode Materials, Joule. 1 (2017) 522–547. doi:10.1016/j.joule.2017.08.001.

[4] M.N. Obrovac, V.L. Chevrier, Alloy Negative Electrodes for Li-Ion Batteries, Chem. Rev. 114 (2014) 11444–11502. doi:10.1021/cr500207g.

[5] C. Delmas, Sodium and Sodium-Ion Batteries: 50 Years of Research, 29 (2018) 1703137–1703139. doi:10.1002/aenm.201703137.

[6] J.-Y. Hwang, S.-T. Myung, Y.-K. Sun, Sodium-ion batteries: present and future, Chem. Soc. Rev. 334 (2017) 928. doi:10.1039/C6CS00776G.

[7] M. Winter, The Solid Electrolyte Interphase – The Most Important and the Least Understood Solid Electrolyte in Rechargeable Li Batteries, Zeitschrift Für Physikalische Chemie. 223 (2009) 1395–1406. doi:10.1524/zpch.2009.6086.

[8] C.K. Chan, R. Ruffo, S.S. Hong, Y. Cui, Surface chemistry and morphology of the solid electrolyte interphase on silicon nanowire lithium-ion battery anodes, Journal of Power Sources. 189 (2009) 1132–1140. doi:10.1016/j.jpowsour.2009.01.007.

[9] K. Xu, Nonaqueous Liquid Electrolytes for Lithium-Based Rechargeable Batteries, 104 (2004) 4303–4417. doi:10.1021/cr030203g.

[10] Z. Liu, T. Song, U. Paik, Sb-based electrode materials for rechargeable batteries, Journal of Materials Chemistry a: Materials for Energy and Sustainability. 6 (2018) 8159–8193. doi:10.1039/C8TA01782D.

[11] R. Al-Salman, S.J. Sedlmaier, H. Sommer, T. Brezesinski, J. Janek, Facile synthesis of micrometer-long antimony nanowires by template-free electrodeposition for next generation Li-ion batteries, J. Mater. Chem. A. 4 (2016) 12726–12729. doi:10.1039/C6TA04731A.

[12] J. He, Y. Wei, T. Zhai, H. Li, Antimony-based materials as promising anodes for rechargeable lithium-ion and sodium-ion batteries, Mater. Chem. Front. 2 (2018) 437–455. doi:10.1039/C7QM00480J.

[13] E.D. Jackson, J.M. Mosby, A.L. Prieto, Evaluation of the Electrochemical Properties of Crystalline Copper Antimonide Thin Film Anodes for Lithium Ion Batteries Produced by Single Step Electrodeposition, Electrochimica Acta. 214 (2016) 253–264. doi:10.1016/j.electacta.2016.07.126.

[14] M.C. Schulze, R.K. Schulze, A.L. Prieto, Electrodeposited thin-film Cu_xSb anodes for Li-ion batteries: enhancement of cycle life via tuning of film composition and engineering of the film-substrate interface, J. Mater. Chem. A. 6 (2018) 12708–12717. doi:10.1039/C8TA01798K.

[15] J.M. Mosby, A.L. Prieto, Direct Electrodeposition of Cu 2Sb for Lithium-Ion Battery Anodes, J. Am. Chem. Soc. 130 (2008) 10656–10661. doi:10.1021/ja801745n.

[16] E.D. Jackson, A.L. Prieto, Copper antimonide nanowire array lithium ion anodes stabilized by electrolyte additives, ACS Appl. Mater. Interfaces. 8 (2016) 30379–30386. doi:10.1021/acsami.6b08033.

[17] S.-K. KIM, T.-S. OH, Electrodeposition behavior and characteristics of Ni-carbon nanotube composite coatings, Transactions of Nonferrous Metals Society of China. 21 (2011) s68–s72. doi:10.1016/S1003-6326(11)61063-7.

[18] S. Arai, Y. Suwa, M. Endo, Cu/Multiwalled Carbon Nanotube Composite Films Fabricated by Pulse-Reverse Electrodeposition, J. Electrochem. Soc. 158 (2011) D49–D53. doi:10.1149/1.3518414.

[19] P.-M. Hannula, A. Peltonen, J. Aromaa, D. Janas, M. Lundström, B.P. Wilson, et al., Carbon nanotube-copper composites by electrodeposition on carbon nanotube fibers, Carbon. 107 (2016) 281–287. doi:10.1016/j.carbon.2016.06.008.

[20] S. Arai, M. Endo, Carbon Nanofiber-Copper Composites Fabricated by Electroplating, Electrochem. Solid-State Lett. 7 (2004) C25–C26. doi:10.1149/1.1644354.

[21] B.J. Landi, M.J. Ganter, C.D. Cress, R.A. DiLeo, R.P. Raffaelle, Carbon nanotubes for lithium ion batteries, Energy Environ. Sci. 2 (2009) 638–654. doi:10.1039/b904116h.

[22] S.-W. Kim, D.T. Ngo, J. Heo, C.-N. Park, C.-J. Park, Electrodeposited Germanium/Carbon Composite as an Anode Material for Lithium Ion Batteries, Electrochimica Acta. 238 (2017) 319–329. doi:10.1016/j.electacta.2017.04.027.

[23] M. Uysal, T. Cetinkaya, A. Alp, H. Akbulut, Production of Sn/MWCNT nanocomposite anodes by pulse electrodeposition for Li-ion batteries, Applied Surface Science. 290 (2014) 6–12. doi:10.1016/j.apsusc.2013.10.162.

[24] J.H. Lee, B.-S. Kong, S.B. Yang, H.-T. Jung, Fabrication of single-walled carbon nanotube/tin nanoparticle composites by electrochemical reduction combined with vacuum filtration and hybrid co-filtration for high-performance lithium battery electrodes, Journal of Power Sources. 194 (2009) 520–525. doi:10.1016/j.jpowsour.2009.04.045.

[25] C. Sotowa, G. Origi, M. Takeuchi, Y. Nishimura, K. Takeuchi, I.Y. Jang, et al., The Reinforcing Effect of Combined Carbon Nanotubes and Acetylene Blacks on the Positive Electrode of Lithium-Ion Batteries, ChemSusChem. 1 (2008) 911–915. doi:10.1002/cssc.200800170.

[26] X. Liu, Y. Du, X. Xu, X. Zhou, Z. Dai, J. Bao, Enhancing the Anode Performance of Antimony through Nitrogen-Doped Carbon and Carbon Nanotubes, J. Phys. Chem. C. 120 (2016) 3214–3220. doi:10.1021/acs.jpcc.5b11926.

[27] M. Alaf, H. Akbulut, Electrochemical energy storage behavior of Sn/SnO2 double phase nanocomposite anodes produced on the multiwalled carbon nanotube buckypapers for lithium-ion batteries, Journal of Power Sources. 247 (2014) 692–702. doi:10.1016/j.jpowsour.2013.09.020.

[28] L.-F. Cui, L. Hu, J.W. Choi, Y. Cui, Light-Weight Free-Standing Carbon Nanotube-Silicon Films for Anodes of Lithium Ion Batteries, ACS Nano. 4 (2010) 3671–3678. doi:10.1021/nn100619m.

[29] E.F. de la Cruz, Y. Zheng, E. Torres, W. Li, W. Song, K. Burugapalli, Zeta Potential of Modified Multi-walled Carbon Nanotubes in Presence of poly (vinyl alcohol) Hydrogel, International Journal of Electrochemical Science. 7 (2012) 3577–3590.

[30] J. Sun, L. Gao, W. Li, Colloidal Processing of Carbon Nanotube/Alumina Composites, Chem. Mater. 14 (2002) 5169–5172. doi:10.1021/cm020736q.

[31] A. Darwiche, C. Marino, M.T. Sougrati, B. Fraisse, L. Stievano, L. Monconduit, Better Cycling Performances of Bulk Sb in Na-Ion Batteries Compared to Li-Ion Systems: An Unexpected Electrochemical Mechanism, J. Am. Chem. Soc. 134 (2012) 20805–20811. doi:10.1021/ja310347x.

[32] M. He, K. Kravchyk, M. Walter, M.V. Kovalenko, Monodisperse Antimony Nanocrystals for High-Rate Li-ion and Na-ion Battery Anodes: Nano versus Bulk, Nano Lett. 14 (2014) 1255–1262. doi:10.1021/nl404165c.

[33] J. Park, S. Rajendran, H. Kwon, Effects of substrate morphology and ageing on cycle performance of a Sn-anode fabricated by electroplating, Journal of Power Sources. 159 (2006) 1409–1415. doi:10.1016/j.jpowsour.2005.11.064.

[34] N.-R. Shin, Y.-M. Kang, M.-S. Song, D.-Y. Kim, H.-S. Kwon, Effects of Cu substrate morphology and phase control on electrochemical performance of Sn–Ni alloys for Li-ion battery, Journal of Power Sources. 186 (2009) 201–205. doi:10.1016/j.jpowsour.2008.09.095.

CHAPTER 4 – TUNING CONJUGATION AND TRANSPORT PROPERTIES IN ANNEALED POLYACRYLONITRILE FILMS AS COATINGS AND ELECTROLYTES FOR SECONDARY BATTERY ANODES[1]

Overview

Critical limiting factors in next generation electrode materials for rechargeable batteries include short lifetimes, poor reaction reversibility, and safety concerns. Many of these challenges are caused by detrimental interactions between electrode materials and the electrolyte. Thermally annealed polyacrylonitrile has recently shown empirical success in mitigating such detrimental interactions when used as an electrode coating, though the mechanisms by which it does so are not well understood. This is a common problem in the battery community: an additive or a coating improves certain battery characteristics, but without a deeper understanding of how or why, design rules to further move new chemistries along can't be developed. Herein, we systematically investigate the effect of annealing parameters on the properties of polyacrylonitrile electrode coatings to identify the structural basis for such beneficial properties. The annealing conditions allow us to controllably tune the degree of conjugation in the electrode coatings, which correlates well to the onset of electronic conduction and rise of Li-ion diffusivity in the coatings. These results reveal the structure-property relationships that make annealed polyacrylonitrile such an effective electrode coating material. Not only do those relationships inform design principles for polyacrylonitrile based coatings, but they also identify a new strategy for synthesizing next generation electrode coatings and solid electrolytes.

---

[1] This chapter will be submitted to the Journal of the American Chemical Society for review with Maxwell C. Schulze and Amy L. Prieto as authors. The experiments were performed and the paper written by Maxwell C. Schulze with guidance from Amy L. Prieto.

Introduction

Rechargeable batteries based on Li-ion intercalation into layered electrode structures are becoming more widespread in their use for demanding energy storage applications such as electric vehicles [1] and large-scale grid energy storage [2]. With the energy density provided by those electrode chemistries approaching its theoretical maximum, new chemistries that can provide higher energy storage densities will help those technologies become ubiquitous [3]. Indeed, the research community has reported on many new high capacity electrode materials such as alloying anodes (Sb, Sn, and Si) [4] and conversion cathodes (sulfur) [5] that can provide larger theoretic maximum and demonstrable energy densities compared to intercalation-based electrodes. "Beyond Li-ion chemistries" such as Li, Na, K, and Mg metal batteries promise even higher energy storage capacities [3] with additional bonuses of using fewer or more abundant resources to minimize environmental impacts of large-scale production of these electrodes.

However, most of the proposed next generation electrode materials suffer from shortcomings such as poor reversibility, short lifetimes, and safety concerns [5]. While many of these shortcomings can be addressed by engineering the morphology/architecture of the electrodes themselves, battery performance is largely limited by the electrodes reacting with the electrolyte to form the solid electrolyte interface (SEI) layer [6]. On intercalation electrodes the SEI layer effectively passivates the electrode surface from further reaction with the electrolyte with minimal impact to performance of the cell. Such a passivation is less effective on high energy density electrodes, which undergo significant volume or surface changes during battery cycling that mechanically destabilize the SEI layer and expose new electrode surfaces to the electrolyte [6,7]. Repeated formation of a mechanically unstable SEI layer irreversibly consumes the working ion and other electrolyte components. Concomitant loss of reversible capacity leads to short lifetimes, while formation of dendritic deposits and gaseous byproducts is a safety hazard [8].

Electrode coatings [9], artificial SEI layers [10], and solid electrolytes (either inorganic ceramics [11] or polymer electrolytes [12]) have shown success in mitigating the detrimental effects of mechanically unstable SEI layer formation on next generation electrodes, though major improvements are few and far between. Recently, there have been several reports that empirically show the use of annealed polyacrylonitrile (PAN) as a coating material to improve the performance of Si alloy [13,14] or magnesium metal [15] anodes. At low temperatures between 200-300˚C, PAN undergoes the following transformation where the nitrile groups cyclize to form conjugated structures:

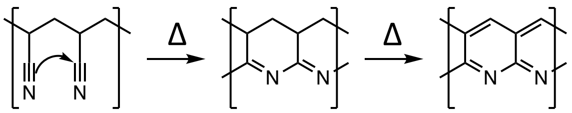

The authors attribute the formation of these conjugated structures to annealed PAN's ability to protect electrode surfaces during continuous volume changes by selectively allowing certain electrolyte components (working ions) through while providing mechanical support and, in some cases, additional electron conduction pathways. However, the reports express surprise over annealed PAN's ability to conduct ions (Li^+ and Mg^{2+}) so well and identify other unexplained electrochemical behaviors of the material, such as the large overpotential that is required to drive only the 1st lithiation of an annealed Sn/PAN electrode [16]. Additionally, despite being extensively studied in the context of industrial carbon fiber production, the specific types of structural features reported in annealed PAN vary widely and are very sensitive towards the annealing conditions (temperatures, times, and presence of oxygen) [17-19] and nature of the polymer (impurities from polymerization, inclusion of co-monomers, molecular weight, and stereochemistry) [20-22]. As such, there is a limited understanding of how the different structural features of annealed PAN influence its performance as an electrode coating material. Developing a fundamental understanding of those structure-property relationships would allow annealed PAN or similar materials to be further develop as effective electrode coatings.

Herein we present the first systematic study of annealed PAN as a battery electrode coating material to explore the idea that conjugated domains formed during the annealing process can be controlled to tune the electronic and ionic conductivity of the resulting material. Importantly, the ability to tune the electronic and ionic conductivity of such an electrode coating material would enable the material to be produced with the properties of an ideal SEI layer or electrolyte: low electronic and high ionic conductivities. Specifically, we use the time and temperature of the annealing process to tune the degree of conjugation in the PAN coatings. Targeted electrochemical experiments allow us to correlate the degree of conjugation to the onset of electronic conduction and rise of Li-ion diffusivity through the PAN coatings. The results lay the groundwork for tuning the properties of PAN-based coatings to optimize next generation electrode materials as well as suggest a new strategy for designing solid electrolytes with high ion diffusivities.

Experimental

Preparation of annealed PAN electrodes

A 1 M (~5 wt%) polyacrylonitrile (PAN) in N,N-dimethyl-formamide (DMF) solution based on moles of monomer units was prepared by first adding PAN powder (1.06 g, Aldrich, 181315, Lot #MKBD6325V, average Mw 150,000) to DMF (20 mL, >99.8, DriSolv, DX1727-6, Lot #52022). The mixture was stirred with a magnetic stir-bar on a hot plate set at 80 ˚C for several hours until a clear and colorless solution was formed. The solution was cooled to ambient temperature before being used to spin-coat substrates.

A suspension of 25 wt% Sb powder in a 10 wt% solution of PAN in DMF was prepared by first adding ball milled Sb powder (100 mg, 99.5%, Alfa Aesar, 10099, cryo ball-milled at 30 Hz for 30 minutes, 9 times) to DMF (2.7 g) and stirring with a magnetic stir-bar at ambient temperature until a homogenous suspension was formed. Powdered PAN (300 mg) was then added and the mixture stirred on a hotplate set to 80˚C for several hours until the PAN was fully dissolved. The solution was then cooled to ambient temperature before being used to spin-coat substrates.

Electrodeposited Sb@Ni electrodes were prepared by modifying a previously reported aqueous Sb deposition solution (400 mM citric acid, 25 mM Sb_2O_3, titrated to pH 6 with KOH) [23,24]. The Sb was electrodeposited onto a Ni foil (Shop-aid, Inc., Alloy 200/201, 0.001" thickness, >99.00% Ni, Lot #83944) masked to a 2" diameter circle in a 3-electrode cell. The Ni foil was positioned under a SS mesh counter electrode and was held at -1.05 V vs. a SCE reference electrode until 100 mC/cm^2 of charge was passed. Circular punches of 3/8" diameter were taken from this deposit and used as the Sb@Ni electrodes in the following spin coatings, anneals, and electrochemical experiments.

The PAN@SS and PAN@Sb@Ni electrodes were made by spin-coating stainless-steel (SS) disks (MTI, CR2025 spacer, SS304, Φ 15.5 mm by T 0.2 mm) or Sb@Ni electrodes, respectively, with the 1 M PAN solution using a MTI VTC-100 Vacuum Spin Coater set with the following parameters: 2000 rpm for 20 seconds followed immediately by 8000 rpm for 10 seconds. The Sb/PAN@PAN@SS electrodes were made by first spin coating a SS disk with the 1 M PAN solution as before. The PAN@SS substrate was then cured on a hotplate at 100˚C for

10 minutes before being spin-coated at 8000 rpm for 120 seconds with the 25 wt% suspension of Sb powder in 10 wt% PAN solution to produce the Sb/PAN@PAN@SS electrodes.

All electrodes were annealed in a Lindberg (Model 55322-3, 2" OD alumina tube) tube furnace under flowing argon. The electrode to be annealed was placed in an alumina boat, placed in the center of the tube, and the tube sealed. The tube was evacuated then refilled with argon three times before argon was set to flow over the sample at 100 mL/min. The temperature was ramped to the desired annealing temperature at the maximum ramp rate (~50 ˚C/min). The annealing time was started when the desired temperature was reached. When the annealing time was reached, the tube furnace was turned off and opened to quench the sample to ambient temperature; the sample remained under flowing argon during the cooling time.

FT-IR characterization of annealed PAN samples

Immediately after removing from the tube furnace, the FT-IR spectra of the annealed PAN@SS samples were measured by pressing the annealed PAN film onto the diamond ATR crystal of a Nicolet iS50 FT-IR spectrometer. The spectra were baselined to the low and high ends of the measurement range and to a local minimum around 1700 cm^{-1} present in every spectrum.

Electrochemical characterization of annealed PAN electrodes

All electrodes were assembled into Li-ion coin half-cells (with a liquid electrolyte of 1M $LiPF_6$ in 50/50 vol% EC/DEC) in an argon filled glovebox. Briefly, the coin cell was layered in the following order: a ½" diameter circular punch of Li foil was placed into the negative coin cell case (MTI, CR2025 cases SS304, with polypropylene sealing gasket), 3 drops of electrolyte, 5/8" diameter circular punch of polypropylene separator (MTI, Li-ion battery separator film, 25 µm thick, Batch #120313), 3 drops of electrolyte, 3/4" diameter circular punch of polypropylene separator, 3 drops electrolyte, working electrode (an uncoated SS disk was added to the PAN@Sb@Ni electrodes as a rigid backing), wave spring, and the positive coin cell case. The coin-cell assembly was pressed at 0.9 T using a compact digital pressure controlled electric crimper (MTI MSK-160E). The cells were allowed to rest for at least 12 hours before any electrochemical testing.

Electrochemical experiments were carried out on the coin cells using either an Arbin cycler (Model LBT20084) for the galvanostatic/potentiostatic experiments, a Gamry Interface 1010 for the electrochemical impedance spectroscopy (EIS), or a Gamry Reference 3000 potentiostat for the variable rate cyclic voltammetry (CV). The EIS was run between 300 kHz – 100 mHz with an AC excitation of 10 mV vs. OCV.

Results

Structural characterization of annealed PAN films using FT-IR

To prepare samples for annealing and subsequent characterization, PAN was first spin-coated onto stainless steel substrates (referred to as PAN@SS) and annealed under flowing argon for a set of different times and temperatures, as shown in Figure 4.1. The spin-coating parameters were chosen to produce uniform films with a thickness of ~0.5 μm, which was determined by the cross-sectional SEM image seen in Figure 4.2. All of the annealed PAN films were similar in appearance, exhibiting the same opalescent bronze color regardless of annealing conditions, though they did darken slightly over several hours upon exposure to air, suggesting the produced films were reactive with oxygen or moisture. As such, all the following characterizations were done quickly to minimize the exposure of the samples to air.

The annealed PAN films were first characterized with ATR FT-IR. Representative spectra of the annealed PAN films are shown in Figure 4.3 in the supplementary information,

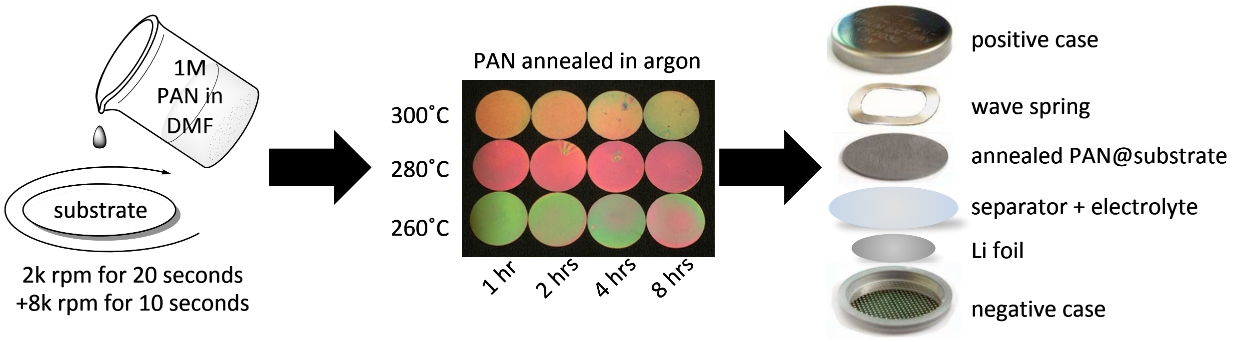

Figure 4.1: (Left) Schematic depicting the spin coating parameters for making the PAN films, which were then annealed. (Center) Photograph of the PAN films coated onto stainless steel (SS) substrates annealed under different conditions. (Right) Schematic depicting the use of the annealed PAN films as electrodes in lithium half-cells to study their transport properties.

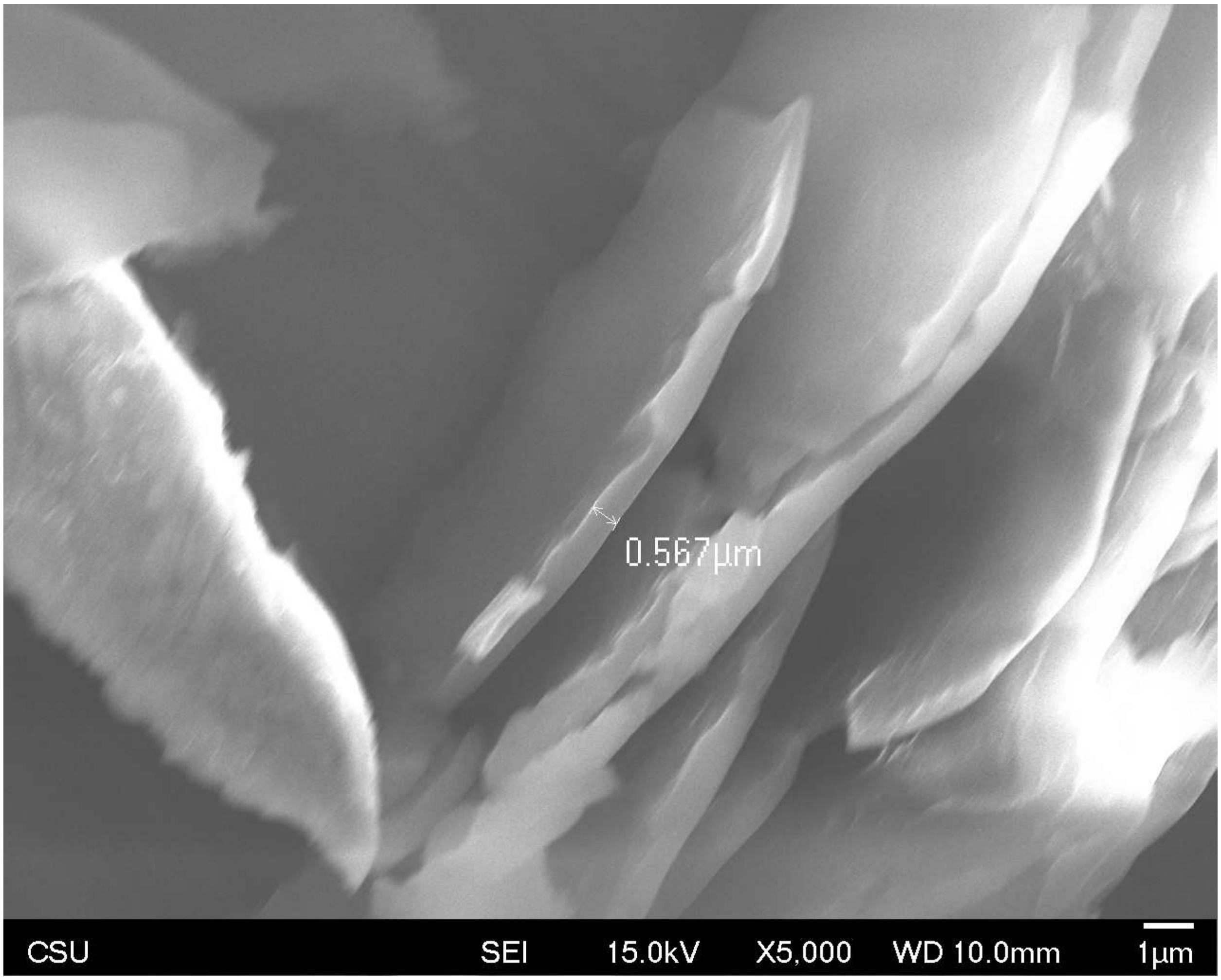

Figure 4.2: An SEM image of an annealed PAN film that was purposely damaged to expose an edge of the film to be measured. The thicknesses of the films prepared this way were measured around 0.5 um thick.

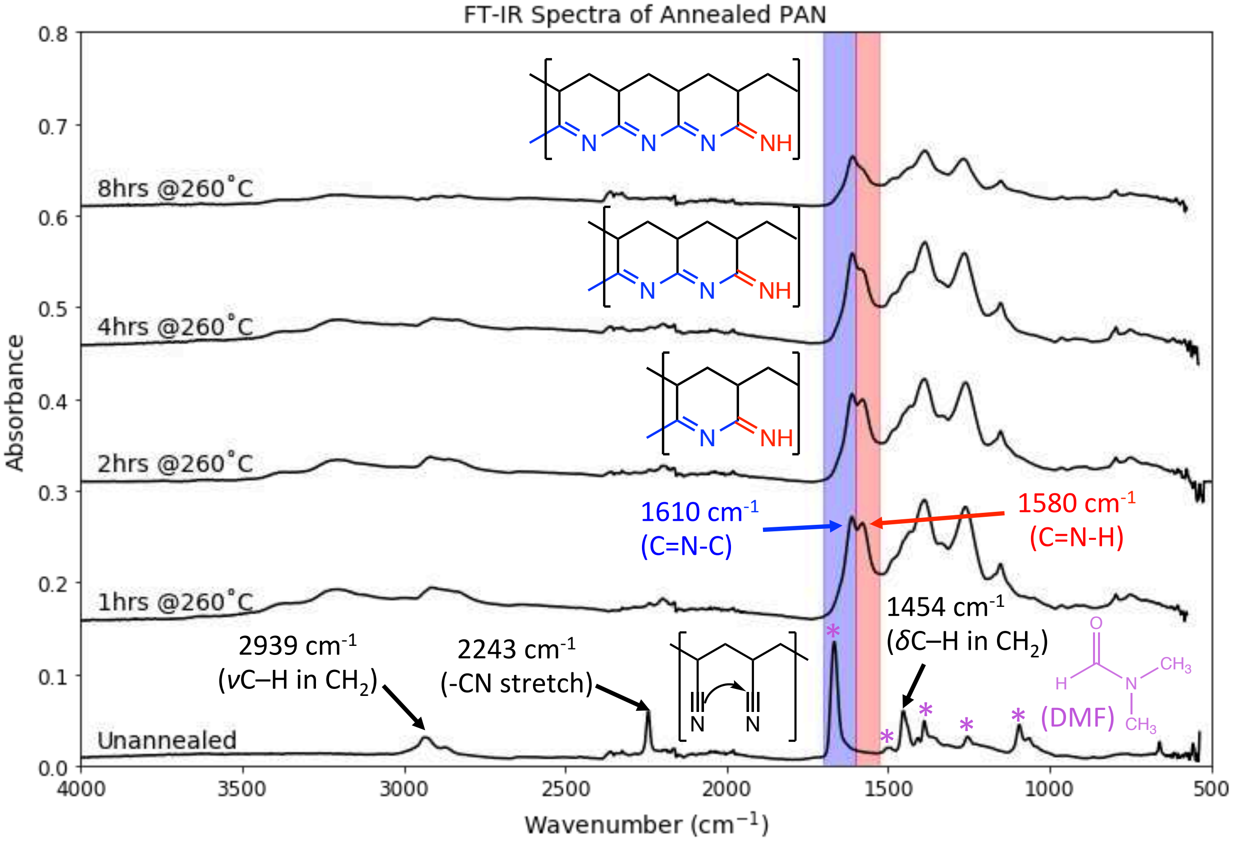

Figure 4.3: Representative FT-IR spectra of annealed PAN films. Critical features in the IR spectra are marked or highlighted and correlate to the structural features indicated in the inlayed structures.

and they match those previously reported in literature [17,18,20,22]. Upon annealing, the nitrile stretch at 2243 cm^{-1} disappears as a series of intense and overlapping peaks in the 1000-1800 cm^{1} range appear. This spectral evolution corresponds to the reaction of adjacent nitrile groups to form fused-ring ladder conjugated structures in annealed PAN. As depicted in Figure 4.3, the ladder structure only has one conjugated imine edge, while the methylene backbone of the polymer remains fully saturated. While some previous reports suggest that fully aromatic structures (sp^2 carbon only) form during the annealing, the presence of some absorption peaks around 2900 cm^{-1} even after annealing indicates that there is at least some sp^3 carbon present in the annealed structure. This is in contrast to PAN annealed under air, where the presence of oxygen promotes the full aromatization of fused-ring ladder structure as well as the introduction of oxygen functionality (ketone and hydroxyl groups) [17,19,21,25,26]. Such reactions with oxygen are likely what is occurring when the argon-annealed PAN films are exposed to air at ambient temperatures. While there is no change in the IR spectrum of the argon annealed PAN films over a few hours of air exposure, there is blending/blurring of some absorption peaks after several months of air exposure, suggesting aromatization and oxygen functionalization of conjugated domains occurs slowly.

Figure 4.4 shows the region in the FT-IR spectra between 1000-1800 cm^{-1} for every annealing condition. For the sample annealed at 260˚C for 1 hour an absorption peak doublet is present around 1600 cm^{-1}. We attribute the left peak at 1610 cm^{-1} (blue) to the presence of a secondary imine, which corresponds to the middle of a –C=N–C edge of the fused ring conjugated domain depicted. We attribute the right peak at 1580 cm^{-1} (red) to a primary imine, which corresponds to the depicted –C=N–H functionality that terminates a conjugated domain. Representative structures are inlayed in Figure 4.4 and are based on a qualitative comparison of

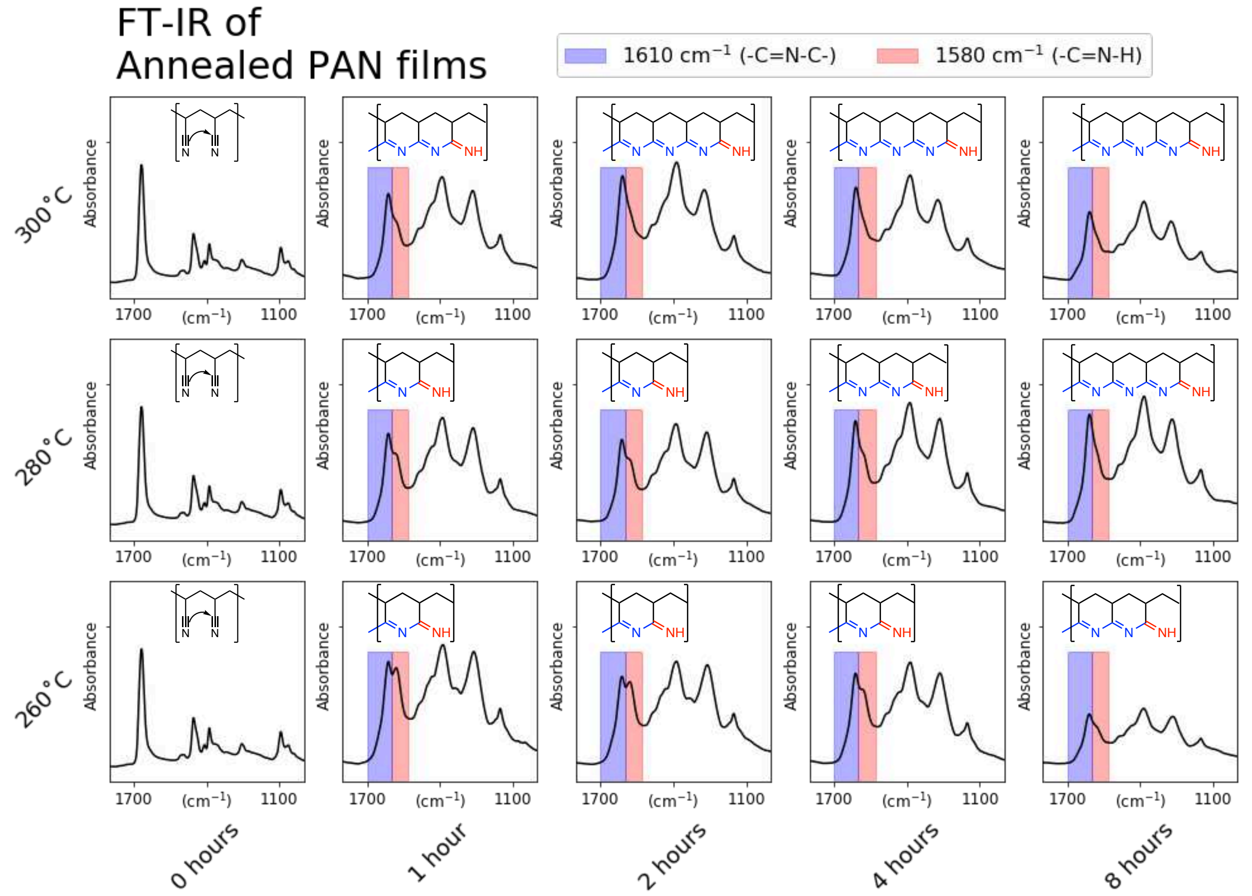

Figure 4.4: A selected area of the FT-IR spectra of PAN films annealed under every condition. We have assigned the features at 1610 cm^{-1} and 1580 cm^{-1} to secondary-imine and primary-imine functionalities, respectively. The disappearance of the peak at 1580 cm^{-1} corresponds well to the onset of the electrically conducting behavior. Examples of the conjugated structures we expect exist in the annealed PAN films are inlayed and their important functionalities indicated on the spectra.

the imide peak intensities. As the 1610 cm^{-1} (fused-ring) peak intensity increases relative to the 1580 cm^{-1} (terminal) peak, the length of conjugated domains likely increases. This demonstrates that the degree of conjugation in the annealed PAN films can be tuned simply by changing the annealing conditions.

Electronic behavior of annealed PAN films

To assess the effect of degree of conjugation on the electronic behavior of the annealed PAN films, we first assembled the PAN@SS samples into Li-ion half-cells as depicted in Figure 4.1. The half-cells serve as an electrochemical cell where electrochemical impedance spectroscopy (EIS) can be used to assess the electronic behavior of the annealed PAN. However, initial EIS measurements of the as-assembled cells showed no observable difference between electrodes. All the annealed PAN@SS electrodes exhibit high impedance behavior similar to unannealed PAN@SS electrodes. This is likely due to the fact that the types of structures produced as a result of annealing exhibit semiconducting behavior and little electronic conductivity unless doped [27-30]. As such, we attempted to n-dope the annealed PAN films by galvanostatically sweeping the cells to a low potential of 0.01 V vs. Li/Li^+. Such an n-doping reaction would involve the injection of an electron into a conjugated domain in the annealed PAN film from the SS substrate along with a charge compensating Li^+ from the liquid electrolyte.

Figure 4.5 shows the voltage profiles measured for each cell during the galvanostatic sweep. The voltage profiles with pink backgrounds show negligible capacity during the sweep, indicating that PAN films annealed at those conditions do not exhibit any redox activity and are not n-doped, which we attribute to their small degree of conjugation. The voltage profiles with green backgrounds show the voltage plateau at low potentials during the sweep, indicating that

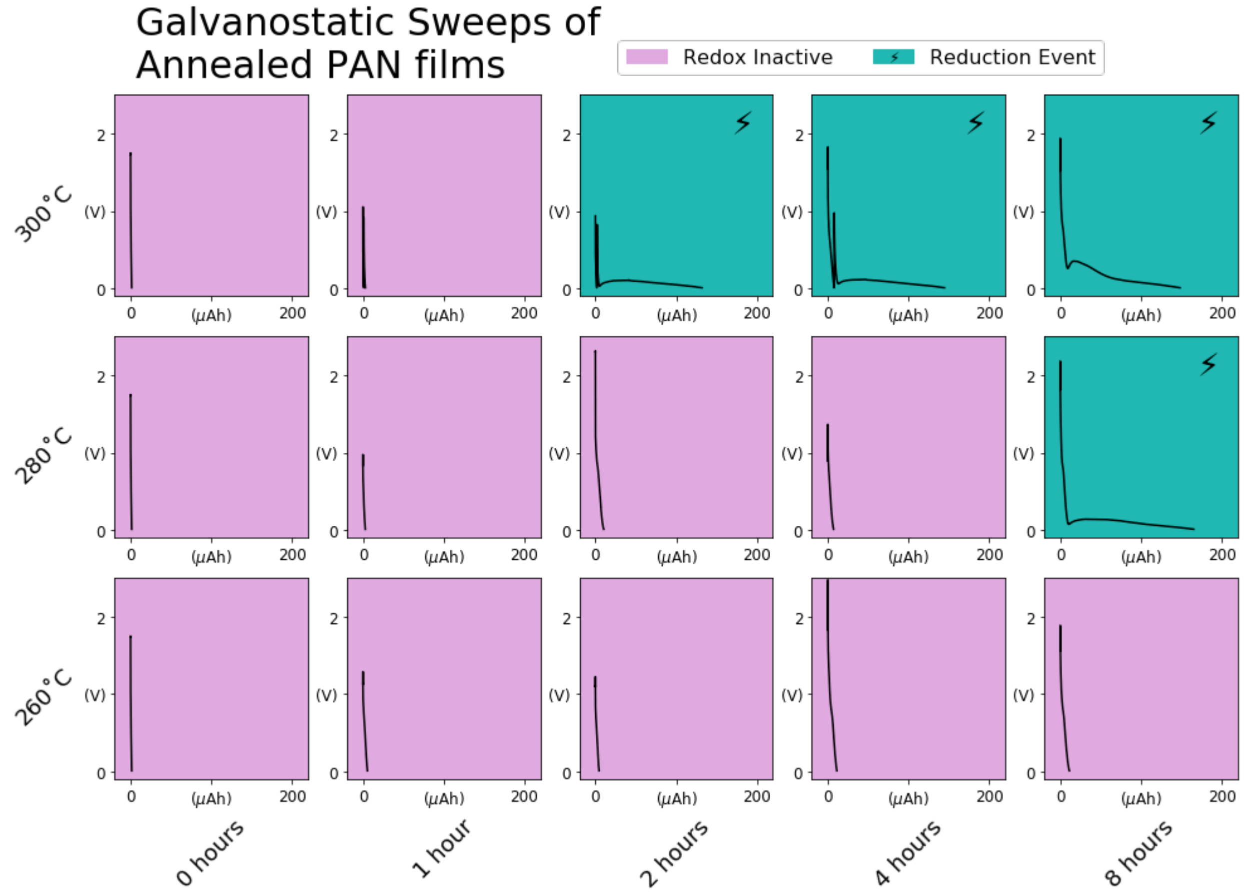

Figure 4.5: Voltage profiles obtained during galvanostatic sweeps of PAN films annealed at every condition. The slight rise in voltage at potentials approaching 0 V vs. Li/Li$^+$ followed by the sloping voltage plateau indicates some redox activity in PAN films annealed at those conditions (green background).

some reduction event is occurring. We attribute the reduction to the intercalation of Li-ions into the annealed PAN film, which is analogous to the injection of an electrons (n-doping) into the conduction band of the annealed PAN film along with charge compensating Li-ions. Note that this only occurs in cells where the PAN@SS electrodes have been annealed at higher temperatures and longer times, indicating there is a higher degree of conjugation in the annealed PAN films. The shape of the voltage profiles, with a slight rise in potential at the beginning can be rationalized by the annealed PAN films becoming more electrically conducting upon n-doping. The films are initially relatively electrically insulating, which makes the initial Li-ion intercalation require a slight overpotential. However, upon initial n-doping of the PAN films, their electronic conductivity rises and the overpotential for continued Li-ion intercalation decreases, resulting in the slight rise in half-cell voltage during the galvanostatic sweeps despite a reducing current being applied.

To further verify that the voltage plateaus observed in Figure 4.5 correspond to n-doping of the annealed PAN films and the concomitant rise in electronic conductivity, EIS measurements of half-cells were performed after the galvanostatic sweeps. Figure 4.6 shows the impedance vs. frequency for each cell before (blue trace) and after (red trace) the galvanostatic sweeps. The impedance traces of all of the PAN films before the galvanostatic sweeps are approximately the same, with low impedance values at high frequencies sloping to high impedance values at low frequencies with some subtle features. After the galvanostatic sweeps, the n-doped PAN films (green backgrounds) exhibit decreased impedance values at all frequencies, with shallow plateaus at both the low and high frequencies. The shapes of these impedance spectra match that of an uncoated and electrically conducting SS electrode (see Figure 4.7), indicating that the n-doped PAN films also exhibit electrically conducting behavior.

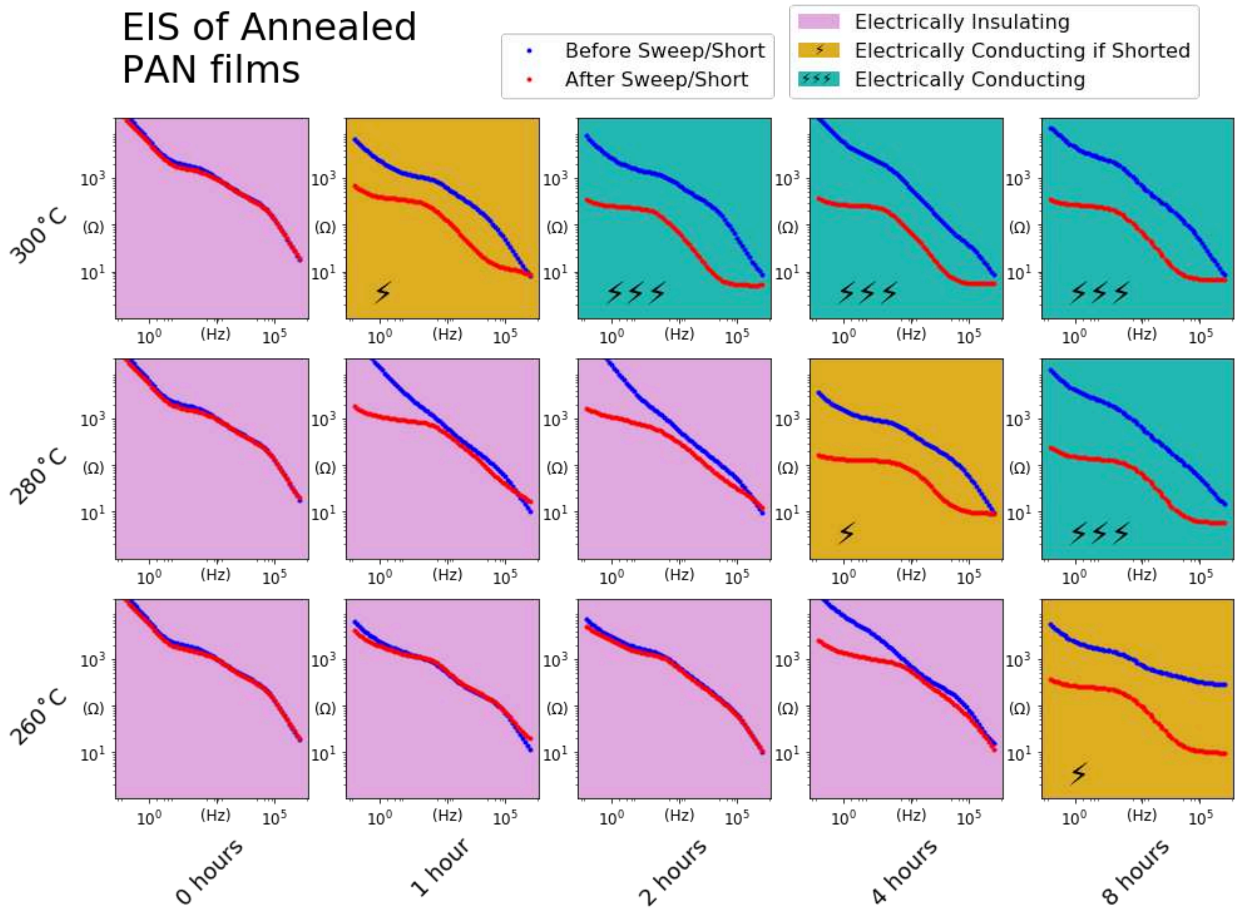

Figure 4.6: Impedance values measured using EIS of the PAN films annealed at every condition before the galvanostatic sweeps of their half-cells (blue) and after the galvanostatic sweeps or an additional 24-hour 0.01 V potentiostatic "short" (red). The background colors of the EIS spectra indicate the behavior of the PAN film annealed under those conditions as either electrically insulating (pink), electrically conducting after the galvanostatic sweep (green), or electrically conducting after an additional 24-hour potentiostatic "short" (yellow).

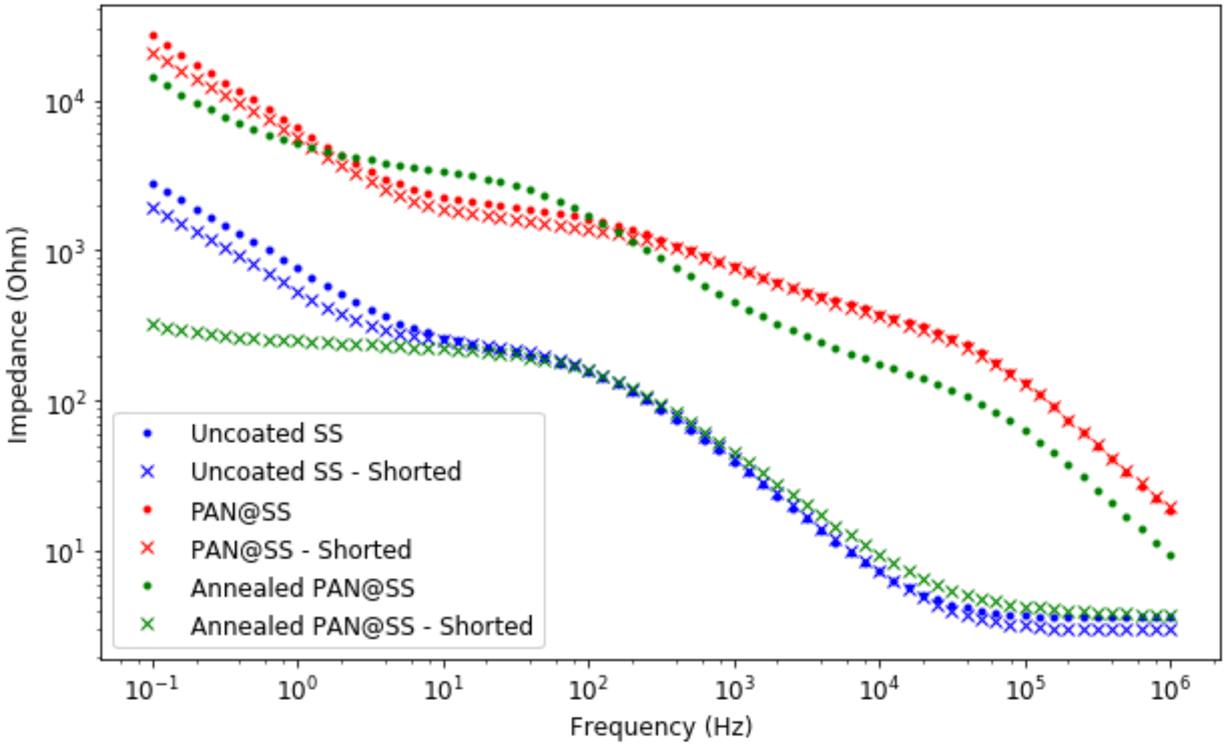

Figure 4.7: Several representative EIS spectra of annealed PAN electrodes in Li-ion half-cells. The annealed PAN@SS electrode was annealed at 300˚C for 3 hours so it is sufficiently conjugated to be electrically conducting when n-doped (shorted).

The low impedance values at the high frequency end of the spectra are a result of the PAN films' electronically conducting behavior, while the higher impedance plateau at the low frequency side of the spectra are dominated by the ionic behavior of the liquid electrolyte at the electrode surface.

It was noted that replicate PAN@SS electrodes annealed at some conditions (280˚C, 4 hours) exhibited different behaviors during the galvanostatic sweep depending on the applied current density, sometimes exhibiting redox inactivity and sometimes becoming n-doped. This suggests that under those specific annealing conditions, the PAN films were near the threshold of the degree of conjugation required to see one behavior versus the other. In such threshold samples, a galvanostatic sweep at a high current density may reach the voltage limit of 0.01 V vs. Li/Li^+ before the PAN film becomes n-doped, while a galvanostatic sweep at a lower current density would n-dope the PAN film.

To ensure that n-doping of these threshold samples occurs if possible, all of the half-cells indicating no redox activity during the sweep were "shorted" by holding the voltage at 0.01 V vs. Li/Li^+ for 24 hours. The impedance of the "shorted" cells was remeasured, and in some cases exhibited the impedance behavior of the n-doped PAN films. These threshold samples are indicated by the yellow backgrounds in Figure 4.6. The samples with the pink backgrounds are those that exhibited the same impedance behavior before and after the "short", identifying PAN films annealed under those conditions as insufficiently conjugated to become n-doped. For certain annealing conditions (280˚C 1 & 2 hours, 260˚C 4 hours) the impedance exhibited low frequency plateaus without exhibiting a high frequency plateau, suggesting that the degree of conjugation in those PAN films could be enough to promote higher ionic conductivity without becoming n-doped and electrically conducting. This particular phenomenon is being further investigated.

To verify that annealed PAN films exhibiting electronic conductivity after n-doping are relevant for coatings as battery electrodes, we fabricated an electrode depicted in Figure 4.8 (top). We chose to use Sb as an active material because it reversibly lithiates at ~1V vs. Li/Li^+, which is sufficiently positive to be distinct from the n-doping of PAN near 0 V vs. Li/Li^+. The ball-milled Sb powder is suspended in a PAN layer that is isolated from the SS substrate by a PAN-only layer, to form a Sb/PAN@PAN@SS electrode. This ensures that to see reversible lithiation of the Sb, electrons have to conduct through the annealed PAN. We chose to anneal this electrode at 280˚C for 4 hours so it would exhibit the threshold electrically conductive behavior, requiring it to be "shorted" to be n-doped and become electrically conducting.

The electrode was assembled into the same Li-ion half-cell configuration as before and Figure 4.8 (bottom) shows its voltage profile during a series of tests. The cell was first cycled at 1 $\mu A/cm^2$ between 2-0.3 V vs. Li/Li^+ (denoted by #1). The Sb (de)lithation potential falls within this range, though the n-doping of the annealed PAN does not. The absence of any voltage plateaus in the ~1 V range indicate the Sb is not lithiating, and the annealed PAN is not electrically conducting. These cycles are followed by galvanostatic cycles at 1 $\mu A/cm^2$ between 2-0.01 V vs. Li/Li^+ (denoted by #2), which now includes the potential at which the annealed PAN could become n-doped. However, because the annealing conditions were chosen to produce PAN films near the threshold to be n-doped, the PAN remains non-conducting and no Sb lithiation is observed. To n-dope the PAN, the cell is potentiostatically "shorted" at 0.01 V vs. Li/Li^+. (denoted by #3). The current was monitored during this step (not shown) and rose to -10 μA before dropping back to <1 μA, indicating some reduction events had occurred. The cell was

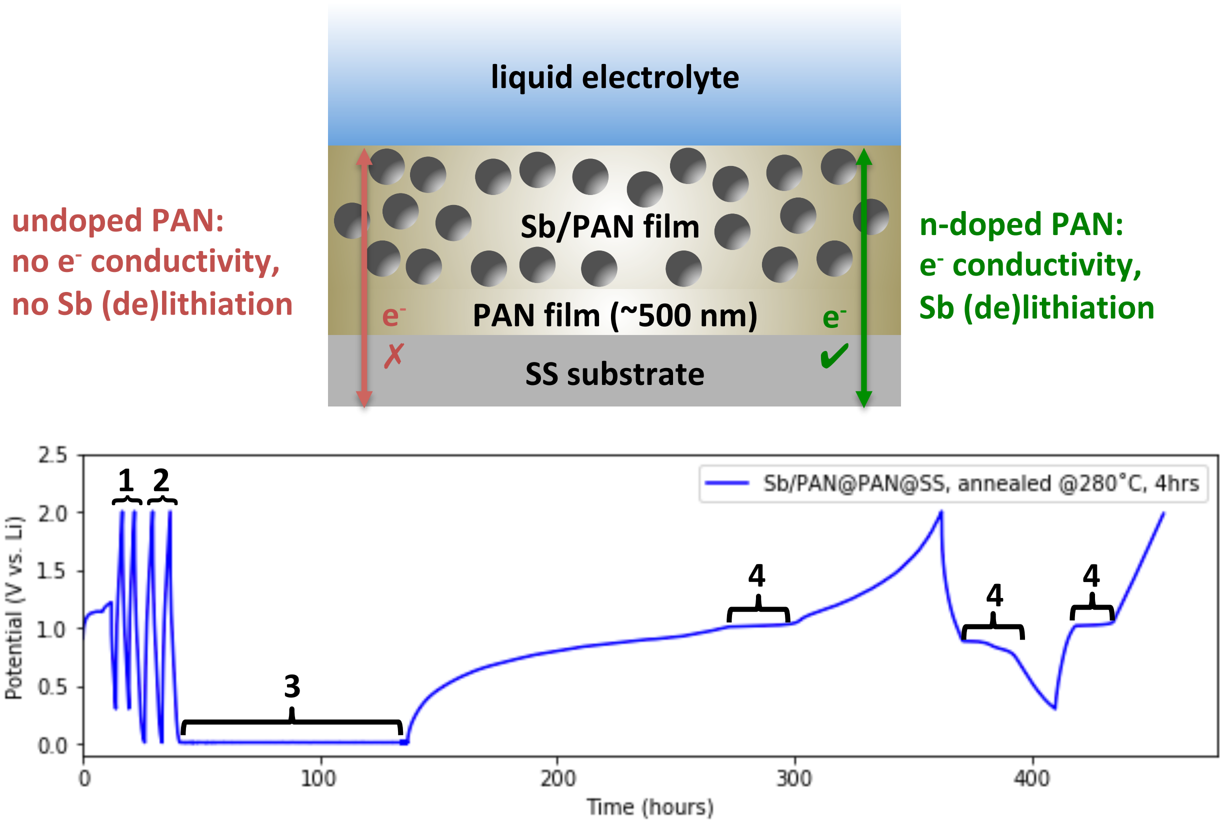

Figure 4.8: (Top) Schematic depicting an Sb/PAN@PAN@SS electrode designed to demonstrate the "doping" of and subsequent electrical conduction in annealed PAN films. (Bottom) Voltage profile obtained from galvanostatic/potentiostatic cycling of the annealed Sb/PAN@PAN@SS electrode in a lithium half-cell. Galvanostatic cycles at 1μA/cm^2 between 0.3-2 V vs. Li/Li$^+$ **(1)** and between 0.01-2 V vs. Li/Li$^+$ **(2)** show no Sb (de)lithiation activity. A potentiostatic hold at 0.01 V vs. Li/Li$^+$ **(3)** n-dopes the annealed PAN so that the following galvanostatic cycles at 1 μA/cm^2 between 0.3-2 V show Sb (de)lithiation activity **(4)**.

then again galvanostatically cycled at 1 μA/cm^2 between 2-0.3 V vs. Li/Li$^+$. During the initial sweep back to 2 V, the voltage shows a sloping profile, suggesting that some of the Li that intercalated into the annealed PAN is now de-intercalating. There is also a distinctly flat plateau at ~1 V that corresponds to the delithiation of Sb, indicating that during the "shorting" process, the PAN became n-doped and electrically conducting, thus allowing the Sb to also be lithiated. On subsequent cycles between 2-0.3 V vs. Li/Li$^+$, there are additional flat plateaus at ~0.9 V then at ~1 V vs. Li/Li$^+$ (denoted by #4), corresponding to Sb lithiation then delithiation, showing that annealed PAN still exhibits electron conductivity even after significant amounts of Li de-intercalation. The behavior displayed in Figure 4.8 is reproducible for different annealing conditions and n-doping procedures (galvanostatically or potentiostatically) given that the PAN film is sufficiently annealed to become n-doped.

Ionic transport in annealed PAN films

To measure the effect of annealing condition and degree of conjugation on mass transport through the annealed PAN films, we fabricated another Sb-containing electrode that is depicted in Figure 4.9A. The electrode was fabricated by first electrodepositing a thin layer of Sb onto a Ni metal substrate. Electrodeposition ensures the Sb is well electrically connected to the current collector, and the film was kept thin enough to minimize mechanical degradation during (de)lithiation. A layer of PAN was then spin-coated onto the Sb layer as before, and the entire electrode annealed. The architecture requires that Li-ion conduct through the PAN layer in order (de)lithiate the Sb layer, thus allowing us to probe the diffusivity through the annealed PAN layer. Several of these electrodes were made and annealed at 280˚C for 1, 2, 4, and 8 hours to include annealing conditions that produce annealed PAN films with insulating, threshold, and

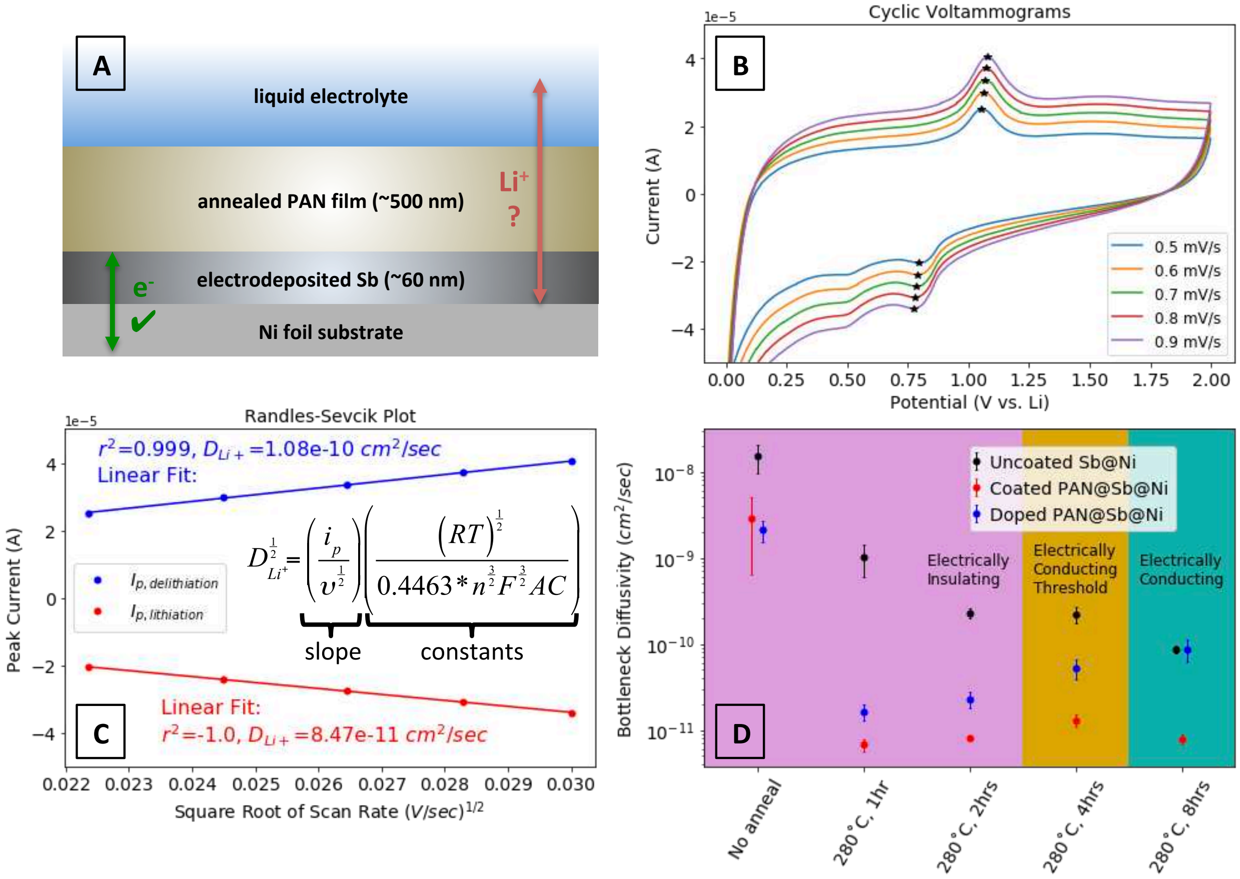

Figure 4.9: (A) Schematic depicting a PAN@Sb@Ni electrode designed to quantify the mass transport limitations through annealed PAN films. (B) Representative variable rate cyclic voltammograms of an annealed n-doped PAN@Sb@Ni electrode assembled into a lithium half-cell. The cyclic voltammograms for all electrodes annealed @ 280˚C can be found in Appendix C. (C) A representative Randles-Sevcik plot that uses the CV peak current values marked with stars. (D) Bottleneck diffusivity values determined from the Randles-Sevcik plots derived from the Sb@Ni and PAN@Sb@Ni electrodes annealed at 280˚C for various times (all values shown in Figure 4.10).

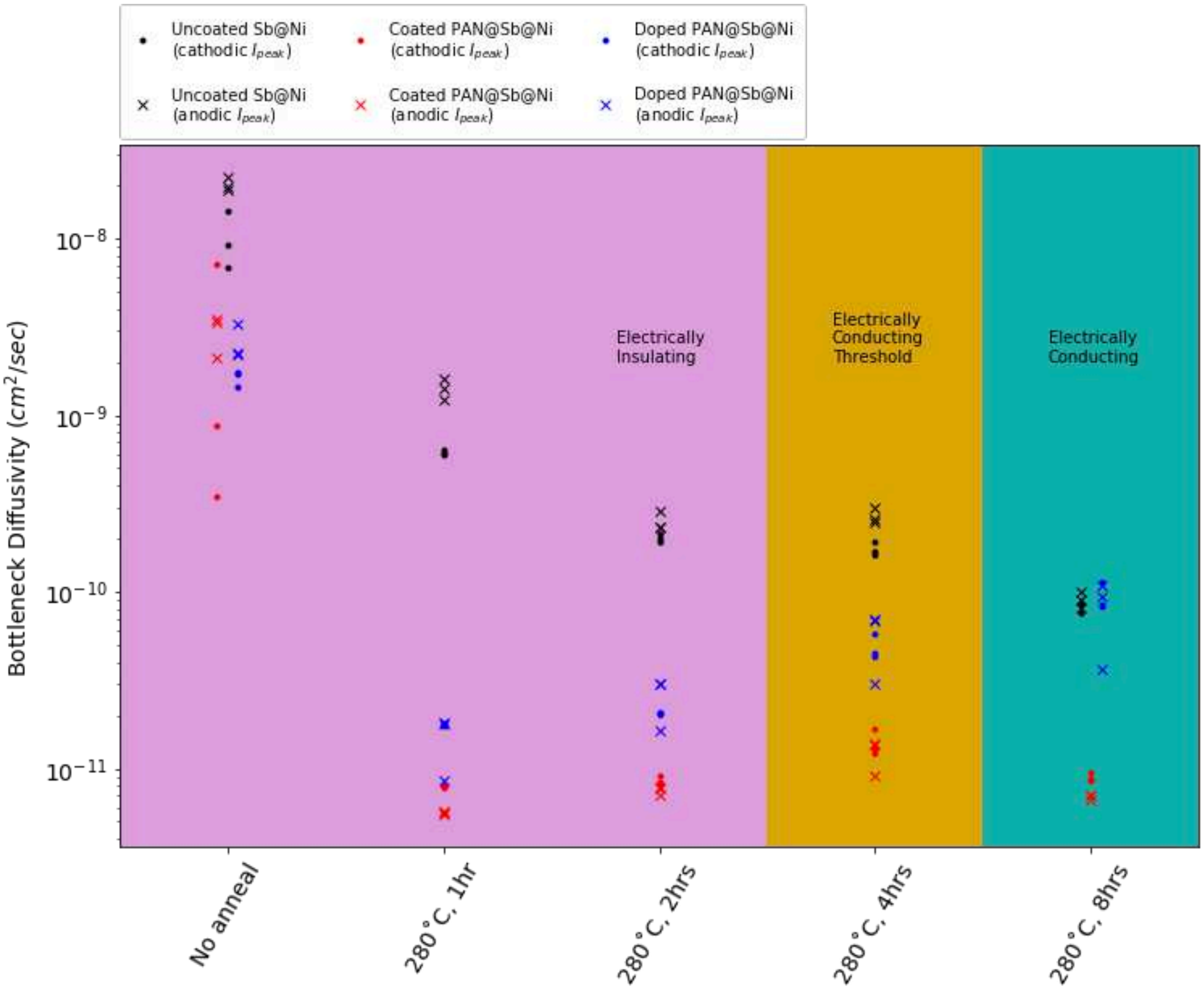

Figure 4.10: Bottleneck diffusivities calculated using the Randles-Sevcik equation.

conducting electrical behaviors. The Li-ion diffusivity in the annealed PAN layers was assessed using variable rate cyclic voltammetry (CV).

Example CVs between 2-0.01 V vs. Li/Li^+ are shown in Figure 4.9B, where the peak currents corresponding to reversible (de)lithiation are marked with stars. During a CV in most electrochemical cells, peaks occur in the current response because the rate of the associated reaction exceeds the transport of the redox reactant to the electrode surface and a reactant concentration gradient forms. In simple systems, such as a dissolved redox species interacting with an inert metal electrode, the Randles-Sevcik relationship relates the peak current values (i_p, A) and the scan rate (ν, V/sec) to the diffusivity of the electroactive reactant [31]. In more complex systems such as the PAN@Sb@Ni electrode depicted in Figure 4.9A, rate limiting concentration gradients can form in the Sb film, the PAN layer, and the liquid electrolyte. Thus, the peak current values measured during a CV of such a system would result from a convolution of the ion diffusivities in each of those layers, with the layer of the lowest ion diffusivity dominating the peak current response. As a result, the diffusivity values calculated using the Randles-Sevcik equation in Figure 4.9C are semi-empirical "bottleneck diffusivities" for the entire electrode, rather than representing intrinsic material properties. Figure 4.9C demonstrates such a calculation by plotting the peak current values from the CVs in Figure 4.9B vs. the square root of the scan rate to show a linear relationship. The slope of the linear fit ($i_p/\nu^{1/2}$) of those peak current values is proportional to the bottleneck ion diffusivity (D, cm^2/sec), where R is the gas constant ($J\ K^{-1}\ mol^{-1}$), T is the temperature (K), n is the number of electrons in redox process (1 for $1\ e^- + Li^+ + 1/3\ Sb \rightarrow 1/3\ Li_3Sb$), F is Faraday's constant (C/mol), A is the area of the electrode (cm^2), and C is the concentration (mol/cm^3).

Figure 4.9D shows bottleneck diffusivities calculated from variable rate CVs on half-cells with PAN@Sb@Ni electrodes annealed at 280˚C for 1, 2, 4, and 8 hours. Data from control samples with annealed but uncoated Sb@Ni electrodes are also shown to demonstrate that the calculated bottleneck diffusivity values are dominated by Li-ion diffusion through the annealed PAN layer rather than in the Sb layer. Each data point is the bottleneck diffusivity average of 3 consecutive sets of CVs on a single electrode, which verifies the electrode components are stable and give reproducible measurements (complete CV data can be found in Appendix C). The error bars are the standard deviation of the 3 consecutive measurements. The background color of the plot indicates the electronic behavior of the n-doped PAN films for each of the listed annealing conditions

The bottleneck diffusivity values for the uncoated Sb@Ni controls are shown in black. In the unannealed sample, the diffusivity value is highest ($>10^{-8}$ cm^2/s) and is likely dominated by diffusion of Li-ions in the Sb film. Upon annealing the uncoated Sb@Ni controls, the diffusivity drops to $\leq 10^{-9}$ cm^2/s for the 1, 2, and 4 hour anneals and finally down to $\sim 10^{-10}$ cm^2/s for the 8 hour anneal. The decrease in diffusivity values with longer annealing times could be due to an increase in the crystallinity of the Sb layer or the formation of Ni-Sb intermetallic phases. Powder X-ray diffraction of the electrodes was unable to confirm either possibility as the films were too thin to give sufficient diffraction signals. Regardless, measurements of these uncoated electrodes serve as empirical controls for diffusivity measurements of the PAN coated electrodes. Diffusivity measurements for the PAN@Sb@Ni electrodes are shown in red. It should be noted that the CVs for these electrodes start and end at 2 V vs. Li, so the annealed PAN films can be considered to be undoped. While the unannealed PAN@Sb@Ni electrode exhibits only a slightly lower bottleneck diffusivity than the uncoated Sb@Ni electrode, the annealed PAN@Sb@Ni electrodes all exhibit bottleneck diffusivities ~10^{-11} cm^2/s, regardless of the annealing time. Before annealing, the PAN layer likely swells in the liquid electrolyte to form a gel that exhibits fast and near-liquid ion diffusivity [32-35]. After annealing, the PAN films do not swell in the electrolyte and their ion diffusivities are comparatively low.

The PAN@Sb@Ni electrodes only begin to exhibit annealing-time-dependent diffusivity values once the annealed PAN layers have a chance to become n-doped (Figure 4.9D, blue data). Each of the PAN@Sb@Ni electrodes was held at 0.01 V vs. Li for 48 hours to provide opportunity for the annealed PAN layer to become n-doped. The variable rate CVs were then run starting and ending at 0.01 V vs. Li. The PAN@Sb@Ni electrodes annealed for 1 and 2 hours did not show a substantial increase in ion diffusivity after this "doping" step, likely because those annealing times are insufficient to produce large enough conjugated domains in the PAN layers to become n-doped. In contrast, the electrodes annealed for 4 and 8 hours exhibit more substantial increases of ion diffusivity after the "doping" step, likely because the PAN layers in these electrodes are sufficiently conjugated to become n-doped. We attribute the increase in ion diffusivity after the n-doping of the PAN layer to the delocalization of the Li counter-anion charge over large conjugated domains. The charge delocalization results in a polarizable matrix that reduces the coulombic drag of a diffusing Li-ion compared to an undoped layer. It is interesting to note that for the electrodes annealed for 4 hours the diffusivity of the n-doped PAN@Sb@Ni is still less than the uncoated Sb@Ni control, indicating the PAN layer is still the layer of lowest ion diffusivity in the electrode. This is in contrast to the electrodes annealed for 8 hours, where the diffusivity of the n-doped PAN@Sb@Ni electrode matches that of the uncoated Sb@Ni control at ~10^{-10} cm^2/s. This suggests that the diffusivity in the PAN layer likely exceeds the measured value, because Sb layer has become the layer that dominates the measured bottleneck diffusivity. Again, we attribute the increased ion diffusivity in the n-doped PAN layer to the greater extent of charge delocalization in conjugated domains that have grown in size with increased annealing time.

Discussion

Using unannealed vs. annealed PAN as battery coatings or electrolytes

The ability to tune the electronic and ionic conductivity of PAN by simply changing the annealing parameters makes annealed PAN a versatile and battery relevant material. To further understand why it is so effective as an electrode coating, we must consider how all of its properties are affected by the annealing procedure. In its unannealed form, PAN membranes will gel with typical organic liquid electrolytes and maintain comparatively high ion diffusivity [32,34]. As such, unannealed PAN could serve as a gelled polymer electrolyte or ionically conducting electrode coating/binder to provide mechanical stability to large volume change electrode materials while lowering the flammability hazard of a battery cell [33]. However, because unannealed PAN will gel with liquid electrolyte, it would do little to exclude electrolyte components like the carbonate solvents from reacting with the surface of electrode active materials to form the SEI layer. In this sense, unannealed PAN is unable to mitigate one of the most significant limiting factors of next generation electrode materials.

Upon annealing under the conditions discussed in this study, PAN undergoes significant chemical and physical changes. Annealed PAN is macroscopically very brittle and can be easily ground into a fine powder when not coated onto a substrate, which may translate to a high material hardness. This is likely the result of the formation of mechanically rigid conjugated domains and significant crosslinking between molecular chains (when nitrile groups on different polymer chains cyclize together) [16]. Annealed PAN also does not exhibit any kind of macroscopic swelling in typical organic liquid electrolytes, indicating that it likely does not absorb solvent molecules to form a gel. These combined properties make annealed PAN coatings able to provide mechanical support to larger volume change electrode active materials [13,14] but also chemically protects their surfaces from exposure to liquid electrolyte components and concomitant SEI formation [15].

If PAN is annealed to such a degree that it remains electrically insulating, it could also be used as a dry solid polymer electrolyte, albeit an electrolyte with low ion diffusivity. It is likely that electrically insulating annealed PAN will only exhibit ion conductivity if it is exposed to a liquid electrolyte or has a charge balancing anion-cation pair introduced another way. Experiments are underway to explore how introducing Li-salts before annealing affects the transport properties of the annealed PAN. If PAN is annealed to such a degree that it becomes conjugated enough to be n-doped, it could no longer serve as an electrolyte material as its electronic conductivity would be too high. However, it could be used effectively as a mixed conducting electrode coating/binder, being able to conduct ions without ever being exposed to a liquid electrolyte [16] or other salt. This is because the counter anions that mediate ion conductivity through such an annealed PAN coating are the conjugated domains that have been n-doped by the electrode.

Implications for high diffusivity solid polymer electrolytes

In this study we have shown that n-doped conjugated domains increase Li-ion diffusivity through annealed PAN by delocalizing the charge compensating anion in highly polarizable domains. Previous studies on other systems demonstrate that the polarizability of a conjugated domain generally increases with the size of the domain [36,37], with greater polarizability leading to higher ionic conductivities [38]. This is analogous to "lattice softening" in inorganic electrolytes where small non-polarizable halide ions can be substituted with larger more polarizable ions to increase ion diffusivity in the electrolyte [39]. This effect is not exclusive to Li-ions and can apply to any ion that might want to be conducting in a battery system (Na^+, Mg^{2+}, K^+, Ca^+, Zn^{2+}, Al^{3+}). The n-doped PAN studied herein would be unsuitable as an electrolyte material because the n-doping of the conjugated domains is coupled to onset of electronic conductivity. However, the correlation of the conjugated domain size and the ionic diffusivity suggests a strategy for developing solid polymer electrolyte materials based on conjugated domains.

Figure 4.11 shows the hypothetical ionic and electronic conductivities of an electrolyte matrix with tunable conjugation, where the n-doping of the conjugated domains is decoupled from any electron conduction through the matrix. Such a doping procedure would have to be achieved by chemical doping of the domains in solution before casting the solid matrix, for example. In such a system, the ionic conductivity would rise at smaller fraction of conjugation than the electronic conductivity. This can be rationalized using the percolation theory of conduction [40]. For example, if electrons have to conduct through nearest-neighbor (through-bond or pi-pi stacking) interactions but ions can conduct through nearest- and next-nearest-neighbor interactions (ion near enough to conjugated domain to polarize it), the percolation threshold for conduction will always be lower for the ions than for the electrons (as seen in Figure 4.11) [41]. The green star marks the behavior of an ideal electrolyte, where the difference between the ionic and electronic conductivities is maximized. This would be the case given that the ion conductivity is high enough for the desired power density of the cell and the electronic conductivity is low enough to result in negligible self-discharge rates.

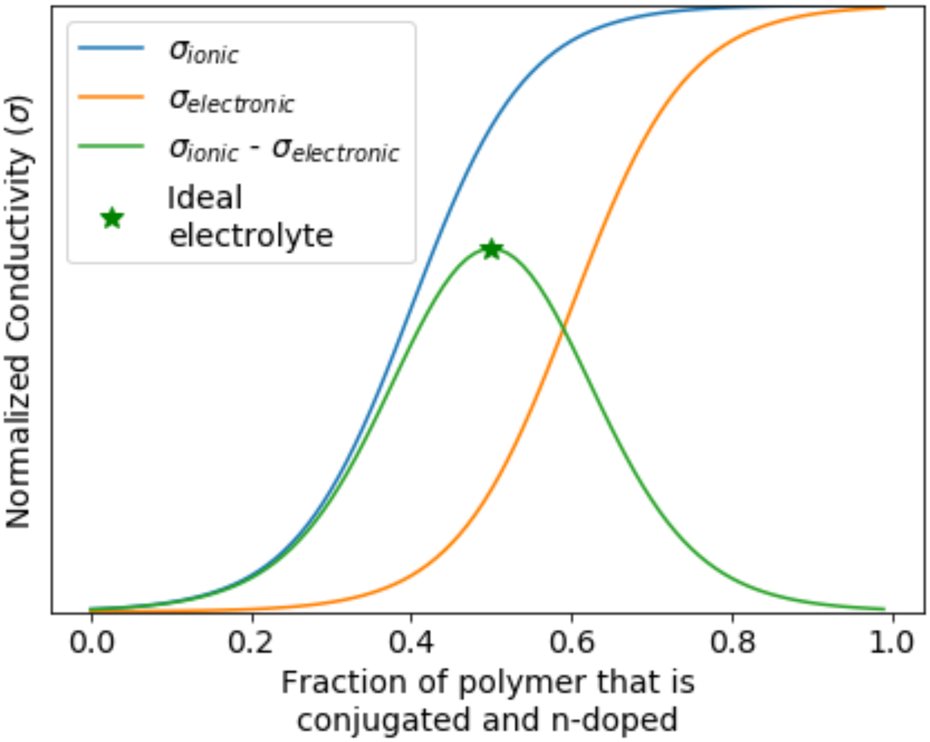

Figure 4.11: An imagined relationship between ionic and electronic conductivity in a polymer electrolyte as a function of the fraction of the polymer that is conjugated and n-doped. In such a system, the n-doping of the conjugated domains would be decoupled from any electronic conduction through the polymer.

While annealed PAN has demonstrated useful properties, it is not the ideal model system to test the relationship shown in Figure 4.11. When annealing PAN the formation of conjugated domains is not precisely controlled, and the ionic percolation threshold may be very close to electronic percolation threshold, making it difficult to tune conjugation to ideal electrolyte behavior via annealing conditions alone. A polymer system where the degree of conjugation is more precisely controlled could achieve such a behavior. Approaches to this could include forming conjugated domains using reactant stoichiometry, or even forming the conjugated domains in monomers before polymerization. Challenges in producing and utilizing these types of conjugated domain electrolytes would likely include their reactivity with oxygen, which would require air-free synthesis and processing during and after the n-doping step. Similarly, the n-doped domains would be susceptible to oxidation at the interface with many cathode materials, where a different type of electrolyte/interface would be needed. One might initially think to address these problems by introducing electron-withdrawing groups to the conjugated domains to lower their HOMO energy levels and make them more stable towards oxidation. However, such groups would localize electron density and decrease polarizability of the domains, thereby decreasing the ion diffusivity. Such materials would more closely resemble traditional polymer electrolytes, where anions are localized to electron withdrawing functionality, making them stable to oxidation but not very polarizable.

Conclusions

In summary, we have developed a fundamental understanding of how annealed PAN films can benefit the performance of next generation electrode materials for rechargeable batteries. The formation of conjugated domains in annealed PAN films can be monitored using FT-IR and can be easily controlled by simply changing the annealing time or temperature. If a

PAN film is sufficiently annealed, it can be n-doped at low potentials, where electrons from an electrode are delocalized into its conjugated domains with the concomitant intercalation of cations. The n-doping process provides additional electronic conduction pathways in battery electrodes, while the delocalization of negative charges in the conjugated domains results in fast ion conduction through the annealed PAN films. These results not only help to clarify why annealed PAN provides such beneficial properties for electrode materials in recent reports, but they also inform some design principles for its future use in the development of next generation electrode materials. Additionally, we discuss how the ability to precisely control the size and concentration of conjugated domains in organic and polymeric solids could be used to design solid electrolytes with high ionic conductivities mediated by charge delocalization in the conjugated domains.

CHAPTER 4 REFERENCES

[1] D. Bresser, K. Hosoi, D. Howell, H. Li, H. Zeisel, K. Amine, et al., Perspectives of automotive battery R&D in China, Germany, Japan, and the USA, Journal of Power Sources. 382 (2018) 176–178. doi:10.1016/j.jpowsour.2018.02.039.

[2] T.M. Gür, Review of electrical energy storage technologies, materials and systems: challenges and prospects for large-scale grid storage, Energy Environ. Sci. 11 (2018) 2696–2767. doi:10.1039/C8EE01419A.

[3] M. Winter, B. Barnett, K. Xu, Before Li ion batteries, Journal of Chemical Education. 23 (2018) 11433–11456. doi:10.1021/acs.chemrev.8b00422.

[4] M.N. Obrovac, V.L. Chevrier, Alloy Negative Electrodes for Li-Ion Batteries, Chem. Rev. 114 (2014) 11444–11502. doi:10.1021/cr500207g.

[5] J.W. Choi, D. Aurbach, Promise and reality of post-lithium-ion batteries with high energy densities, Nat. Rev. Mater. 1 (2016) 16013–17. doi:10.1038/natrevmats.2016.13.

[6] J. Meng, H. Guo, C. Niu, Y. Zhao, L. Xu, Q. Li, et al., Advances in Structure and Property Optimizations of Battery Electrode Materials, Joule. 1 (2017) 522–547. doi:10.1016/j.joule.2017.08.001.

[7] Y. Zhao, P. Stein, Y. Bai, M. Al-Siraj, Y. Yang, B.-X. Xu, A review on modeling of electro-chemo-mechanics in lithium-ion batteries, Journal of Power Sources. 413 (2019) 259–283. doi:10.1016/j.jpowsour.2018.12.011.

[8] M.R. Palacin, A. de Guibert, Why do batteries fail? Science. 351 (2016) 1253292–1253292. doi:10.1126/science.1253292.

[9] J. Lang, Y. Long, J. Qu, X. Luo, H. Wei, K. Huang, et al., One-pot solution coating of high quality LiF layer to stabilize Li metal anode, Energy Storage Materials. 16 (2019) 85–90. doi:10.1016/j.ensm.2018.04.024.

[10] Y. Liu, D. Lin, P.Y. Yuen, K. Liu, J. Xie, R.H. Dauskardt, et al., An Artificial Solid Electrolyte Interphase with High Li-Ion Conductivity, Mechanical Strength, and Flexibility for Stable Lithium Metal Anodes, Adv. Mater. 29 (2017) 1605531–8. doi:10.1002/adma.201605531.

[11] F. Zheng, M. Kotobuki, S. Song, M.O. Lai, L. Lu, Review on solid electrolytes for all-solid-state lithium-ion batteries, Journal of Power Sources. 389 (2018) 198–213. doi:10.1016/j.jpowsour.2018.04.022.

[12] H. Zhang, C. Li, M. Piszcz, E. Coya, T. Rojo, L.M. Rodriguez-Martinez, et al., Single lithium-ion conducting solid polymer electrolytes: advances and perspectives, Chem. Soc. Rev. 46 (2017) 797–815. doi:10.1039/C6CS00491A.

[13] A. Heist, D.M. Piper, T. Evans, S.C. Kim, S.S. Han, K.H. Oh, et al., Self-Contained Fragmentation and Interfacial Stability in Crude Micron-Silicon Anodes, J. Electrochem. Soc. 165 (2018) A244–A250. doi:10.1149/2.0811802jes.

[14] D.M. Piper, T.A. Yersak, S.B. Son, S.C. Kim, C.S. Kang, K.H. Oh, et al., Conformal Coatings of Cyclized-PAN for Mechanically Resilient Si nano-Composite Anodes, Adv. Energy Mater. 3 (2013) 697–702. doi:10.1002/aenm.201200850.

[15] S.B. Son, T. Gao, S.P. Harvey, K.X. Steirer, A. Stokes, A. Norman, et al., An artificial interphase enables reversible magnesium chemistry in carbonate electrolytes, Nature Chemistry. 10 (2018) 532–539. doi:10.1038/s41557-018-0019-6.

[16] N.A. Dunlap, J. Kim, K.H. Oh, S.-H. Lee, Slurry-Coated Sheet-Style Sn-PAN Anodes for All-Solid-State Li-Ion Batteries, J. Electrochem. Soc. 166 (2019) A915–A922. doi:10.1149/2.0151906jes.

[17] S. Xiao, B. Wang, C. Zhao, L. Xu, B. Chen, Influence of oxygen on the stabilization reaction of polyacrylonitrile fibers, J. Appl. Polym. Sci. 127 (2013) 2332–2338. doi:10.1002/app.37930.

[18] T.J. Xue, M.A. McKinney, C.A. Wilkie, The thermal degradation of polyacrylonitrile, Polymer Degradation and Stability. 58 (1997) 193–202. doi:10.1016/S0141-3910(97)00048-7.

[19] Z. Bashir, A critical review of the stabilisation of polyacrylonitrile, Electrochimica Acta. 29 (1991) 1081–1090. doi:10.1016/0008-6223(91)90024-D.

[20] Q. Ouyang, L. Cheng, H. Wang, K. Li, Mechanism and kinetics of the stabilization reactions of itaconic acid-modified polyacrylonitrile, Polymer Degradation and Stability. 93 (2008) 1415–1421. doi:10.1016/j.polymdegradstab.2008.05.021.

[21] I. Shimada, T. Takahagi, M. Fukuhara, K. Morita, A. Ishitani, FT-IR study of the stabilization reaction of polyacrylonitrile in the production of carbon fibers, Journal of Polymer Science Part a: Polymer Chemistry. 24 (1986) 1989–1995. doi:10.1002/pola.1986.080240819.

[22] N. Grassie, R. McGuchan, Pyrolysis of polyacrylonitrile and related polymers—III. Thermal analysis of preheated polymers, Electrochimica Acta. 7 (1971) 1357–1371. doi:10.1016/0014-3057(71)90032-2.

[23] J.M. Mosby, A.L. Prieto, Direct Electrodeposition of Cu 2Sb for Lithium-Ion Battery Anodes, J. Am. Chem. Soc. 130 (2008) 10656–10661. doi:10.1021/ja801745n.

[24] M.C. Schulze, R.K. Schulze, A.L. Prieto, Electrodeposited thin-film Cu_xSb anodes for Li-ion batteries: enhancement of cycle life via tuning of film composition and engineering of the film-substrate interface, J. Mater. Chem. A. 6 (2018) 12708–12717. doi:10.1039/C8TA01798K.

[25] Y. Xue, J. Liu, J. Liang, Kinetic study of the dehydrogenation reaction in polyacrylonitrile-based carbon fiber precursors during thermal stabilization, J. Appl. Polym. Sci. 127 (2013) 237–245. doi:10.1002/app.37878.

[26] W. Watt, W. Johnson, Mechanism of oxidisation of polyacrylonitrile fibres, Nature. 257 (1975) 210–212. doi:10.1038/257210a0.

[27] M. Suzuki, K. Takahashi, S. Mitani, Electrical Properties of Evaporated Polyacrylonitrile Films, Jpn. J. Appl. Phys. 14 (1975) 741–746. doi:10.1143/JJAP.14.741.

[28] M.H. Whangbo, R. Hoffmann, R.B. Woodward, Conjugated one and two dimensional polymers, Proc. R. Soc. Lond. a. 366 (1979) 23–46. doi:10.1098/rspa.1979.0037.

[29] J.J. Ritsko, G. Crecelius, J. Fink, Thermal transformation of local to extended electronic states in polymers, Phys. Rev. B. 27 (1983) 2612–2614. doi:10.1103/PhysRevB.27.2612.

[30] T.C. Chung, Y. Schlesinger, S. Etemad, A.G. Macdiarmid, A.J. Heeger, Optical studies of pyrolyzed polyacrylonitrile, Journal of Polymer Science: Polymer Physics Edition. 22 (1984) 1239–1246. doi:10.1002/pol.1984.180220708.

[31] L.R. Faulkner, A.J. Bard, Electrochemical methods: fundamentals and applications, 2nd ed., John Wiley and Sons, Hoboken, NJ, 2002.

[32] P. Hu, J. Chai, Y. Duan, Z. Liu, G. Cui, L. Chen, Progress in nitrile-based polymer

electrolytes for high performance lithium batteries, J. Mater. Chem. A. 4 (2016) 10070–10083. doi:10.1039/C6TA02907H.

[33] H. Akashi, K. Sekai, K. Tanaka, A novel fire-retardant polyacrylonitrile-based gel electrolyte for lithium batteries, Electrochimica Acta. 43 (1998) 1193–1197. doi:10.1016/S0013-4686(97)10019-6.

[34] K.M. Abraham, H.S. Choe, D. Pasquariello, Polyacrylonitrile electrolyte-based Li ion batteries, Electrochimica Acta. 43 (1998) 2399–2412. doi:10.1016/S0013-4686(97)10168-2.

[35] H.S. Choe, B.G. Carroll, D.M. Pasquariello, K.M. Abraham, Characterization of Some Polyacrylonitrile-Based Electrolytes, Chem. Mater. 9 (1997) 369–379. doi:10.1021/cm9604120.

[36] M.T. Zhao, B.P. Singh, P.N. Prasad, A systematic study of polarizability and microscopic third-order optical nonlinearity in thiophene oligomers, The Journal of Chemical Physics. 89 (1988) 5535–5541. doi:10.1063/1.455560.

[37] M. Gussoni, M. Rui, G. Zerbi, Electronic and relaxation contribution to linear molecular polarizability. an analysis of the experimental values, Journal of Molecular Structure. 447 (1998) 163–215. doi:10.1016/S0022-2860(97)00292-5.

[38] T. Takahashi, K. Nagagiri, Y. Iwadate, F. Utsuno, H. Yamaguchi, T. Ohkubo, Li conduction pathways in solid-state electrolytes: Insights from dynamics and polarizability, Chemical Physics Letters. 698 (2018) 234–239. doi:10.1016/j.cplett.2018.03.014.

[39] M.A. Kraft, S.P. Culver, M. Calderon, F. Böcher, T. Krauskopf, A. Senyshyn, et al., Influence of Lattice Polarizability on the Ionic Conductivity in the Lithium Superionic Argyrodites Li 6PS 5X (X = Cl, Br, I), J. Am. Chem. Soc. 139 (2017) 10909–10918. doi:10.1021/jacs.7b06327.

[40] W.Y. Hsu, J.R. Barkley, P. Meakin, Ion Percolation and Insulator-to-Conductor Transition in Nafion Perfluorosulfonic Acid Membranes, Macromolecules. 13 (1980) 198–200. doi:10.1021/ma60073a041.

[41] K. Malarz, S. Galam, Square-lattice site percolation at increasing ranges of neighbor bonds, Phys. Rev. E. 71 (2005) 016125. doi:10.1103/PhysRevE.71.016125.

CHAPTER 5 – IMPORTANT MATERIALS FOR NEXT GENERATION BATTERY DEVELOPMENT: ELECTROLYTE ADDITIVES, INTERFACIAL COATINGS, AND SOLID ELECTROLYTES[1]

Overview

The widespread success of the Li-ion battery is largely attributable to its so far unsurpassed performance in providing large energy densities with long cycle lifetimes, properties that arise from the careful selection and interfacing of all cell components. Electrode materials for next generation batteries promise improved energy densities while using more affordable and abundant resources, though they still suffer from poorly interfacing components that result in short cycle lifetimes. Herein we provide a general overview of battery materials research, highlighting the chemical factors that make currently used Li-ion batteries so successful. The chemical and mechanical stability of interfaces in batteries is the most important factor that currently limits the overall performance of next generation electrodes, making the research and development of materials to stabilize these interfaces essential to progressing the field.

Introduction

The initial release of the Li-ion battery in the early 1990's catalyzed the rapid expansion of portable electronic technologies, ranging from cell phones to laptop computers to more recently utility scale grid energy storage systems and all-electric vehicles with driving ranges approaching those of gasoline powered vehicles. It took careful research by the scientific community to combine materials in just the right way to produce such a successful battery technology. In the nearly three decades since its release, the scientific community has continued to make great strides in understanding the subtle chemical mechanisms of its operation, resulting

---

[1] This chapter will be submitted to the Royal Society of Chemistry journal: Chemical Communications for review with Maxwell C. Schulze and Amy L. Prieto as authors. The paper written by Maxwell C. Schulze with guidance from Amy L. Prieto.

in continued improvements in the energy densities, lifetimes, safety factors, and affordability of its newest iterations. Today's Li-ion batteries can boast energy densities greater than 250 Wh/kg and costs of less than $200 USD per kWh [1], compared to 80 Wh/kg with costs exceeding $1000 USD per kWh when it was first released [2,3]. With continued improvements it is believed that Li-ion batteries and their next generation counterparts can make significant contributions to the integration of transient renewable energy sources such as wind and solar into existing energy grid infrastructures [4] and to the electrification of vehicular transportation on widespread scales [1].

Herein, we review the basic electrochemical energy storage principles of battery cells, discussing in particular the materials used in the Li-ion battery and how both their individual properties and interactions with each other have resulted in such a successful technology. With the context of how and why Li-ion batteries work so well, we then discuss potential next-generation battery materials that promise improvements in battery energy densities and enable the option of using a wider range of resources that are more abundant. The use of these next-generation materials comes with the challenge of interfacing all of the battery cell components with sufficient stability to achieve the high reversibility and long lifetimes that Li-ion batteries exhibit. We finally review research performed within the last 10 years that represents the most significant contributions to this end, highlighting in particular the need for continued research in electrolyte additives, electrode coatings, and solid electrolytes.

Battery basics and the Li-ion battery

Energy can be stored electrochemically via the coupling of two reactions that occur at different redox potentials. In a rechargeable electrochemical battery cell (as depicted in Figure 5.1a) each electrode contains an active material where such a redox reaction occurs, the electrode

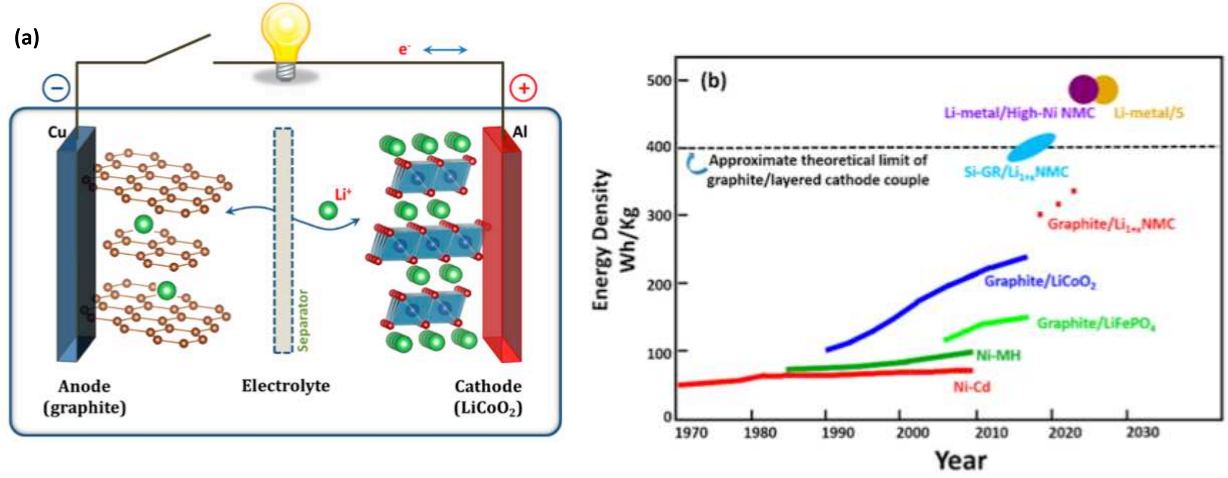

Figure 5.1: **(a)** A schematic of a rechargeable electrochemical energy storage cell. Two electrodes that can conduct both ions and electrons are separated by an electrolyte that conducts only ions, forcing the electrons to travel through an external circuit to power a device. The electrodes used in the prototypical Li-ion battery are a graphite anode and a layered transition metal oxide cathode like $LiCoO_2$. **(b)** A plot showing the energy density improvements of several rechargeable battery chemistries (anode-cathode pairs). The dotted horizontal line shows the approximate theoretical limit of the electrodes used in today's Li-ion batteries. Panel **(a)** is reproduced from Ref. [5] with permission of the American Chemical Society. Panel **(b)** is reproduced from Ref. [2] with permission of the American Chemical Society.

with the more negative (reduced) potential being the anode and the electrode with the more positive (oxidized) potential being the cathode. The electrolyte is typically a solution absorbed into the porous architecture of the electrodes to provide a large electroactive surface area that translates to high current densities and a large power output for the cell. A porous polyolefin film soaked in the electrolyte solution is sandwiched between the electrodes to prevent internal shorting while allowing ion conduction between the electrodes. When delivering stored energy, the anode's active material is oxidized while the cathode's active material is reduced, thus delivering an electromotive force across an external circuit to power an electrical device. At the same time, charge-compensating ions conduct through the electrolyte from the anode to the cathode to maintain net charge neutrality of the electrodes. To store energy the battery cell is recharged by applying the opposite electromotive force to the external circuit, reversing the redox reactions and moving the charge compensation ions back to the anode. For the battery to remain rechargeable for many energy delivery and storage cycles (cycle lifetimes for state-of-the-art Li-ion batteries are typically >80% capacity retention for more than 1000 cycles), the redox reactions and corresponding ion conduction must be reversible with high efficiency, which is one of the most significant challenges in the development of working rechargeable battery systems. Finally, the energy density of the battery cell can be estimated using:

$$Energy = V_{cell} * Q_{cell}$$

The difference in potential between the redox reactions is the cell voltage (V_{cell}) and the amount of redox active electrons and their charge compensation ions in the cell is the cell capacity (Q_{cell}). Thus to maximize a battery cell's energy density, the electrode active materials are chosen to provide the largest V_{cell} and Q_{cell} possible.

With the ideal battery behaviors in mind, it is no wonder that the materials used in the Li-ion battery have resulted in its high energy density, long cycle lifetime, and resulting technological success. Figure 5.1a shows the prototypical electrode materials used in Li-ion batteries (graphite anode and $LiCoO_2$ cathode) while Figure 5.1b shows the history of the achievable energy densities of the Li-ion battery (blue trace) compared to other existing battery chemistries and some proposed future battery chemistries. The layer structure of the graphite anode can form the intercalated LiC_6 compound, a reaction with an extremely reduced redox potential of ~0.10 V vs. Li^+/Li. On the cathode side, about half an equivalent of Li-ions can be deintercalated from the similarly layered structure of $LiCoO_2$ at a high redox potential of ~3.9 V vs. Li^+/Li. Combining the two electrodes results in the high ~3.7 V single cell potential that can be expected of many commercially available Li-ion batteries. Additionally, the layered structures provide host lattices for the Li-ions that undergo no structural rearrangements and minimal volume changes during intercalation/deintercalation processes, resulting in extremely reversible redox reactions that translate to long cycle lifetimes for the cell.

The careful selection of the remaining cell components (current collectors and electrolyte) is also essential for the high reversibility and the long cycle lifetime of Li-ion batteries. For example, a Cu foil is used as the current collector that supports the anode material because it is chemically stable at the anode's low potential; Al foil is used as the cathode's current collect for its analogous chemical stability via surface passivation at a high potential [2]. If the current collectors were to be accidentally switched, the effect on the cell would be disastrous, as the Cu would oxidize and leach Cu^+ and Cu^{2+} into the electrolyte while the Al would alloy with Li at the low potentials, ultimately disintegrating both current collectors. The electrolyte used in Li-ion batteries is typically a highly soluble Li-salt ($LiPF_6$ is most commonly used) dissolved in aprotic polar solvents composed of organic carbonates (typically mixtures of ethylene carbonate, diethyl carbonate, dimethyl carbonate). Given that the electrolyte is not thermodynamically stable at the extreme potentials of the electrodes, it is specifically designed to form kinetically passivating interfaces with the electrodes commonly referred to as the solid electrolyte interface (SEI) layer [6]. A poorly passivating SEI allows continuous decomposition of electrolyte components to form gaseous products, irreversibly trap Li in insoluble inorganic salts, and can even result in the degradation of the electrodes themselves[2]. Electrolyte additives that act as sacrificial precursors to better passivating SEI layers are largely responsible for the improvements in cycle lifetimes of Li-ion batteries [7].

Next generation electrode materials

Engineering optimizations can continue to increase the energy density that Li-ion batteries provide only up to a theoretical maximum (marked by the dotted line in Figure 5.1b) that is limited by the particular combination of electrode active materials. The layered host lattices, small Li stoichiometries, and presence of heavy transition metals in those electrode materials results in comparatively small cell capacities relative to commonly researched next generation electrode materials. The "holy grail" of next generation anodes is simply the electrochemical plating and stripping of Li-metal, where the absence of any host lattice that adds dead weight to the electrode results in the anode's theoretical maximum gravimetric capacity being an order of magnitude more than graphite's[3]. Similarly, a next-generation cathode made of

---

[2] When propylene carbonate is used in a liquid electrolyte, the solvent co-intercalates into the graphite layers with the Li-ion and destroys the graphite structure by exfoliating the layers. This turned out to be a major hurdle in the development of the Li-ion battery that was eventually solved by using ethylene carbonate instead of propylene carbonate based solvents. The fact that the two solvent molecules differ in structure by only a single methyl group despite significantly different results in the lithiation of graphite exemplifies that the careful selection of all cell components in the Li-ion battery was essential for its success [2].

[3] While we primarily discuss how the mass of all cell components affects its gravimetric capacity and energy density, the volumetric energy density reported in Wh/L is an equally, if not more important metric depending on

sulfur is comparatively light and also exhibits a theoretic maximum gravimetric capacity an order of magnitude greater than the heavy Co containing $LiCoO_2$ cathode. The larger capacities of a Li-metal anode and a sulfur cathode result in the Li-metal/sulfur battery having practical energy densities around 500 Wh/kg (see Figure 5.1b) and theoretic values around 2500 Wh/kg despite a smaller single cell potential ~2.2 V [8].

The Li-sulfur battery is truly just the tip of the iceberg in terms of potential next generation electrode materials. In theory, many of the lighter electropositive alkali and alkaline earth metals could serve as suitable next generation metallic anode materials with their cationic forms (Na^+, Mg^{2+}, K^+, Ca^{2+}) taking the role of the charge-compensation ions in the battery [9]. Even some main group elements have been considered as high capacity anodes that Li alloys with in high stoichiometries (Li_3Sb, $Li_{4.4}Sn$, $Li_{15}Si_4$) [10] or as metallic anodes (reversible plating/stripping of Al^{3+} or Zn^{2+}) [9]. To compare the energy densities that could possibly be achieved with these next generation anode materials, we calculate the energy density of a cell where each anode material is paired with a hypothetical cathode. The absolute redox potential and capacity of the hypothetical cathode was chosen to be reasonably reflective of experimentally reported high performance cathode materials for these chemistries, most of which are a transition metal oxide/phosphate phases that are continually being discovered[4].

Such calculated energy density values for various anode materials are shown in Figure 5.2a and were calculated using the parameters displayed in Table 5.1. Because energy density calculations are most meaningful and representative when they are calculated for a pair of

---

the battery's application. The effect of the volume of all cell components on its volumetric energy density does not always follow the same trends as gravimetric energy density because of the varying densities of the materials used.

[4] Sulfur is also a viable high capacity cathode for many of these alternative ion chemistries. However, because room temperature Li-sulfur batteries have yet to be commercialized, we have chosen to compare the energy densities of the next generation anode materials by pairing them with a hypothetical cathode that has parameters more typical of already proven transition metal oxide cathodes like $LiCoO_2$ used in the Li-ion battery.

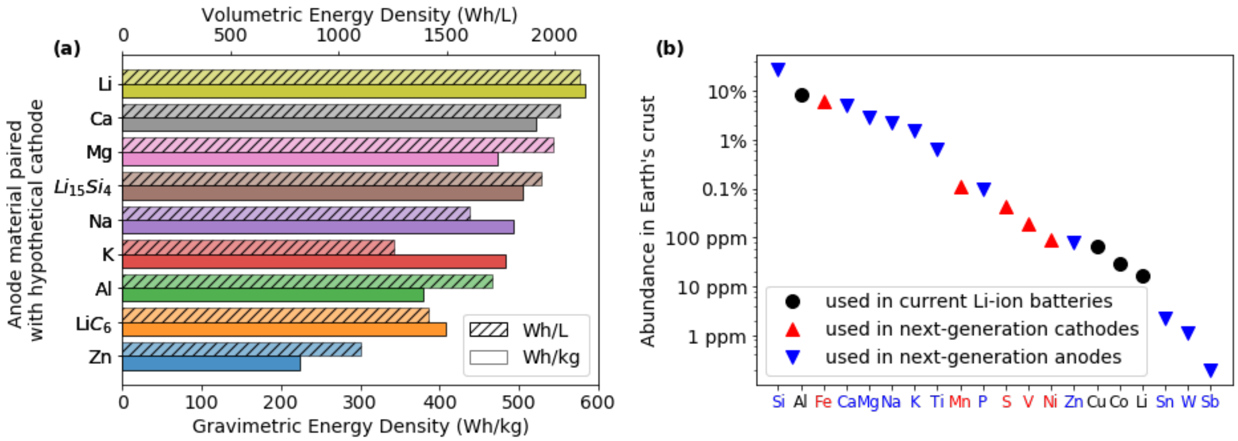

Figure 5.2: **(a)** Theoretical energy limits for several anode materials when paired with a hypothetical cathode: 1V vs. NHE, 150 mAh/g, 700 mAh/cm^3. These values are overestimates of practically attainable energy densities because the mass and volume of other cell components (current collectors, electrolyte, separators, and packaging) are neglected, though they do demonstrate the approximate relative performance between different anode materials. **(b)** The crustal abundance of several battery materials relevant elements.

Table 5.1: The potentials and storage capacities of the next generation electrode materials shown in Figure 5.2a. These values were used to calculate the full-cell energy storage densities when the electrodes are paired with the hypothetical cathode shown in the first row.

Electrode Materials	**Potential (V vs. NHE)**	**Electrode Capacity**		**Full-Cell Capacity**		**Full-Cell Voltage**	**Full-Cell Energy**	
		(mAh/g)	**(mAh/cm^3)**	**(mAh/g)**	**(mAh/cm^3)**		**Wh/kg**	**Wh/L**
Cathode	1	150	700	———	———	———	———	———
LiC_6	-2.915	339	746	104	361	3.915	407	1414
$Li_{15}Si_4$	-2.64	1857	2229	139	533	3.640	505	1939
Li	-3.045	3861	2062	144	523	4.045	584	2114
Na	-2.714	1166	1128	133	432	3.714	494	1604
Mg	-2.37	2205	3833	140	592	3.370	473	1995
Al	-1.66	2979	8046	143	644	2.660	380	1713
K	-2.925	685	591	123	320	3.925	483	1258
Ca	-2.87	1337	2073	135	523	3.870	522	2025
Zn	-0.763	820	5854	127	625	1.763	224	1102

electrodes, each of the anode materials was paired with a hypothetical universal cathode, the parameters of which are displayed in the first row of Table 5.1. The parameters chosen are fairly close to those exhibited by $LiCoO_2$ in a Li-ion battery so the capacity values and electrode potential should be roughly representative of intercalation style cathode materials that could intercalate ions from each of the anode materials. This makes the values displayed in Figure 5.2a not rigorously steadfast, but offer a useful comparison between the energy densities when using any given anode material. The calculations neglect the mass and volume of all other cell components, including the current collectors, separators, binders, electrolyte, pore space, and packaging, so they represent the maximum theoretical values that can be achieved by minimizing the mass and volume contributions of those components.

The anode materials are shown in the 1st column of Table 5.1 where the redox reaction of each anode material is simply the plating/stripping of the element shown (except for LiC_6 and $Li_{15}Si_4$ which are the (de)intercalation of Li into graphite and (de)alloying of Li with Si, respectively). The potential of each electrode material shown in the 2nd column is the electrochemical potential at which the electrode's redox reaction occurs. For redox reactions that occur across a range of electrochemical potentials (such as the alloying of Li with Si) this value is the average electrochemical potential. The electrode capacities (Q_{anode}, $Q_{cathode}$) shown in the 3rd and 4th columns are calculated from the stoichiometry and crystal density of the phases shown in the first columns. For LiC_6 and $Li_{15}Si_4$ in particular, these values include the mass and volume of the lithium in the anode material. The full cell voltage shown in the 7th column is simply the difference between the electrode potentials of the anode and cathode while the full-cell capacities (Q_{cell}) shown in the 5th and 6th columns can be calculated using the following equation:

$$\frac{1}{Q_{cell}} = \frac{1}{Q_{anode}} + \frac{1}{Q_{cathode}}$$

Finally, the full-cell energies shown in the final columns are the product of the full-cell capacities and full-cell voltage. These are the values that are displayed in Figure 5.2a.

The energy densities displayed in Figure 5.2a represent theoretic maximum achievable energy densities because they neglect the mass and volume of all other cell components such as the current collectors, separators, electrolyte, and inactive electrode components that are often necessary for proper functioning of the battery. From a theoretical standpoint, the figure demonstrates that the energy density of batteries with Li-ion chemistry can still be improved by substituting the graphite (LiC_6) anode in the prototypical Li-ion battery with a high capacity silicon anode ($Li_{15}Si_4$) or even a Li-metal anode. Additionally, it shows that many of the alternative ion chemistries using metal anodes of Zn, Al, K, Na, Mg, or Ca can have comparable or even improved energy densities compared to the Li-ion battery using a graphite anode. These alternative ion chemistries have the additional advantage of using elements that are very abundant in the Earth's crust, as shown in Figure 5.2b [11]. By using electrodes sourced from a wide variety of more abundant resources, the production of batteries for electric vehicles and grid energy storage on massive scales could be made significantly more feasible and affordable than relying exclusively on less abundant resources like Li and Co that are limited to certain areas of the world [12].

Despite the numerous potential benefits of next generation electrode materials like high-capacity alloying anodes (Si), metallic anodes, and sulfur cathodes, they remain largely unused in commercial applications. Academic studies of these materials have identified bottlenecks in their technological development, a primary one being the poor reversibility of their redox reactions and prohibitively short cycle lifetimes that arise from their mechanically dynamic operation. Alloying and conversion type electrodes like Si and sulfur, respectively, endure significant rearrangement and volume changes of their atomic structures during operation, while metallic anodes repeatedly electroplate and strip electrode surfaces. These dynamics not only result in physical degradation (cracking and pulverization) of electrodes that can electrically isolate the electrode material from the current collector, but also in the SEI being unstable and poorly passivating over many cycles. The concomitant short cycle lifetimes of these mechanically dynamic electrodes are in contrast to the long-lived intercalation electrodes currently used in Li-ion batteries, where non-dynamic host lattices for the working ions allow the formation of stable SEI layers and high reversibility. As such, the most important work in the development of next generation electrode materials is to understand and mitigate the mechanical and chemical instability of electrodes and their interfaces with electrolytes.

Critical material advances for electrode and interfacial stability

As previously mentioned, many of the next generation electrode materials are high capacity anodes that alloy with working ions and result in significant structural rearrangements and volume changes. To mitigate the mechanical degradation problems associated with the volume expansions, the research field has dedicated a significant amount of effort to producing these types of electrodes as nano-scale architectures. Kovalenko's research group has nicely summarized in Figure 5.3 some benefits and drawbacks of using nanostructured electrode materials [13]. In particular, the nano-structuring strategy has shown success in preventing mechanical degradation and allows the use of electrode active materials that have prohibitively low electronic or ionic conductivity in bulk form. However, nano-structuring also increases electrode materials' synthetic costs and enhances surface related effects, of which kinetic passivation by SEI formation is included.

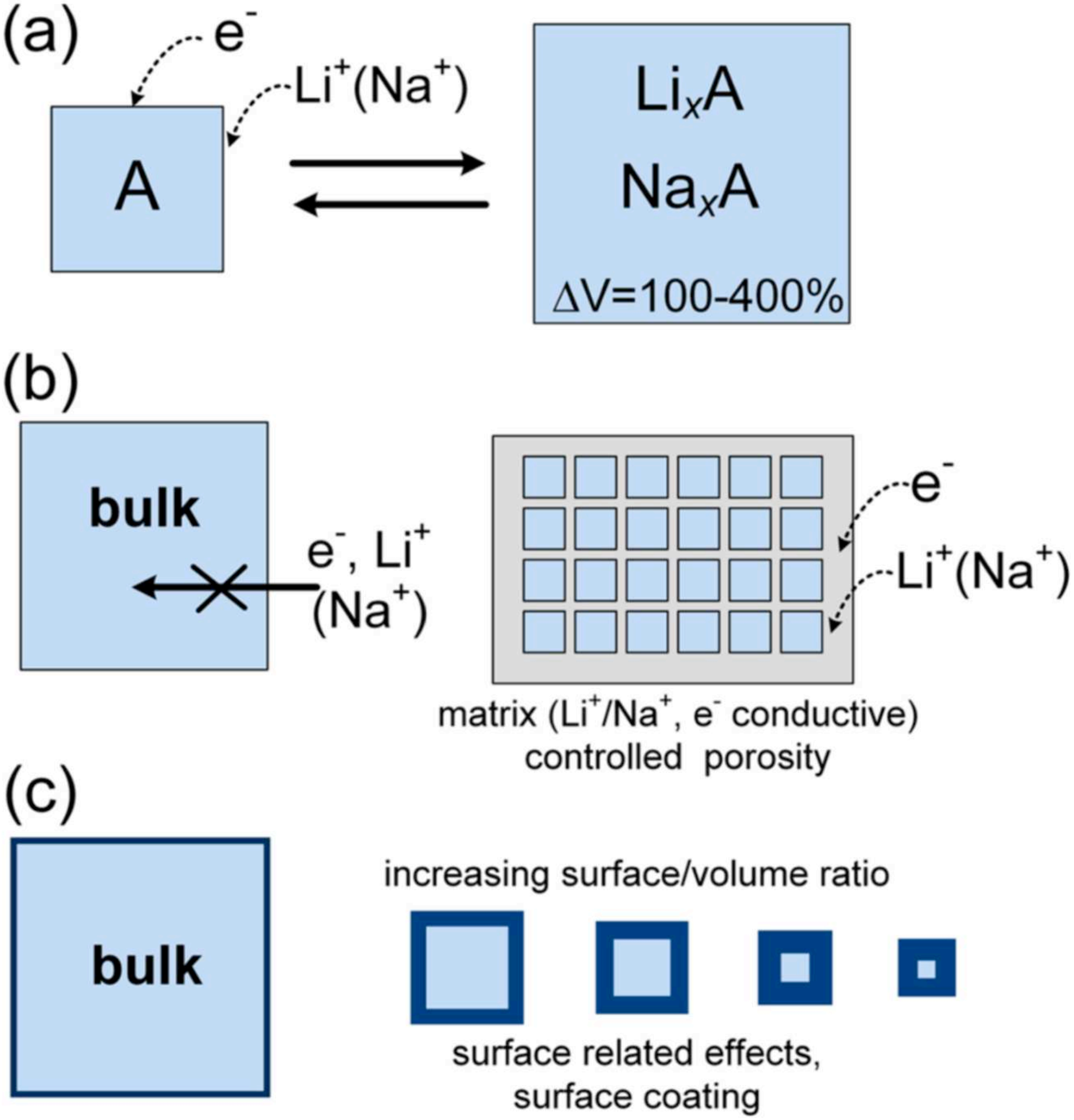

Figure 5.3: Major effects of downsizing on the electrochemical performance of electrode materials. (a) Volumetric changes associated with insertion and removal of the alkali ions become less detrimental and better accommodated; (b) poor ionic/electronic conductors become usable when prepared as a nanocomposite in a conductive matrix; (c) increased surface-to-volume ratio improves the kinetics of Li/Na insertion/removal, enhances other surface-related phenomena (e.g., modifies electrochemical potential), and allows efficient interfacing with other components or surface coating. However, detrimental processes such as excessive consumption of electrolytes for the formation of SEI layer and reactions of electrode materials with electrolytes are often enhanced as well. This figure is reproduced from Ref. [13] with permission of the American Chemical Society.

To quantify the efficacy of passivation by the SEI and its influence on reversibility and cycle lifetime of new electrode materials, an electrode’s coulombic efficiency (CE) value is commonly reported. The value represents what fraction of the charge passed is reversible on any given charge-discharge cycle of an electrode. Typically, an electrode’s CE value is low (<95%) on its first cycle and nominally rises to values close to 100% over the next few cycles as the SEI is formed and passivates the electrode surface to prevent side reactions. The maximum steady state CE value and the number of cycles it takes to reach that value are reflective of how well passivating the SEI is and plays a major role in the cycle lifetime of the electrode. The Dahn research group has demonstrated that high precision measurements of a cell’s CE and charge transfer resistance (measured using electrochemical impedance spectroscopy) can be used to predict its cycle lifetime [14]. They also show that electrolyte additives can work synergistically to improve a cell’s cycle lifetime by increasing its CE to extremely high values, reflecting the additives’ ability to make the electrodes’ reactions highly reversible.

As mentioned before, electrolyte additives that assist in the formation of well-passivating SEI layers are largely responsible in improving the cycle lifetimes of not only Li-ion batteries but also batteries with next generation electrodes. With continually advanced analytical techniques, researches have been able to identify chemical and structural bases for how specific electrolyte additives are beneficial for SEI formation. The Grey research group in particular has used solid state NMR to elucidate the role of electrolyte additives such as vinylene carbonate (VC) and fluoroethylene carbonate (FEC) in SEI formation in Li-ion batteries [7,15,16]. In particular, they find that additives like VC and FEC can even be effective on mechanically dynamic electrode materials like Si in a Li-ion battery. Figure 5.4 shows that the additives assist in the formation of a cross-linked polymeric SEI that selectively allows only Li-ions to access

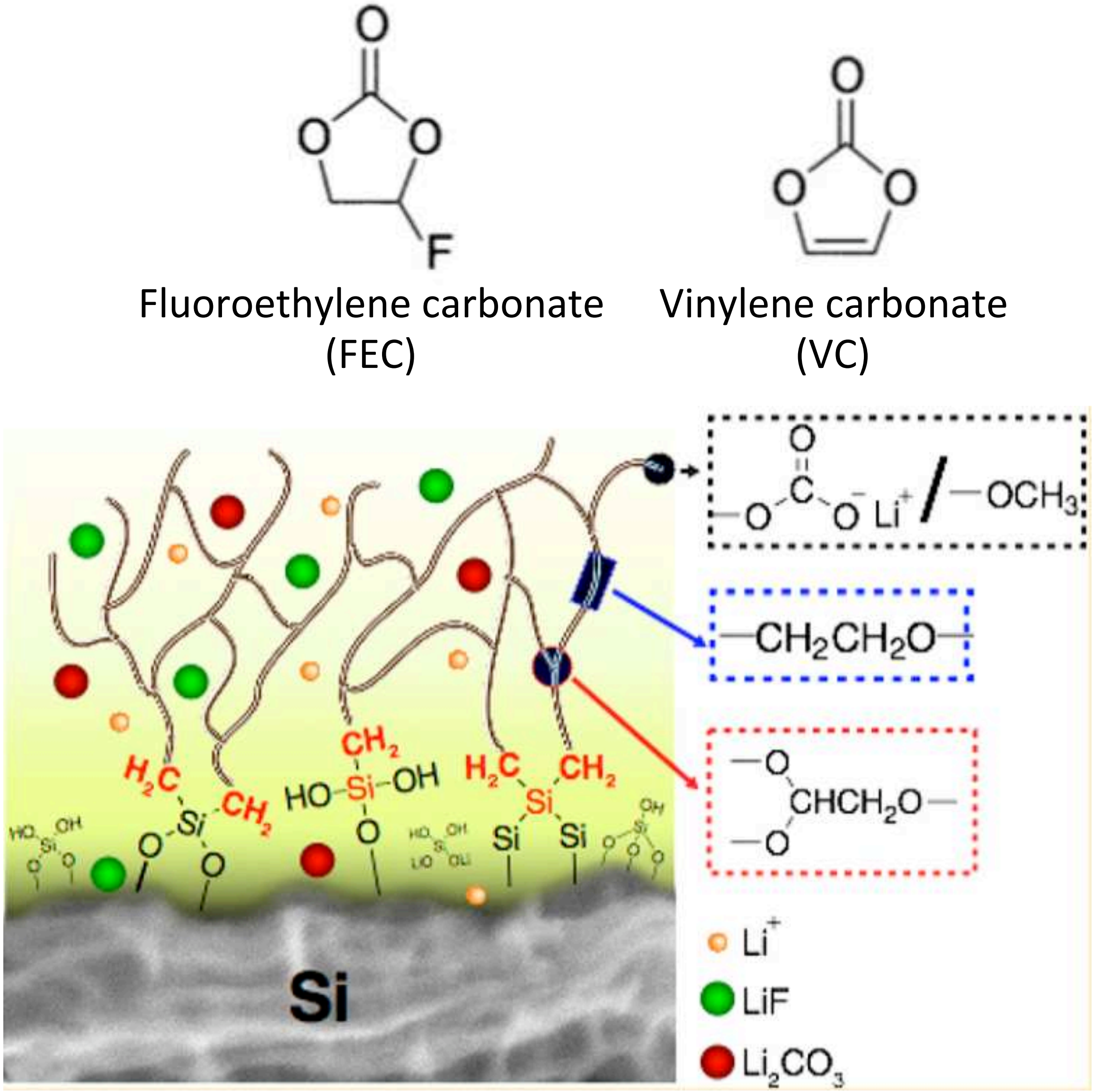

Figure 5.4: The addition of electrolyte additives such as fluoroethylene carbonate (FEC) and vinylene carbonate (VC) extend cell cycle lifetime by forming crosslinked polymeric solid-electrolyte-interface layers that better mechanically and chemically passivate electrode surfaces. This figure is adapted from Ref. [15] with permission of the American Chemical Society.

the Si active material while being mechanically robust enough to handle the large volume changes of the Si active material. Knowing that mechanical integrity is a requirement for the SEI layers on mechanically dynamic electrodes, electrolyte additives and even artificial SEI layers (electrode coatings) can be designed to impart such mechanical robustness.

Electrode coatings can be designed to be mechanically robust in addition to exhibiting the selective ion conductivity that the SEI typically provides. Recently, there have been a number of reports that utilize the thermally induced self-cyclization reaction of polyacrylonitrile (PAN) to make cyclized PAN (cPAN) electrode coatings. The structure of cPAN shown in Figure 5.5 has shown success in mitigating the mechanical instability of Si alloy anodes in Li-ion batteries while maintaining their reversible electroactivity [17]. Similarly, a cPAN based coating has also shown success in enabling the reversible operation of a Mg-metal anode in a Mg-ion battery [18]. In both cases the cPAN coatings enable the performance of the Si and Mg-metal electrodes by simultaneously providing the necessary ion conductivity and the mechanical strength to accommodate their volume changes and dynamically changing surfaces. Unlike a chemically passivating SEI, cPAN coatings are electronically conducting, making the formation of an in-situ formed SEI layer at their interface with the electrolyte still necessary. However, the mixed conducting (ionic and electronic) nature of cPAN coatings makes them a unique interfacial material in all-solid-state batteries.

All-solid-state batteries are thought of as the ultimate safety upgrade for many rechargeable battery technologies. If liquid electrolytes typically made with flammable solvents can be substituted with non-flammable solid electrolytes that have sufficiently high ionic conductivities and appropriate mechanical properties, safety issues associated with internal shorts and thermal runaway of batteries can be eliminated. Figure 5.6 shows the recently reported

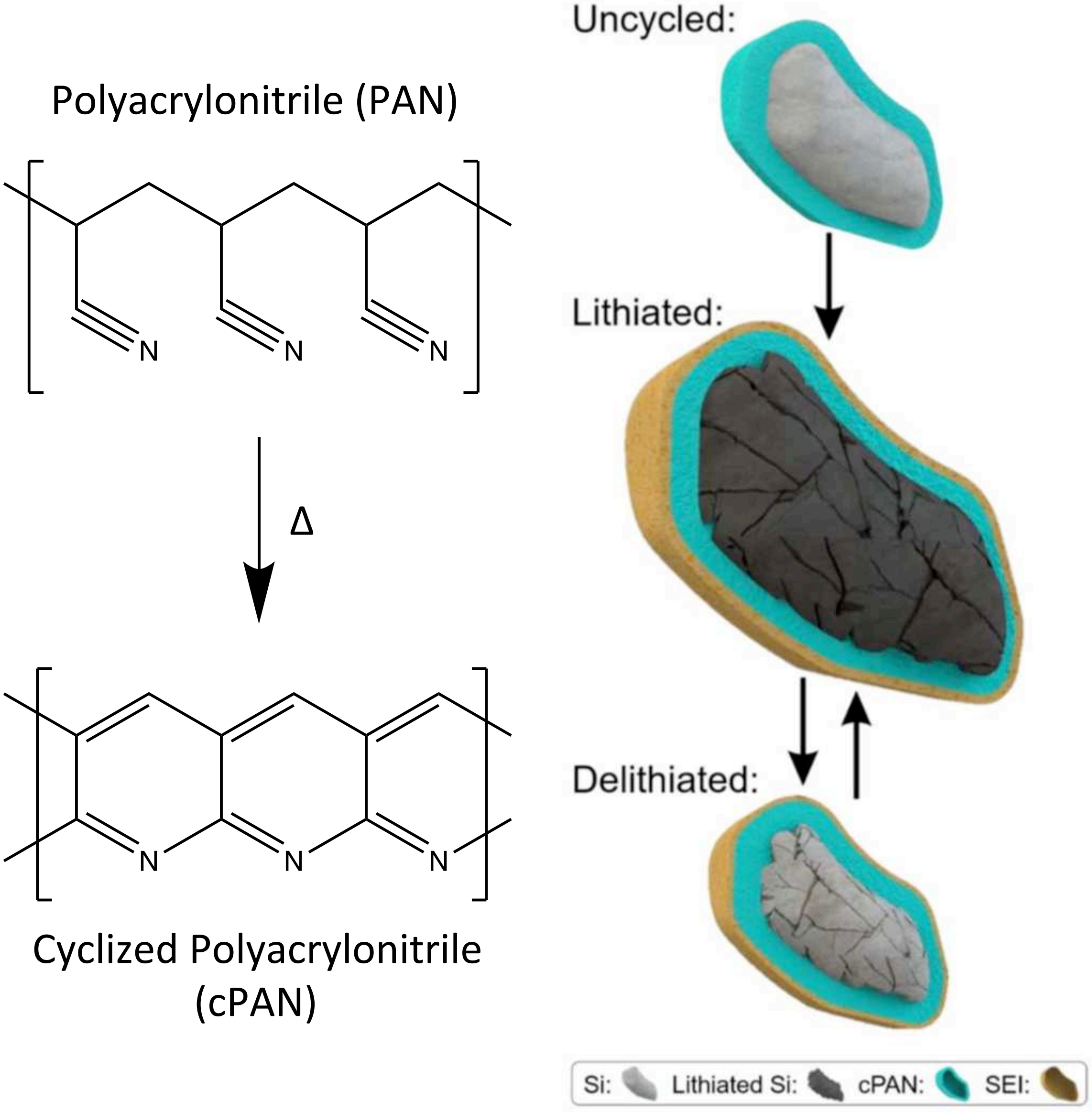

Figure 5.5: Polyacrylonitrile (PAN) annealed under inert atmosphere undergoes a self-cyclization reaction to form cyclized-PAN (cPAN) that has been shown as an effective electrode coating that mechanically stabilizes and contains large volume change particles while still maintaining the transport properties required for the particle to reversible store ions. This figure is adapted from Ref. [17] with permission of the electrochemical Society.

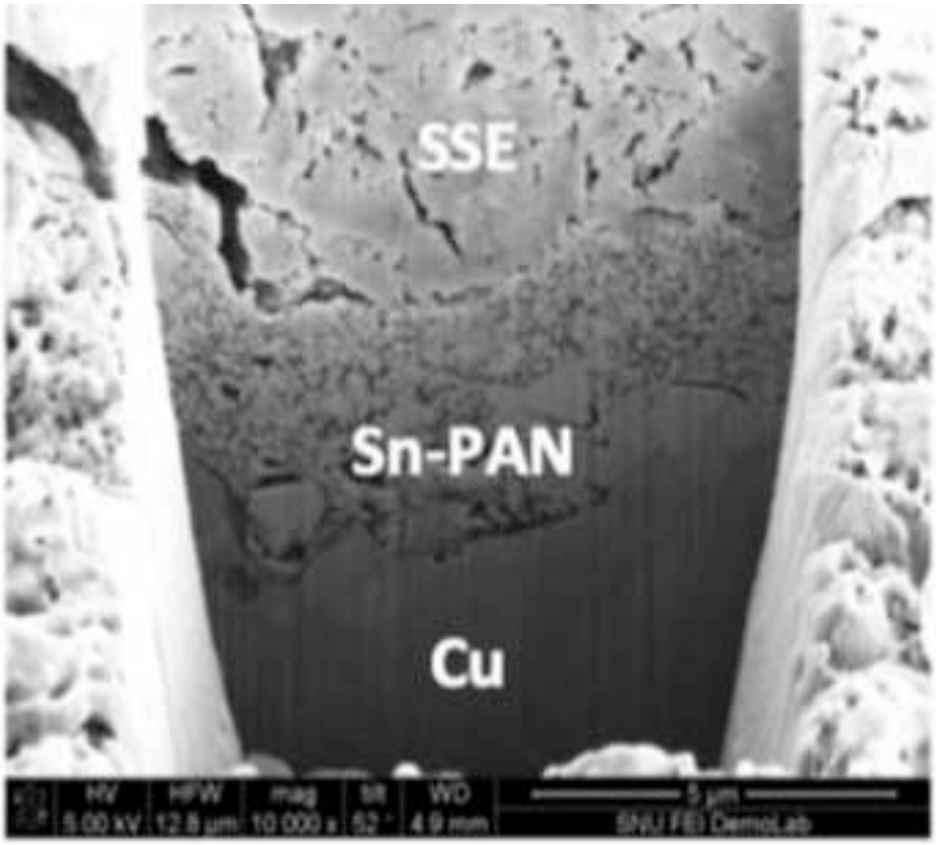

Figure 5.6: An all-solid-state battery using cPAN as a mixed-conducting matrix that the Sn electrode active material particles are embedded in. Amorphous 77.5 Li_2S - 22.5 P_2S_5 sulfide is used as the solid-state electrolyte. This figure is adapted from Ref. [19] with permission of the Electrochemical Society.

electron microscope image of an all-solid-state Li-ion battery using a Sn alloying anode and an amorphous glass solid electrolyte [19]. As mentioned previously, this particular design is enabled by embedding the Sn active material particles in a mixed conducting matrix of cPAN, again demonstrating the utility of interfacial coatings. While there are many known solid electrolytes, the continued discovery of solid electrolytes with high ion conductivities at ambient temperature could benefit the development of all-solid-state batteries. Additionally, while the solid-liquid electrolyte interface is eliminated in all-solid-state batteries, the chemical and mechanical stability of the electrode-electrolyte interface is still a challenge that needs to be considered [20]. For example, the migrations of Fe^{2+} from an $LiFePO_4$ cathode into a solid electrolyte has been observed [21], necessitating the development of interfacial layers that can chemically stabilize these solid-solid interfaces, such as the boron-nitride utilized in an all-solid-state Li-metal battery [22].

Conclusions

The retrospective examination of the chemical factors that have made Li-ion batteries so successful helps to inform the design of materials for next generation batteries. Figure 5.7 outlines what we believe to be the most impactful classes of battery materials that have been studied over the past decade and that should continue to be pursued by the research community. The materials specifically address the unstable chemical and mechanical interfaces of next generation electrode materials with both liquid and solid electrolytes. Electrolyte additives have proven their worth in extending the cycle lifetimes of Li-ion batteries while more recently demonstrating benefits to the cycle lifetime of high capacity Li-ion battery anodes. The ability of the electrolyte additives to extend cycle lifetimes by producing more mechanically and chemically robust SEI layers also inspires the development of “artificial SEI” layers as electrode

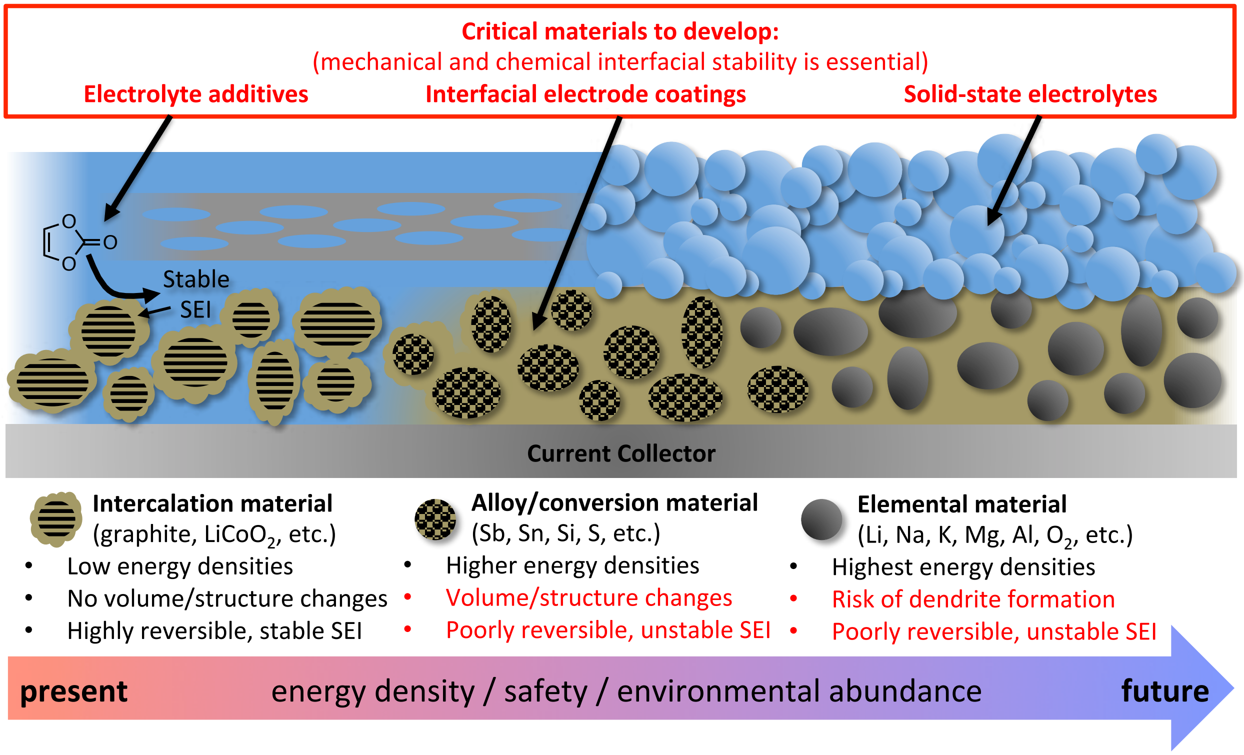

Figure 5.7: As batteries transition to using more abundant electrode materials that can result in higher energy densities, the design of the battery needs to evolve as well. Unstable interfaces between electrodes and electrolytes will need to be addressed with new and better electrolyte additives, electrode coatings, and solid electrolytes. The effective development and implementation of these critical materials would lead to affordable batteries that exhibit high safety factors, high energy densities, and long cycle lifetimes.

coatings. The use of electrode coatings to alleviate mechanical degradation of high capacity Si anodes in Li-ion batteries as well as enable the reversible operation of Mg-metal batteries demonstrates that such coatings can be invaluable for next generation electrode materials. Finally, solid-state electrolytes present yet another approach to enabling the use of high energy density metallic anodes while eliminating the flammability hazards of rechargeable batteries. The chemical and mechanical stability of material interfaces in all-solid-state batteries remains as important if not more important to consider and address than in cells with liquid electrolytes. Despite the significant challenges highlighted herein, the successful development of next generation batteries with new chemistries only requires that each of the cell components are carefully chosen to result in favorable interactions with each other, as was done to result in the advent of the Li-ion battery.

CHAPTER 5 REFERENCES

[1] R. Schmuch, R. Wagner, G. Hörpel, T. Placke, M. Winter, Performance and cost of materials for lithium-based rechargeable automotive batteries, Nature Energy. (2018) 1–12. doi:10.1038/s41560-018-0107-2.

[2] M. Winter, B. Barnett, K. Xu, Before Li ion batteries, Journal of Chemical Education. 23 (2018) 11433–11456. doi:10.1021/acs.chemrev.8b00422.

[3] B. Nykvist, M. Nilsson, Rapidly falling costs of battery packs for electric vehicles, Nature Clim Change. 5 (2015) 329–332. doi:10.1038/nclimate2564.

[4] T.M. Gür, Review of electrical energy storage technologies, materials and systems: challenges and prospects for large-scale grid storage, Energy Environ. Sci. 11 (2018) 2696–2767. doi:10.1039/C8EE01419A.

[5] J.B. Goodenough, K.-S. Park, The Li-Ion Rechargeable Battery: A Perspective, J. Am. Chem. Soc. 135 (2013) 1167–1176. doi:10.1021/ja3091438.

[6] F.A. Soto, Y. Ma, J.M.M. de la Hoz, J.M. Seminario, P.B. Balbuena, Perla, Formation and growth mechanisms of solid-electrolyte interphase layers in rechargeable batteries, Chem. Mater. 27 (2015) 7990–8000. doi:10.1021/acs.chemmater.5b03358.

[7] A.L. Michan, B.S. Parimalam, M. Leskes, R.N. Kerber, T. Yoon, C.P. Grey, et al., Fluoroethylene Carbonate and Vinylene Carbonate Reduction: Understanding Lithium-Ion Battery Electrolyte Additives and Solid Electrolyte Interphase Formation, Chem. Mater. 28 (2016) 8149–8159. doi:10.1021/acs.chemmater.6b02282.

[8] Q. Pang, X. Liang, C.Y. Kwok, L.F. Nazar, Review—The Importance of Chemical Interactions between Sulfur Host Materials and Lithium Polysulfides for Advanced Lithium-Sulfur Batteries, J. Electrochem. Soc. 162 (2015) A2567–A2576. doi:10.1149/2.0171514jes.

[9] C.-X. Zu, H. Li, Thermodynamic analysis on energy densities of batteries, Energy Environ. Sci. 4 (2011) 2614–11. doi:10.1039/c0ee00777c.

[10] M.N. Obrovac, V.L. Chevrier, Alloy Negative Electrodes for Li-Ion Batteries, Chem. Rev. 114 (2014) 11444–11502. doi:10.1021/cr500207g.

[11] M. Winter, Abundance in Earth's Crust, WebElements.com. (2007). https://web.archive.org/web/20070309033534/http://www.webelements.com/webelements/properties/text/image-flash/abund-crust.html (accessed June 19, 2019).

[12] E.A. Olivetti, G. Ceder, G.G. Gaustad, X. Fu, Lithium-Ion Battery Supply Chain Considerations: Analysis of Potential Bottlenecks in Critical Metals, Joule. 1 (2017) 229–243. doi:10.1016/j.joule.2017.08.019.

[13] M.F. Oszajca, M.I. Bodnarchuk, M.V. Kovalenko, Precisely Engineered Colloidal Nanoparticles and Nanocrystals for Li-Ion and Na-Ion Batteries: Model Systems or Practical Solutions? Chem. Mater. 26 (2014) 5422–5432. doi:10.1021/cm5024508.

[14] J.C. Burns, A. Kassam, N.N. Sinha, L.E. Downie, L. Solnickova, B.M. Way, et al., Predicting and Extending the Lifetime of Li-Ion Batteries, J. Electrochem. Soc. 160 (2013) A1451–A1456. doi:10.1149/2.060309jes.

[15] Y. Jin, N.-J.H. Kneusels, L.E. Marbella, E. Castillo-Martínez, P.C.M.M. Magusin, R.S. Weatherup, et al., Understanding Fluoroethylene Carbonate and Vinylene Carbonate Based Electrolytes for Si Anodes in Lithium Ion Batteries with NMR Spectroscopy, J.

Am. Chem. Soc. 140 (2018) 9854–9867. doi:10.1021/jacs.8b03408.

[16] Y. Jin, N.-J.H. Kneusels, P.C.M.M. Magusin, G. Kim, E. Castillo-Martínez, L.E. Marbella, et al., Identifying the Structural Basis for the Increased Stability of the Solid Electrolyte Interphase Formed on Silicon with the Additive Fluoroethylene Carbonate, J. Am. Chem. Soc. 139 (2017) 14992–15004. doi:10.1021/jacs.7b06834.

[17] A. Heist, D.M. Piper, T. Evans, S.C. Kim, S.S. Han, K.H. Oh, et al., Self-Contained Fragmentation and Interfacial Stability in Crude Micron-Silicon Anodes, J. Electrochem. Soc. 165 (2018) A244–A250. doi:10.1149/2.0811802jes.

[18] S.B. Son, T. Gao, S.P. Harvey, K.X. Steirer, A. Stokes, A. Norman, et al., An artificial interphase enables reversible magnesium chemistry in carbonate electrolytes, Nature Chemistry. 10 (2018) 532–539. doi:10.1038/s41557-018-0019-6.

[19] N.A. Dunlap, J. Kim, K.H. Oh, S.-H. Lee, Slurry-Coated Sheet-Style Sn-PAN Anodes for All-Solid-State Li-Ion Batteries, J. Electrochem. Soc. 166 (2019) A915–A922. doi:10.1149/2.0151906jes.

[20] W.D. Richards, L.J. Miara, Y. Wang, J.C. Kim, G. Ceder, Interface stability in solid-state batteries, Chem. Mater. (2015) acs.chemmater.5b04082–28. doi:10.1021/acs.chemmater.5b04082.

[21] M.F. Groh, M.J. Sullivan, M.W. Gaultois, O. Pecher, K.J. Griffith, C.P. Grey, Interface Instability in LiFePO4–Li3+xP1–xSixO4 All-Solid-State Batteries, Chem. Mater. 30 (2018) 5886–5895. doi:10.1021/acs.chemmater.8b01746.

[22] Q. Cheng, A. Li, N. Li, S. Li, A. Zangiabadi, T.-D. Li, et al., Stabilizing Solid Electrolyte-Anode Interface in Li-Metal Batteries by Boron Nitride-Based Nanocomposite Coating, Joule. (2019). doi:10.1016/j.joule.2019.03.022.

APPENDIX A – CRITICAL CORRESPONDENCE WITH ANDY MARTINOLICH

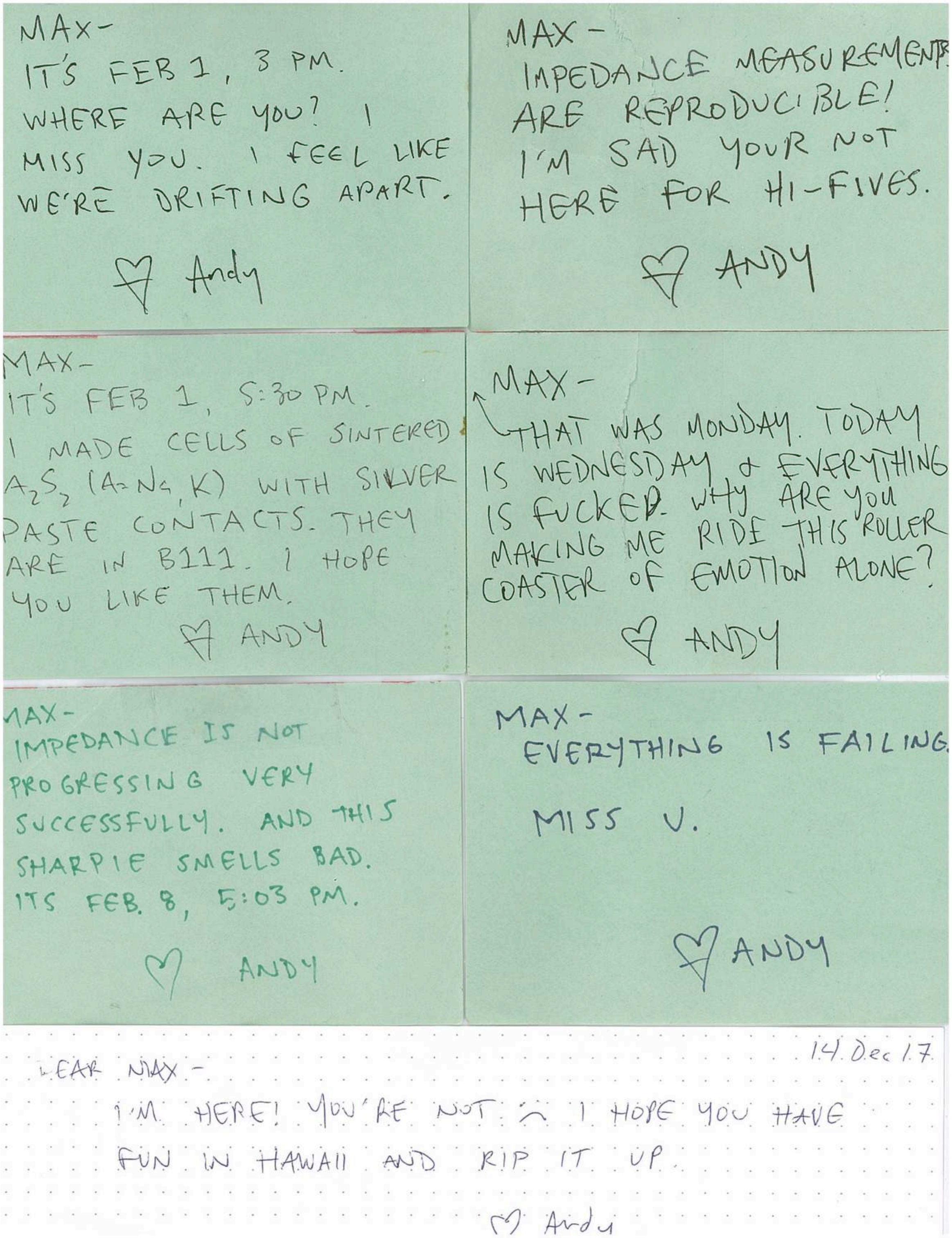

MAX -
IT'S FEB 1, 3 PM.
WHERE ARE YOU? I
MISS YOU. I FEEL LIKE
WE'RE DRIFTING APART.

♡ Andy

MAX -
IMPEDANCE MEASUREMENTS
ARE REPRODUCIBLE!
I'M SAD YOUR NOT
HERE FOR HI-FIVES.

♡ ANDY

MAX -
IT'S FEB 1, 5:30 PM.
I MADE CELLS OF SINTERED
A_2S_2 (A=Na, K) WITH SILVER
PASTE CONTACTS. THEY
ARE IN B111. I HOPE
YOU LIKE THEM.

♡ ANDY

↑ MAX -
THAT WAS MONDAY. TODAY
IS WEDNESDAY & EVERYTHING
IS FUCKED. WHY ARE YOU
MAKING ME RIDE THIS ROLLER
COASTER OF EMOTION ALONE?

♡ ANDY

MAX -
IMPEDANCE IS NOT
PROGRESSING VERY
SUCCESSFULLY. AND THIS
SHARPIE SMELLS BAD.
ITS FEB. 8, 5:03 PM.

♡ ANDY

MAX -
EVERYTHING IS FAILING.

MISS U.

♡ ANDY

---

14. Dec 17.

DEAR MAX -
I'M HERE! YOU'RE NOT ☹ I HOPE YOU HAVE
FUN IN HAWAII AND RIP IT UP.

♡ Andy

APPENDIX B – PYTHON CODE USED TO CALCULATE ENERGY DENSITIES AND GENERATE FIGURE 1.2

Server Information:

You are using Jupyter notebook.

The version of the notebook server is **4.4.1** and is running on:

```
Python 3.5.2 |Enthought, Inc. (x86_64)| (default, Mar  2 2017, 08:29:05)  [GCC 4.2.1 Compatibl
e Apple LLVM 6.0 (clang-600.0.57)]
```

Current Kernel Information:

```
Python 3.5.2 |Enthought, Inc. (x86_64)| (default, Mar  2 2017, 08:29:05)  Type "copyright", "cre
dits" or "license" for more information.  IPython 5.6.0 -- An enhanced Interactive Python. ?
-> Introduction and overview of IPython's features. %quickref -> Quick reference. help      -> Pyt
hon's own help system. object?   -> Details about 'object', use 'object??' for extra details.
```

```
import matplotlib.pyplot as plt
import numpy as np
from pylab import figure
from pylab import rcParams
from itertools import cycle
import matplotlib

CC_t=15 #thickness of current collectors in um
Sep_t=20 #thickness of separator in um

#Parameters for the LiCoO2 (LCO) cathode
LCO_V=3.9 #voltage of cathode (V vs. Li/Li+)
LCO_Qg=150 #gravimetric capacity (mAh/g)
LCO_Qv=150*5.05 #volumetric capactiy (mAh/cm3)
LCO_t=55 #Thickness in um
LCO_Vfrac=0.7 #Volume fraction
LCO_Qa=(LCO_Vfrac*LCO_Qv*LCO_t)/10000 #arreal capacity (mAh/cm2)
AC_ratio=1.1 #ratio of anode to cathode

#Parameters for the various anode materials
C_V=.125 #voltage of electrode (V vs. Li/Li+)
C_Qg=372 #gravimetric capacity of electrode (mAh/g)
C_Qv=791 #volumetric capacity of electrode (mAh/cm3)

Sb_V=.948
```

```
Sb_Qg=660
Sb_Qv=1771

Sn_V=.504
Sn_Qg=993
Sn_Qv=2111

Si_V=.4
Si_Qg=3579
Si_Qv=2194

Li_V=0
Li_Qg=0
Li_Qv=2058

#Other parameters
D_Cu = 8.96 #density of copper current collector (g/cm3)
D_Al = 2.7 #density of aluminum current collector (g/cm3)
D_PP = 0.855 #density of polypropylene (g/cm3)
Vfrac_PP = 0.6 #volume fraction of porous polypropylene separator
MM_Li = 6.941 #molar mass of Li (g/mol)
MM_LiCoO2 = 97.87 #molar mass of LiCoO2 (g/mol)

anodes = [
    [C_V,C_Qg,C_Qv],
    [Sb_V,Sb_Qg,Sb_Qv],
    [Sn_V,Sn_Qg,Sn_Qv],
    [Si_V,Si_Qg,Si_Qv],
    [Li_V,Li_Qg,Li_Qv]
                     ]

MVfrac=np.arange(0,1.01,0.01) #list of mass or volume fraction ranging from 0 to 1

matplotlib.rcParams.update({'font.size': 14})
FullCellStack = figure(figsize=(18,5))
labels = cycle(['Graphite','Antimony','Tin','Silicon','Lithium'])

#Calculate and plot the gravimetric energy densities
gravimetric = FullCellStack.add_subplot(121)

#Calculations for all anodes except Li-metal
for anode in anodes[:-1]:
    A_m=(AC_ratio*LCO_Qa)/(MVfrac*anode[1])   #mass of anode (g/cm2)
```

```
    A_E=2*LCO_Qa*(LCO_V-anode[0])/(2*(A_m+(LCO_Qa/LCO_Qg)) #energy (Wh) divided
by mass of electrodes
                              +CC_t/10000*(D_Cu+D_Al) #mass of current collectors (g)
                              +Sep_t/10000*D_PP*Vfrac_PP) #mass of separators (g)
    gravimetric.plot(MVfrac,A_E,label=next(labels))

#Calculations for Li-metal anode
anode = anodes[-1]
A_E=2*LCO_Qa*(LCO_V-anode[0])/(2*((LCO_Qa/LCO_Qg)*(1-(MM_Li/(MM_LiCoO2*2)))
#energy (mWh) divided by mass of cathode minus half of Li (g)
                              +(LCO_Qa/LCO_Qg)*(MM_Li/(MM_LiCoO2*2))/MVfrac ) #mass of Li on
anode side + excess (g)
                              +CC_t/10000*(D_Cu+D_Al) #mass of current collectors (g)
                              +Sep_t/10000*D_PP*Vfrac_PP) #mass of separators (g)
gravimetric.plot(MVfrac,A_E,label=next(labels))

#Formatting plot
plt.hlines(250,0,1,label='''Baseline (250 Wh/kg)''',linestyle=':')
plt.title('Gravimetric Energy Density')
plt.ylabel('Stack Energy (Wh/kg)')
plt.xlabel('Mass-fraction of active material in anode')
plt.legend()

#Calculate and plot the volumetric energy densities
volumetric = FullCellStack.add_subplot(122)
for anode in anodes:
    A_t=(AC_ratio*LCO_Qa)/(MVfrac*anode[2])*10000 #thickness of anode (um)
    A_E=2*LCO_Qa*(LCO_V-anode[0])*10000/(2*(CC_t+Sep_t+A_t+LCO_t)) #energy (Wh/L)
    volumetric.plot(MVfrac,A_E,label=next(labels))

#Formatting plot
plt.hlines(750,0,1,label='''Baseline (750 Wh/L)''',linestyle=':')
plt.title('Volumetric Energy Density')
plt.ylabel('Stack Energy (Wh/L)')
plt.xlabel('Volume-fraction of active material in anode')
plt.legend()
plt.show()
```

APPENDIX C – ALL CYCLIC VOLTAMMERTY DATA DISCUSSED IN FIGURE 4.9

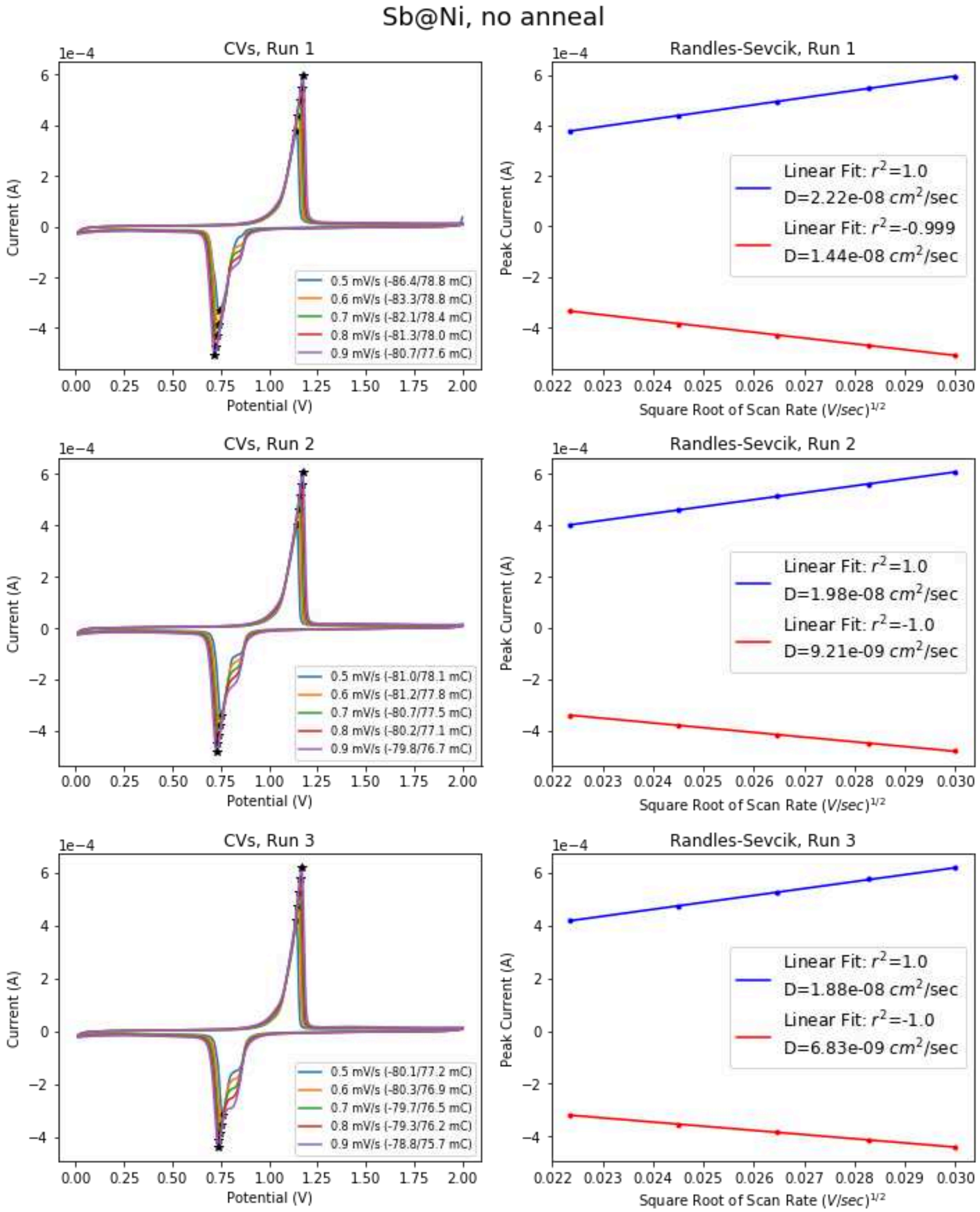

Figure C.1: Variable rate CVs of the uncoated and unannealed Sb@Ni electrode with the corresponding bottleneck diffusivities calculated using the Randles-Sevcik equation.

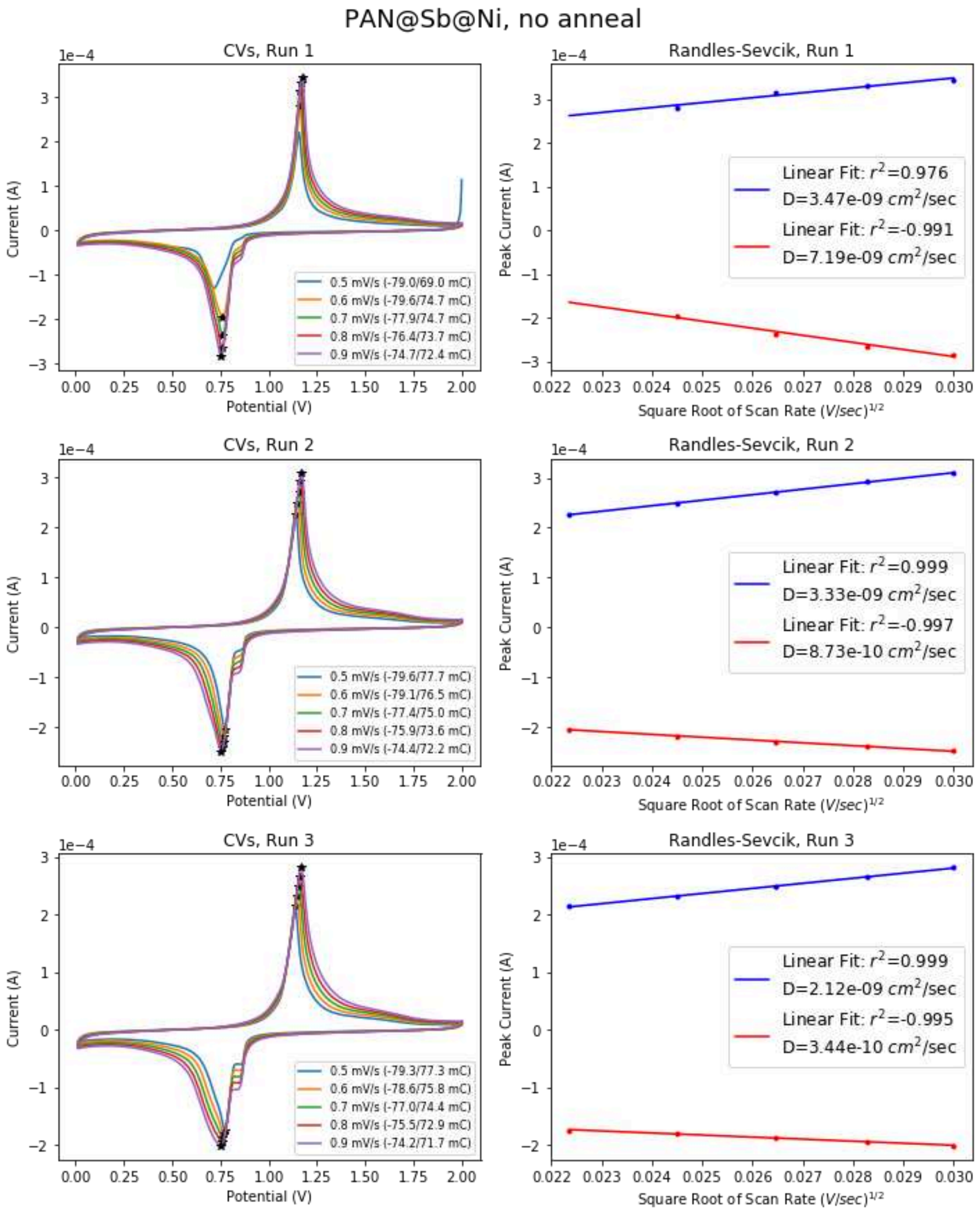

Figure C.2: Variable rate CVs of the unannealed PAN@Sb@Ni electrode with the corresponding bottleneck diffusivities calculated using the Randles-Sevcik equation.

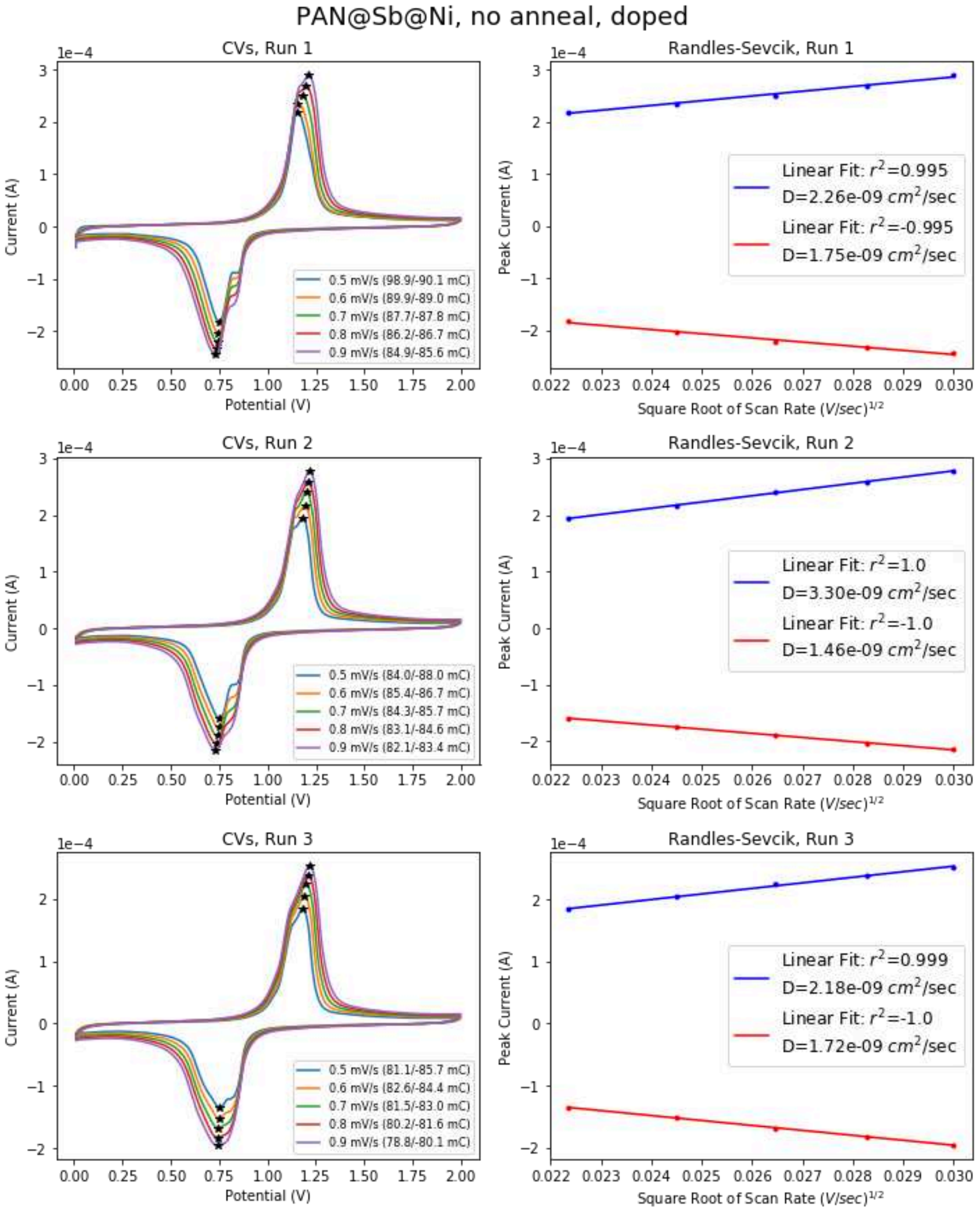

Figure C.3: Variable rate CVs of the unannealed and doped (shorted) PAN@Sb@Ni electrode with the corresponding bottleneck diffusivities calculated using the Randles-Sevcik equation.

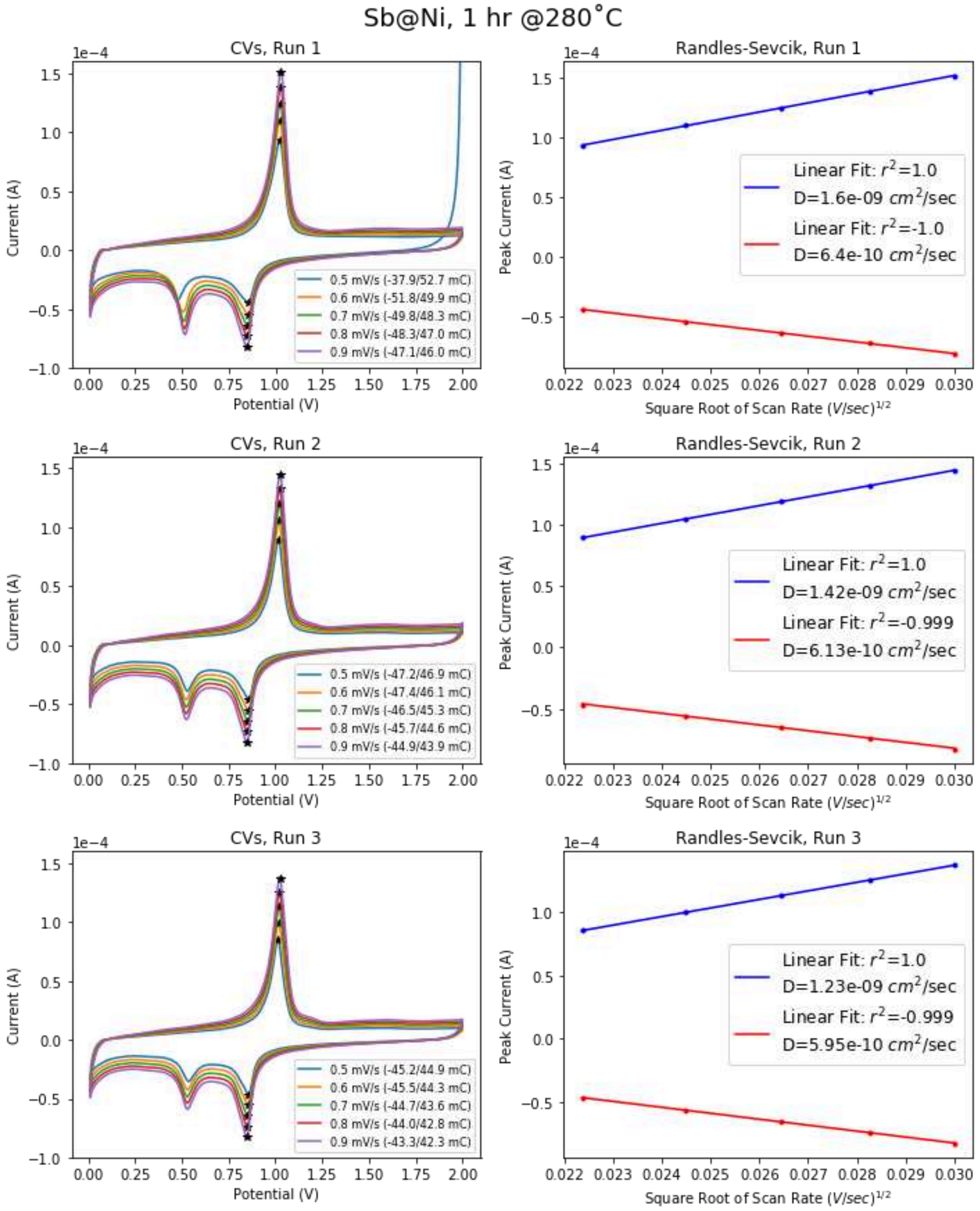

Figure C.4: Variable rate CVs of the uncoated and 1 hour annealed Sb@Ni electrode with the corresponding bottleneck diffusivities calculated using the Randles-Sevcik equation.

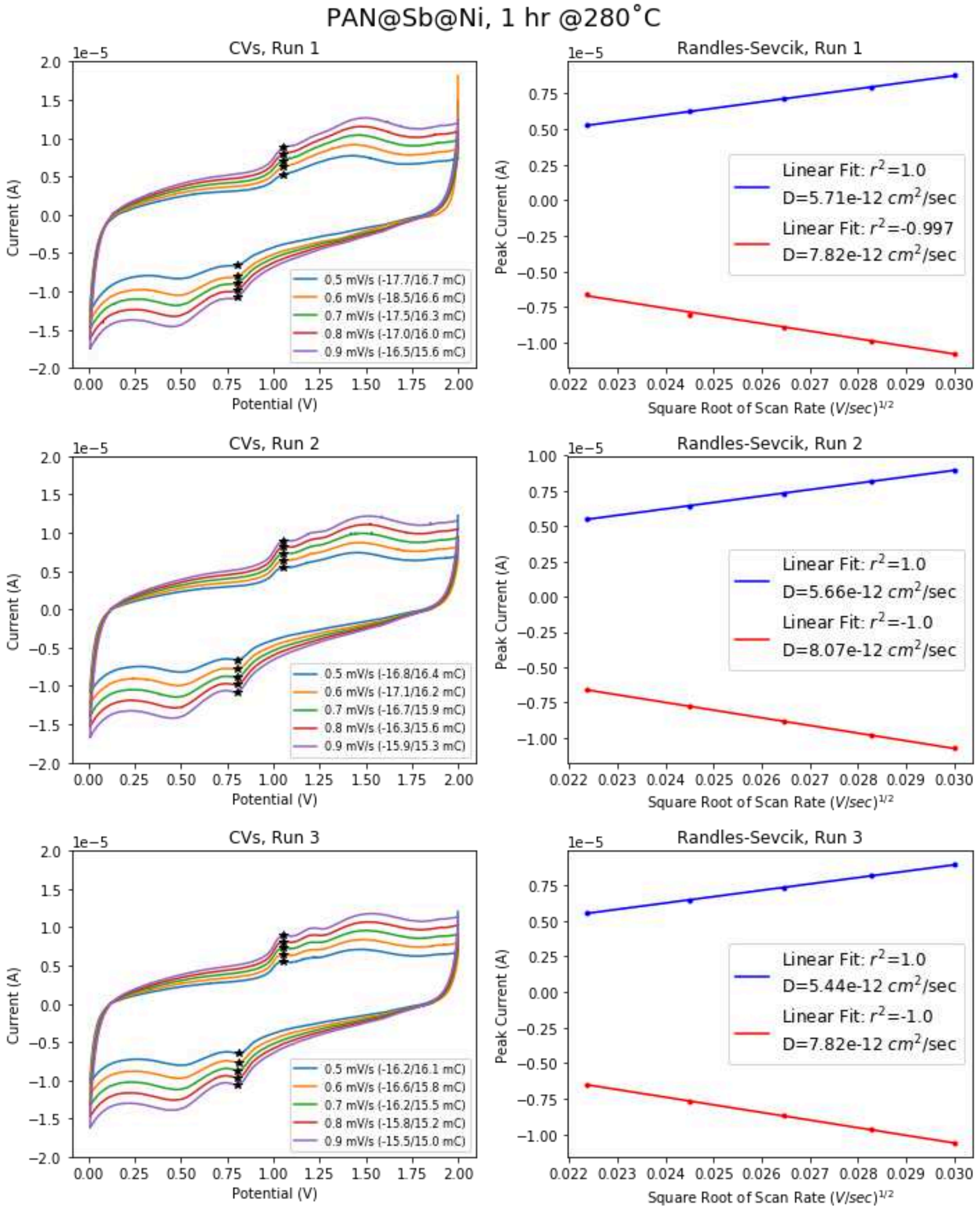

Figure C.5: Variable rate CVs of the 1 hour annealed PAN@Sb@Ni electrode with the corresponding bottleneck diffusivities calculated using the Randles-Sevcik equation.

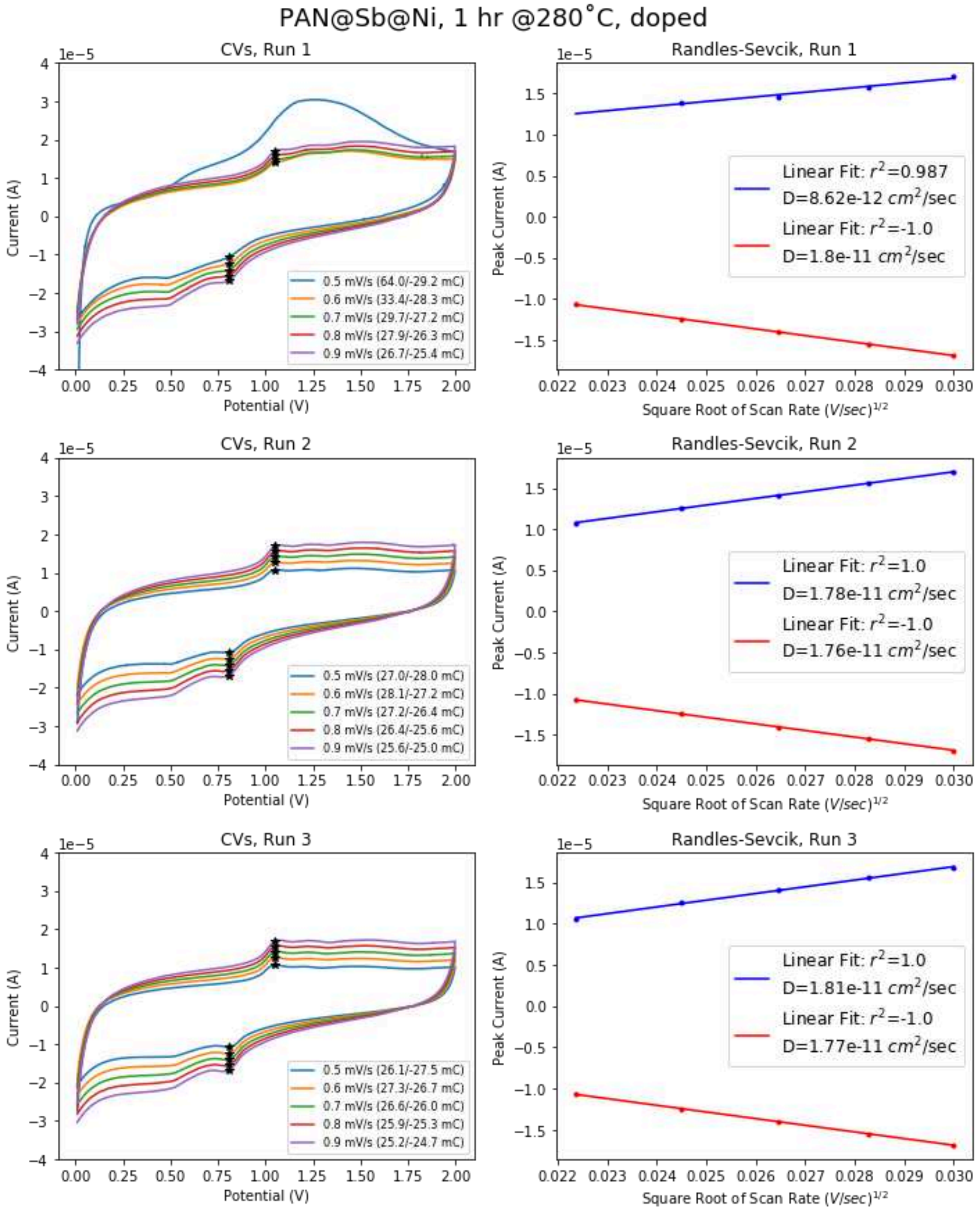

Figure C.6: Variable rate CVs of the 1 hour annealed and doped (shorted) PAN@Sb@Ni electrode with the corresponding bottleneck diffusivities calculated using the Randles-Sevcik equation.

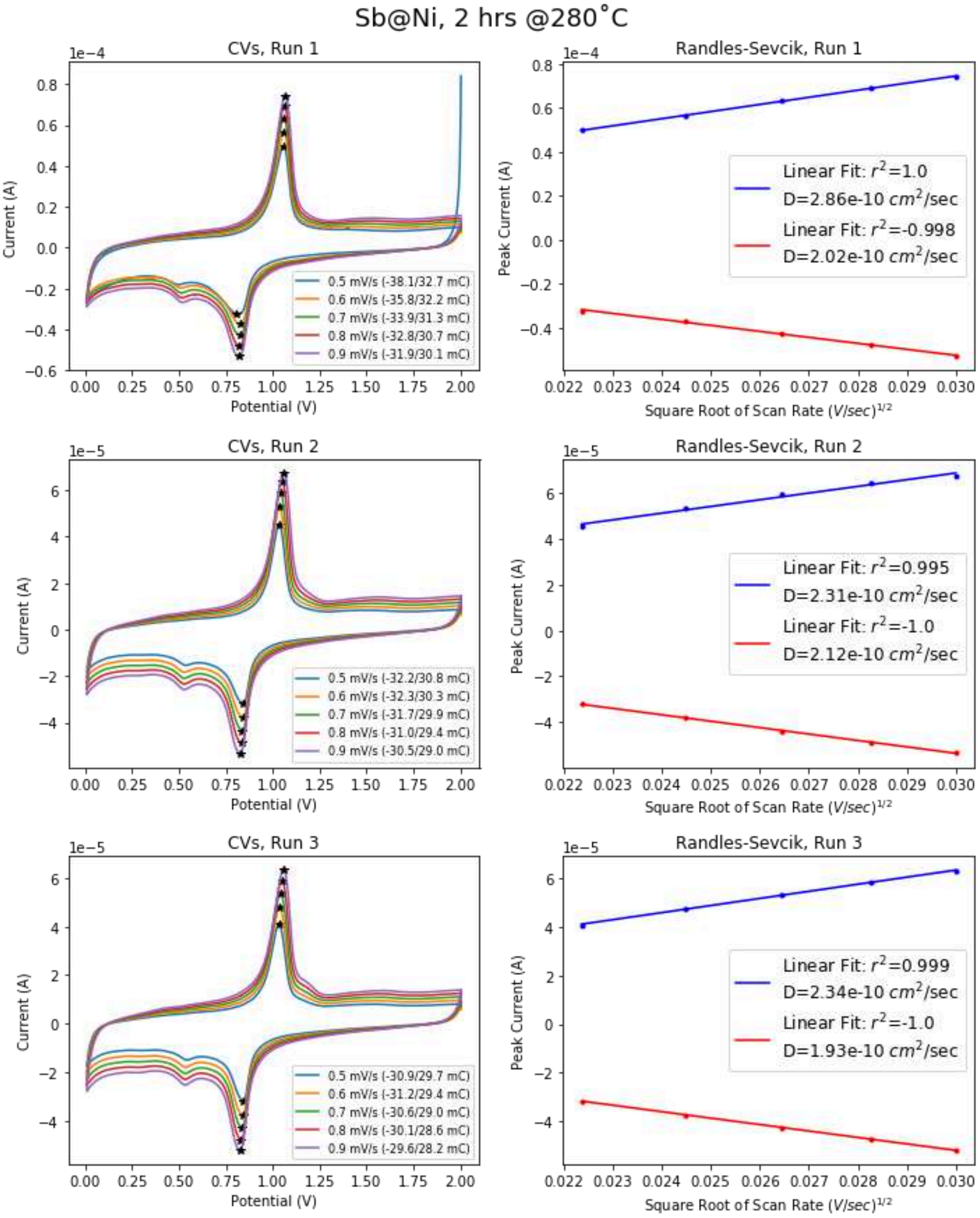

Figure C.7: Variable rate CVs of the uncoated and 2 hour annealed Sb@Ni electrode with the corresponding bottleneck diffusivities calculated using the Randles-Sevcik equation.

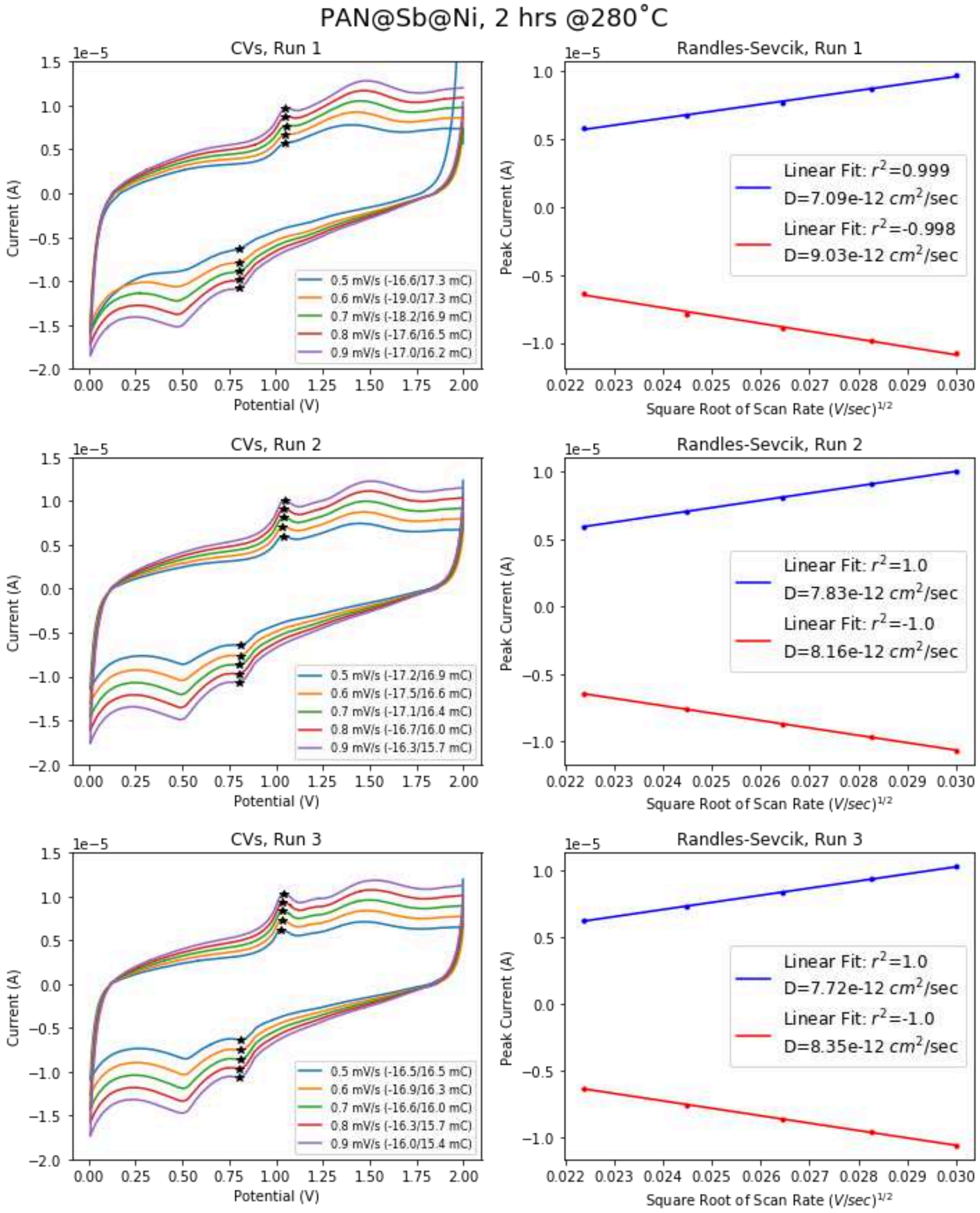

Figure C.8: Variable rate CVs of the 2 hour annealed PAN@Sb@Ni electrode with the corresponding bottleneck diffusivities calculated using the Randles-Sevcik equation.

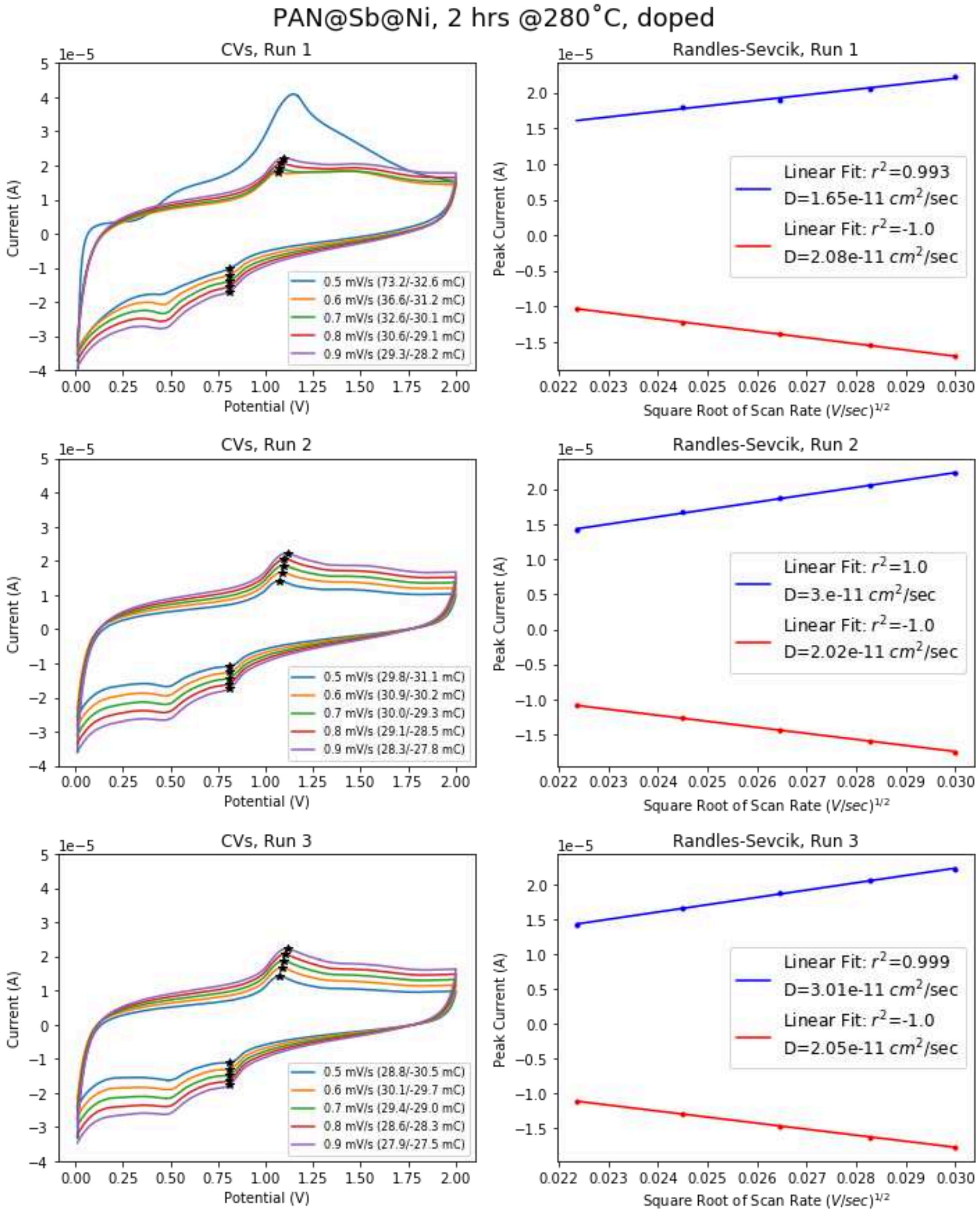

Figure C.9: Variable rate CVs of the 2 hour annealed and doped (shorted) PAN@Sb@Ni electrode with the corresponding bottleneck diffusivities calculated using the Randles-Sevcik equation.

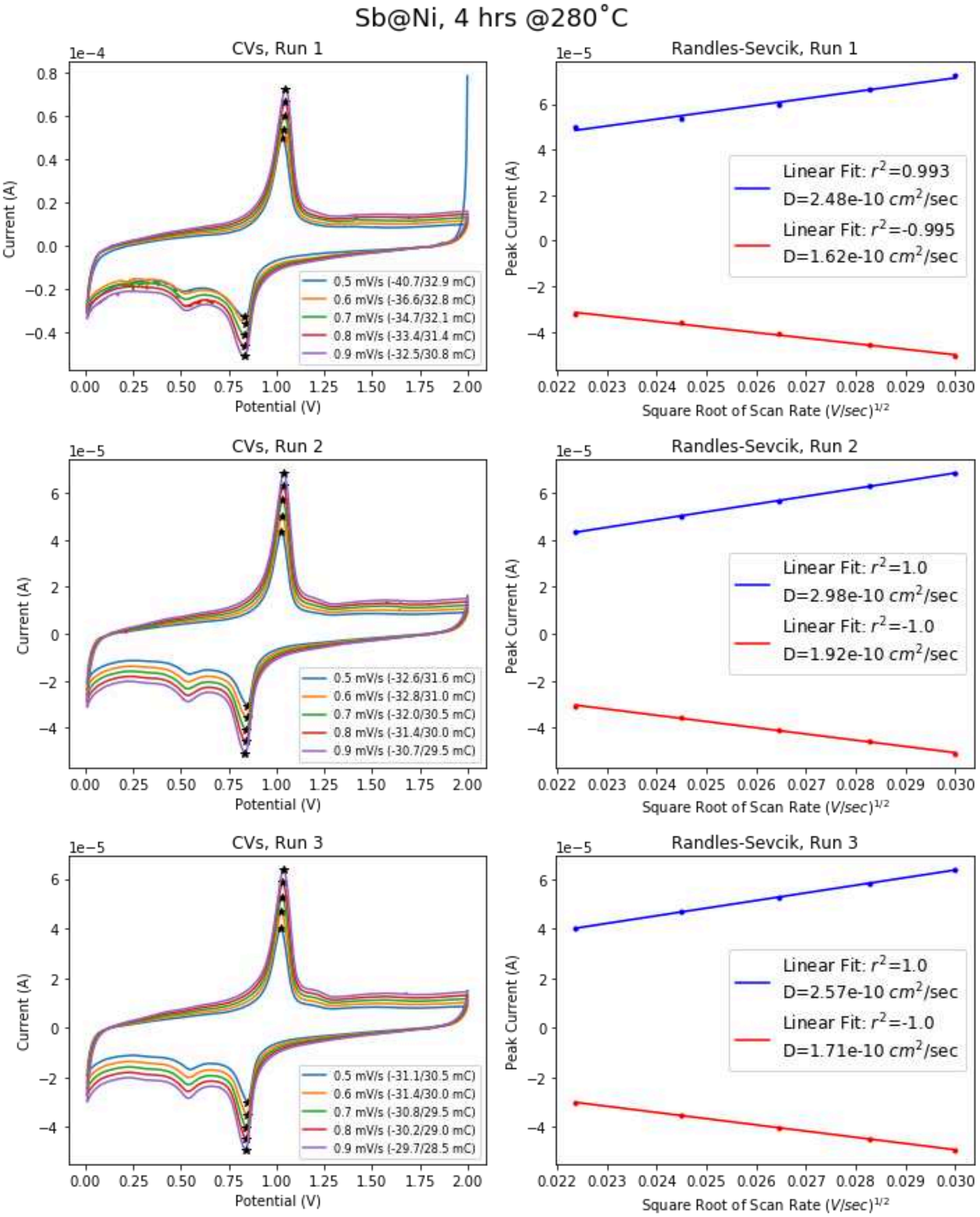

Figure C.10: Variable rate CVs of the uncoated and 4 hour annealed Sb@Ni electrode with the corresponding bottleneck diffusivities calculated using the Randles-Sevcik equation.

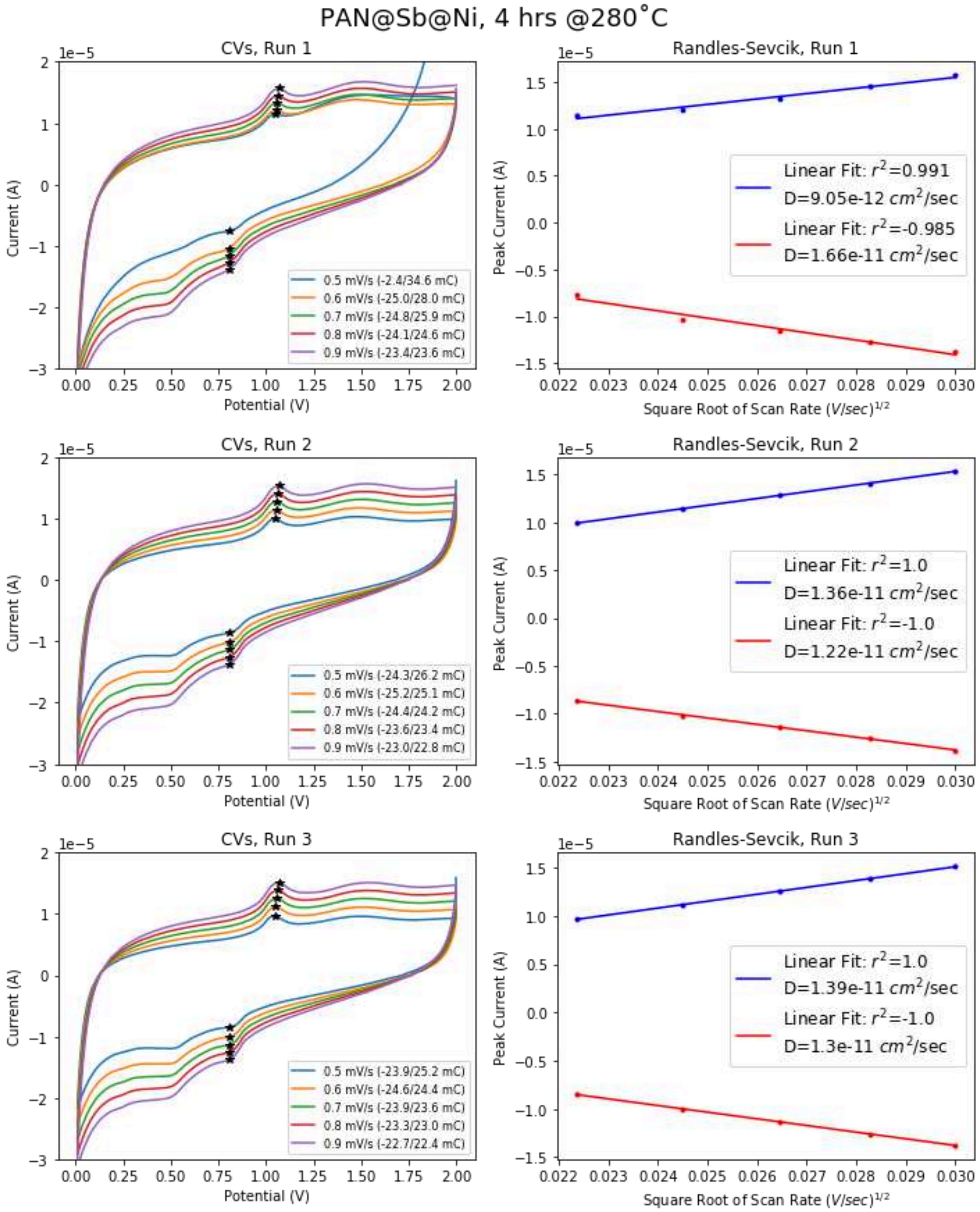

Figure C.11: Variable rate CVs of the 4 hour annealed PAN@Sb@Ni electrode with the corresponding bottleneck diffusivities calculated using the Randles-Sevcik equation.

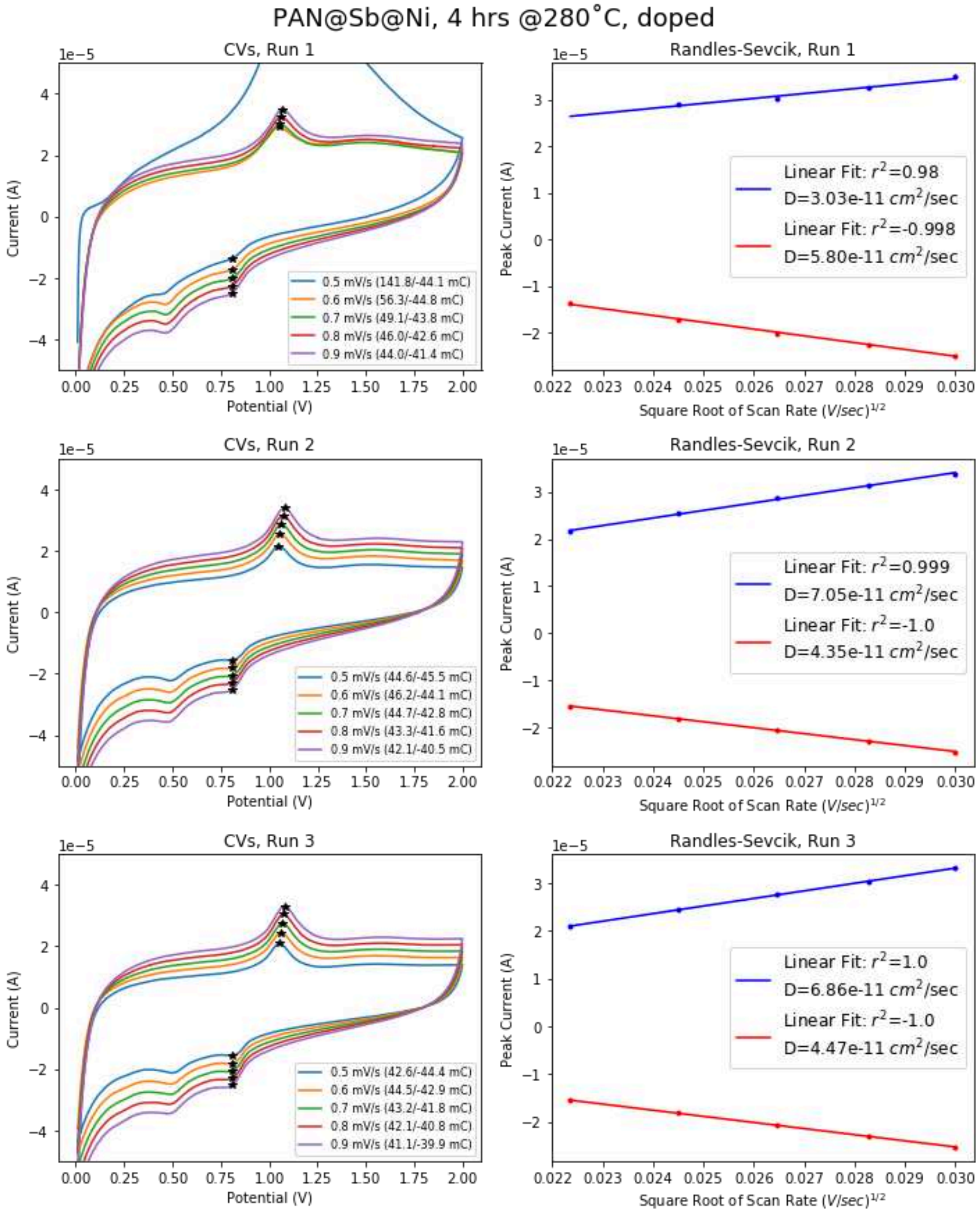

Figure C.12: Variable rate CVs of the 4 hour annealed and doped (shorted) PAN@Sb@Ni electrode with the corresponding bottleneck diffusivities calculated using the Randles-Sevcik equation.

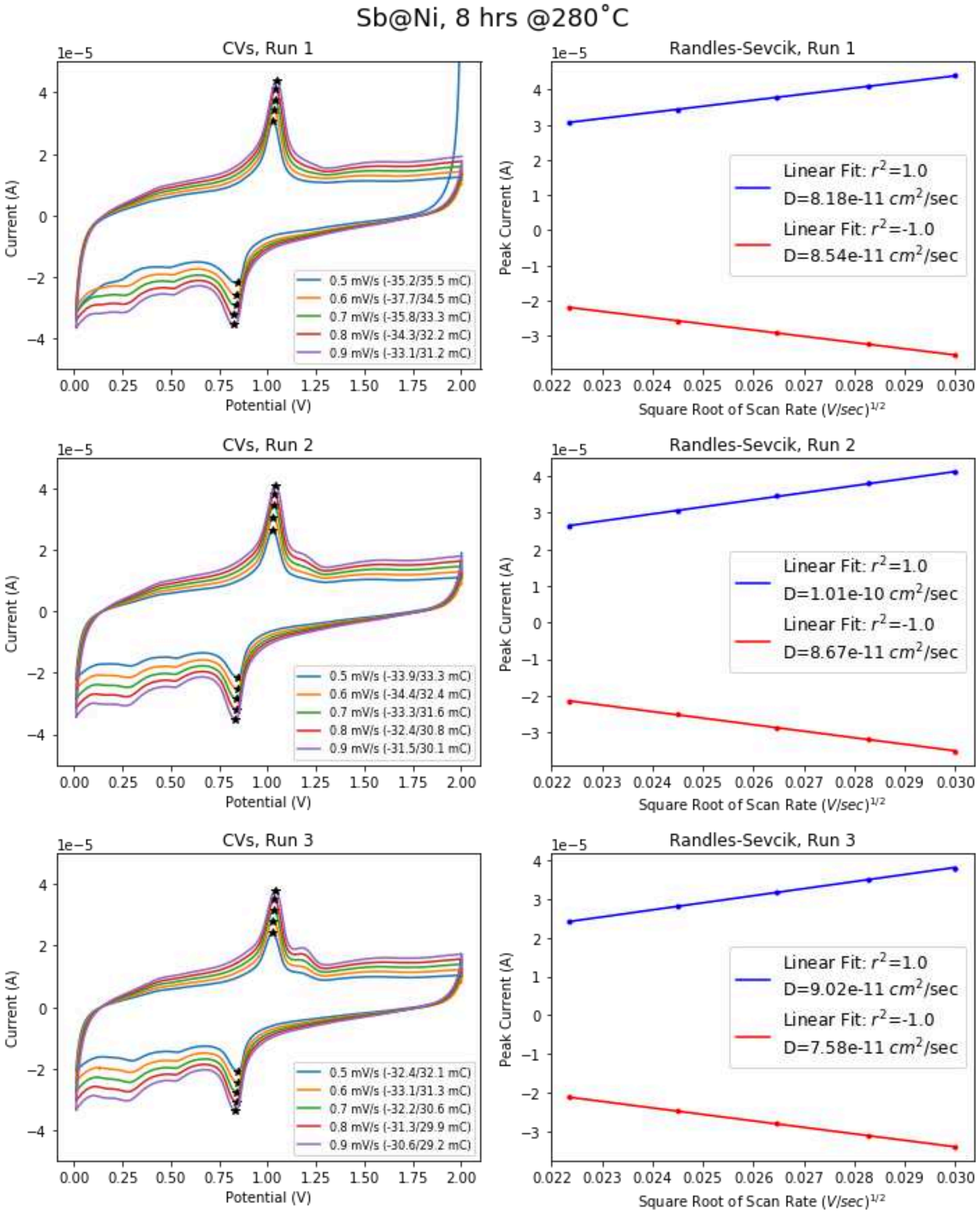

Figure C.13: Variable rate CVs of the uncoated and 8 hour annealed Sb@Ni electrode with the corresponding bottleneck diffusivities calculated using the Randles-Sevcik equation.

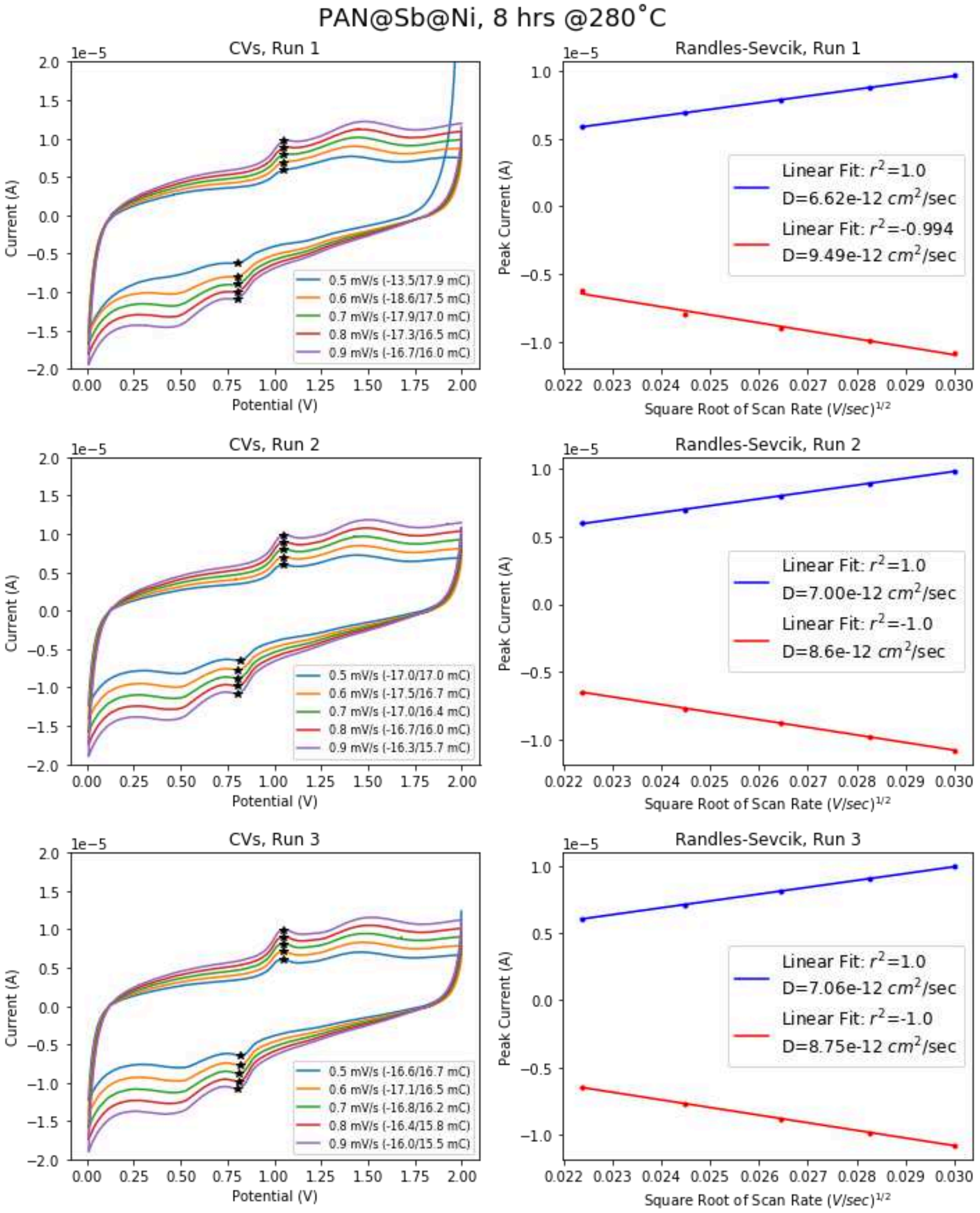

Figure C.14: Variable rate CVs of the 8 hour annealed PAN@Sb@Ni electrode with the corresponding bottleneck diffusivities calculated using the Randles-Sevcik equation.

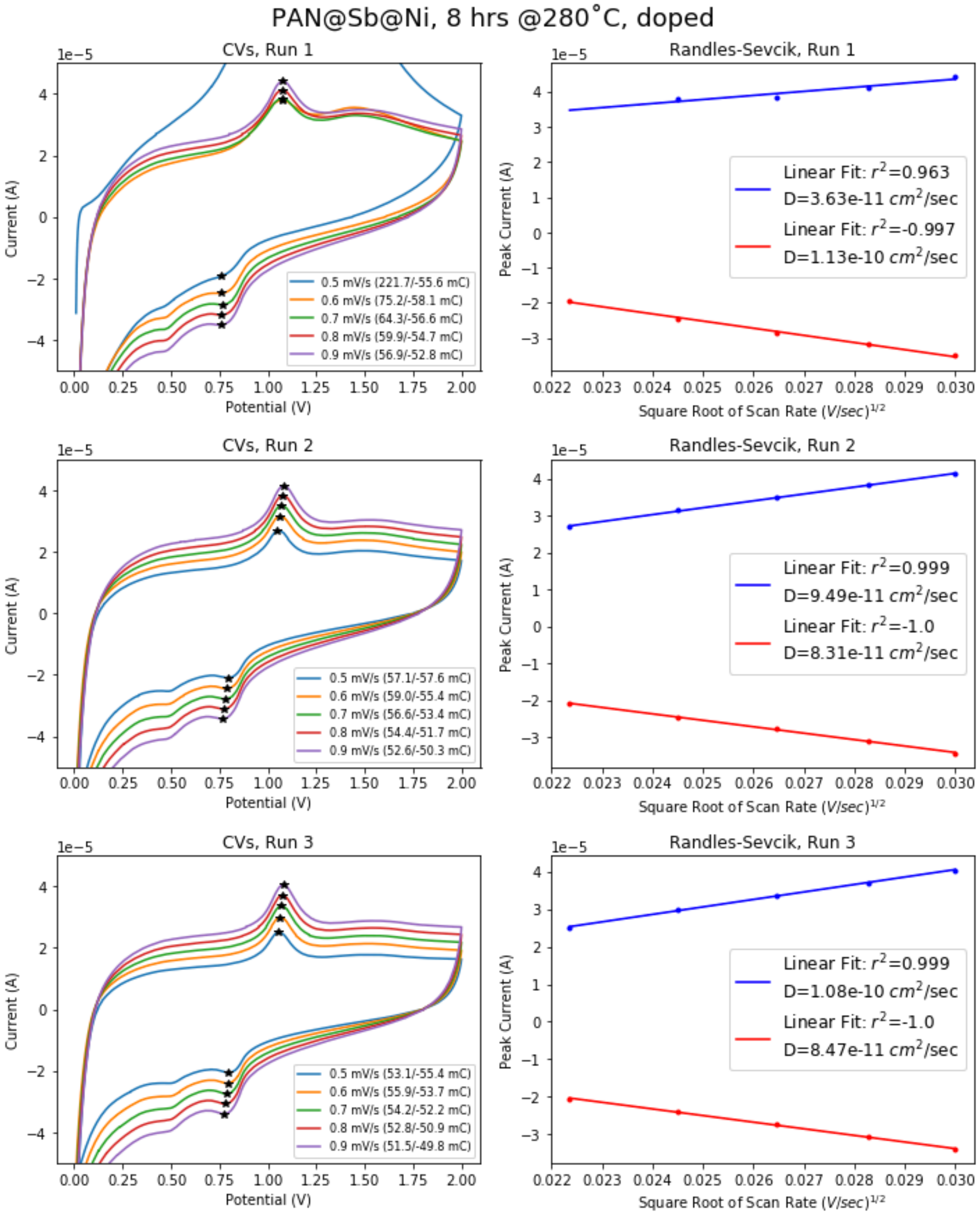

Figure C.15: Variable rate CVs of the 8 hour annealed and doped (shorted) PAN@Sb@Ni electrode with the corresponding bottleneck diffusivities calculated using the Randles-Sevcik equation.

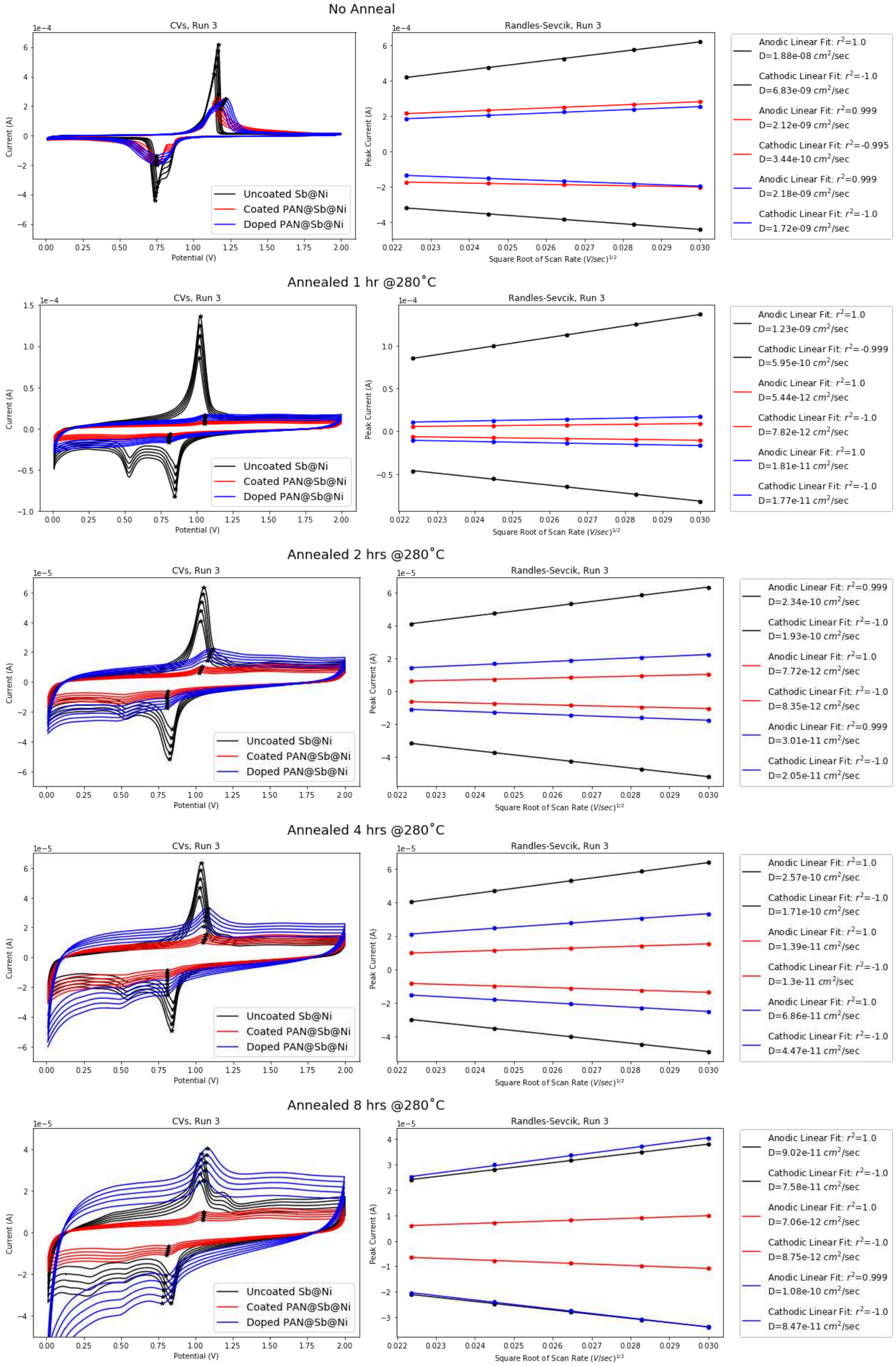

Figure C.16: Variable rate CVs of all electrodes with the corresponding bottleneck diffusivities calculated using the Randles-Sevcik equation.

APPENDIX D – PYTHON LEARNING WORKSHEET AND USEFUL SCRIPTS

Python Tutorial Introduction

This tutorial was compiled by Max Schulze to teach the basics of Python coding to other members of the Prieto research lab such that they could import, process, and plot battery and other research related data. The complete tutorial is a folder with worksheet-style Jupyter notebooks along with some associated data files. By working through the tutorial, hopefully anybody with no prior coding experience can learn the basic of how to code in Python, as well as apply that code to some practically relevant processing and plotting of some battery data that is commonly collect in the Prieto research group.

The main tutorial worksheet is a Jupyter notebook "*Python Tutorial.ipynb*" that was adapted by Max from a document obtained from Jamie Neilson and checked for correctness with help from Chris Rom. The Jupyter notebook can be treated like a worksheet for learning Python and its data processing and plotting capabilities. It walks you through basic ideas behind coding by explaining what bits of code do before and after you run them. In places, it will prompt you to try filling in places left intentionally blank. There are answers filled in to these portions in the "*Answers.ipynb*" document should you get stuck. While it is hopefully detailed enough that you should be able to work through it on your own, working through it with another person familiar with Python will probably be more effective.

Because the whole point of using code is to save you time on your data processing and to make sweet looking figures, several codes that were used in the production of this dissertation (often in adapted forms) are included in the Jupyter notebook *"Useful Codes for Battery Data.ipynb"*. Feel free to use them as you will. Take them and modify them as much as you'd like to fit your specific application. They can likely be modified to be useful on non-battery related data. If you learn something cool that improves the code or does something new and cool, share it with others that might also be able to use it!

This appendix includes the content of the “*Python Tutorial.ipynb*” and *“Useful Codes for Battery Data.ipynb”* Jupyter notebooks as well as the output figures for the latter. Max or other members of the Prieto research lab can make the entire tutorial available upon request.

Python Tutorial.ipynb

Learning the basics of programming with python

Hello world! This is a good way to test the simple input/output. The "print" function is also an invaluable tool for checking and troublshooting script as you're writing it, as you'll see later. Click your cursor into the box below and press shift+return together to run the code.

```
print("hello world")
```

Throughout this workbook, sections of code will contain comments to help explain and clarify what the code does. Comments are denoted by a "#" and will change the color of any text in the same line after it. "Commented" text will not be run when the code is run, so it can be useful for "commenting out" sections of code that you don't want to run instead of deleting them entirely. Try running the following code as an example:

```
print('This is code so it will be run')

#This is not code so it won't be displayed

print('Comments can even be in the same line as code') #Like this!
```

Single-element variables

Python is an object based programming language, so you can name variables anything you want and connect them to any type of object. Below, let's attach an object known as a STRING (a sequence of letters or words) to a variable that we'll name "squirrel", then test to see if the assignment was made:

```
squirrel = "I love pizza!"

print(squirrel)
```

Variables can also be attached to numbers as INTEGER or FLOAT type objects:

```
a = 2
```

```
b = 3
c = 2.
d = 3.
print(a,b,c,d)
```

The next thing to do is to try some simple math operations:

```
print(a+b)
print(c+d)
print(a/b)
print(c/d)
```

You've just illustrated the difference between an INTEGER and a FLOAT. An INTEGER is just that. If you input a number without a decimal point, Python will interpret it as an INTEGER. If you add a decimal, it will become a floating-point precision number. For the basic user, this just means that the number can be a fraction. However, for serious calculations, one has to pay attention to floating-point precision – the computer can store an irrational number to only a finite precision; it rounds off the rest. The errors due to round-off do matter in some instances. If you are working with very precise numbers, there are strategies that you can use to store more values to memory.

Python is extremely powerful and popular in its ability to hand and manipulate many types of objects and data types, including STRINGS (i.e., letters and words), but we will not cover that in this tutorial. However, we will cover the use of LIST, ARRAY, DICTIONARY, and DATAFRAME type objects. They will be the method by which we store data.

Keeping all these variables and object types straight can sometimes be confusing, but the "type()" command may help you troubleshoot:

```
print(type(a)) #'a' is an INTEGER
print(type(d)) #'d' is a FLOAT
```

Is it possible to reassign variables? Is it possible to add a string and a float?

Play around a bit with your own variable assignments and math operations to see:

Multi-element variables

In the above examples, each variable was assigned one value. Python is very powerful in its ability to handle a single datum as well as groups of data. Let us say we want to store a 3-D spatial coordinate (in a Cartesian reference) as a variable, r1 = (0.1, 0.2, 0.3) – the position is 0.1 along x, 0.2 along y, and 0.3 along z. Then, we want another coordinate, r2 = (0.4, −0.1, 0.0). We can load those coordinates into memory as a LIST of FLOATS:

```
r1 = [0.1, 0.2, 0.3]
r2 = [0.4, -0.1, 0.0]
```

If we want to call back the y value of the LIST r2, then we would type: r2[1] This recalls the 2nd ELEMENT in the LIST. In Python, we start counting at "0":

```
r2[1]
```

Sometimes, we might want to add LISTS, as if to add the vectors. If we perform the operation by adding the LISTS r1 and r2 directly, this does not work:

```
r1+r2
```

Python just catenates the LISTS end-to-end. That is not what we wanted! This is because LIST type objects are designed to behave this way, which are ideal for some operations.

If we wanted to add each FLOAT to a corresponding FLOAT in another LIST to make a new LIST, r3, then we need to add each element together individually, then assign each individual element to a place in memory in the computer:

```
r3 = [ r1[0]+r2[0], r1[1]+r2[1], r1[2]+r2[2] ] #combined into one line

r4 = [
   r1[0]+r2[0],
   r1[1]+r2[1],
   r1[2]+r2[2]
            ] #separated into multiple lines for clarity

print(r3)
print(r4)
```

However, that is way too tedious to type out over and over again, especially if you are trying to add data sets, each with 3000 data points. Instead, we should combine the addition with a logical operation: a “for loop”. A “for loop” says, for some variable in some sequence, do some operations:

```
for variable in sequence:

       Statement1  Statement2  ...  Statementn
```

Anything that we want to be looped over must be indented with the tab key. By thinking about what sequence we want to loop over, we can do some powerful operations.

Looping Statements

We can loop over the three ELEMENTS in the sequence [0,1,2] to perform the element-by-element addition of "r1" and "r2":

```
r5 = [0,0,0]  #Defines "r5" as a LIST with three ELEMENTS, zeroes will do as place holders

for index in [0,1,2]: #This tells Python to perform the indented operation with index=0, then index=1, then index=2
   r5[index] = r1[index] + r2[index]
   #This would be part of loop because it is indented
#This wouldn't be part of loop because it's not indented
```

```
print(r5) #This now has the same values of the list "r4" where we manually performed an element-by-element addition
```

If we want to perform an element-by-element addition over many more ELEMENTS without manually writing a sequence, we can use:

```
r6 = [1,1,2,3,5,8,13,21,24,45]
r7 = [5,6,7,8,9,0,1,2,3,4]
r8 = [0,0,0,0,0,0,0,0,0,0]

for index in range(len(r8)):    #The function "len(r8)" generates a sequence equal in length to the length of "r8"
    r8[index] = r6[index] + r7[index]    #"len(r8)" is equivalent to [0,1,2,3,4,5,6,7,8,9]

print(r8)
```

It loops through ten integers. This is because we told it to make a sequence from 0 to the length of r8, which was defined by len(r8). The next line is then indented with the tab key; the loop will perform every thing that is indented. Here, it will add each ELEMENT of r6 and r7, and assign it to the same ELEMENT index of r8.

It becomes a little tedious if you have to write a loop every time you want to manipulate a LIST. Since we plan on working with a lot of groups of numbers, we want to use a module in Python called, “numpy” (pronounced: numb pie). Numpy has many pre-defined routines for doing these types of options.

Using numpy

To load in the numpy module, we need to type in:

```
import numpy as np
```

Now, if we want to access a numpy command, we add the prefix, “np.*”. In numpy, there is a special type of object called a numpy ARRAY that has special properties that make doing some mathematical manipulations easier than with LISTS:

```
r1 = np.array([0.1, 0.2, 0.3])
r2 = np.array([0.4, -0.1, 0.0])
```

Now, "r1" and "r2" are numpy ARRAYS.

If we want to numerically add the ARRAYS, numpy knows to loop through each individual ELEMENT:

```
r3=r1+r2
print(r3)
```

Now, we can perform many mathematical operations on the two ARRAYS, in an element-by-element fashion:

```
print(r1-r2)          # subtraction
```

```
print(r1*3.0)         # multiplication by a scalar
print(r1**2)          # squaring
print(r1*r2)          # element-by-element multiplication
print(r2/r1)          # element-by-element division
print(3.0*r1-0.5*r2)  # combination of operations
```

Note: In Python, the exponent symbol is denoted by **.

Python also knows vector algebra:

```
print(np.dot(r1,r2))    # Dot product (i.e., scalar product)
print(np.cross(r1,r2))  # Cross products
print(np.cross(r2,r1))  # Remember that the order of operations matters
```

Logical Operations

In programming, we can perform logical operations. These can be conditional statements. A nice review can be found here:

http://en.wikibooks.org/wiki/Python_Programming/Conditional_Statements

An example of this could be, if a value exists in my ARRAY, print it. Here is an example where I want to see if any of my coordinates in "r1" have the value, 0.2:

```
for index in range(len(r1)):
    if r1[index]==0.2:          #logical operation work by tab indentation similar to looping operations
        print ('0.2 is in "r1"')
```

In Python, you could also do this with a list of strings:

```
classList = ['Zeke', 'Xavier', 'Zeki', "Mista Dobalina", 'Zev', 'Tretch', 'Zahlen', 'Zeus']
for index in range(len(classList)):
    if classList[index]=='Zeus':
        print("Zeus is the" ,index+1, 'th student in class')
```

Try writing your own for loop with a conditional statement that prints each of the names in the class list that start with the letter "Z":

```
PLACE FOR LOOP HERE
    if classList[index].startswith('Z'):  #use this conditional statement in your loop
        WHAT HAPPENS WHEN THE CONDITIONAL STATEMENT IS SATISFIED
```

There are also if-else statements: if condition one is met, do this, else, check a second conditional statement, else do something:

```
for index in range(len(classList)):
    if classList[index]=='Mista Dobalina':
        print('Mista Dobalina is in class')
        break      #when the conditional statement is met, this tells python to stop running the loop
```

```
    else:
        print(classList[index],"is not Mista Dobalina")

print('Mista Dobalina, Mista Bob Dobalina')
```

Note when it does not meet the "if" statement, it moves on to print what is in the "else" condition. Once the "if" condition is met, it prints a different line and the "break" command tells the python to stop running the "for" loop and move on to the next code.

Lists of Lists and Dictionary Type Objects

So far we have worked with LISTS/ARRAYS of STRING/FLOAT values. However, the data processing capabilities of Python expand in complexity when you realize that you can make a LIST of LISTS or a LIST of ARRAYS. An example of this might be if you have x and y and z coordiantes for an object at several time points:

```
coordinates = [ [0,0,0], [1,2,3], [2,4,6], [3,8,9] ] #Here we have x,y,z coordinates for four time points

#As usual with LISTS, we can index into an ELEMENT by its order in the LIST

print(coordinates[1]) #Here, we recall the LIST of x,y,z values for the second time point

print(coordinates[1][2]) #Here, we recall the "z" value from the second time point by indexing in a second time
```

Try indexing into "coordinates" to recall the coordiantes in the fourth time point. Then try indexing in twice to recall the "y" value of the third time point:

With LISTS or ARRAYS, we recall their ELEMENTS using the number of their order in the sequence. If instead, we want to recall values by a name we can use an object called a DICTIONARY. Like an actually dictionary, this objects type uses a "key" (some word) to recall some element associated with that "key" (the word's defenition).

Below is an example of a dictionary that stores the same x,y,z values for the four time point that we used above:

```
coordinates = {}    #Curly brackets are used to indicate the object is a DICTIONARY

coordinates['x'] = [0,1,2,3]  #Sets a "key" named "x" to a LISTS of the x values for the four time points
coordinates['y'] = [0,2,4,8]
coordinates['z'] = [0,3,6,9]

print(coordinates)  #This will let us see how Python structures a DICTIONARY type object
```

Let's see how to recall ELEMENTS from a DICTIONARY:

```
print(coordinates['x'])        #Recalls the LIST of "x" values
print(coordinates['y'][2])      #Recalls the "y" value for the 3rd time point
```

```
print(coordinates[1])          #Note how this returns an error
```

The last line of code above returns an error because DICTIONARY objects have no order to their ELEMENTS. The only way to recall a DICTIONARY's ELEMENT is to use the ELEMENT's key, and the INTEGER "1" is not a key in the dictionary we are using.

While we don't use any DICTIONARIES for the rest of this tutorial, we do use object types that have DICTIONARY like attributes. For example, we will use a DATAFRAME type object that we can recall ARRAYS from using a name we give to each ARRAY in the DATAFRAME. More on this soon.

Loading in some battery data, then plotting it

This part of the tutorial gets a little more advanced. Let's say you have some cycling data from the Arbin battery cycler or Gamry potentiostat. You'd like to load it into Python, then plot it. I like to use the "numpy" and "pandas" modules in Python – they simplify and speed up a lot of routine operations that we would like to use. Also, there is a module that allows to you make nice plots called, "matplotlib." Installing these modules is easy with the help of some internet searching if they're not already installed.

First, let's load in these modules:

```
import matplotlib.pyplot as plt
import numpy as np
import pandas as pd
```

In jupyter notebooks, we can add a 'magic" command which embeds zoomable plots into the browser:

```
%matplotlib notebook
#If this command is not used at the beginning, "plt.show()" will need to be used to display any pl
ots
```

When working with new modules and their functions, many python environments have helpful features to see what is in a module and how functions work. Below, place your cursor after the pandas module shortcut, "pd." and type tab to display a dropdown menu of available functions in the Pandas module.

You can scroll through the menu to find what you're looking for or you can start typing a function that you think you might need to narrow down your options. Use this to find the "pd.read_excel" function.

Many functions and objects have documentation, which can tell you how the function works, what kind of inputs it needs, and what it outputs. Try it by typing a "?" after the read_excel function below then run it to see its documentation:

```
pd.
```

Let's use the read_excel function to import some data from the "Arbin_Cycling_Data.xlsx" file included. Open the file in excel to examine its format. We want to get the "Cycle Index", "Charge Capacity", and "Discharge Capacity" data columns from the last sheet in the workbook. Find those columns and fill in the "usecols" parameter below with the corresponding column letters. Note that different instruments may format their .xlsx files differently, so it's best to doublecheck the columns in the sheet you want to upload.

The code below may take a few moments to run because it is running through many operations:

```
cycle_data = pd.read_excel('Arbin_Cycling_Data.xlsx',  #excel file where data is located
        sheet_name=-1,                        #selects the last sheet in the excel workbook to be used
        usecols='ENTER COLUMN LETTERS HERE',          #these are the columns in the excel sheet that data is loaded from
        names=['cycle','charge','discharge'])         #variable names corresponding to each data column

#check to verify data was loaded properly and see how the imported data are structured
print(cycle_data)

#Errors can occur here depending on the version of python you have installed.
#See (parse_cols v. usecols)
#https://stackoverflow.com/questions/48199383/getting-an-error-importing-excel-file-into-pandas-selecting-the-usecols-paramete
#And (sheetname v. sheet_name)
#https://stackoverflow.com/questions/47975866/pandas-read-excel-parameter-sheet-name-not-working
```

This function reads the data into a Pandas DATAFRAME type object, which has similar properties to DICTIONARIES and ARRAYS making it a useful way to import data to be manipulated and plotted.

Specific parts of the data can be recalled from the DATAFRAME by name and/or index within the set.

```
print(cycle_data['charge'])        #recalls the entire set of charge capacity values
print(cycle_data['charge'][9])     #recalls the exact charge capacity for the 10th cycle
```

Now that we have imported the data and learned how to recall specific parts of it, let's make a capacity vs. cycle number plot using "plt.plot". The "plot" function requires an input of the x,y values to be plotted (in that order). The values can be individual FLOATS or an entire column of DATAFRAME values as shown below.

Once plotted, try zooming and shifting the plot using the provided tools at the bottom before pressing the power button to freeze it in place.

```
plt.plot(cycle_data['cycle'],cycle_data['discharge'])
plt.plot(cycle_data['cycle'],cycle_data['charge'])
```

The plot above autoscales the axes to fit all the data and automatically assigns each of the charge and discharge capacity data different colors and plots them as solid lines. Let's enhance the plot by adding labels and custom limits for the axes, a title, a legend, and customizing the color/appearance of the data:

```
#Here we do some simple mathematical manipulation of the capacity data in the same line that w
e plot it

mass = 0.00092          #mass of active material in grams
                        #"1000" is the conversion factor from Ah to mAh

plt.plot(cycle_data['cycle'],cycle_data['discharge']/mass*1000,'b.', label='Discharge Capacity') #"
b." means "blue dot"
plt.plot(cycle_data['cycle'],cycle_data['charge']/mass*1000,'r.', label='Charge Capacity') #"r." me
ans "red dot"

plt.xlabel('Cycle (#)')
plt.ylabel('Specific Capacity (mAh/g)')
plt.xlim(0,50)
plt.ylim(0,600)
plt.legend()   #This function makes a legend for data with labels that were specified when they w
ere plotted
plt.title('Cycle Lifetime of Sb Anode in Li-ion Half Cell')
```

Importing impedance data and making multiple plots

Next, let's try importing and plotting some data from a text file that has some complex header information. In a text editor, open up the provided text file from a Gamry potentiostat: "Gamry_EIS_Data.DTA"

Note how there is a multi-line header with non-data information, followed by a data table for the OCV measurement, followed by another multi-line header before the EIS data-table we are interested in plotting.

If we assume the number of lines before the data we are interested in can change depending on how long the OCV measurement is made, let's make a custom counter to know how many lines to skip before importing the relevant data:

```
datafile = open('Gamry_EIS_Data.DTA', encoding='latin1')
#This lets python open the entire datafile, and tells it how it's encoded
#(otherwise the code hangs on the infinity symbol)

counter=0                  #assigns a variable to an INTEGER as our "line counter"
for line in datafile:          #loops over a sequence were every ELEMENT is a line in the datafile
    counter += 1
    if line.startswith('ZCURVE'):  #"ZCURVE" appears just before the data of interest
        counter += 1
        break            #This stops the for-loop when the if-statement is satisfied
```

```
print(counter)          #Check to see if the counter value seems appropriate for # of lines to skip
```

Let's import the EIS data now that we know how many header lines to skip. See if you can use the function documentation to give "np.genfromtxt" the right inputs to import the EIS from "Gamry_EIS_Data.DTA".

Import at least: Frequency (Freq), Real Impedance (Zreal), Imaginary Impedance (Zimag), Impedance Modulus (Zmod), and Phase Shift (Zphz)

Check to make sure the data imported properly by printing the Freq data and verifying it ranges from values around 10^6 to 10^-1.

```
np.genfromtxt?
```

```
EIS_data = np.genfromtxt(GIVE THE FUNCTION INPUTS HERE)
```

```
print(EIS_data['Freq'])
```

Let's use the EIS data that you've imported to make a Bode plot with Zmod and Zphz vs. Freq on separate y-axes. Fill in the code below:

```
from pylab import figure
Bode_plot = figure()     #this defines a FIGURE that we can make multiple plots on

bode1 = Bode_plot.add_subplot(111)     #assigns variable "bode1" to a subplot in the figure
                                       #the "111" tells the subplot will be in a grid of 1 row, 1 column, in position 1
                                       #more on this later

#Fill in the next line to plot the Zmod data as a function of Freq as blue dots without connecting lines
bode1.plot(FILL IN HERE)
#The Formatting here sets axis labels, the plot title, and scales the axes to be logarithmic
bode1.set_ylabel('Impedance ($\Omega$)',color='b')
bode1.set_yscale('log')
bode1.set_xlabel('Frequency (Hz)')
bode1.set_xscale('log')
bode1.set_title('Bode Plot')

bode2 = Bode_plot.add_subplot(111, sharex=bode1, frameon=False)
                                    #this subplot "bode2" is overlapped with "bode1" and shares its x-axis
                                    #but now we can tell it to have a different y-axis than "bode1"

#Fill in the next line to plot the Zphz data as a function of Freq as red x's without connecting lines
bode2.plot(FILL IN HERE)
```

```
# #The Formatting here sets the axis label and moves it to the right side of the figure
bode2.yaxis.tick_right()
bode2.yaxis.set_label_position("right")
bode2.set_ylabel('Phase Shift (°)',color='r')
```

EIS data is often times plotted in a Nyquist plot (imaginary vs. real impedance). Let's use subplots to plot both Bode and Nyquist plots in the same figure. Fill in below to plot -Zimag vs. Zreal:

```
EIS_fig = figure(figsize=[10,5]) #defines a FIGURE and specifies its width and height

#same as before except now we put the sublot in postition 1 (left) of a 1 row, 2 column plot
bode1 = EIS_fig.add_subplot(121)
bode1.plot(EIS_data['Freq'],EIS_data['Zmod'], 'b.', linestyle='none')
bode1.set_ylabel('Impedance ($\Omega$)',color='b')
bode1.set_yscale('log')
bode1.set_ylabel('Frequency (Hz)')
bode1.set_xscale('log')
bode1.set_title('Bode Plot')

#same as before except now we put the sublot in postition 1 (left) of a 1 row, 2 column plot
bode2 = EIS_fig.add_subplot(121, sharex=bode1, frameon=False)
bode2.plot(EIS_data['Freq'],EIS_data['Zphz'], 'rx', linestyle='none')
bode2.yaxis.tick_right()
bode2.yaxis.set_label_position("right")
bode2.set_ylabel('Phase Shift (°)',color='r')

nyquist = EIS_fig.add_subplot(122)
#now we put the sublot in postition 2 (right) of a 1 row, 2 column plot

#Use the next line to plot the Zimag data as a function of Zreal as black dots without connecting lines
nyquist.plot(FILL IN HERE)
nyquist.set_ylabel('Imag. Impedance ($\Omega$)',color='k')
nyquist.set_xlabel('Real Impedance ($\Omega$)',color='k')
nyquist.set_title('Nyquist Plot')
nyquist.set_aspect('equal',adjustable='datalim') #Nyquist plots should have equally scaled axes

#Try plotting, then place a simple one-line command here to prevent the axis labels from overlapping and plot again:
```

The above figure with two subplots has overlapping axis labels!!! As a demonstration of how many helpful resources are available to help with coding on the internet, do a quick google search:

"python overlapping subplot labels"

You should be able to easily find a one line of code solution to this issue.

Importing, processing, and plotting of voltage data for many cycles

Sometimes it can be useful to plot voltage data from battery cycling over many cycles. Because these data sets become much larger than we've worked with before, we will need to develop new techniques for importing data from multiple sheets in an excel spreadsheet and be able to sort 10's of thousands of rows of data into individual cycles.

Let's take a look at the "Arbin_Cycling_Data.xlsx" file again. Note that there are two separate sheet tabs that make up the complete data set of a combined 73,000 rows of data!

First, import all of it into a pandas DATAFRAME by running the code below. This may take a few moments as the code needs to loop through 73,000 rows of data.

```
#Previously, we used a 'relative path' to load our data,
#because this python file and the desired data are in the same folder.
#Another way to access a file is with an 'absolute path', like shown below.
#Absolute paths are useful if the python file and the data are in different folders.
from os import path
folder = '/Users/maxwellschulze/Desktop/Learning Python Prieto Lab v1/'
filename = 'Arbin_Cycling_Data.xlsx'
filePath = path.join(folder, filename)



from xlrd import open_workbook
workbook = open_workbook(filePath) #opens the entire excel workbook

all_data = pd.DataFrame()    #Assigns variable name "all_data" to an empty DATAFRAME

#loops over all the sheets in the workbook from the 2nd to the 2nd-from-last
for sheet in range(1,workbook.nsheets-1):
    data = pd.read_excel(filename, sheet_name=sheet,
            usecols='B,E,F,H,I,J',
            names=['time','step','cycle','voltage','charge','discharge'])
    all_data = all_data.append(data)  #adds data from each sheet to same DATAFRAME

print(all_data)          #check to see if data was imported correctly
```

Use the space below to plot the battery voltage vs. time for the entire dataset. Then add labels to the plot and use a command to zoom in on just the first couple cycles of the battery so you can make out the voltage profiles for each cycle.

```
plt.plot()
plt.xlabel()
```

```
plt.ylabel()
plt.xlim()
plt.title()
```

Plotting voltage vs. time generates a nice plot because both of those values are continuous over the entire dataset and never reset. In contrast, if we plot voltage vs. discharge and charge capacity (which reset to zero every cycle) we get the following:

```
plt.plot(all_data['charge']/mass*1000,all_data['voltage'], label='Charge')
plt.plot(all_data['discharge']/mass*1000,all_data['voltage'], label='Discharge')
plt.xlabel('Capacity (mAh/g)')
plt.ylabel('Potential (V vs. Li)')
plt.title('Voltage Profiles of Sb Anode in Li-ion Half Cell')
plt.legend()
```

The above plot would be more useful if there weren't all kinds of vertical lines connecting discontinuos data and you could distinguish the voltage profile for each cycle. This can be done by sorting the DATAFRAME by the "cycle" and "step" columns (i.e. charge/discharge step) and recalling and plotting voltage for every cycle and step separately.

First, let's sort the data:

```
#This command sorts the DATAFRAME by values in both the "cycle" and "step" columns
#It returns the sorted data as a new GROUPBY type object.
data_by_cycle = all_data.groupby(['cycle','step'])

#This command will display the size (# of data rows) of each group and demonstrate how the GROUBY object is structured
data_by_cycle.size()
```

Recalling a group of data from this GROUPBY object will return a pandas DATAFRAME which can be used to recall data from as before. To do this we will use the GROUPBY attribute "get_groups".

Below, we will recall a DATAFRAME with the Cycle 5 Discharge data:

```
discharge_index = 2    #A value determined by the user's schedule file on the Arbin instrument

#This recalls a DATAFRAME object that includes only "cycle 5 discharge data"
print(data_by_cycle.get_group((5,discharge_index)))

#You can then recall a specific column from that DATAFRAME as an ARRAY by indexing the column's name
print(data_by_cycle.get_group((5,discharge_index))['voltage'])
```

Now that we can sort and recall data from specific cycles and steps, lets plot voltage vs. discharge/charge capacity for every cycle using a for loop:

```
discharge_index = 2    #A value determined by the experimenter's schedule file on the Arbin instrument
charge_index = 3       #A value determined by the experimenter's schedule file on the Arbin instrument
num_cycles = 100       #Maximum number of cycles for this battery

for cycle in range(1,num_cycles+1):    #loops over all cycles of battery

    #recalls and plots discharge capacity and voltage data for every cycle
    discharge = data_by_cycle.get_group((cycle,discharge_index))['discharge']/mass*1000
    voltage = data_by_cycle.get_group((cycle,discharge_index))['voltage']
    plt.plot(discharge,voltage)

    #same for charge data
    charge = data_by_cycle.get_group((cycle,charge_index))['charge']/mass*1000
    voltage = data_by_cycle.get_group((cycle,charge_index))['voltage']
    plt.plot(charge,voltage)

plt.xlabel('Capacity (mAh/g)')
plt.ylabel('Potential (V vs. Li)')
plt.title('Voltage Profiles of Sb Anode in Li-ion Half Cell')
```

While we can see that the voltage profiles for every cycle and step have been separately plotted (no more vertical lines), python cannot automatically assign different colors to 200 different traces. Instead we can plot only a select number of cycles and steps that we wish to view.

Cycles 1, 2, 10, 50, and 100 would make up a nice representative set. Since we only have a few traces being shown, let's also add labels to each trace and display a legend.

```
for cycle in [1,2,10,50,100]: #The "for" statement now loops over a set of cycle numbers manually provided in a list

    discharge = data_by_cycle.get_group((cycle,discharge_index))['discharge']/mass*1000
    voltage = data_by_cycle.get_group((cycle,discharge_index))['voltage']
    p = plt.plot(discharge, voltage, label='Discharge '+str(cycle)) #Assigns cycle specific label to each discharge trace

#'str()' is a function that converts the "cycle" INTEGER into a STRING onject
#so it can be concatenated onto the end of the 'Discharge' STRING

#To match the charge and discharge curve colors we first give the above discharge plot the variable name "p"
#We can then recall its color below when we set "color = p[0].get_color()" for the charge plot

    charge = data_by_cycle.get_group((cycle,charge_index))['charge']/mass*1000
```

```
    voltage = data_by_cycle.get_group((cycle,charge_index))['voltage']
    plt.plot(charge, voltage, color = p[0].get_color(), linestyle = '--', label='Charge '+str(cycle)) #Assigns cycle specific label to each discharge trace

plt.xlabel('Capacity (mAh/g)')
plt.ylabel('Potential (V vs. Li)')
plt.title('Voltage Profiles of Sb Anode in Li-ion Half Cell')
plt.legend()
```

We can use the same DATAFRAME sorted by cycle to do a slightly more complicated mathematical analysis of our voltage data. A "differential capacity plot" shows dQ/dV vs. V to show subtle features in the voltage profiles.

While we could manually calculate values for dQ (capacity differential) and dV (voltage differential) by taking the difference between a voltage value and the value before it in the array, numpy has a built in function for calculating such values. Tab complete the "np.g" below to find the function that you think might help with this. Remember you can access a function's documentation by typing "?" after it and running the code.

```
np.g
```

Use the numpy function you've discovered to calculate the values for dQ (capacity) and dV (voltage) then plot dQ/dV vs. voltage.

```
for cycle in range(1,num_cycles+1):

    discharge = data_by_cycle.get_group((cycle,discharge_index))['discharge']/mass*1000
    voltage = data_by_cycle.get_group((cycle,discharge_index))['voltage']
    #write your code for calculating dQ and dV for discharge capacities here and plot dQ/dV vs. V
    dq = ???
    dv = ???
    plt.plot(???)

    charge = data_by_cycle.get_group((cycle,charge_index))['charge']/mass*1000
    voltage = data_by_cycle.get_group((cycle,charge_index))['voltage']
    #write your code for calculating dQ and dV for discharge capacities here and plot dQ/dV vs. V
    dq = ???
    dv = ???
    plt.plot(???)

plt.ylabel('dQ/dV')
plt.xlabel('Potential (V vs. Li)')
plt.title('Differential Capacity of Sb Anode in Li-ion Half Cell')
plt.tight_layout()
```

Make the plot more useful to view by displaying only cycles 1, 2, 10, 50, and 100. Add appropriate labels for those cycles to be used in a legend, and zoom in on the interesting part of the plot between 0.6 V and 1.2 V. Change the code appropriately:

```
for cycle in [FILL IN HERE]:

    discharge = data_by_cycle.get_group((cycle,discharge_index))['discharge']/mass*1000
    voltage = data_by_cycle.get_group((cycle,discharge_index))['voltage']
    dqdv = np.gradient(discharge)/np.gradient(voltage)
    p = plt.plot(voltage, dqdv, label=ADD LABEL HERE)

    charge = data_by_cycle.get_group((cycle,charge_index))['charge']/mass*1000
    voltage = data_by_cycle.get_group((cycle,charge_index))['voltage']
    dqdv = np.gradient(charge)/np.gradient(voltage)
    plt.plot(voltage, dqdv, color = p[0].get_color(), label=ADD LABEL HERE)

plt.xlim(FILL IN HERE)
plt.ylabel('dQ/dV')
plt.xlabel('Potential (V vs. Li)')
plt.title('Differential Capacity of Sb Anode in Li-ion Half Cell')
plt.legend()
plt.tight_layout()
```

One way that I've found useful to visualize many cycles at onces, but may not be so useful for generating publishable figures is to use color gradients. Below, I've specified the color for each cycle to be determined by a colormap "gnuplot" which returns a color along a gradient when given an input in between 0 and 1.

```
for cycle in range(1,num_cycles+1):

    discharge = data_by_cycle.get_group((cycle,discharge_index))['discharge']/mass*1000
    voltage = data_by_cycle.get_group((cycle,discharge_index))['voltage']
    dqdv = np.gradient(discharge)/np.gradient(voltage)
    plt.plot(voltage, dqdv, color=plt.cm.gnuplot(cycle/num_cycles)) #color is specified by gnuplot gradient
                                                          #"cycle/num_cycles" is used to give input between 0 and 1

    charge = data_by_cycle.get_group((cycle,charge_index))['charge']/mass*1000
    voltage = data_by_cycle.get_group((cycle,charge_index))['voltage']
    dqdv = np.gradient(charge)/np.gradient(voltage)

    #this conditional statement simply adds labels to only the first and last cycles plotted
    #so when a legend is created it doesn't show 100 different colors (too many)
    if cycle == 1 or cycle == num_cycles:
```

```
        plt.plot(voltage, dqdv, color=plt.cm.gnuplot(cycle/(num_cycles)), label = "Cycle "+str(cycle))
    else:
        plt.plot(voltage, dqdv, color=plt.cm.gnuplot(cycle/num_cycles))

plt.xlim(0.6,1.2)
plt.ylabel('dQ/dV')
plt.xlabel('Potential (V vs. Li)')
plt.title('Differential Capacity of Sb Anode in Li-ion Half Cell')
plt.legend()
plt.tight_layout()
```

Useful Codes for Battery Data.ipynb

Imports packages used in the following codes

```
import matplotlib.pyplot as plt
import numpy as np
import pandas as pd
from pylab import figure
from pylab import rcParams
from xlrd import open_workbook
from itertools import cycle

rcParams['figure.figsize'] = 12, 8 #Sets a reasonable figure size for this notebook
```

Imports data from Arbin excel file and plots discharge and charge vs. cycle on left axis and coulombic efficiency vs. cycle on right axis

```
cycle_data = pd.read_excel('Arbin_Cycling_Data.xlsx',
        sheet_name=-1,
        usecols='A,F,G',    #these columns change depending on which Arbin the data originated
        names=['cycle','charge','discharge'])


mass = 0.00092          #mass of active material in grams
                #"1000" is the conversion factor from Ah to mAh

cycle_fig = figure()

capacity = cycle_fig.add_subplot(111)
capacity.plot(cycle_data['cycle'],cycle_data['discharge']/mass*1000,'b.', label='Discharge Capacity')
capacity.plot(cycle_data['cycle'],cycle_data['charge']/mass*1000,'r.', label='Charge Capacity')
```

```
capacity.set_xlabel('Cycle (#)')
capacity.set_ylabel('Specific Capacity (mAh/g)')
capacity.set_xlim(0,100)
capacity.set_ylim(0,1000)
plt.legend(loc="lower left")

CE = cycle_fig.add_subplot(111, sharex=capacity, frameon=False)
CE.plot(cycle_data['cycle'],
        (cycle_data['charge']/cycle_data['discharge'])*100,'kx', label='Coulombic Efficiency')
CE.yaxis.tick_right()
CE.yaxis.set_label_position("right")
CE.set_ylabel('Coulombic Efficiency (%)',color='k')
CE.set_ylim(60,102)

plt.title('Cycle Lifetime of Sb Anode in Li-ion Half Cell')
plt.legend(loc='upper right')
plt.show()
```

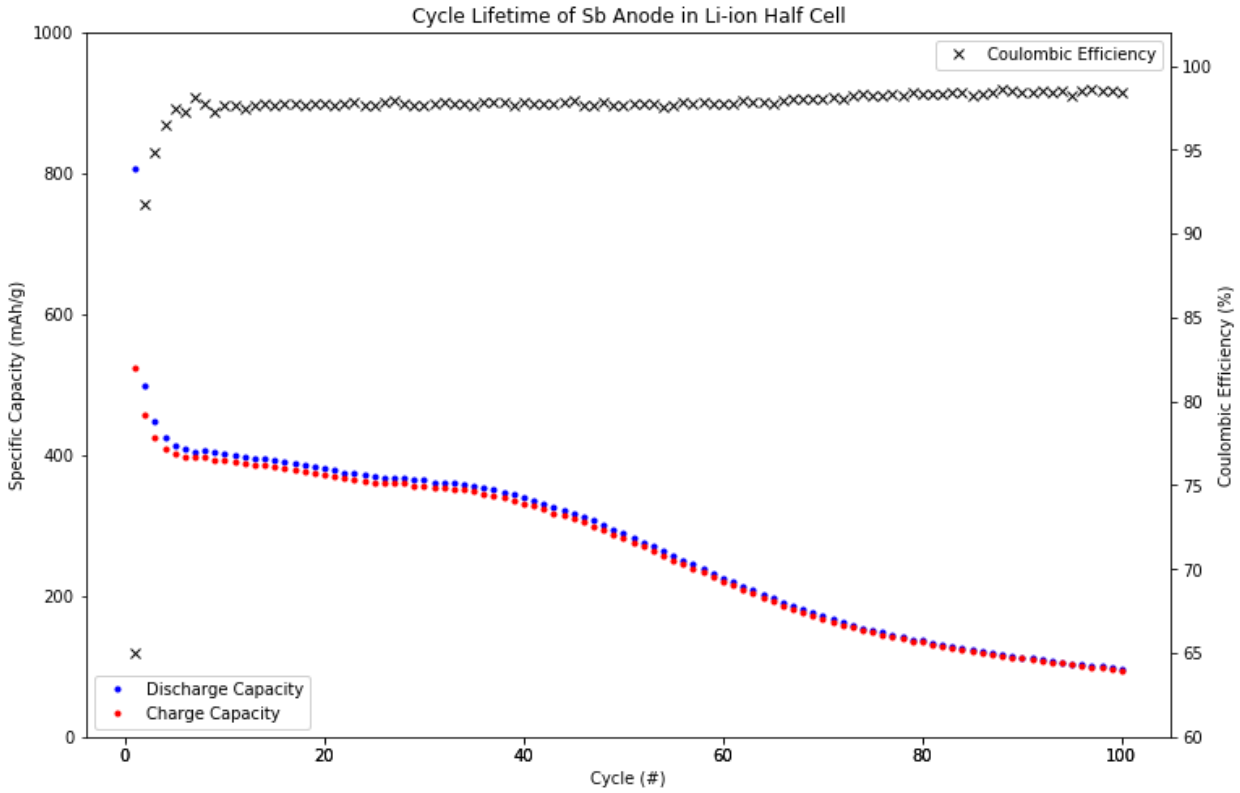

Imports data from Arbin excel file and plots discharge, charge, and excess capacity vs. cycle

```
#cycle_data = pd.read_excel('Arbin_Cycling_Data.xlsx',
 #      sheet_name=-1,
  #     usecols='A,F,G',     #these columns change depending on which Arbin the data originated
   #    names=['cycle','charge','discharge'])
```

```
mass = 0.00092          #mass of active material in grams
                        #"1000" is the conversion factor from Ah to mAh

plt.plot(cycle_data['cycle'],cycle_data['discharge']/mass*1000,linestyle='-', color='b', label='Discharge Capacity')
plt.plot(cycle_data['cycle'],cycle_data['charge']/mass*1000,linestyle='--', color='b', label='Charge Capacity')
plt.plot(cycle_data['cycle'],
    (np.cumsum(cycle_data['discharge']-cycle_data['charge'])/mass*1000),
    linestyle=':', color='b', label='Excess Capacity')

plt.xlabel('Cycle (#)')
plt.ylabel('Specific Capacity (mAh/g)')
plt.xlim(0,100)
plt.ylim(0,1000)
plt.legend()
plt.title('Cycle Lifetime of Sb Anode in Li-ion Half Cell')
plt.show()
```

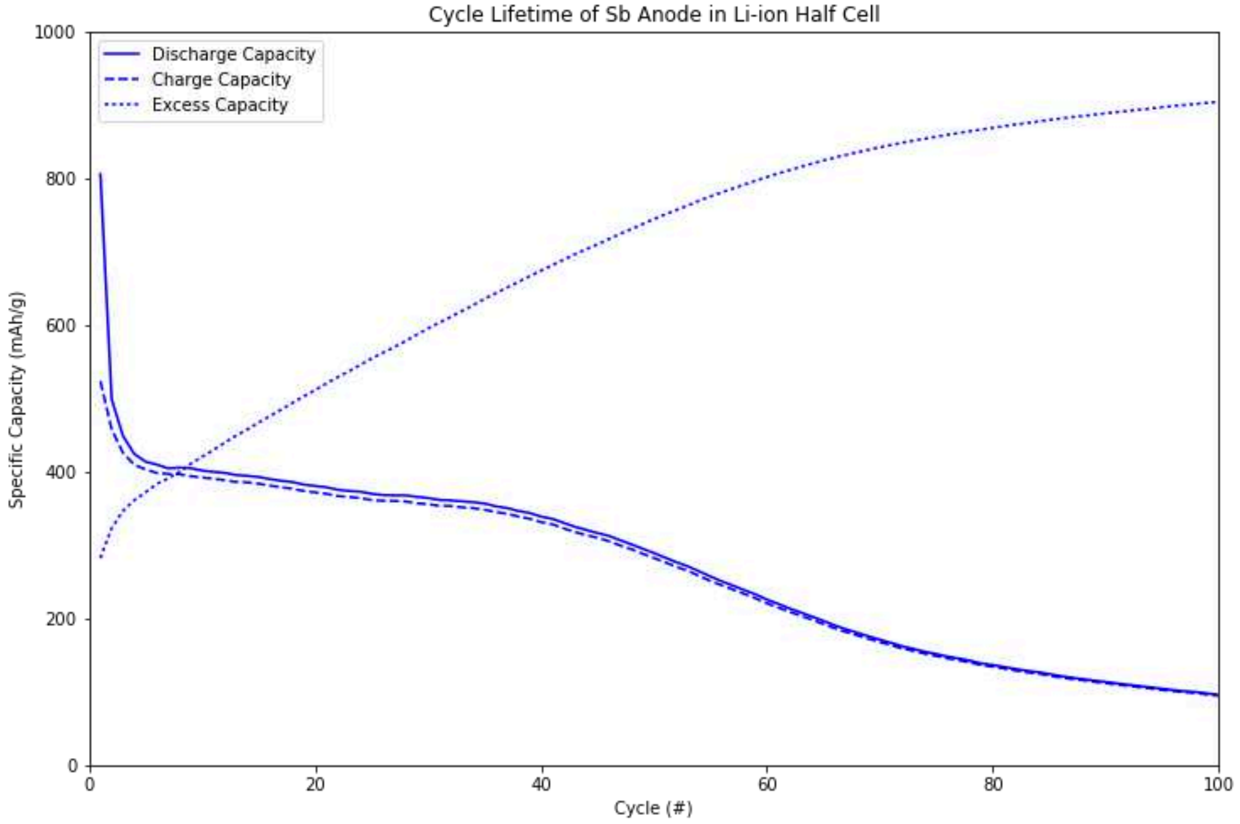

Imports multiple data sets from a list of Arbin excel files and plots discharge, charge, and excess capacity vs. cycle for all of them in different color sets

```
files = ['Arbin_Cycling_Data.xlsx','Arbin_Cycling_Data_2.xlsx','Arbin_Cycling_Data_3.xlsx']

mass = {} #(g)
mass['Arbin_Cycling_Data.xlsx'] = 0.00092    #mass of active material in grams
mass['Arbin_Cycling_Data_2.xlsx'] = 0.00082
mass['Arbin_Cycling_Data_3.xlsx'] = 0.00072

colorcycle = cycle(["b","g","r"]) #an iterable list of colors for data from each sample

for file in files:
    cycle_data = pd.read_excel(file,
            sheet_name=-1,
            usecols='A,F,G',    #these columns change depending on which Arbin the data originated
            names=['cycle','charge','discharge'])

    colors = next(colorcycle)
    plt.plot(cycle_data['cycle'],cycle_data['discharge']/mass[file]*1000,
             linestyle='-', color=colors, label=file+' Discharge Capacity')
    plt.plot(cycle_data['cycle'],cycle_data['charge']/mass[file]*1000,
             linestyle='--', color=colors, label=file+' Charge Capacity')
    plt.plot(cycle_data['cycle'],(np.cumsum(cycle_data['discharge']-cycle_data['charge'])/mass[file
]*1000),
             linestyle=':', color=colors, label=file+' Excess Capacity')

plt.xlabel('Cycle (#)')
plt.ylabel('Specific Capacity (mAh/g)')
plt.xlim(0,100)
plt.ylim(0,1000)
plt.legend()
plt.title('Cycle Lifetime of Sb Anode in Li-ion Half Cell')
plt.show()
```

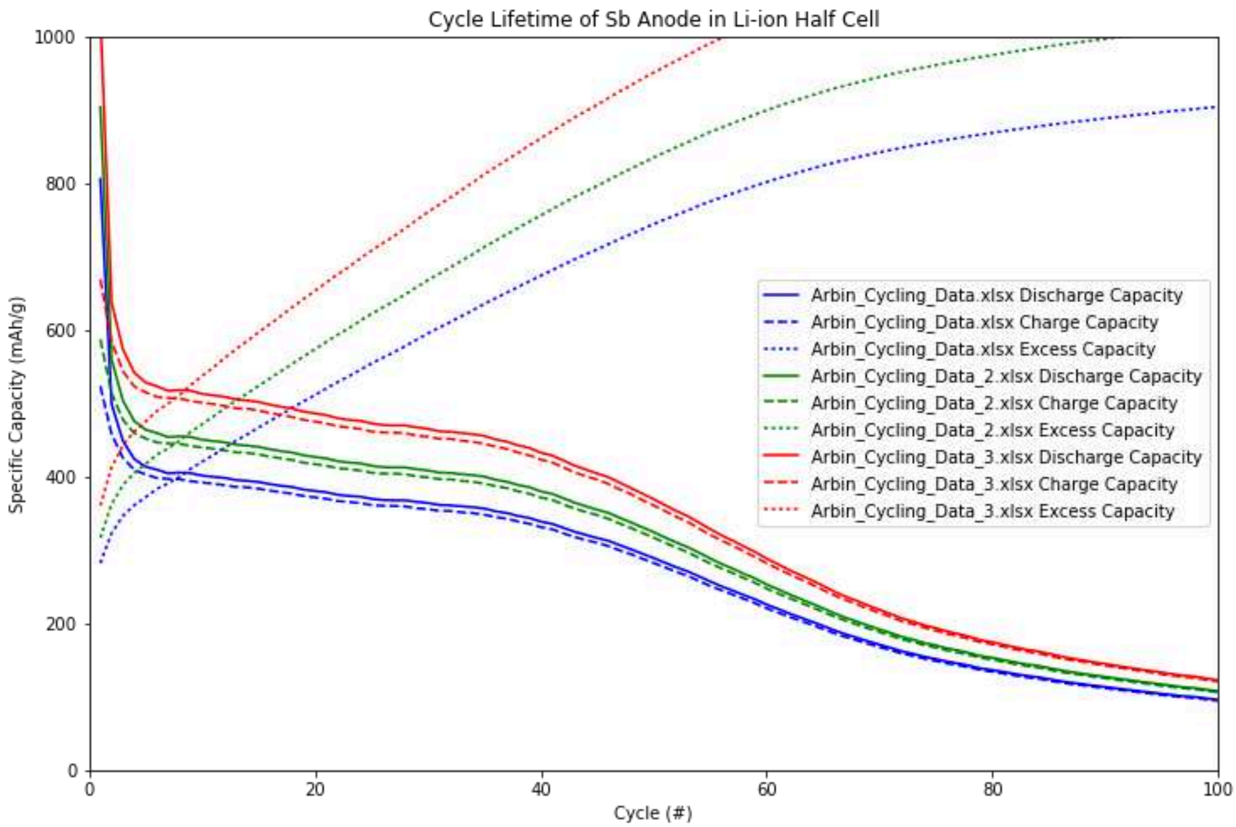

Imports EIS data from Gamry ".DTA" file and outputs Bode plot

```
datafile = open('Gamry_EIS_Data.DTA', encoding='latin1')
#set encoding as "latin1" otherwise the code hangs on the infinity symbol

counter=0
for line in datafile:
    counter += 1
    if line.startswith('ZCURVE'):  #"ZCURVE" appears just before the data of interest
        counter += 1
        break

EIS_data = np.genfromtxt('Gamry_EIS_Data.DTA',
                         skip_header = counter,
                         usecols=(2,3,4,6,7),
                         names=['Freq','Zreal','Zimag','Zmod','Zphz'])

Bode_plot = figure()

bode1 = Bode_plot.add_subplot(111)
bode1.plot(EIS_data['Freq'],EIS_data['Zmod'], 'b.', linestyle='none')
bode1.set_ylabel('Impedance ($\Omega$)',color='b')
```

```
bode1.set_yscale('log')
bode1.set_ylabel('Frequency (Hz)')
bode1.set_xscale('log')
bode1.set_title('Bode Plot')

bode2 = Bode_plot.add_subplot(111, sharex=bode1, frameon=False)
bode2.plot(EIS_data['Freq'],EIS_data['Zphz'], 'rx', linestyle='none')
bode2.yaxis.tick_right()
bode2.yaxis.set_label_position("right")
bode2.set_ylabel('Phase Shift (˚)',color='r')

plt.show()
```

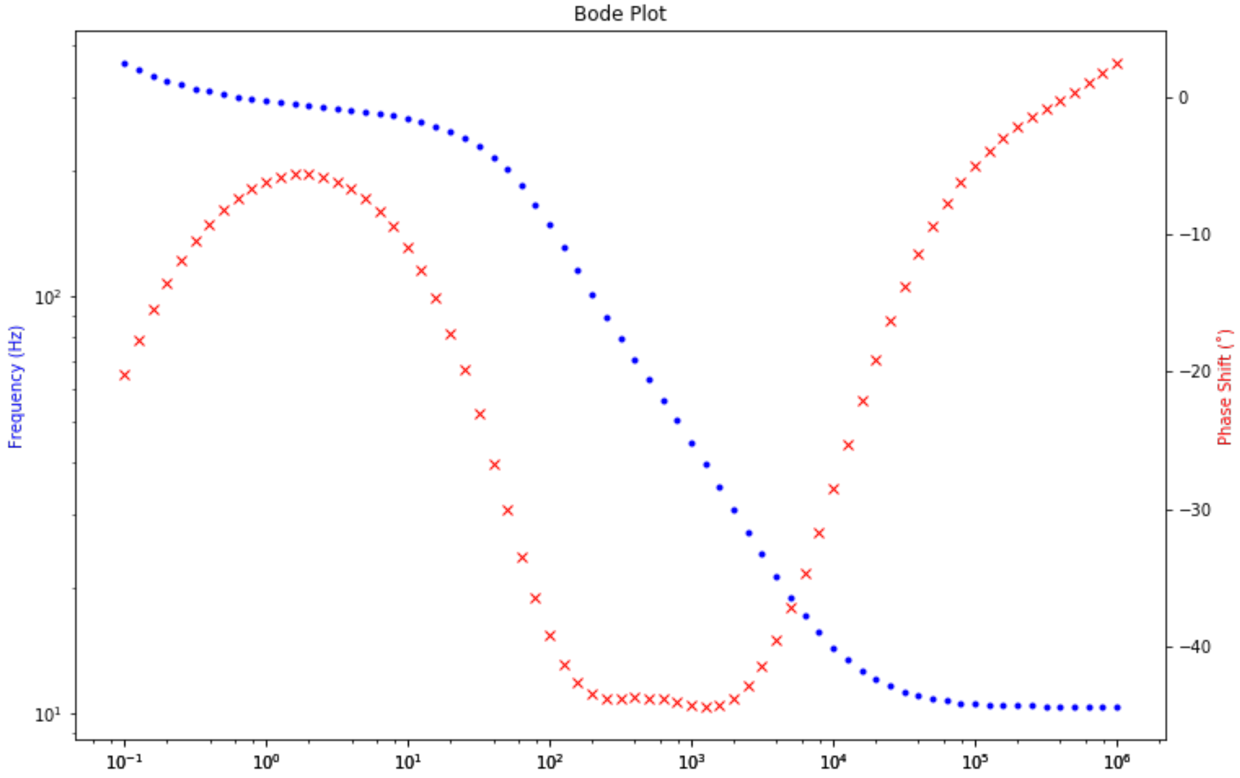

Imports EIS data from Gamry ".DTA" file and outputs Nyquist plot

```
datafile = open('Gamry_EIS_Data.DTA', encoding='latin1')
#set encoding as "latin1" otherwise the code hangs on the infinity symbol

counter=0
for line in datafile:
   counter += 1
   if line.startswith('ZCURVE'):  #"ZCURVE" appears just before the data of interest
      counter += 1
      break
```

```
EIS_data = np.genfromtxt('Gamry_EIS_Data.DTA',
                         skip_header = counter,
                         usecols=(2,3,4,6,7),
                         names=['Freq','Zreal','Zimag','Zmod','Zphz'])

plt.plot(EIS_data['Zreal'],-EIS_data['Zimag'], 'k.', linestyle='none')
plt.ylabel('Imag. Impedance ($\Omega$)',color='k')
plt.xlabel('Real Impedance ($\Omega$)',color='k')
plt.title('Nyquist Plot')
plt.axes().set_aspect('equal', 'datalim') #Nyquist plots should have equally scaled axes
plt.show()
```

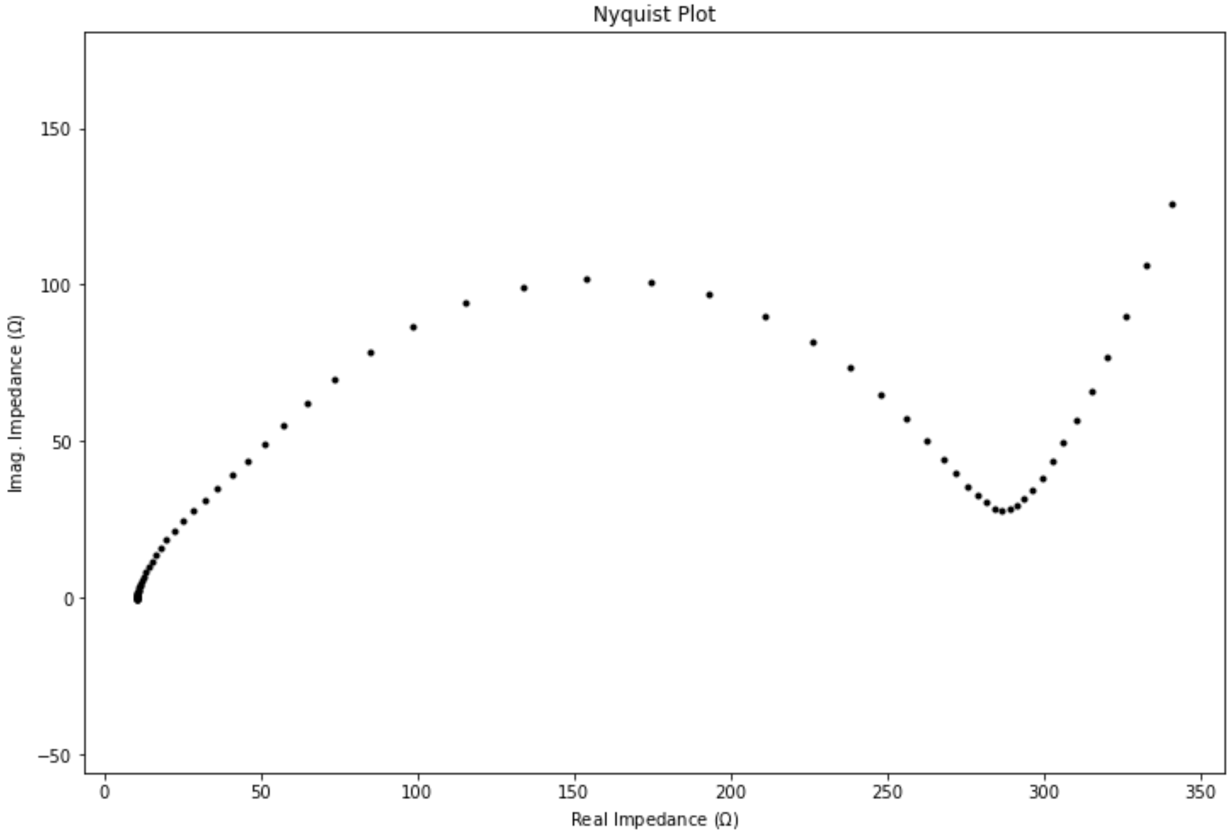

Imports EIS data from Gamry ".DTA" file and outputs Bode and Nyquist plots together

```
datafile = open('Gamry_EIS_Data.DTA', encoding='latin1')
#set encoding as "latin1" otherwise the code hangs on the infinity symbol
counter=0
for line in datafile:
    counter += 1
    if line.startswith('ZCURVE'):  #"ZCURVE" appears just before the data of interest
        counter += 1
        break
```

```
EIS_data = np.genfromtxt('Gamry_EIS_Data.DTA',
                         skip_header = counter,
                         usecols=(2,3,4,6,7),
                         names=['Freq','Zreal','Zimag','Zmod','Zphz'])

EIS_fig = figure(figsize=[14,6])

bode1 = EIS_fig.add_subplot(121)
bode1.plot(EIS_data['Freq'],EIS_data['Zmod'], 'b.', linestyle='none')
bode1.set_ylabel('Impedance ($\Omega$)',color='b')
bode1.set_yscale('log')
bode1.set_ylabel('Frequency (Hz)')
bode1.set_xscale('log')
bode1.set_title('Bode Plot')

bode2 = EIS_fig.add_subplot(121, sharex=bode1, frameon=False)
bode2.plot(EIS_data['Freq'],EIS_data['Zphz'], 'rx', linestyle='none')
bode2.yaxis.tick_right()
bode2.yaxis.set_label_position("right")
bode2.set_ylabel('Phase Shift (˚)',color='r')

nyquist = EIS_fig.add_subplot(122)
nyquist.plot(EIS_data['Zreal'],-EIS_data['Zimag'], 'k.', linestyle='none')
nyquist.set_ylabel('Imag. Impedance ($\Omega$)',color='k')
nyquist.set_xlabel('Real Impedance ($\Omega$)',color='k')
nyquist.set_title('Nyquist Plot')
nyquist.set_aspect('equal',adjustable='datalim') #Nyquist plots should have equally scaled axes

plt.tight_layout()
plt.show()
```

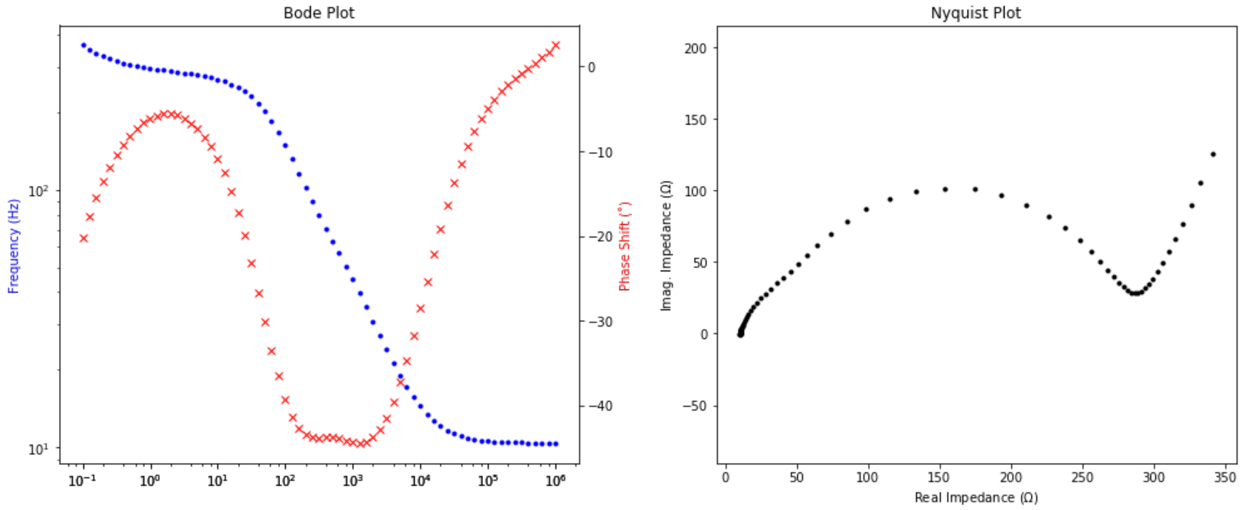

Imports voltage data from Arbin excel file and plots voltage vs. time

```
filename = 'Arbin_Cycling_Data.xlsx'
workbook = open_workbook(filename)

all_data = pd.DataFrame()

for sheet in range(1,workbook.nsheets-1):
  data = pd.read_excel(filename, sheet_name=sheet,
        usecols='B,E,F,H,I,J',
        names=['time','step','cycle','voltage','charge','discharge'])
  all_data = all_data.append(data)

plt.plot(all_data['time']/3600,all_data['voltage'])
plt.xlabel('Time (hours)')
plt.ylabel('Potential (V vs. Li)')
plt.xlim(11,100)
plt.title('Voltage Profile of Sb Anode in Li-ion Half Cell')
plt.show()
```

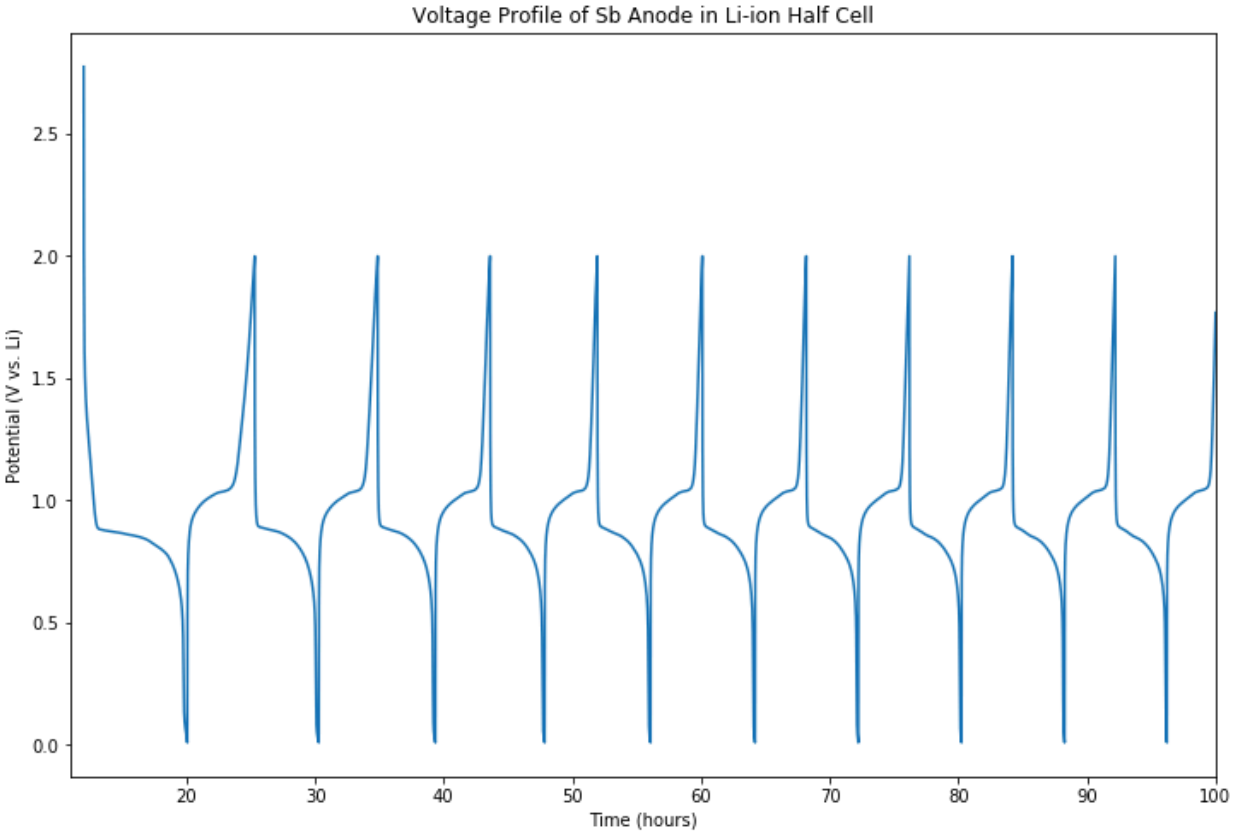

Imports voltage data from Arbin excel file and plots voltage vs. capacity for select cycles

```
discharge_index = 2    #value determined by schedule file on the Arbin instrument
```

```
charge_index = 3      #value determined by schedule file on the Arbin instrument
mass = 0.00092        #mass of active material in grams

filename = 'Arbin_Cycling_Data.xlsx'
workbook = open_workbook(filename)

all_data = pd.DataFrame()

for sheet in range(1,workbook.nsheets-1):
    data = pd.read_excel(filename, sheet_name=sheet,
            usecols='B,E,F,H,I,J',
            names=['time','step','cycle','voltage','charge','discharge'])
    all_data = all_data.append(data)

data_by_cycle = all_data.groupby(['cycle','step'])

for cycle in [1,2,10,50,100]:

    discharge = data_by_cycle.get_group((cycle,discharge_index))['discharge']/mass*1000
    voltage = data_by_cycle.get_group((cycle,discharge_index))['voltage']
    p = plt.plot(discharge, voltage, label='Discharge '+str(cycle))

    charge = data_by_cycle.get_group((cycle,charge_index))['charge']/mass*1000
    voltage = data_by_cycle.get_group((cycle,charge_index))['voltage']
    plt.plot(charge, voltage, color = p[0].get_color(), linestyle='--', label='Charge '+str(cycle))

plt.xlabel('Capacity (mAh/g)')
plt.ylabel('Potential (V vs. Li)')
plt.title('Voltage Profiles of Sb Anode in Li-ion Half Cell')
plt.legend()
plt.show()
```

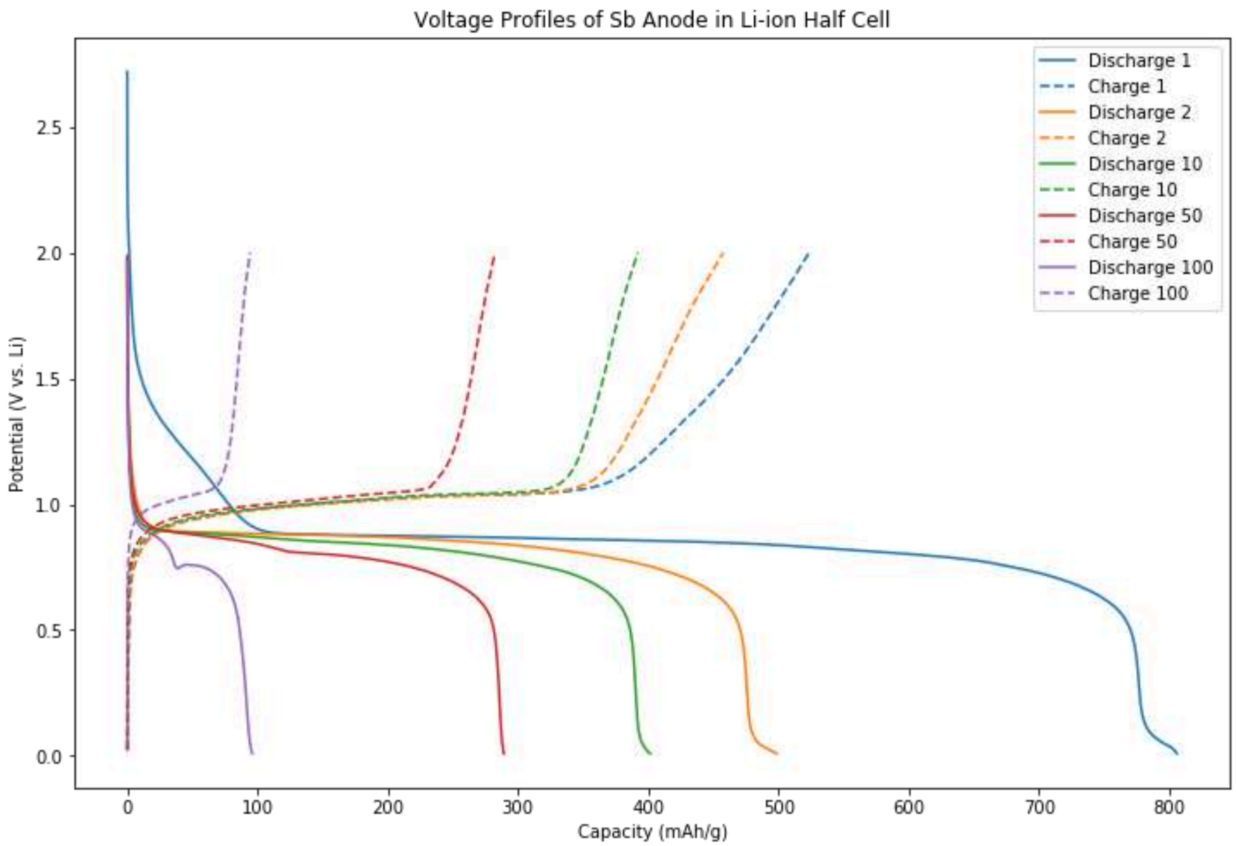

Imports voltage data from Arbin excel file and plots dQ/dV vs. voltage for select cycles

```
discharge_index = 2    #value determined by schedule file on the Arbin instrument
charge_index = 3       #value determined by schedule file on the Arbin instrument
mass = 0.00092         #mass of active material in grams

filename = 'Arbin_Cycling_Data.xlsx'
workbook = open_workbook(filename)

all_data = pd.DataFrame()

for sheet in range(1,workbook.nsheets-1):
    data = pd.read_excel(filename, sheet_name=sheet,
            usecols='B,E,F,H,I,J',
            names=['time','step','cycle','voltage','charge','discharge'])
    all_data = all_data.append(data)

data_by_cycle = all_data.groupby(['cycle','step'])

for cycle in [1,2,10,50,100]:

    discharge = data_by_cycle.get_group((cycle,discharge_index))['discharge']/mass*1000
```

```
    voltage = data_by_cycle.get_group((cycle,discharge_index))['voltage']
    dqdv = np.gradient(discharge)/np.gradient(voltage)
    p = plt.plot(voltage, dqdv, label='Discharge '+str(cycle))

    charge = data_by_cycle.get_group((cycle,charge_index))['charge']/mass*1000
    voltage = data_by_cycle.get_group((cycle,charge_index))['voltage']
    dqdv = np.gradient(charge)/np.gradient(voltage)
    plt.plot(voltage, dqdv, color=p[0].get_color(), label='Charge '+str(cycle))

plt.xlim(0.5,1.3)
plt.ylabel('dQ/dV')
plt.xlabel('Potential (V vs. Li)')
plt.title('Differential Capacity of Sb Anode in Li-ion Half Cell')
plt.legend()
plt.tight_layout()
plt.show()
```

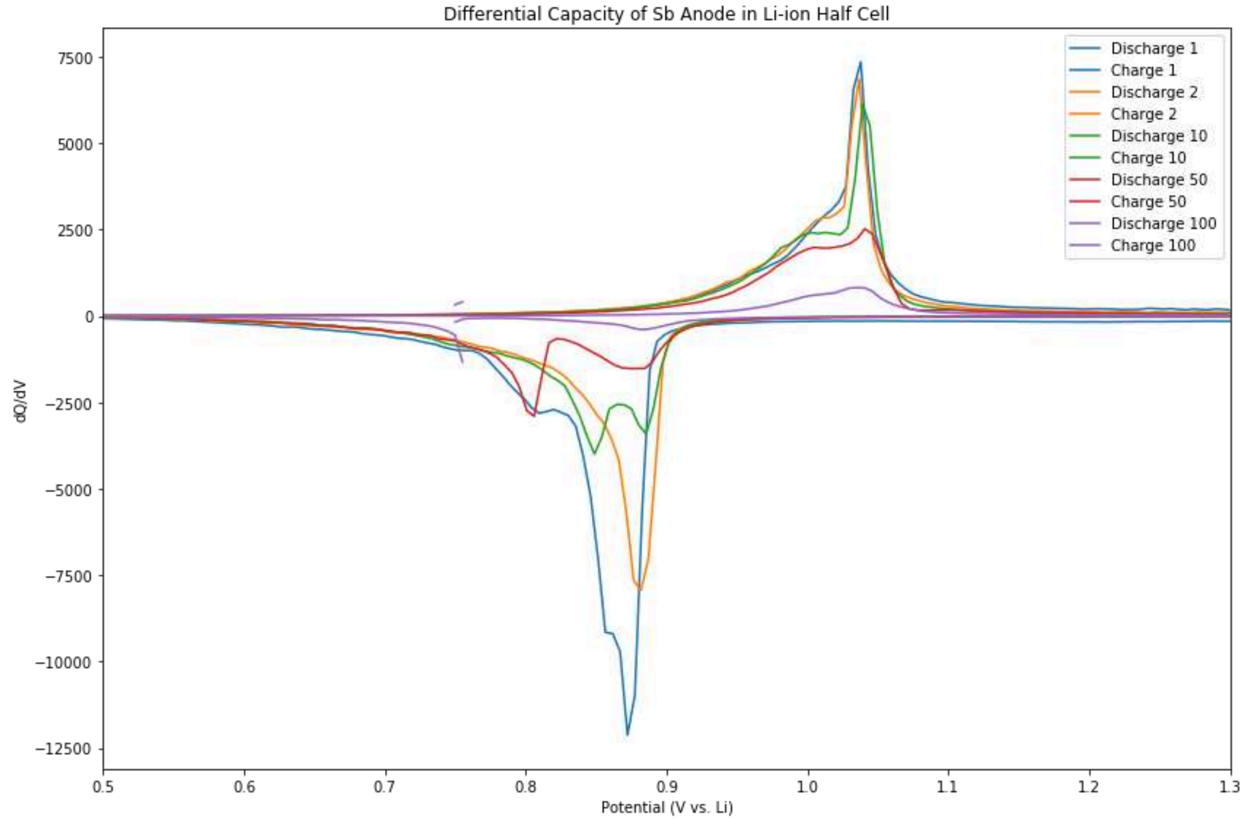

Imports voltage data from Arbin excel file and plots dQ/dV vs. voltage for all cycles with color gradient

```
discharge_index = 2    #value determined by schedule file on the Arbin instrument
charge_index = 3       #value determined by schedule file on the Arbin instrument
mass = 0.00092         #mass of active material in grams
```

```
filename = 'Arbin_Cycling_Data.xlsx'
workbook = open_workbook(filename)

all_data = pd.DataFrame()

for sheet in range(1,workbook.nsheets-1):
    data = pd.read_excel(filename, sheet_name=sheet,
            usecols='B,E,F,H,I,J',
            names=['time','step','cycle','voltage','charge','discharge'])
    all_data = all_data.append(data)

data_by_cycle = all_data.groupby(['cycle','step'])

num_cycles = all_data['cycle'].iat[-1]-1
for cycle in range(1,num_cycles+1):

    discharge = data_by_cycle.get_group((cycle,discharge_index))['discharge']/mass*1000
    voltage = data_by_cycle.get_group((cycle,discharge_index))['voltage']
    dqdv = np.gradient(discharge)/np.gradient(voltage)
    plt.plot(voltage, dqdv, color=plt.cm.gnuplot(cycle/num_cycles))

    charge = data_by_cycle.get_group((cycle,charge_index))['charge']/mass*1000
    voltage = data_by_cycle.get_group((cycle,charge_index))['voltage']
    dqdv = np.gradient(charge)/np.gradient(voltage)

    #adds labels to only first and last cycles so legend isn't huge
    if cycle == 1 or cycle == num_cycles:
        plt.plot(voltage, dqdv, color=plt.cm.gnuplot(cycle/(num_cycles)), label = "Cycle "+str(cycl
e))
    else:
        plt.plot(voltage, dqdv, color=plt.cm.gnuplot(cycle/num_cycles))

plt.xlim(0.6,1.2)
plt.ylabel('dQ/dV')
plt.xlabel('Potential (V vs. Li)')
plt.title('Differential Capacity of Sb Anode in Li-ion Half Cell')
plt.legend()
plt.tight_layout()
plt.show()
```

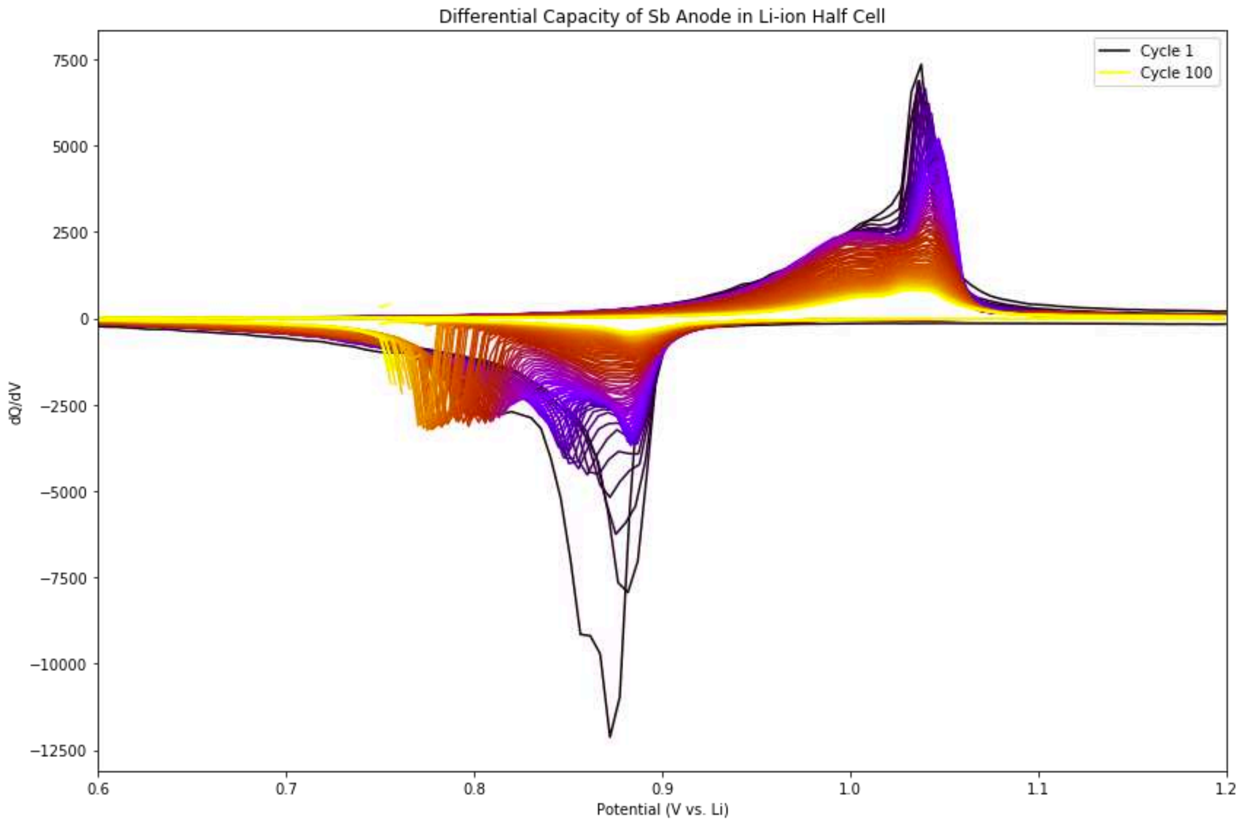
Differential Capacity of Sb Anode in Li-ion Half Cell
Cycle 1
Cycle 100
7500
5000
2500
0
−2500
−5000
−7500
−10000
−12500
dQ/dV
0.6
0.7
0.8
0.9
1.0
1.1
1.2
Potential (V vs. Li)

APPENDIX E – [EEEEE!!!] SOME PIKA PICTURES FOR YOUR ENJOYMENT

Near Mount of the Holy Cross, 6:56 am, July 29, 2018

Near Maroon Peak,
9:32 am, September 20, 2018

Near Mount of the Holy Cross,
7:03 am, July 29, 2018

Near Fancy Lake, Colorado,
6:57 pm, July 22, 2017

Near Ptarmigan Lake, Colorado,
2:24 pm, September 18, 2016

Pictures taken by Maxwell Schulze.